Transactions of the ASME

EDITORIAL STAFF
Mng. Dir., Publ., J. J. FREY
Director, Technical Publishing, JOS. SANSONE
Managing Editor, CORNELIA MONAHAN
Editorial Production Assistant, BETH DARCHI

FLUIDS ENGINEERING DIVISION
Technical Editor
FRANK M. WHITE (1984)
Executive Secretary
L. T. NELSON (1984)
Calendar Editor
M. F. ACKERSON

Associate Editors
Fluid Machinery
BUDUGUR LAKSHMINARAYANA (1982)
WILLIAM E. THOMPSON (1984)
Fluid Measurements
THEODORE R. HEIDRICK (1984)
Fluid Mechanics
SHLOMO CARMI (1984)
CHARLES DALTON (1983)
KIRTI N. GHIA (1984)
BRIAN E. LAUNDER (1982)
Fluid Transients
M. HANIF CHAUDHRY (1983)
Polyphase Flow
PAUL H. ROTHE (1983)
OKITSUGU FURUYA
Review Articles
KENNETH E. HICKMAN (1982)

FOREIGN CORRESPONDENTS
Europe and Russia
JACQUES CHAUVIN
Europe and Russia
JOHN H. HORLOCK
India and Middle East
ARUN PRASAD
Japan and China
YASUTOSHI SENOO

BOARD ON COMMUNICATIONS
Chairman and Vice President
MICHAEL J. RABINS

Members-at-Large
W. BEGELL, J. CALLAHAN, M. HELMICH, D. KOENIG, M. KUTZ, F. LANDIS, J. W. LOCKE, J. ORTLOFF, C. PHILLIPS, K. REID

OFFICERS OF THE ASME
President, ROBERT B. GAITHER
Executive Director and Sec'y, BURKE E. NELSON
Treasurer, ROBERT A. BENNETT

The Journal of FLUIDS ENGINEERING (USPS 278-480) is edited and published quarterly at the offices of The American Society of Mechanical Engineers, United Engineering Center, 345 E. 47th St., New York, N. Y. 10017. Cable Address, "Mechaneer," New York. **Second-class** postage paid at New York, **CHANGES OF ADDRESS** must be received at Society headquarters seven weeks before they are to be effective. Please send old label and new address. **PRICES:** To members, $30.00, annually; to nonmembers, $60.00. Single copies, $20.00 each. Add $5.00 for postage to countries outside the United States and Canada. **STATEMENT** from By-Laws. The Society shall not be responsible for statements or opinions advanced in papers or . . . printed in its publications (B7.1, Par. 3).

INDEXED by the Engineering Index, Inc.

Journal of Fluids Engineering

Published Quarterly by The American Society of Mechanical Engineers

VOLUME 104 • NUMBER 3 • SEPTEMBER 1982

270 Fluids Engineering Calendar

274 Professor Dr. Hermann Schlichting—In Memory

275 Recent Developments in Particulate/Gas Separation
M. S. Ojalvo

276 Particle Sizing Techniques and Their Applications
R. A. Bajura and F. Durst

277 Assessment of Present and Future Directions of Polyphase Transport
C. T. Crowe

279 REVIEW—Theoretical Models of Gas-Liquid Flows
G. B. Wallis

284 REVIEW—Combined Measurements of Particle Velocities, Size Distributions, and Concentrations
Franz Durst

297 REVIEW—Numerical Models for Dilute Gas-Particle Flows
C. T. Crowe

304 Two-Way Coupling Effects in Dilute Gas-Particle Flows (82-WA/FE-1)
M. Di Giacinto, F. Sabetta, and R. Piva

313 Diagnostic Measurements of Fuel Spray Dispersion
J. M. Tishkoff, D. C. Hammond, Jr., and A. R. Chraplyvy

318 Fluid Structure Interaction in Piping by Component Synthesis
F. J. Hatfield, D. C. Wiggert, and R. S. Otwell

326 The Form Drag of Three-Dimensional Bluff Bodies Immersed in Turbulent Boundary Layers
H. Sakamoto, M. Moriya, S. Taniguchi, and M. Arie

335 Transient Response of Fluid Viscoelastic Lines
E. Rieutord

342 Experiments on Fluidelastic Instability of Cylinders Clusters in Axial Flow
M. P. Paidoussis, Ll. R. Curling, and J. O. Gagnon

350 Curved Ducts With Strong Secondary Motion: Velocity Measurements of Developing Laminar and Turbulent Flow
A. M. K. P. Taylor, J. H. Whitelaw, and M. Yianneskis

360 The Viscous-Gravity Jet in Stagnation Flow
J. O. Cruickshank and B. R. Munson

363 Observations and Measurements of Flow in a Partially-Filled Horizontally Rotating Cylinder
R. F. Gans and S. M. Yalisove

367 The Structure of Turbulent Plane Couette Flow
M. M. M. El Telbany and A. J. Reynolds

373 Drag-Characterization Method for Arbitrarily Rough Surfaces by Means of Rotating Disks
P. S. Granville

378 On the Prediction of Swirling Flowfields Found in Axisymmetric Combustor Geometries
D. L. Rhode, D. G. Lilley, and D. K. McLaughlin

385 Flow Aerodynamics Modeling of an MHD Swirl Combustor: Calculations and Experimental Verification
A. K. Gupta, J. M. Beér, J. F. Louis, A. A. Busnaina, and D. G. Lilley

393 A Study of Shock Waves in Three-Dimensional Transonic Flow
W. N. Dawes and L. C. Squire

Technical Brief

400 Spreading Rate Reattachment of Coaxial Jets of High Mean-Velocity Ratio
N. W. M. Ko and H. Au

402 Discussion on Previously Published Papers

Announcements and Special Notices

269 New ASME Prior Publication Policy

269 Submission of Papers

269 Statement of Experimental Uncertainty

296 Call for Papers—Fourth Symposium on Turbulent Shear Flow

303 Call for Participation—Industrial Forum on Fluid Transients

312 Call for Papers—Mini-Symposium on Advances in Grid Generation

334 Errata on a Previously Published Paper by I. C. Shepherd

341 Call for Papers—Symposium on Unsteady Turbulent Boundary Layers and Friction

359 Call for Papers—1983 Winter Annual Meeting

377 Call for Papers—Symposium on Measurements in Fluid Transients

392 Call for Papers—1984 Fluids Engineering Conference

406 Symposium on Aerodynamics of Transportation

Professor Dr. Hermann Schlichting – In Memory

Professor Dr. Hermann Schlichting

Professor Emeritus Dr.-Phil Dr.-Ing HERMANN SCHLICHTING died on June 15, 1982, at the age of 75, in Göttingen, Germany. He was one of the great men of our subject and of our times. As a likable, happy man with an uncomplicated character and sharp scientific mind, he gloried in the study of the motion of fluids. His contributions are his legacy to us and will be a storehouse of information and a source of inspiration for many generations to come. His deep physical insight, mathematical ability of high order, and skill in the design and execution of many experiments inspired generations of engineers and scientists. His death impoverishes us all. The fluids engineering community and The American Society of Mechanical Engineers extend their deepest sympathies to Frau Schlichting.

EDITOR'S NOTE:

The following three short articles summarize the activities of the three panel sessions held at Century Two Emerging Technology Conference Symposium on Polyphase Flow and Transport Technology, which took place in August 1980. These summaries are followed by three longer Review Articles—by G. B. Wallis, F. Durst, and C. Crowe—which are updated versions of the keynote papers those authors delivered at the conference. This symposium opened up some interesting new research areas in polyphase flow, and it is appropriate that the highlights have been gathered together here for the JFE readership.

Recent Developments in Particulate/Gas Separation

M. S. Ojalvo[1]

1 Introduction

Recently there has been a substantial growth in research dealing with new concepts and methods in particulate/gas separation, such as electrostatic filtration, high gradient magnetic separation, the utilization of acoustics in particulate/gas separation, and other methods. Some of the most recent advances in this field were discussed by a panel during the "Symposium on Polyphase Flow and Transport Technology," ASME Century 2—Emerging Technology Conferences, August 13-15, 1980. The following is a brief summary of the presentations by the members of the panel.

2 Electrostatically Enhanced Fibrous and Fabric Filtration

Following a brief introductory statement by the Panel Moderator, Dr. M. S. Ojalvo, a presentation on the stated subject was made by Dr. T. Ariman of the University of Tulsa. According to him, fine particulates, smaller than 3 μm in aerodynamic diameter, are of great concern because they persist in the atmosphere without settling out rapidly, penetrate human beings' natural defenses, and lodge themselves in the lungs. Fine particles in the 0.1 to 1 μm range also are the most difficult to collect. This difficulty has made fine particles the focus of intense pollution technology interest in recent years. Among several control means, fibrous filters are mostly utilized for the efficient removal of submicron sized particles from gases. Recent experimental and analytical investigations have shown that the electrostatic charge on fibers and/or particles effectively assist filtration by attracting particles from a greater distance, influencing particle agglomeration and thus collection efficiency and service life. In the first part of the presentation by Ariman, some of the recent developments in the analytical investigations of electrostatically enhanced fibrous filters were reviewed.

On the other hand, fabric filtration systems have been employed in industry for over a century with relatively few technological modifications. However, with the recent substantial increases in energy costs, attention has been given to operating expenses (e.g., energy consumption). As a result, the filtration systems of yesteryear may not be the best approach for future applications. Recently, an external electric field has been considered in fabric filtration of industrial dust with promising results. An increase in the collection efficiency, especially for fine particulates, and a decrease in pressure drop was observed. The second part of the presentation by Ariman was devoted to the discussion of the recent developments in electrostatic fabric filtration of industrial dust and its possible extension to the control of diesel emissions.

[1] Director, Particulate and Multiphase Processes Program, National Science Foundation, Washington, D.C. 20550.

Contributed by the Fluids Engineering Division for publication in the JOURNAL OF FLUIDS ENGINEERING.

3 Recent Developments in the Theory and Performance of Fibrous Filters

According to Dr. W. Bergman of Lawrence Livermore National Laboratory, one of the most efficient and cost effective means for removing airborne particles from gas streams is the use of fibrous filters. Recent developments in electrifying fibrous filters have significantly enhanced their already good performance. Experiments have shown that electrifying the filter increases its efficiency and its service life. The techniques used for continuously electrifying the filter include precharging the aerosols, polarizing the filter fibers with an external field, or both. When the electrification process is turned off, the filter returns to its original nonelectrified state. A new permanently charged filter, made from electret fibers, has also been recently developed. This filter has similar properties to the electrified filters generated by electric fields. These new developments have already been incorporated into commercially available filters.

New theoretical studies of the electrified filter have also been conducted by Dr. Bergman and his associates which show the increased efficiency is due to a complex, dynamic process involving charge accumulation and dissipation on the filter fibers and electric fields due to the fiber charge, the filter bed charge, and the external electric field. The theoretical explanation for the increased service life has also been developed based on an increased surface deposit and more compact morphology around individual fibers.

In addition to the above developments on electrified filters, Dr. Bergman indicated that major progress has been recently made in understanding the complex process of filter clogging. The major theoretical and experimental findings were reviewed.

4 Some Observations of the Influence of an Applied Electric Field on Particle-Air Systems

Dr. G. Clover of Iowa State University briefly discussed his research in the stated field. Glass and copper particles were tested in the electric suspension (clouds of particles), the electrofluidized bed, and the electropacked bed. Experimental observations were made on the influence of an applied electric field (ac and dc) in altering the heat, mass, momentum, and charge transfer characteristics for particle diameters greater than 20 μm. Dr. Clover's important observations include the following: (1) that the concept of saltation velocity in horizontal pneumatic transport is unnecessary in the electric suspension, (2) the diffusion process for near-spheres has been isolated in the electric suspension with measured diffusion coefficients $\sim 10^{-3} m^2/s$; (3) that injected bubbles and gas diffusion can be tracked in-situ in the electrofluidized and the electropacked beds by measuring particle surface resistivity.

5 "Charging" Ahead with Fabric Filters

E. R. Frederick of the Air Pollution Control Association indicated that from extensive experimental data with substantial field verification, it is evident that naturally produced electrostatic charges play a critically important role in the

filtration process and can be utilized to provide optimum operational parameters. When the filter medium and collected particulate are appropriately balanced electrostatically, performance in terms of pressure drop, efficiency, cleanability and durability are maximized.

Most, but not all, particulates form porous aggregates and this transformation is the important consequence of a favorable filter/dust electrostatic relationship. For particulates that experience this type of cake formation readily, the conversion occurs simply by even the moderate electrostatic charge polarity differences occurring naturally between the medium and the particles. Some dusts attain the porous cake structure only with filter fabrics that develop charges of high intensity and long duration. Fortunately, only relatively few dusts do not form porous aggregates on the filter surface regardless of the electrostatic balance achieved. Even these can be collected efficiently, however, with media that offer suitable electrostatic features.

According to Frederick, while filter fabric quality as well as performance may be determined quite simply by triboelectrification tests, these same properties for particulates are not so readily defined. However, he stated that by conducting bench scale experimental filtration tests and employing suitable supporting instruments, information may be obtained to specify the role of electrostatics in the collection process. In this way, filtration performance can be related to the electrostatic charge polarity, magnitude and sometimes discharge rate of the media.

6 High Gradient Magnetic Separation

David Kelland of MIT presented a concise summary of the research work at MIT in the stated field. He pointed out that various particulates can be separated from each other or from a carrier fluid by taking advantage of differences in their magnetic susceptibilities. High gradient magnetic separation, a technique developed at the Francis Bitter National Magnet Laboratory at MIT for dealing with paramagnetic particulates, has now been applied to materials whose susceptibilities range over nine orders of magnitude, from ferromagnetic to diamagnetic. Applications of this technique to particule collection from gases include direct coal desulfurization and steel furnace dust collection. In addition to matrix separators such as HGMS devices, open gradient magnetic separators and fluidized beds have been used to make particulate/gas separations.

7 Closing Remarks

The general consensus of the panel discussion was that a substantial progress was being made particularly with the laboratory scale experiments in the use of electrostatics in fibrous and fabric filters, electrofluidized and electropacked beds. Electrostatics appears to have a strong effect in the control of fine particulates by providing an increase in the collection efficiency. A substantial decrease in the pressure drop, i.e., an important savings in energy consumption was also observed in both fabric and fibrous filtration of particulates.

An important recent development was also reported that high gradient magnetic separation has now been applied to diamagnetic particles.

Particle Sizing Techniques and Their Applications

R. A. Bajura[1] and F. Durst[2]

1 Introduction

Measurements of particle velocities, size distributions, and concentration are of considerable interest to environmental control and protection agencies as well as engineers and scientists working on aerosol problems. In these areas, the need for detailed experimental investigations has been expressed on many occasions. A panel session was organized as part of the "Symposium on Polyphase Flow and Transport Technology" at the ASME Century 2—Emerging Technologies Conference, August, 1980, to address topics in the measurement of aerosols. The following is a brief description of subjects treated by the panel.

2 Panel Membership

The panel was organized by F. Durst with assistance from R. Bajura and R. Arndt. A cross-section of experts was sought to address the wide range of topics encountered in aerosol research. The panel consisted of the following members:

Dr. Franz Durst (Chairman)
Sonderforschungsbereich 80
University of Karlsruhe

Dr. H. Fissan
Institut für Aerosoltechnik
Gesamthochschule Duisburg

Dr. B. Harris
Process Measurements Section
Control Systems Laboratory,
U.S. EPA

Dr. B.Y.H. Liu
Mechanical Engineering Dept.
University of Minnesota

Dr. D. A. Lundgren
Department of Environmental Engineering Sciences
University of Florida

Dr. G. Newton
Lovelace Biomedical & Environmental Center
Albuquerque, NM

3 Presentations by Panelists

Topics discussed by the panelists were separated into four major areas which were summarized during short presentations by the following persons:

1. Transport Characteristics of Particle Sizing Equipment (Fissan/Liu)
2. Mechanical Particle Collectors and Their Employment (Harris/Newton)
3. Optical Particle Sizing Systems and Other Non-Intrusive Techniques (Durst/Fissan)
4. Application of Particle Sizing Equipment (Liu/Lundgren)

Audience participation in the discussion occurred after the presentations in the above four areas and at the conclusion of the session.

Transport losses in sampling lines must be considered in determining the true characteristics of flowing aerosols. Deposition of particles by settling and/or turbulent transport on the walls of the sampling tube or by impaction due to particle inertia in bends, will lead to an underestimation of the particulate loading in a stream. The size distribution in the collected sample will also be altered since the larger particles are preferentially deposited. Concern must also be given to the possibility of the condensation of water vapor which could lead to agglomeration of particles. Further chemical reaction may also occur in the sampling lines.

Mechanical particle collectors based upon the principle of inertial separation in devices such as cyclones are typically

[1]Mechanical and Aerospace Engineering, West Virginia University, Morgantown, West Va. 26506.
[2]Institute of Hydromechanics, University of Karlsruhe, Karlsruhe, West Germany.
Contributed by the Fluids Engineering Division for publication in the JOURNAL OF FLUIDS ENGINEERING.

filtration process and can be utilized to provide optimum operational parameters. When the filter medium and collected particulate are appropriately balanced electrostatically, performance in terms of pressure drop, efficiency, cleanability and durability are maximized.

Most, but not all, particulates form porous aggregates and this transformation is the important consequence of a favorable filter/dust electrostatic relationship. For particulates that experience this type of cake formation readily, the conversion occurs simply by even the moderate electrostatic charge polarity differences occurring naturally between the medium and the particles. Some dusts attain the porous cake structure only with filter fabrics that develop charges of high intensity and long duration. Fortunately, only relatively few dusts do not form porous aggregates on the filter surface regardless of the electrostatic balance achieved. Even these can be collected efficiently, however, with media that offer suitable electrostatic features.

According to Frederick, while filter fabric quality as well as performance may be determined quite simply by triboelectrification tests, these same properties for particulates are not so readily defined. However, he stated that by conducting bench scale experimental filtration tests and employing suitable supporting instruments, information may be obtained to specify the role of electrostatics in the collection process. In this way, filtration performance can be related to the electrostatic charge polarity, magnitude and sometimes discharge rate of the media.

6 High Gradient Magnetic Separation

David Kelland of MIT presented a concise summary of the research work at MIT in the stated field. He pointed out that various particulates can be separated from each other or from a carrier fluid by taking advantage of differences in their magnetic susceptibilities. High gradient magnetic separation, a technique developed at the Francis Bitter National Magnet Laboratory at MIT for dealing with paramagnetic particulates, has now been applied to materials whose susceptibilities range over nine orders of magnitude, from ferromagnetic to diamagnetic. Applications of this technique to particule collection from gases include direct coal desulfurization and steel furnace dust collection. In addition to matrix separators such as HGMS devices, open gradient magnetic separators and fluidized beds have been used to make particulate/gas separations.

7 Closing Remarks

The general consensus of the panel discussion was that a substantial progress was being made particularly with the laboratory scale experiments in the use of electrostatics in fibrous and fabric filters, electrofluidized and electropacked beds. Electrostatics appears to have a strong effect in the control of fine particulates by providing an increase in the collection efficiency. A substantial decrease in the pressure drop, i.e., an important savings in energy consumption was also observed in both fabric and fibrous filtration of particulates.

An important recent development was also reported that high gradient magnetic separation has now been applied to diamagnetic particles.

Particle Sizing Techniques and Their Applications

R. A. Bajura[1] and F. Durst[2]

1 Introduction

Measurements of particle velocities, size distributions, and concentration are of considerable interest to environmental control and protection agencies as well as engineers and scientists working on aerosol problems. In these areas, the need for detailed experimental investigations has been expressed on many occasions. A panel session was organized as part of the "Symposium on Polyphase Flow and Transport Technology" at the ASME Century 2—Emerging Technologies Conference, August, 1980, to address topics in the measurement of aerosols. The following is a brief description of subjects treated by the panel.

2 Panel Membership

The panel was organized by F. Durst with assistance from R. Bajura and R. Arndt. A cross-section of experts was sought to address the wide range of topics encountered in aerosol research. The panel consisted of the following members:

Dr. Franz Durst (Chairman)
Sonderforschungsbereich 80
University of Karlsruhe

Dr. H. Fissan
Institut für Aerosoltechnik
Gesamthochschule Duisburg

Dr. B. Harris
Process Measurements Section
Control Systems Laboratory,
U.S. EPA

Dr. B.Y.H. Liu
Mechanical Engineering Dept.
University of Minnesota

Dr. D. A. Lundgren
Department of Environmental Engineering Sciences
University of Florida

Dr. G. Newton
Lovelace Biomedical & Environmental Center
Albuquerque, NM

3 Presentations by Panelists

Topics discussed by the panelists were separated into four major areas which were summarized during short presentations by the following persons:

1. Transport Characteristics of Particle Sizing Equipment (Fissan/Liu)
2. Mechanical Particle Collectors and Their Employment (Harris/Newton)
3. Optical Particle Sizing Systems and Other Non-Intrusive Techniques (Durst/Fissan)
4. Application of Particle Sizing Equipment (Liu/Lundgren)

Audience participation in the discussion occurred after the presentations in the above four areas and at the conclusion of the session.

Transport losses in sampling lines must be considered in determining the true characteristics of flowing aerosols. Deposition of particles by settling and/or turbulent transport on the walls of the sampling tube or by impaction due to particle inertia in bends, will lead to an underestimation of the particulate loading in a stream. The size distribution in the collected sample will also be altered since the larger particles are preferentially deposited. Concern must also be given to the possibility of the condensation of water vapor which could lead to agglomeration of particles. Further chemical reaction may also occur in the sampling lines.

Mechanical particle collectors based upon the principle of inertial separation in devices such as cyclones are typically

[1]Mechanical and Aerospace Engineering, West Virginia University, Morgantown, West Va. 26506.
[2]Institute of Hydromechanics, University of Karlsruhe, Karlsruhe, West Germany.
Contributed by the Fluids Engineering Division for publication in the JOURNAL OF FLUIDS ENGINEERING.

used to remove larger particles (say 7 micrometers and larger in aerodynamic diameter). A dual cyclone sampling system with cut-off diameters of 15 and 2.5 micrometers was discussed. This system employs a cascade impactor after the second cyclone to collect the smaller sized particles in the outlet stream. This device was designed to meet criteria for measuring aerosols in the respirable range. A high pressure, high temperature cascade impactor used in sampling coal-fired gas streams at the Morgantown Energy Technology Center was described. It was noted that valid measurements under operating conditions typically encountered in combustion systems are difficult to obtain.

Interest in optical particle sizing equipment was focused on the use of laser doppler anemometry (LDA) techniques and other optical techniques utilizing the light scattering characteristics of particles. Sizing information can be obtained with both laser and white light sources. The optical methods offer rapid analysis of the particulate loading in a flow stream in real time without the excessive delay encountered in analyzing particles collected on a filter, for example. Optical systems can therefore be used for on-line control functions. Furthermore, it is not necessary to insert a probe into the system to withdraw a sample for analysis. However, the optical systems suffer the disadvantage of requiring clear viewing windows, especially if the size measurements are to be made on the basis of the absolute light intensity received by the detector.

Particle sizing equipment is required for application in a variety of flows. Atmospheric aerosols are sampled under conditions where the particles settle on filters due to gravity or they may be aspirated from calm air into an impactor for sizing and concentration measurements. Industrial applications require the monitoring of contaminants at specific locations near a work place by a fixed sampling apparatus and also near individuals by the use of personal cyclones carried by workers. Many instruments and techniques are available for specific applications.

4 Recommendations

The measurement of the size and concentration of particulates in flow streams is an important, but a difficult and at times tedious task. Furthermore, there are many flows in the natural and industrial environments in which suspended particles influence or even dominate heat and mass transfer processes. Detailed studies of these transfer processes require suitable measuring techniques to provide information on particle velocity, size distribution and concentration and on variations of these quantities with time and in space.

The need for local measurements to examine spatial distribution of size and concentration and the necessity to have instantaneous records of these quantities to study transient variations, impose special instrument requirements. Instruments for this purpose are presently under development in many laboratories and are applied in others.

Among developers and users, very often only special knowledge exists on a few of the available techniques to carry out particle velocity, particle size and particle concentration measurements and this hampers the choice of the most optimum or most advanced technique for particular applications. This fact stresses the need to bring together on a regular basis research workers, instrument developers, and users in the field of particle sizing methods and their application in order to exchange existing information and to contribute in this way to the further development of modern particle sizing techniques. In addition to identifying the capabilities and advantages of available instrumentation, it is equally important to identify the inherent limitations of these systems as part of the overall evaluation process.

Assessment of Present and Future Directions of Polyphase Transport

C. T. Crowe[1]

1 Introduction

As part of its centennial year activities, The American Society of Mechanical Engineers held a series of Emerging Technology Conferences at a special meeting in San Francisco in August, 1980. The Fluids Engineering Division's contribution to this activity was a symposium on Polyphase Flow and Transport Technology. Sessions were organized for the presentation of papers and panel discussions in three areas: Gas/Liquid Flows, Gas/Solid Flows, and Slurry Flows. This paper is a summary of the concluding session of the symposium (Session FE-7) which was moderated by C. T. Crowe.

2 Comments From Industry Panelists

Richard Hill, manager of Slurry Systems, Bechtel Corp., stated that the greatest potential for slurry transport is moving large tonnages over long distances. Coal is a prime candidate for slurry transport. Other products amenable to slurry transport include iron and copper concentrates, phosphates, bauxite, and wood chips. Also, it may be a viable method for carrying tailings long distances from the milling operation.

The use of conveying media for slurry transport other than water is also under study. There is interest in using methanol or crude oil for the transport of coal. Also, the use of CO_2 or fine particles as the conveying media may be feasible.

Slurry transport has a promising future but several technical problems must be resolved. These include the development of pumping systems for coarse materials at high concentrations, high-capacity effective dewatering systems, and the use of lined pipe for transport of coarse materials over long distances.

Marion Vardaman of Stearns-Rogers, Denver, presented some of the problems encountered in polyphase transport in coal gasification systems. He described two systems, the CO_2 acceptor process and the BIGAS system. In the CO_2 acceptor process, there is the dilute phase transport of limestone and the transport of char by flue gases which must be controlled and monitored. Currently the flow rate is monitored by pressure-drop measurements. The BIGAS process is a two stage entrained bed process which is characterized by high yields of methane and carbon conversion. Coal is crushed, transported by a water slurry, pressurized, heated, mixed with recycled gas and spray dried before being fed to the second stage of the gasifier. The char is separated and fed to the first stage to be burned with oxygen and steam to provide heat for the second stage. Measurement of the char feed to the first stage is very important to ensure system safety.

Vardaman indicated two problem areas which need attention: the measurement of solids flow rate in dense and dilute systems and the control of erosion.

3 Comments From Government Panelists

Morris Ojalvo, director of the Particulate and Multiphase Processes Program at National Science Foundation, reviewed the mission of the National Science Foundation and the growth of his program since its inception in 1975. The program supported 26 grants worth .3 million in 1976 to 62 grants worth 3 million in 1980. The main areas of focus are: 1) characterization of individual particles such as physical and

[1]Department of Mechanical Engineering, Washington State University, Pullman, Wash.

Contributed by the Fluids Engineering Division for publication in the JOURNAL OF FLUIDS ENGINEERING.

used to remove larger particles (say 7 micrometers and larger in aerodynamic diameter). A dual cyclone sampling system with cut-off diameters of 15 and 2.5 micrometers was discussed. This system employs a cascade impactor after the second cyclone to collect the smaller sized particles in the outlet stream. This device was designed to meet criteria for measuring aerosols in the respirable range. A high pressure, high temperature cascade impactor used in sampling coal-fired gas streams at the Morgantown Energy Technology Center was described. It was noted that valid measurements under operating conditions typically encountered in combustion systems are difficult to obtain.

Interest in optical particle sizing equipment was focused on the use of laser doppler anemometry (LDA) techniques and other optical techniques utilizing the light scattering characteristics of particles. Sizing information can be obtained with both laser and white light sources. The optical methods offer rapid analysis of the particulate loading in a flow stream in real time without the excessive delay encountered in analyzing particles collected on a filter, for example. Optical systems can therefore be used for on-line control functions. Furthermore, it is not necessary to insert a probe into the system to withdraw a sample for analysis. However, the optical systems suffer the disadvantage of requiring clear viewing windows, especially if the size measurements are to be made on the basis of the absolute light intensity received by the detector.

Particle sizing equipment is required for application in a variety of flows. Atmospheric aerosols are sampled under conditions where the particles settle on filters due to gravity or they may be aspirated from calm air into an impactor for sizing and concentration measurements. Industrial applications require the monitoring of contaminants at specific locations near a work place by a fixed sampling apparatus and also near individuals by the use of personal cyclones carried by workers. Many instruments and techniques are available for specific applications.

4 Recommendations

The measurement of the size and concentration of particulates in flow streams is an important, but a difficult and at times tedious task. Furthermore, there are many flows in the natural and industrial environments in which suspended particles influence or even dominate heat and mass transfer processes. Detailed studies of these transfer processes require suitable measuring techniques to provide information on particle velocity, size distribution and concentration and on variations of these quantities with time and in space.

The need for local measurements to examine spatial distribution of size and concentration and the necessity to have instantaneous records of these quantities to study transient variations, impose special instrument requirements. Instruments for this purpose are presently under development in many laboratories and are applied in others.

Among developers and users, very often only special knowledge exists on a few of the available techniques to carry out particle velocity, particle size and particle concentration measurements and this hampers the choice of the most optimum or most advanced technique for particular applications. This fact stresses the need to bring together on a regular basis research workers, instrument developers, and users in the field of particle sizing methods and their application in order to exchange existing information and to contribute in this way to the further development of modern particle sizing techniques. In addition to identifying the capabilities and advantages of available instrumentation, it is equally important to identify the inherent limitations of these systems as part of the overall evaluation process.

Assessment of Present and Future Directions of Polyphase Transport

C. T. Crowe[1]

1 Introduction

As part of its centennial year activities, The American Society of Mechanical Engineers held a series of Emerging Technology Conferences at a special meeting in San Francisco in August, 1980. The Fluids Engineering Division's contribution to this activity was a symposium on Polyphase Flow and Transport Technology. Sessions were organized for the presentation of papers and panel discussions in three areas: Gas/Liquid Flows, Gas/Solid Flows, and Slurry Flows. This paper is a summary of the concluding session of the symposium (Session FE-7) which was moderated by C. T. Crowe.

2 Comments From Industry Panelists

Richard Hill, manager of Slurry Systems, Bechtel Corp., stated that the greatest potential for slurry transport is moving large tonnages over long distances. Coal is a prime candidate for slurry transport. Other products amenable to slurry transport include iron and copper concentrates, phosphates, bauxite, and wood chips. Also, it may be a viable method for carrying tailings long distances from the milling operation.

The use of conveying media for slurry transport other than water is also under study. There is interest in using methanol or crude oil for the transport of coal. Also, the use of CO_2 or fine particles as the conveying media may be feasible.

Slurry transport has a promising future but several technical problems must be resolved. These include the development of pumping systems for coarse materials at high concentrations, high-capacity effective dewatering systems, and the use of lined pipe for transport of coarse materials over long distances.

Marion Vardaman of Stearns-Rogers, Denver, presented some of the problems encountered in polyphase transport in coal gasification systems. He described two systems, the CO_2 acceptor process and the BIGAS system. In the CO_2 acceptor process, there is the dilute phase transport of limestone and the transport of char by flue gases which must be controlled and monitored. Currently the flow rate is monitored by pressure-drop measurements. The BIGAS process is a two stage entrained bed process which is characterized by high yields of methane and carbon conversion. Coal is crushed, transported by a water slurry, pressurized, heated, mixed with recycled gas and spray dried before being fed to the second stage of the gasifier. The char is separated and fed to the first stage to be burned with oxygen and steam to provide heat for the second stage. Measurement of the char feed to the first stage is very important to ensure system safety.

Vardaman indicated two problem areas which need attention: the measurement of solids flow rate in dense and dilute systems and the control of erosion.

3 Comments From Government Panelists

Morris Ojalvo, director of the Particulate and Multiphase Processes Program at National Science Foundation, reviewed the mission of the National Science Foundation and the growth of his program since its inception in 1975. The program supported 26 grants worth .3 million in 1976 to 62 grants worth 3 million in 1980. The main areas of focus are: 1) characterization of individual particles such as physical and

[1]Department of Mechanical Engineering, Washington State University, Pullman, Wash.

Contributed by the Fluids Engineering Division for publication in the JOURNAL OF FLUIDS ENGINEERING.

chemical properties, size, shape, and charge, etc., 2) particle generation and modification of particle size, 3) interfacial forces, and 4) particulate processing such as transport and separation.

Dr. Ojalvo also made reference to the Fine Particle Research Institute (FPRI) which is supported by industry and funds university research. Currently sixteen companies each provide $12,000 per year to fund research on solid-solid separation, powder flow, slurry rheology and agglomeration of particles in fluidized beds.

Subject areas of interest to the long range plans of NSF's particulate and multiphase processing program include: 1) basic mechanisms in fluidized bed operation, 2) separation processes at extreme conditions, 3) fine particle research, and 4) slurries and suspensions.

John Walsh of the Jet Propulsion Laboratory in Pasadena, who represented the views of the Department of Energy, reviewed the very complex problems in the development of coal gasification and liquification plants. Resolution of the technical problems to yield safe, reliable and environmentally acceptable processes is essential to securing the necessary capital investment for construction.

One important factor in safety is the accurate and reliable measurement of coal feed rate. It is anticipated that a flow rate of 40,000 tons of coal per day must be measured with an accuracy of 1/2 of one percent. Besides flow rate, a reliable measure of ash and carbon content, as well as heating value of the coal, is needed. The importance of measurement accuracy is apparent when one realizes that a 4 percent reduction in carbon in the carbon-oxygen reaction in the gasifier increases the flame speed by a factor of 10 which, in turn, can lead to destruction of the system. Another factor is the erosive nature of coal which can have a hardness of 9.5 compared to a diamond at 10. Under rapid depressurization, a tungsten-carbide flow component can have a life time of the order of minutes.

Another area of concern is the flow of coal-ash-solvent and hydrogen in coal liquification processes. Small changes, a few percent, of the solids concentration can change the viscosity by a factor of a 1000. Also, if the flashing of the mixture to distill the final coal product is not well controlled, the mixture can coke, turning into a solid mass.

John Walsh concluded that the polyphase technology related to mass flow measurement, rapid depressurization and mixing in coal gasification and liquification processes to design safe, reliable and environmentally acceptable systems is not currently available. He stated that these areas must be the focus of future research and development.

4 Comments From University Panelists

Professor Franz Durst of Karlsruhe University, Germany, discussed current and future directions of research in polyphase transport from the viewpoint of the academician. He began by stating that the role of the University should be in seeking understanding of processes and not generating correlations. This understanding will ultimately provide the knowledge for the design of functional, reliable systems. Also, the university is the training ground for engineers and scientists who will ultimately be responsible for process design and development.

Professor Durst indicated the laser Doppler anemometer is a promising instrument for monitoring and measuring two-phase flows. Better optical systems and supporting electronics are being developed continually. It is now possible to measure local particle size, velocity and concentration to obtain slip velocities—a key element in property transfer rates. Development will continue in measurements at higher particle concentrations with the use of smaller probes. Amplitude and frequency measurements will allow discrimination between phases and determination of local velocity differences. Preliminary studies show that particle-gas velocity differences can alter the turbulence level of the gas. Also, measurements of this nature will help improve the predictive capability for particle deposition on surfaces.

Professor Durst concluded by reiterating the need to support basic research at universities to train engineers and scientists and develop a firm understanding of processes requisite to the design and development of industrial systems.

Professor Christopher Brennen of the California Institute of Technology began his commentary by stating that more emphasis should be given to global flow measurement. He stated that point (LDV, optical probes) measurements are, for the most part, limited to dilute flows and few can be extended to dense suspensions. Instruments for global measurements feature gamma ray and light absorption, electrical inductance measurements, electromagnetic effects, Doppler shift measurements, and simply, recording pressure drop.

Professor Brennen stated that there is a need for new ideas for modeling the flow of dense suspensions. Previous studies have shown that the random motion of the particles dominates the flow. His approach has been to first study the flow of granular material with no conveying medium. Understanding this flow will serve as a first step toward understanding the flow of dense suspensions.

5 Assessment

The participants in the session represented wide backgrounds of technological experience. Industry is faced with problems for which there are no ready solutions. Our success in treating these problems will ultimately decide the feasibility of slurry transport and coal gasification/liquifaction plants. Government laboratories and funding agencies are keenly aware of these problems. Universities recognize that short term solutions are not adequate and must continue to pursue studies which seek basic understanding while providing training for the future engineers and scientists who will have to deal first hand with these problems.

Review—Theoretical Models of Gas-Liquid Flows

G. B. Wallis
Professor,
Thayer School of Engineering,
Dartmouth College,
Hanover, N.H. 03755

Two-phase flow is an "insecure" science. Many factors influence the phenomena, limiting the value of theory unless supported and guided by observation. Several methods of analysis are available; they should be used carefully and often need to be adapted in an "ad hoc" way to solve particular problems. Current efforts are concentrated on the separated (two-fluid) theoretical model and the development of improved instrumentation.

Introduction

Kenneth Boulding, on the occasion of his presidential address to the American Association for the Advancement of Science [1], made the distinction between "secure" and "insecure" science: between classical physics, on the one hand, in which theory and experiment tend to agree clearly and repeatably, and cosmology, on the other hand, which studies a very large universe with a very small and biased sample and is likely to be eternally discovering unexpected events. Boulding defined a field of knowledge as insecure if the available data only cover a small part of the total field and if the actual structures and relationships in it are extremely complex. He might have been describing two-phase gas-liquid flow in industrial geometries.

One of the themes of this paper is this insecurity in the prediction of two-phase flow and the care that has to be taken to avoid the temptation of claiming an analytical precision that is greater than the degree to which the problem can be defined. Common causes for this state of affairs are: the infinite variety of interfacial geometries and flow regimes; enduring effects of past history; various forms of nonequilibrium, such as nucleation during phase change; large influences of small impurities, such as foaming agents, and minor geometrical changes, such as roughness in a nozzle, that can cause the early breakup of liquid jets; phenomena such as fluctuations that couple the behavior of system components that one would like to treat as independent.

These uncertainties were pointed out by Batchelor [2] who stated in his keynote address at the Symposium on Two-phase Flow Systems in Haifa in 1971 that he did not see "the kind of secure foundations and body of theory which turn a collection of particular problems into a subject." His view was that "those ad hoc primitive hypotheses . . . must be replaced by precise concepts and rigorous methods."

The basic theory of two-phase flow already exists in the form of classical fluid mechanics which describes the details of the motion of either phase. Unfortunately, the application of rigorous reasoning from fundamentals, such as the Navier-Stokes equations, is a hopeless task in all but the most academic examples. Therefore, we are forced to develop composite, often approximate, concepts and to be both hopeful and dubious about applying them to apparently similar problems in different fields. These methods, which will be discussed later, rest on assumptions that have restricted validity. It is doubtful whether there is any consistent way in which the complexity of the problem can be reduced to suit all applications. Nevertheless, I have seen a "request for proposal" from a sponsoring agency stating: "the contractor will develop methods for describing the transient response of ------ using the basic equations of two-phase flow", the assumption having already been made that meaningful and useful basic equations can be defined and that the empirical terms that are needed in all such analyses can be identified and known sufficiently accurately, without the long period of patient diagnostic experimentation that has historically characterized all significant developments in engineering fluid mechanics, let alone two-phase flows.

Another example of a bold attempt to make a great theoretical leap forward is in the analysis of nuclear loss-of-coolant accidents by means of computer codes. The tempting vision is of an organizing scheme for computation of the behavior of a very complex system with numerous interacting parts, many of which are not understood individually, based on a universal method of analysis. Once a set of initial assumptions has been made, the emphasis tends to be on methods for solving the resulting set of equations rather than on assessing the reliability with which the mathematical framework can describe the physics. I would have more confidence in this approach if I did not myself have so much difficulty representing the behavior of relatively well-defined components in these systems. At the very least, if one wishes to rely on theory for predictions, knowing that many of the terms in the equations have an empirical basis, it would be wise to support the computer studies with extensive underpinnings of experimental evidence: something that may be limited by cost. It should also be remembered that the basic scientific method consists of a tenacious attempt to disprove hypotheses, not to "verify" them.

Methods of Analysis of Two-Phase Flow

Table 1 lists several classes of possible approaches to the

Contributed by the Fluids Engineering Division and based on a Keynote Address presented at the ASME Polyphase Flow and Technology Symposium, San Francisco, Calif., August 13, 1980. Manuscript received by the Fluids Engineering Division, September 26, 1980.

Table 1 Methods of analysis in two-phase flow (numbers indicate the numbers of papers in the Symposium Volume [3] that use each approach)

Descriptive-experimental	14
Correlation	8
Homogeneous flow	0
Separated flow	5
Continuum (e.g., Navier-Stokes)	1
Ad hoc	9

analysis of two-phase flow. The numbers of papers in the Symposium Volume [3] that use each technique are indicated (some papers are counted more than once, since they use several approaches). It is easy to see which methods are the most popular.

The first approach listed in the table involves the very important process of observing and trying to explain "what happens," describing the observable characteristics, such as flow pattern, and recording the dependence of measured parameters, such as pressure drop, on controlled variables, such as flow rates.

Correlation is the simplest "cookbook" form of analysis in which patterns in the data are represented quantitatively, preferably using dimensionless groups that are physically motivated. Particularly when the phenomena are complicated (e.g., turbulence in single phase flow), correlations for composite concepts such as friction factor, or the Martinelli parameters [4, 5] in two-phase flow, are the most useful products of research; there may be little to be gained by further elaborate investigations of the details of the flow field. (If the reader is still unconvinced of the point about "insecurity" he might examine the extent of experimental scatter in Martinelli's original data.)

The first item in the table that really involves analysis is *Homogeneous Flow* [6]. Now, two-phase flow is a flow that is divided into subregions with recognizably different properties. By definition, such a flow can never be homogeneous, since in that case every element would have identical properties. The homogeneous theory of two phase flow is an attempt to represent the flow as if it were a single-phase flow, using "effective properties" and established techniques. It is the theory, not the reality, that is homogeneous. "A theory is not a duplicate of the real world but a diagram of what some simpler but in part similar world might be [10]." While this theory may provide a reasonable representation of some variables of interest, such as pressure drop in annular-mist flow, it may be misleading in another context, such as the prediction of "dryout" that depends on the fraction of the liquid that flows as a film on the wall and is not typical of the average flow.

In the *Separated Flow Model* [7, 11–25] (sometimes called the two-fluid or heterogeneous flow theory) each phase has different properties, such as temperature, density, and velocity, and is assumed to satisfy some form of the usual conservation laws for mass, momentum, and energy. Each parameter is some sort of average [26–30]. Averaging introduces errors that are corrected by adding more terms or coefficients to the equations [31, 32]. The *Drift Flux* theory [8] is a reduced version of this approach.

Table 2 Advantages and disadvantages of the separated flow model

Advantages:

- It reduces to the homogeneous model in the limit.
- Specific cases (e.g., fluidization, sprays, annular flow, countercurrent flow, some nozzle flows) can be handled very well.
- There is considerable room for empiricism and adjustable coefficients.
- It can be used as a framework for solving "system" problems.

Disadvantages:

- There is a complex array of equations to be solved. The choice of form may influence the character of the solution.
- The form of the equations changes as flow regimes develop.
- An immense empirical input is needed to account for all flow regimes, interaction terms and correction coefficients.
- All situations cannot be handled (i.e., the detailed three-dimensional aspects may not be readily reducible to simpler "average" forms).

Separated flow theory may be a good way of representing a spray, for example [33–35] or annular flow without droplet entrainment [9].

In setting up the conservation equations one may arbitrarily choose, within limits, to designate certain terms as primary and others as empirical, particularly when dealing with interactions between phases (e.g., should the momentum exchange due to phase change be included in the drag coefficient? Should the velocity of the droplets or the film or some weighted average be chosen to represent the liquid in annular-mist flow? Should the core in annular-mist flow be treated as a gas that interacts with both the droplets and the film, or as a homogeneous mixture of gas and drops that interacts with the liquid film as the second phase? Should "apparent mass" effects appear in the inertia terms or the interaction terms?). This is a subjective choice. As long as consistency and mathematical probity are maintained, there is no more fundamental principle to which one can appeal to determine which version is more correct. The only criterion is utility for the particular purpose for which one is performing the analysis. All alternatives require empiricism to take care of "what is left out" (perhaps a criterion for selection is that this empiricism should be simple). There is rarely a clear, basic constitutive equation except for highly idealized models that are geometrically simple and are at best an approximation to a much more complicated reality.

Table 2 lists some advantages and disadvantages of the separated flow model.

Averaging

Realizing that the separate flow model has weaknesses, some theoreticians have sought greater precision by being more explicit about averaging. This usually means that terms in the equations appear as integrals over space and time of continuum parameters such as velocity. This is a good exercise but so far it has not led to any useful results, because eventually the equations have to be solved for a finite set of variables that are often indistinguishable from what would have been generated from a much less sophisticated starting point.

Nomenclature

a = acceleration
A = area of cross-section
C_D = drag coefficient for a droplet
C_i = friction factor at gas-liquid interface
d = drop diameter
D = pipe diameter
f = force
g = acceleration due to gravity
m = mass
Q = volumetric flow rate
t = time
v = velocity
x,y,z = Cartesian coordinates
y = fraction of total liquid flow that is on the wall
α = void fraction
ρ = density

Subscripts

f,g = liquid, gas
i,j = each of two phases
1 = on the wall
2 = entrained

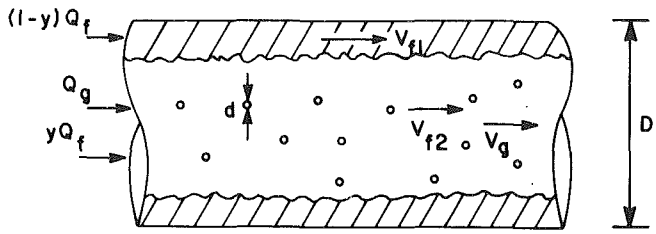

Fig. 1 A sketch of annular-mist flow

This leads to another point—the relation of the solution variables to experimentally measurable quantities. The average velocities of the phases, v_i and v_j, in the separated flow model are not directly measurable. One can measure the volumetric flow rate, Q_j, the area of the duct, A, and the volume fraction α_i, and deduce v_i to be

$$v_i = \frac{Q_i}{A\alpha_i} \tag{1}$$

This is a much easier and more practical approach than the definition based on an integral over space and time:

$$v_i = \frac{\int v_i dx dy dz dt}{\int dx dy dz dt} \tag{2}$$

Besides, it is probably hard to measure the instantaneous value of v_i near interfaces which may mean, in some regimes, most of the flow volume (Durst reports some success at measuring local velocity in particulate systems [35]). Therefore, v_i in equation (1) is defined as the simplest velocity that can be related to measurement—an excellent reason for using it as a basis for analysis.

In steady flow it is even harder to deduce the average velocity since the instantaneous flow rate may not be accurately measurable. Usually the only parameter that is easy to measure is pressure at the wall. The same pressure history may be reasonably modelled by many theories, using different solution variables and equations and an adequate number of adjustable coefficients.

Indeed, the difficulty of making almost any accurate measurement of the details of the flow is one of the major causes of the "insecurity" that was mentioned at the start of this paper. Without unequivocal measurements it is hard both to find a sound basis for theoretical development and to sort out the spurious theoretical models from those that give an "honest" representation of what is going on.

A Specific Example—Annular-Mist Flow

The hazards of averaging can be illustrated by the simple example of annular-mist flow: one of the most common flow regimes. Figure 1 shows an idealized representation in which a fraction y of the liquid flow is entrained with speed v_{f2}, while a fraction $(1-y)$ flows on the wall with speed v_{f1}, (these speeds are themselves averages of a complicated variation in both space and time). The void fraction is α and the overall fraction of the volume that is occupied by liquid is $(1-\alpha)$.

The fraction of the pipe that is occupied by the liquid film is $(1-y)Q_f/(Av_{f1})$ while the fraction of the pipe occupied by the drops is $yQ_f/(Av_{f2})$. Therefore the fraction of the pipe occupied by all of the liquid is

$$(1-\alpha) = \frac{Q_f}{A}\left(\frac{1-y}{v_{f1}} + \frac{y}{v_{f2}}\right) \tag{3}$$

If this is to be compatible with (1) the average liquid speed must be given by

$$\frac{1}{v_f} = \frac{1-y}{v_{f1}} + \frac{y}{v_{f2}} \tag{4}$$

For instance, if $y = 1/2$, $v_{f1} = 1$, $v_{f2} = 10$, then $v_f = 1.82$, showing a weighting in favor of the liquid film.

If we now compute the momentum flux of the liquid we find that the value predicted assuming that all of the liquid has this average velocity should be multiplied by the correction factor $(yv_{f2} + (1-y)\,v_{f1})/v_f$, or approximately 3 for our numerical example. For the flux of kinetic energy the correction factor is $(yv^2{}_{f2} + (1-y)v_{f1}{}^2)/v_f{}^2$, which exceeds 15 if $y = 1/2$, $v_{f1} = 1$, $v_{f2} = 10$. These are very large correction factors indeed and they are a significant source of error if they cannot be accurately estimated in an analytical scheme based on mass, momentum and energy balances.

In fact, the errors in computing the momentum and kinetic energy fluxes of the liquid for this example are both less than a factor of 2 if we use the apparently less reasonable homogeneous flow model, assuming that all of the liquid travels at the speed of the droplets; however, the liquid fraction in this case is in error by a factor of 5.5

This is not an extreme case. Infinite correction factors are needed, for example, to describe the situation in which droplets are flowing in a direction countercurrent to an equal flow rate of liquid in the film; there is no net liquid flow, but there are definite fluxes of momentum and kinetic energy.

Indeed, in some countercurrent flows the net fluxes of mass and momentum may be in opposite directions.

With errors of this magnitude possible in simple situations it is clear that care must be applied in the use of this theory, particularly when there are large nonuniformities in the flow pattern or the geometry of the enclosing structure.

It may also be a problem to determine the effective one-dimensional "constitutive" equations or interaction terms for the separated flow model. In the annular-mist flow example, suppose that the gas has a velocity v_g and the droplets each have a diameter d in a pipe of diameter D. A reasonable expression for the shear stress exerted by the gas on the liquid film is

$$\tau_i = C_i \frac{1}{2}\rho_g (v_g - v_{f1})^2 \tag{5}$$

where C_i is an "interfacial friction factor." The drag on the droplet cloud per unit length of the duct can be represented by

$$f_d = C_D \frac{1}{2}\rho_g (v_g - v_{f2})^2 \frac{\pi}{4} d^2 n \tag{6}$$

where

$$n = \frac{yQ_f}{v_{f2}\pi d^3/6} = \frac{yv_f(1-\alpha)\pi D^2/4}{v_{f2}\pi d^3/6} \tag{7}$$

is the number of drops per unit length of the duct and C_D is their "drag coefficient."

The force between the phases per unit volume of the duct is then

$$\frac{\tau_i \pi D\sqrt{\alpha} + f_d}{\pi D^2/4}$$

$$= \frac{2\rho_g}{D}\left[C_i(v_g - v_{f1})^2\sqrt{\alpha} + \frac{3}{8}C_D y(1-\alpha)\frac{Dv_f}{dv_{f2}}(v_g - v_{f2})^2\right] \tag{8}$$

If $(1-\alpha) = 0.2$, $C_i = 0.05$, $C_D = 0.5$, $y = 0.5$, $v_{f1} = 1$, $v_{f2} = 10$, $D = 200$mm, $d = 0.2$mm (all of which are reasonable numbers) the term in square brackets becomes, using (3),

$$0.045(v_g - v_{f1})^2 + 3.2(v_g - v_{f2})^2$$

The contribution to the interphase force from the drops is weighted by a factor 3.4/0.045 = 76 relative to the con-

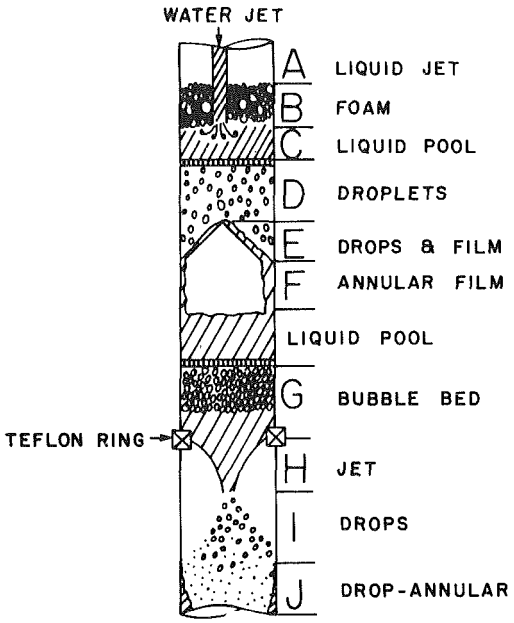

Fig. 2 An example of developing flow patterns in a vertical pipe (The cross-hatched regions denote continuous liquid).

tribution from the film. At the same time the fraction of the liquid in the pipe which is in the film is

$$\frac{(1-y)/v_{f1}}{y/v_{f2}+(1-y)/v_{f1}} = \frac{10}{11}$$

or over 90 percent. Averaging Newton's law, $f=ma$, for the liquid phase is clearly a cavalier business in this case, quite apart from the question of "internal" momentum exchange by droplet deposition and entrainment.

Continuum Models

The most thorough approach to two-phase flow is to treat each phase as a continuum and to obtain a detailed description of the three-dimensional flow field. This may involve, for example, the use of two sets of vector continuity and momentum equations (e.g., Navier-Stokes) together with boundary and interface conditions incorporating the effects of mass transfer and surface tension. Even when the shape of all the interfaces is known (it usually isn't) this is a Herculean task in all but a few special cases.

While these approaches have potential for greater rigor, their use is inevitably restricted to rather well-defined problems and flow regimes. Some successes so far include the flow around single bubbles or drops or arrays of suspended particles in creeping, irrotational or shear flows. Reference [37] cites many such cases, while [38] and [39] are typical examples. Successes also include some well-ordered interfacial waves [40] and various universal velocity profile approaches to annular flow (e.g., [41,42,43]).

Ad Hoc Methods

By "ad hoc" I mean the development of particular analytical approaches for each new problem, drawing upon experience with similar situations, publications that appear to be relevant, and insights that are developed to explain the unique features of the processes. The numbers in Table 1 are a fair indication that this is the most common approach and I believe it is fair to conclude that this is also the most appropriate approach to most problems.

Why is this? It all has to do with the insecurity mentioned at the outset. We have to deal with such an overwhelming variety of different circumstances, combinations of fluid properties and apparatus geometry that the likelihood of success in the application of some "standard technique" to a new situation is quite low, unless accompanied by the sort of "skill in the art" that relates a successful consultant in this field to a clinical medical diagnostician.

As an extreme example, Fig. 2 shows water flowing down a vertical pipe. There is no air flow. Water is poured in the top of the pipe as a central jet (*A*), which could be formed below a standard faucet, for example. This jet splashes into a pool (*C*) and entrains air to make bubbles, which separate under gravity to form a foam (*B*) limited in height by the mechanics of bubble bursting (influenced by trace contaminants) at its upper surface. The liquid pool is retained by a perforated plate in such a way that water drips from individual holes and forms a drop dispersion (*D*) below the plate. These drops are caught by a cone-shaped baffle to form a film (*E*) which is directed to the outer wall of the pipe to create an annular film (*F*). This film impinges on another perforated plate below which a group of air bubbles is trapped. Water percolates through these bubbles in an "inverted, fluidized bed" (*G*). Finally, a ring of non-wettable material separates the flow from the wall to form a new jet (*H*) which accelerates under gravity, eventually breaking up into droplets (*I*), some of which impinge on the wall to form a hybrid drop-annular pattern (*J*). Even if the pipe is very long, a final "fully-developed" pattern may be hard to achieve.

Clearly we have here a whole host of subproblems, each requiring different equations to describe them and, probably, some careful flow visualization before even an adequate verbal description (that usually precedes all analysis) can be developed (e.g., [44]).

Summary

Many aspects of the science of two-phase flow are "insecure" in the sense defined by Boulding. We need to be wary of excessive expectations of the ability of analysis to predict behavior. The experimental base is meager and will probably always be small compared with the immense variety of possible phenomena. Successful theories can be developed for specific applications but they usually require some form of empirical input that must come from extensive experiments if there is to be any claim to generality.

At present the active area of theoretical development is the separated (two-fluid) flow model. It has potential for representing many practical situations (especially those with a well-defined flow regime) as long as one is careful not to vest it with a more general authority than it deserves. There perhaps will be some spectacular successes for it, particularly in its three-dimensional form, because modern computer techniques are making it possible to handle all the simultaneous equations. There will have to be some improved methods of experimentation developed concurrently if the theory is to be supported by thorough tests of its pieces rather than merely overall predictions of system behavior.

The ad hoc approach is likely to retain its preeminence as the dominant method of analysis for the foreseeable future. Rather than a rigorous base of general two-phase flow theory, the theoreticians will have available an evolving bag of tricks, involving a continual interplay between theory and experiment, that must be used with skill and judgment and a realistic awareness of the limitations of the theories, as well as their potential for saving us from being doomed to learn everything by experience.

References

1 Boulding, K. E., "Science: Our Common Heritage," *Science*, Vol. 207, No. 4433, Feb. 1980, pp. 831-836.

2 Batchelor, G. K., "The Mechanics of Two-Phase Systems," *Progress in*

Heat and Mass Transfer, Proceedings of the International Symposium on Two-Phase Systems, Vol. 6, Pergamon Press, 1972.

3 Bajura, R. A. (Ed), "Polyphase Flow and Transport Technology," ASME Symposium on Polyphase Flow and Transport Technology, Century 2—Emerging Technology Conferences, Aug. 1980.

4 Martinelli, R. C., and Nelson, D. B., "Prediction of Pressure Drop during Forced-Circulation Boiling of Water," *Trans. ASME*, Aug. 1948, pp. 695–702.

5 Lockhart, R. W., and Martinelli, R. C., "Proposed Correlation of Data for Isothermal Two-Phase, Two-Component Flow in Pipes," *Chemical Engineering Progress*, Vol. 45, No. 1, Jan. 1949, pp. 39–45.

6 Wallis, G. B., "*One Dimensional Two-Phase Flow*," Chapter 2, McGraw-Hill, 1969.

7 ibid. Chapter 3.

8 ibid. Chapter 4.

9 ibid. Chapter 11.

10 Truesdell, C., and Muncaster, R. G., "*Fundamentals of Maxwell's Kinetic Theory of A Simple Monatomic Gas*," Prologue, Academic Press, 1980.

11 Delhaye, J. M., "Equations Fondamentales des Ecoulements Diphasiques," *Centre d'Etudes Nucléaires de Grenoble*, CEA-R-3429, 1968.

12 Bouré, J. A., "Mathematical Modeling and the Two-Phase Constitutive Equations," *European Two-Phase Flow Group Meeting*, Haifa, June 1975.

13 Bouré, J. A., "On a Unified Presentation of the non-Equilibrium Two-Phase Flow Models," ASME Symposium on Non-Equilibrium Two-Phase Flows, 1975, pp. 1–9.

14 Harlow, F. H., and Amsden, A. A., "Numerical Calculation of Multiphase Fluid Flow," *Journal of Comp. Phys.*, Vol. 17, 1975, pp. 19–52.

15 Yadigaroglu, G., and Lahey, Jr., R. T., "On the Various Forms of the Conservation Equations in Two-Phase Flow," *International Journal of Multiphase Flow*, Vol. 2, 1976, pp. 477–494.

16 Hughes, E. D., Lyczkowski, R. W., and McFadden, J. H., "An Evaluation of the State-of-the-Art Two-Phase Flow Models and Their Applicability to Nuclear Reactor Transient Analysis," *Electric Power Research Institute* report EPRI NP-143, 1976.

17 Wallis, G. B., Richter, H. J., and Kuo, J. T., "The Separated Flow Model of Two-Phase Flow," *Electric Power Research Institute* report EPRI NP-275, 1976.

18 Delhaye, J. M., "Space-Averaged Equations" in Two-Phase Flows and Heat Transfer," (Eds. Kakac, S. and Veziroglu, T.) Vol. 1, 1977 *Hemisphere*, Washington, pp. 59–144.

19 Agee, L. J., Duffey, R. G., and Banerjee, S., "Multi-Fluid Models for Transient Two-Phase Flow," *Electric Power Research Institute* report EPRI NP-618-SR, 1978.

20 Drew, D. A., and Lahey, Jr., R. T., "Application of General Constitutive Principles to the Derivation of Multidimensional Two-Phase Flow Equations," *International Journal Multiphase Flow*, Vol. 5, 1979, pp. 243–264.

21 Rousseau, J. C., and Ferch, R. L., "A Note on Two-Phase Separated Flow Models," *International Journal of Multiphase Flow*, Vol. 5, 1979, pp. 489–493.

22 Banerjee, S., and Chan, A. M. C., "Separated Flow Models-I. Analysis of the Averaged and Local Instantaneous Formulations," *International Journal of Multiphase Flow*, Vol. 6, 1979, pp. 1–24.

23 Wendroff, B., "Two-Fluid Models: A Critical Survey," *Proceedings EPRI Workshop, Basic Two-Phase Flow Modeling in Reactor Safety and Performance*, WS78-143, Vol. 2, 1980.

24 Banerjee, S., "Separated Flow Models-II, Higher Order Dispersion Effects in the Averaged Formulation," *International Journal of Multiphase Flow*, Vol. 6, 1980, pp. 241–248.

25 Chao, B. T., Sha, W. T., and Soo, S. I., "On Inertial Coupling in Dynamic Equations of Components in a Mixture," *International Journal of Miltiphase Flow* Vol. 4, 1978, pp. 219–223. (see Discussions in *Int. J. Multiphase Flow*, Vol. 4, 1978, pp. 585–586, and Vol. 6, 1980, pp. 383–384.)

26 Panton, R., "Flow Properties from the Continuum Viewpoint of a Non-Equilibrium Gas-Particle Mixture," *J. Fluid Mehcanics*, Vol. 31, Part 2, 1968, pp. 273–303.

27 Drew, D. A., "Averaged Equations for Two-Phase Flows," *Studies in Applied Mathematics*, Vol. 50, 1971, pp. 205–231.

28 Ishii, M., "Thermo-Fluid Dynamic Theory of Two-Phase Flow," *Eyrolles*, 1975.

29 Delhaye, J. M., and Achard, J. L., "On the Averaging Operations Introduced in Two-Phase Flow Modelling," *Proceedings 1st OECD/NEA Specialists Meeting on Transient Two-Phase Flow*, Toronto, Vol. 1, 1976, pp. 5–84.

30 Nigmatulin, R., "Spacial Averaging in Mechanics of Heterogeneous and Dispersed Mixtures," *International Journal of Multiphase Flow*, Vol. 5, 1979, pp. 353–385.

31 Roy, R. P., and Ho, S., "Influence of Transverse Intraphase Velocity Profiles and Phase Fraction Distributions on the Character of Two-Phase Flow Equations," *International Journal of Heat and Mass Transfer*, Vol. 23, 1980, pp. 1162–1167.

32 Zuber, N., and Findlay, J. A., "Average Volumetric Concentration in Two-Phase Flow Systems," ASME *Journal of Heat Transfer*, Vol. 87, No. 4, 1965, pp. 453–468.

33 Crowe, C. T., Sharma, M. P., and Stock, D. E., "The Particle-Source-in-Cell Model for Gas-Droplet Flows," ASME JOURNAL OF FLUIDS ENGINEERING, Vol. 99, 1977, pp. 325–332.

34 Crowe, C. T., "Numerical Models for Gas-Particle Flows," Keynote Paper, ASME Symposium on Polyphase Transport Technology, San Francisco, Aug. 1980.

35 Alpert, R. L., and Mathews, M. K., "Calculation of Large-Scale Flow Fields Induced by Droplet Sprays," ASME Symposium on Polyphase Transport Technology, 1980, pp. 115–127.

36 Durst, F., "Experimental Studies of Particulate Two-Phase Flows using Laser-Doppler Techniques," Keynote Paper, ASME Symposium on Polyphase Transport Technology, San Francisco, Aug. 1980.

37 Clift, R., Grace, J. R., and Weber, M. E., "*Bubbles, Drops and Particles*," Academic Press, 1978.

38 Bretherton, F. P., "The Motion of Long Bubbles in Tubes," *Journal of Fluid Mechanics*, Vol. 10, 1961, pp. 166–188.

39 Haber, S., and Hetsroni, G., "The Dynamic of a Deformable Drop Suspended in an Unbounded Stokes Flow," *Journal of Fluid Mechanics*, Vol. 49, Part 2, 1971, pp. 257–277.

40 Ardron, K. H., "One-Dimensional Two-Fluid Equations for Horizontal Stratified Two-Phase Flow," *International Journal of Multiphase Flow*, Vol. 6, 1980, pp. 295–304.

41 Dukler, A. E., "Fluid Mechanics and Heat Transfer in Vertical Falling-Film Systems," *Chemical Engineering Progress*, Symposium Series, Vol. 56, No. 30, 1960.

42 Hewitt, G. F., "Analysis of Annular Two-Phase Flow: Application of The Dukler Analysis to Vertical Upward Flow in a Tube," AERE-R 3680. 1961.

43 Levy, S., and Healzer, J. M., "Prediction of Annular Liquid-Gas Flow with Entrainment-Cocurrent Vertical Pipe Flow with No Gravity," EPRI report NP-1409, May 1980.

44 Brennan, C. E., "Polyphase Flow in Turbomachines," Keynote Paper, ASME Symposium on Polyphase Transport Technology, San Francisco, Aug. 1980.

Franz Durst
Sonderforschungsbereich 80,
Ausbreitungs- und Transportvorgänge in Strömungen,
Universität Karlsruhe,
7500 Karlsruhe, West Germany

REVIEW—Combined Measurements of Particle Velocities, Size Distributions, and Concentrations

The present paper describes combined laser Doppler particle sizing systems which permit simultaneous velocity and size measurements of individual particles. Combined measurements of these properties are achieved by extended laser Doppler anemometers. These extensions require the physics of laser Doppler signal generation to be clarified. A system for measurements of small particles and one to measure the properties of large particles is described. Some applications of these instruments are given.

1 Introduction

Measurements of particle velocities, size distributions and concentrations have become of considerable interest to environmental control and protection agencies as well as to engineers and scientists working on pollution problems. Furthermore, there are many flows in the natural and industrial environment in which suspended particles influence or even dominate heat and mass transfer processes. Detailed studies of these transfer processes require suitable measuring techniques to provide information on particle velocity, size distribution, and concentration and on variations of these quantities with time and in space. The need for local measurements to examine spatial distribution of size and concentration, and the necessity to have instantaneous records to study transient variations, impose special instrumentation requirements. Instruments for this purpose are presently under development in many laboratories and in the present paper descriptions of these developments are given using the author's work at the Universtität Karlsruhe in Germany as an example.

The development and optimization of instruments to measure particle properties is greatly facilitated by physically correct descriptions of the generation of signals. These descriptions are provided in this paper with special emphasis being given to the laser Doppler instrument.

The generation of laser Doppler signals in a dual-beam LDA-system can be readily explained by light scattering from particles penetrating a region in space common to both incident light beams. This region is usually referred to as the measuring volume of the LDA-system although signals may result from outside of this volume, e.g., see Durst (1973). These additional signals are usually not considered in laser Doppler anemometry and are eliminated in actual measurements by designing the receiving optics to only collect light from the crossing region of the two incident light beams, e,g., see Durst and Whitelaw [1].

Laser Doppler signals from dual-beam LDA-systems have also been treated in terms of the so-called fringe model. Rudd [2] showed that the LDA-signal received by the photodetector can be understood to result from scattering particles crossing interference fringes that can *be assumed to be located inside the measuring volume*. This model has been extensively used to explain the generation of laser Doppler signals. The simplicity of this model and the visualization of the fringes in the crossing region of two inclinded laser-beams, lead to the belief that these fringes really exist in the measuring volume and are experienced by scattering particles. The present paper points out that this is incorrect and Section 2 provides detailed derivations to stress this point. The experimental requirements to detect fringes are given in this section and it is pointed out that scattering particles do not possess the necessary properties to experience fringes in the measuring volume of a LDA-system. However, if the properties of the photodetector for the scattered light are attributed to the particle, the resultant LDA-signal can be interpreted as being generated by a particle crossing fringes. These can be assumed to be located in the measuring volume of the LDA-system.

The physical existence of the fringe pattern for scattering particles in the common region of two crossing laser-beams has been the basis of explanations of LDA-signal properties. Section 3 reviews these explanations and gives a physically correct description of LDA-signals, e.g. of their generation and their properties: The information content of LDA-signals is considered and the outcome of studies to measure the particle size from the modulation depth of LDA-signals is discussed. It is pointed out that the fringe model should not be employed to interprete modulation depth variations of LDA-signals in terms of particle size variations.

The information provided in Section 2 and 3 is used in Section 4 where a combined laser Doppler white light particle system is introduced. It is shown that the availability of

Contributed by the Fluids Engineering Division and based on a Keynote Address presented at the ASME Polyphase Flow and Technology Symposium, San Francisco, Calif., August 14–20, 1980, of THE AMERICAN SOCIETY OF MECHANICAL ENGINEERS. Manuscript received by the Fluids Engineering Division, September 26, 1980.

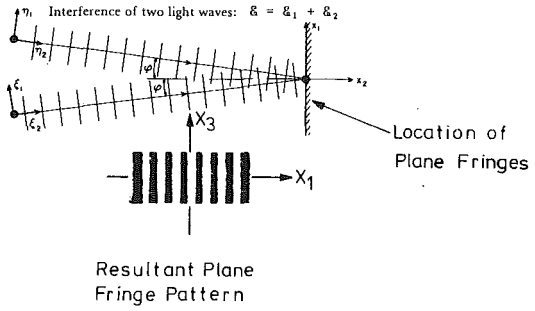

$$Is = (Eo)_1^2 + (Eo)_2^2 + 2(Eo)_1 (Eo)_2 \cos\left[\frac{2\pi}{\lambda} 2X_1 \sin\varphi\right]$$

Fig. 1 Interference fringes from two planes light waves

velocity information permits also the particle volume concentration to be computed.

This instrument is applicable to particles in the micron and submicron range as indicated by some of the applications described in Section 4.

Section 5 introduces an extended laser Doppler system applicable to small and large particles. Systems of this kind permit useful information to be obtained in particulate two-phase flows. Demonstration experiments in Section 5 clearly show this and so do examples of applications in Section 5.

Conclusions and final remarks are provided in Section 6 where the advantages of physically correct considerations to interpret properties of LDA-signals are pointed out. The advantages of nonintrusive measurements of particle properties are stressed.

2 The Generation and Detection of Fringes

Interference fringes can be seen by the human eye in the crossing region of two coherent light beams if the angle between the beam is chosen to yield a fringe distance which can be spatially resolved by the human eye. Fringes also are detected by other square law detectors for electromagnetic waves which resolve the fringes spatially and have a response time much larger than the inverse of the frequency of the light waves. The resultant intensity field may be analytically derived using the two expressions for the interfering plane light waves given in Fig. 1:

$$\epsilon_1 = (E_0)_1 \exp\left[-i(2\pi\nu t - K\eta_2 + \phi_1)\right] \quad (1)$$

$$\epsilon_2 = (E_0)_2 \exp\left[-i(2\pi\nu t - K\xi_2 + \phi_2)\right] \quad (2)$$

The analytical expression for the light intensity is derived by squaring the sum of both electromagnetic waves and by integration with respect to time implying a time constant much larger than the inverse of the wave frequency, i.e.:

$$I = \frac{1}{2T}\int_0^T (\epsilon_1 + \epsilon^*_1 + \epsilon_2 + \epsilon^*_2)^2 dt \quad (3)$$

with $T >> 1/\nu$ one obtains:

$$I = (E_0)_1^2 + (E_0)_2^2 + 2(E_0)_1(E_0)_2 \cos\left[\frac{2\pi}{\lambda}(\xi_2 - \eta_2) + (\phi_2 - \phi_1)\right] \quad (4)$$

The derivations reveal that the intensity field given by equation (4) is only detected if square law detectors for electromagnetic waves are available with integration times much larger than the inverse of the wave frequency. The human eye is a detector of this kind and, therefore, sees the intensity field described by equation (4).

The physical existence of light fringes has been postulated in connection with the scattering action of particles passing the measuring volume of a LDA-optical system irrespective of the general knowledge that the existence of light fringes requires the very special properties owned by square law detectors for electromagnetic waves. These properties are not owned by scattering particles and, hence, light fringes are not experienced as the particles pass the measuring volume of a LDA-system; the fringes physically do not exist as far as the scattering particles are concerned. To stress this fact, derivations of analytical expressions for LDA-signals are repeated below. These clearly show that the postulation of the physical existence of fringes in the measuring volume of a LDA-system is equivalent to attributing to the properties of the scattering particles the properties of the detector for the scattered light.

A particle that penetrates an electromagnetic field of two superimposed light waves, yields scattered waves that can be written as follows:

Nomenclature

a_{ij} = amplitude of scattered light radiation of axial mode j produced by beam i; $i = 1, 2$; $j = 1, \ldots, M$
c = velocity of light
$\{E_0\}_j$ = maximum amplitude of dielectric field of light-wave caused by axial mode j
f_D = doppler frequency detected by electronic equipment
Δf_{mn} = frequency difference between axial modes 'm' and 'n'
Δf_M = axial mode spacing
Δf_{Mj} = axial mode spacing between neighbors of jth order; $j = 1, \ldots M$
ΔF_D = line width of atomic transition in laser resonator
I_Q = intensity of scattered light at the cathode of the photomultiplier
I_S = intensity of scattered light
K = wave number
K_j = wave number of light wave of axial mode j
$\{K_P\}_i$ = unit vector of scattered light wave
L = laser cavity length
$(\{l\}_{K_i})_j$ = unit vector in the direction of incident light beam K; $K = 1, 2$
M = number of excited modes
$\{n\}_i$ = $\{l_1\}_i - \{l_2\}_i$ sensitivity vector of anemometer
R_P = distance from particle center to plane of observation
$(R_P)_0$ = distance R_P for time $t = 0$
$R(\epsilon_s)_i$ = real part of electric field scattered radiation
T = integration time
t = time
$\{U_P\}_i$ = velocity of particle p
x = coordinate in Fig. 1
Δx = fringe spacing
α = Mie-parameter, $\alpha = \frac{2\pi r_p}{\lambda}$
$(\{\epsilon\}_i)_j$ = complex electric field vector of wave scattered of ith beam
η = coordinate perpendicular to laser beam axis
λ = wavelength of light
λ_j = wavelength of wave of axial mode j, $j = 1 \ldots M$
ν_D = Doppler frequency
ξ = coordinate along beam axis
ϕ = phase of lightwave
ϕ_j = phase of wave jth mode
$\Delta\phi_{ij}$ = phase difference of ith and jth mode
ω_j = $2\pi c/\lambda_j$

$$\epsilon_{s,1} = \frac{1}{R_P}(E_{0s})_1 \exp\left[-i(2\pi\nu t - K\eta_2 + \phi_{s,1} - KR_P)\right] \quad (5)$$

$$\epsilon_{s,2} = \frac{1}{R_P}(E_{0s})_2 \exp\left[-i(2\pi\nu t - K\xi_2 + \phi_{s,2} - KR_P)\right] \quad (6)$$

The two scattered light waves are detected at a distance R_P from the particle and the following signal results:

$$I_s = \frac{1}{R_P^2}\left\{(E_{0s})_1^2 + (E_{0s})_2^2 + 2(E_{0s})_1(E_{0s})_2 \cos\left[\frac{2\pi}{\lambda}(\xi_2 - \eta_2) + \Delta\phi_s\right]\right\} \quad (7)$$

Introducing:

$$\eta_2 = x_2 \cos\varphi - x_1 \sin\varphi \quad (8a)$$

$$\xi_2 = x_2 \cos\varphi + x_1 \sin\varphi \quad (8b)$$

yields as the final equation:

$$I_s = \frac{1}{R_P^2}\left\{(E_{0s})_1^2 + (E_{0s})_2^2 + 2(E_{0s})_1(E_{0s})_2 \cos\left[\frac{2\pi}{\lambda}(2x_1 \sin\varphi) + \Delta\phi_s\right]\right\} \quad (9)$$

This equation shows that the scattered light intensity, *detected by a photomultiplier in space*, can be understood to result from a fringe pattern located along the x_1 axis in Fig. 1. Whenever $(2 \cdot x_1 \sin\varphi)$ is equal to an integral number of wavelength an intensity maximum results from the scattering particle and an intensity minimum for:

$$\left(N + \frac{1}{2}\right)\cdot\lambda = 2x_1 \sin\varphi.$$

The derivations show, however, that the resultant signal is caused by both the scattering action of the particle and the properties of the photodetector. Hence a particle on its own does not experience interference fringes as it passes the measuring volume of a laser Doppler system.

3 The Fringe Model in Laser Doppler Anemometry

3.1 Description of the LDA-Signal Generation. The present section reconsiders the generation of LDA-signals by superposition of two scattered lightwaves originating from a small scattering particle penetrating the center of the measuring volume of a dual-beam LDA-system. The derivations are only given for a correctly layed out system, for which the center of the crossing region of the light beams coincides with the focal point of the optical system, see Durst and Stevenson [3]. In such a system, the two intersecting incident light beams can be described as plane waves. Taking into account the various frequencies of a multiaxial mode gas laser, these waves may be analytically described as follows:

$$\epsilon_1 = \sum_{n=1}^{M}(E_{01})_n \cdot \exp\{-i[K_n \cdot \eta_2 - \omega_n t - \phi_n]\} \quad (10)$$

$$\epsilon_2 = \sum_{m=1}^{M}(E_{02})_n \cdot \exp\{-i[K_m \xi_2 - \omega_m t - \phi_m]\} \quad (11)$$

If a scattering particle penetrates these two waves, two scattered spherical lightwaves are generated:

$$\epsilon_{s,1} = \sum_{n=1}^{M}\frac{a_{1,n}}{R_P}\exp\left\{-i\left[\frac{2\pi R_P}{\lambda_n} - \omega_n t - \phi_n + K_n \cdot \eta_2\right]\right\} \quad (12)$$

$$\epsilon_{s,2} = \sum_{m=1}^{N}\frac{a_{1,m}}{R_P}\exp\left\{-i\left[\frac{2\pi R_P}{\lambda_m} - \omega_m t - \phi_m + K_m \cdot \xi_2\right]\right\} \quad (13)$$

Due to the particle motion relative to the light source and the receiver, the coordinates η_2, ξ_2 and the distance R_P change in time:

$$\eta_2 = (\eta_2)_0 - \frac{2\pi}{\lambda_j}\{U_P\}_i\{l_1\}_i t \quad (14a)$$

$$\xi_2 = (\xi_2)_0 - \frac{2\pi}{2}\{U_P\}_i\{l_2\}_i t \quad (14b)$$

$$R_P = (R_P)_0 - \{U_P\}_i\{K_P\}_i \cdot t \quad (15)$$

Introducing these quantities into equations (12) and (13) yields the following expressions for the scattered lightwaves 1, 2:

$$\epsilon_{s,1} = \sum_{n=1}^{M}\frac{a_{1,n}}{R_P}\exp\left\{-i\left[\frac{2\pi(R_P)_0}{\lambda_n} - (\phi_n)_0 - \omega_n t - \frac{2\pi}{\lambda_n}\{U_P\}_i \cdot (\{l_1\}_i - \{K_P\}_i)\cdot t\right]\right\} \quad (16)$$

$$\epsilon_{s,2} = \sum_{m=1}^{M}\frac{a_{2,m}}{R_P}\exp\left\{-i\left[\frac{2\pi(R_P)_0}{\lambda_m} - (\phi_m)_0 - \omega_m t - \frac{2\pi}{\lambda_m}\{U_P\}_i \cdot (\{l_2\}_i - \{K_P\}_i)\cdot t\right]\right\} \quad (17)$$

These expressions were already written in this form by Dopheide and Durst [4].

The two scattered lightwaves given by equations (16) and (17) yield the following light intensity *at the cathode of the photomultiplier*:

$$I_Q = \frac{1}{T}\int_0^T [R(\epsilon_{s,1}) + R(\epsilon_{s,2})]^2 dt \quad (18)$$

Due to the particle velocity being much smaller than the velocity of light, the following relationships are approximately valid.

$$\lambda \approx \lambda_m \approx \lambda_n \text{ and } (\nu_m - \nu_n) << \frac{1}{2}(\nu_m + \nu_n) \quad (19)$$

The expression for the light intensity may be derived from the above equations and is given below. In order to reduce the length of this expression, the following simplifications are introduced:

$$\{n\}_i = \{l_2\}_i - \{l_1\}_i \quad (20a)$$

and

$$\Delta\phi_{mn} = (\phi_m)_0 - (\phi_n)_0 \quad (20b)$$

The light intensity at the photodetectors cathode reads:

$$\begin{aligned} I_Q = {} & \sum_{j=1}^{M}\frac{a_{1j}^2 + a_{2j}^2}{R_P^2} + 2\sum_{j=1}^{M}\frac{a_{1j}\,a_{2j}}{R_P^2}\cos\left\{2\pi\frac{1}{\lambda}\{U_P\}_i\{n\}_i t\right\} + \\ & \sum_{\substack{n=1\\n\neq m}}^{M}\sum_{m=1}^{M}\frac{a_{1n}a_{1m} + a_{2n}a_{2m}}{R_P^2}\cos\{\Delta\phi_{mn} + 2\pi(\nu_m - \nu_n)t\} + \\ & \sum_{\substack{n=1\\n\neq m\\n>m}}^{M}\sum_{m=1}^{M}\frac{a_{1n}a_{2m}}{R_P^2}\cos\left\{\Delta\phi_{mn} + 2\pi t\left[(\nu_m - \nu_n) + \frac{1}{\lambda}\{U_P\}_i\{n\}_i\right]\right\} \\ & \sum_{\substack{n=1\\n\neq m\\n<m}}^{M}\sum_{m=1}^{M}\frac{a_{1n}a_{2m}}{R_P^2}\cos\left\{\Delta\phi_{mn} + 2\pi t\left[(\nu_m - \nu_n) + \frac{1}{\lambda}\{U_P\}_i\{n\}_i\right]\right\} \end{aligned} \quad (21)$$

This is the complete expression for the LDA-signal produced by two crossing, multi-axial mode laser beams. Equation (21) was first given by Dopheide and Durst [4] who pointed out that LDA-signals from multi-axial mode lasers result in signals consisting of various frequencies:

(*a*) The Doppler frequency:

$$f_D = \frac{1}{\lambda}\{U_P\}_i\{n\}_i \tag{22}$$

(*b*) The difference frequency between mode frequencies:

$$\Delta(f_M)_{mn} = (\nu_m - \nu_n) = (m-n)\frac{C}{2L} \tag{23}$$

(*c*) The sums and difference of the above frequencies:

$$(\Delta f_+)_{mn} = (m-n)\frac{C}{2L} + \frac{1}{\lambda}\{U\}_i\{n\}_i \tag{24}$$

$$(\Delta f_-)_{mn} = (m-n)\frac{C}{2L} - \frac{1}{\lambda}\{U\}_i\{n\}_i \tag{25}$$

Figure 2 shows the frequency spectrum of a LDA-signal with all the frequencies given above. This clearly demonstrates that Doppler considerations yield the correct frequencies of LDA-signals produced by lasers with multi-axial mode outputs.

If the basic idea of the fringe model is applied, the above derivations can be repeated in the way given below:

The light intensity distribution in the crossing region of the two incident beams can be calculated using the following relationship:

$$I_r = \frac{1}{T}\int_0^T \{R(\epsilon_1) + R(\epsilon_2)\}^2 dt \tag{26}$$

Introducing equations (10) into the above expression yields:

$$I_r = \frac{1}{T}\int_0^T \left\{ \sum_{n=1}^{M} (E_{01})_n \cos[K_n\eta_2 - \omega_n t - \phi_n] + \sum_{m=1}^{M} (E_{02})_m \cdot\cos[K_m\xi_2 - \omega_m t - \phi_m]\right\}^2 dt \tag{27}$$

Carrying out the squaring and integration yields the following final expression if the approximation in (19) are introduced at the same time:

$$I_r = \sum_{j=1}^{M}[(E_{01})_j^2 + (E_{02})_j^2] + 2\sum_{j=1}^{M}(E_{01})_j(E_{02})_j\cdot\cos\left[\frac{2\pi}{\lambda}(\xi_2-\eta_2)\right]$$
$$\sum_{\substack{n=1\\n\neq m}}^{M}\sum_{m=1}^{M}[(E_{01})_n(E_{01})_m + (E_{02})_n(E_{02})_m]\cdot\cos[\Delta\phi_{mn} + 2\pi(\nu_m-\nu_n)t]$$
$$\sum_{\substack{n=1\\n\neq m\\n>m}}^{M}\sum_{m=1}^{M}(E_{01})_n(E_{02})_m\cos\left\{\Delta\phi_{mn} + 2\pi t(\nu_m-\nu_n) + \frac{2\pi}{\lambda}(\xi_2-\eta_2)\right\} \tag{28}$$
$$\sum_{\substack{N=1\\n\neq m\\n<m}}^{M}\sum_{M=1}^{M}(E_{01})_n(E_{02})_m\cos\left\{\Delta\phi_{mn} + 2\pi t(\nu_m-\nu_n) + \frac{2\pi}{\lambda}(\xi_2-\eta_2)\right\}$$

This clearly shows that the fringe model yields the same frequencies as those derived by Doppler considerations and given in equation (21). Section 2 showed that the difference $(\xi_2 - \eta_2)$ yields the fringe system along the x_1 axis in Fig. 1.

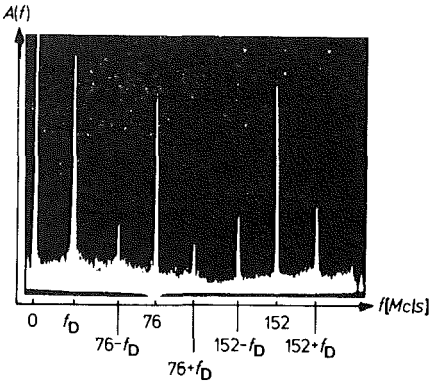

Fig. 2 Complete spectrum of LDA-signal frequencies from multi-axial mode lasers

The fringe system is crossed by the particles and intensity variations yield the resultant laser Doppler signals.

3.2 Application to Particle Sizing. It is well known that the amplitudes of LDA-signals depend on the employed laser power and on the properties of the photomultiplier used in the detection optics. Furthermore, the amplitude and modulation depth of LDA-signals depend on the size of the scattering particles, the optical properties of the particle material, the wavelength of the employed laser radiation, the angle between the two incident light beams, and the size and location of the receiving aperture. Various authors have employed computer programs to predict the strength and modulation depth of LDA-signals on the basis of Mie's (1980) scattering theory, e.g. see Dändliker and Eliason [5], Adrian and Early [6], Cherdron, Durst, and Richter [7]. Comparisons between predictions and experiments clearly showed that the formula described by Mie [8] yields correct predictions of amplitude properties of LDA-signals when correctly applied to both laser beams of an LDA-optical system and taking into accounts the complete arrangement of the transmission and receiving optics, e.g. see Durst and Eliason [9], Durst and Umhauer [10], Adrian and Orloff [11].

The aforementioned investigations clearly demonstrated that Mie's scattering theory can be employed to correctly predict the amplitude of LDA-signals and their dependence on various influencing parameters. Irrespective of this finding, simplified models were proposed on the basis of fringes inside the measuring volume of LDA-systems. The LDA-signal amplitude was proposed to be proportional to the total light flux striking a scattering particle, e.g., see Farmer [12], inside the fringe system. Hence, this model suggests the modulation depth of LDA-signals to be only dependent on the particle diameter relative to the fringe spacing. The dependence of the modulation depth on the optical properties of the particle material, on the size and location of the light collecting aperture etc., is not accounted for by this model. This clearly indicates that its validity is limited to special scattering properties of particles and to very special optical arrangements. Nevertheless, its simple explanation of the dependance of the signal modulation depth on particle size yielded a wide acceptance of this model as being generally applicable.

The limitations of the fringe model to predict amplitude characteristics of LDA-signals have been pointed out by a number of authors. Durst [13] suggests the fringe model to only *heuristically* explain the modulation depth dependence of LDA-singals on particle size. More detailed considerations are provided by Adrian and Orloff [11], Robinson and Chu [14] and Roberds [15] who pointed out the limitations of the fringe model to predict amplitude properties of LDA-signals. These authors show that the signal amplitude and signal visibility can be correctly treated by the fringe model in the scalar

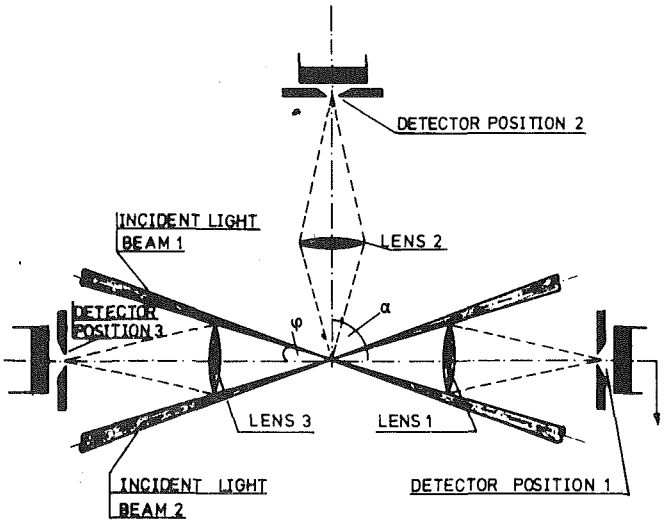

Fig. 3 Sketch of optical arrangements for predictions of LDA-signal properties

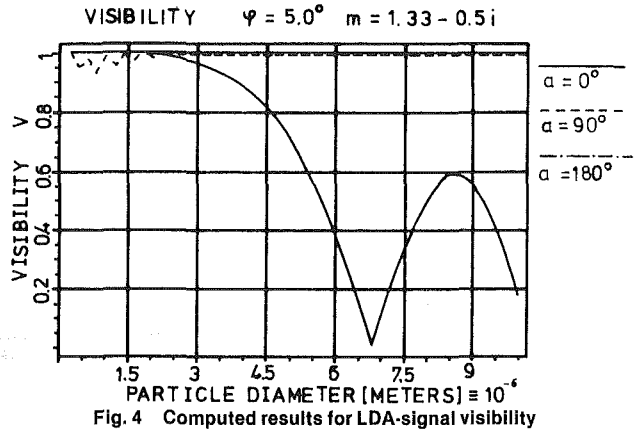

Fig. 4 Computed results for LDA-signal visibility

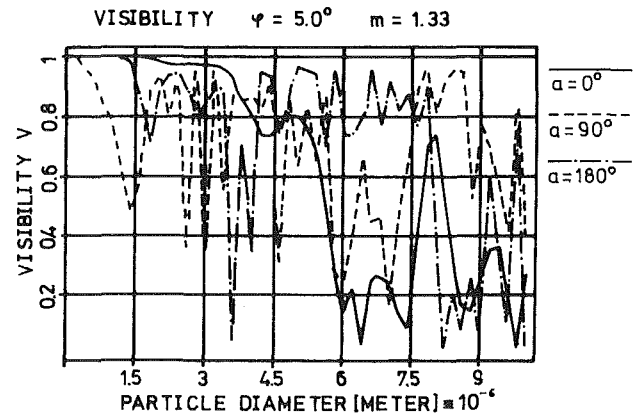

Fig. 5 Computed results for LDA-signal visibility

diffraction theory limit, but only if the scattered light is collected in the forward direction with a large light collecting aperture. Under other conditions, fringe model considerations will yield results that differ from those that are obtained experimentally.

To quantitatively demonstrate the shortcomings of the fringe model for predictions of amplitude properties, computations of the visibility of LDA-signals were carried out using computer program developed by Cherdron, Durst and Richter [7]. Results are shown in Fig. 4 and 5 for one LDA-transmission optics, given in Fig. 3, and various detector aperture locations, α = 0,90 and 180, deg. The results in Fig. 4 and 5 clearly show that large variations in the fringe

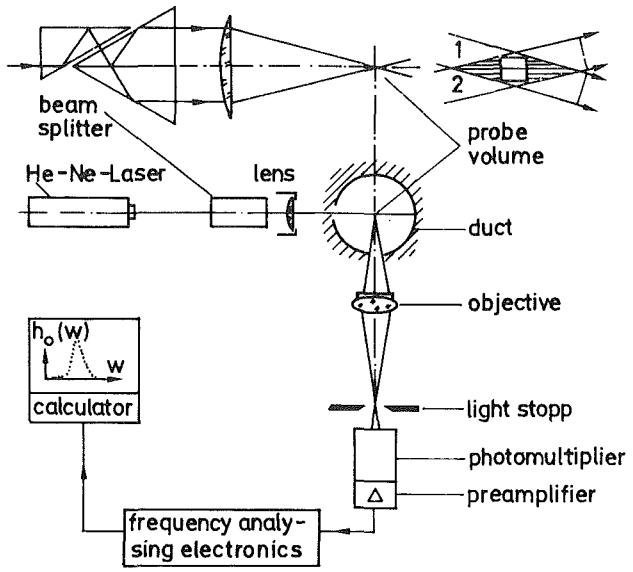

Fig. 6 Optical system

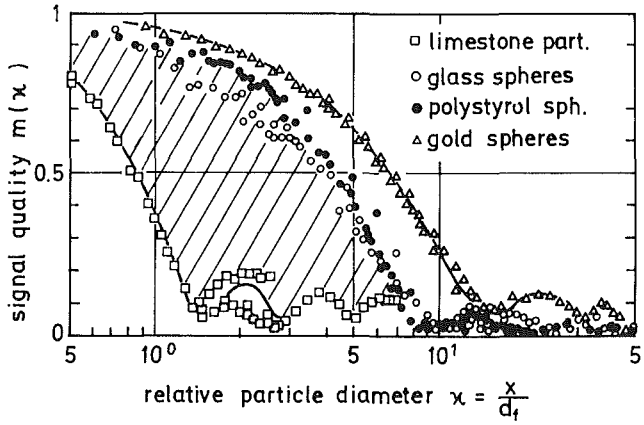

Fig. 7 Optical system and experimental results of A. Stümke and H. Umhauer (1978) showing influence of particle material on signal visibility

visibility exist for the various detector locations and also, fringe visibility is a strong function of the refractive index of the particle material. This fact is reflected by experimental results obtained by Stümke and Umhauer [16] for LDA-signals. They measured the fringe visibility of various particles by changing the fringe spacing with respect to a fixed particle diameter. Their optical system is sketched in Fig. 6 and examples of their results are presented in Fig. 7.

The aforementioned considerations clearly show that any predictions of amplitude characteristics of LDA-signals from the fringe model should be handled with care. Predictions will only agree with the physically correct amplitude properties in the scalar diffraction limit if large detection apertures are used for forward scattered light waves.

4 A System for Measuring Properties of Small Particles

4.1 The Particle Sizing System. Size measurements of individual particles with instruments based on scattered light require detailed knowledge of the response characteristics of the instrument. For accurate size measurements, it is of special importance that the response curve increases *monotonically* with particle size. This requirement cannot be taken for granted as it is apparent if one considers the complex spatial intensity distribution predicted by Mie's theory, see Kerker [17], van de Hulst [18] for spherical

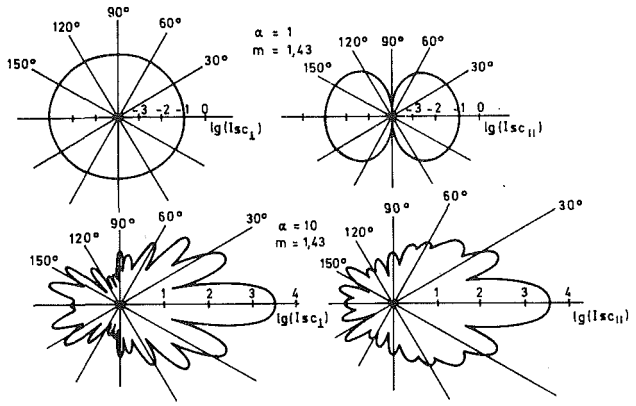

Fig. 8 Spatial light intensity distribution for different particles

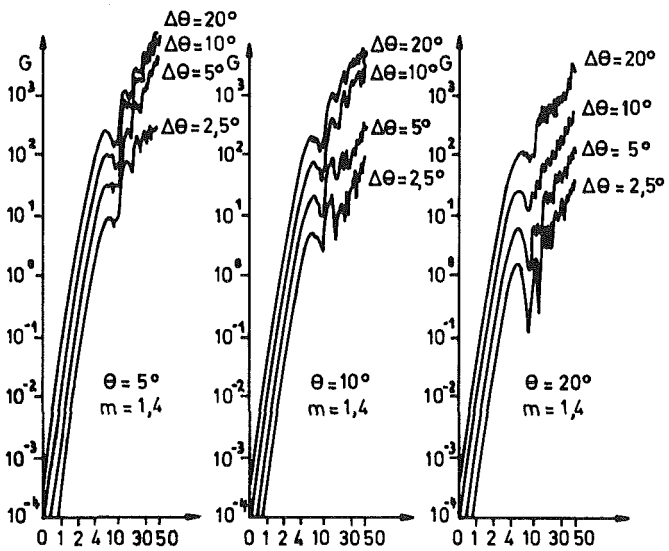

Fig. 9 Average light intensity detected by photodetector as a function of optical geometry

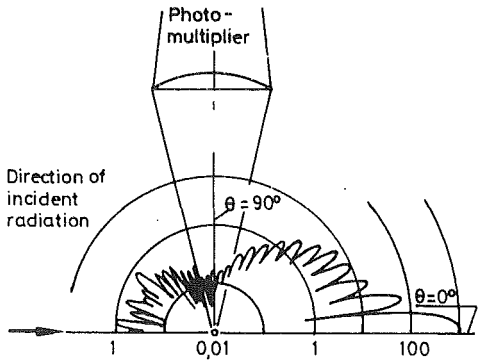

Fig. 10 Integration over light intensity distribution by finite aperture

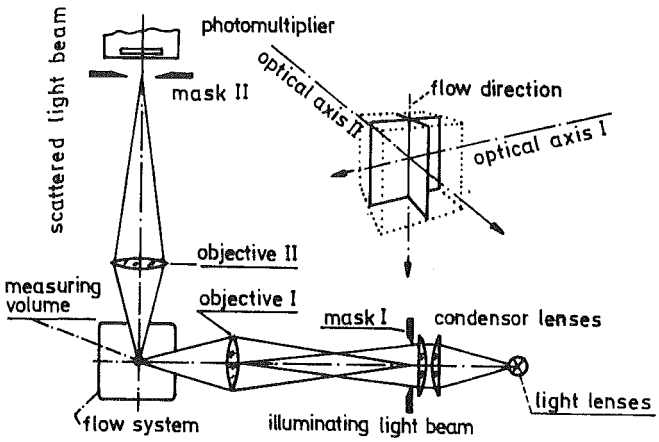

Fig. 11 Schematics of particle sizing systems with a 90 deg illumination and light collecting arrangement

particles, see Fig. 8. The complexity of these intensity patterns readily suggests that, for a given optical system and polydispersed size distributions, equal amplitude signals may be recorded for particles of different sizes, see Fig. 9, yielding severe interpretation problems. However, proper design of the optical system and the use of white light sources permit particle sizing instruments to be designed that have monotonically increasing response curves over a large particle size range.

In considering the design of optical systems for particle size measurements, one also has to be aware of the rapid changes in the scattered light intensity with particle diameter. This variation is of particular importance in the Rayleigh range ($\alpha << 1$) where the scattered light intensity varies with the sixth power of the particle diameter, $I(d) \sim d_p^6$, see Fig. 9. In this range particle sizing of polydispersed size distributions becomes extremely difficult and can only be carried out in steps using different sensitivities of the photodetector.

As the particle becomes larger, the light intensity tends to increase less rapidly with particle diameter. This effect can be seen from Fig. 9 which also indicates that the intensity increases proportional to the square of the particle diameter. This response characteristic can be readily deduced from Mie's theory if the light in the forward scattered light intensity lobe is not detected or can be neglected with respect to the total light power collected over the light collecting lens. Hence, for particles with $\alpha > 20$, a larger size range can be covered with a single amplification setting at the photodetector.

Special optical arrangements are needed to yield particle sizing systems with calibration curves that increase monotonically with particle diameter. This situation is achieved by selecting particular directions for the light collecting optics and by integrating over several intensity lobes of the scattered radiation. In addition, the employment of a white light source provides an integration effect due to the presence of a complete spectrum of wave lengths. Light intensity patterns as indicated in Fig. 10 will result for each wave length of the spectrum; since these have maxima and minima of the light intensity distribution at different locations, the large intensity variations of the individual patterns are smeared out, to provide a nearly even light intensity distribution across the detector aperture.

Using the above ideas, white light particle sizing systems can be designed and built as schematically indicated in Fig. 11. Systems of this kind can be combined with laser Doppler anemometers as described in the following section.

4.2 Integrated Optical System and Data Processing Electronics. Figure 12 shows that this optical arrangement uses a combined laser Doppler particle sizing system. The laser beam is provided by a 5mW He-Ne-laser mounted on to the base plate on which the entire optics is connected. The light beam is split by a beam splitter prism, providing two laser beams of equal light intensity with a beam separation of 50 mm. These beams are passed through one Bragg Cell to preshift the laser radiation to provide a direction sensitive LDA system. The two light beams after the double Bragg Cell are focused by a single lens element (f = 150 mm) and the scattered light in the forward direction is dectected by a light collecting lens (f = 110 mm) and a photomultiplier (EM 9558 B). The output of the photodetector is amplified and then processed by the electronic system described in Section 3.3 in order to yield the required velocity information.

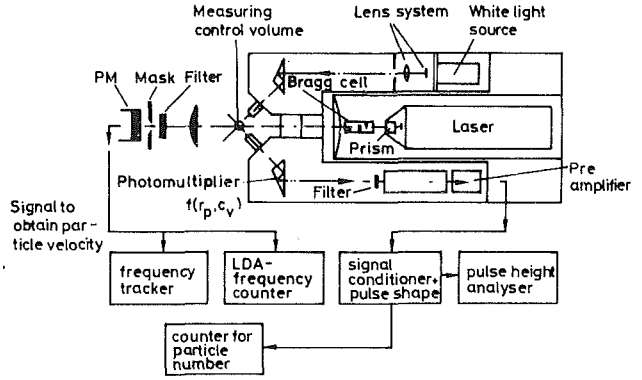

Fig. 12 Schematics of combined laser doppler anemometer and particle sizing system

Measuring the instantaneous particle velocity and counting the particle number penetrating the measuring control volume per unit time permit the particle volume concentration to be computed as follows:

$$\dot{N}_P = A \cdot C_v \cdot |\{U\}_i| \tag{29}$$

The relationship expresses the fact that the flow into the measuring control volume in time dt(see Fig. 13) i.e.,

$$\int\int \{q\}_1 \cdot \{U\}_1 \cdot ds\, dt = \dot{V} s\, dt \tag{30}$$

will carry $c_v \cdot \dot{V}_s \cdot dt$ particles. The volume flux $\dot{V}_s$ can be rewritten as the product of the magnitude of the total velocity vector, $|\{U\}_i|$, and area, A, depending on the size and the shape of the measuring control volume. Introducing time averaged properties permits the second part of the above relationship to be written as given in (29), where A depends not only on properties of the measuring control volume but also on the structure of the flow.

The particle sizing optics is built around the laser Doppler optics to make up a compact optical instrument, see Fig. 12. All components of this instrument are mounted inside a cast aluminium housing and are assembled as subunits that can be inserted easily into the housing through openings in the rear of the optics.

Figure 12 also indicates the location of the white light source and the optical components used in order to provide a uniform light intensity distribution at the mask which is then imaged into the measuring control volume by means of a microscope objective. An adjustable prism is employed to provide a beam direction which forms an angle of 45 deg with the axis of the laser Doppler system. Fine prism adjustments permit this beam to be accurately passed through the center of the focussing microscope objective. The prism can be locked after adjustment and is then insensitive to system vibration.

Construction of the light collection part of the particle sizing optics is similar to that of the illumination part. It consists of a microscope objective which collects the scattered radiation and images the measuring control volume on to a mask in front of the photomultiplier. For convenience, the scattered light is also directed through a prism which bends it by 45 deg and allows the photomultiplier to be located parallel to the laser and the white light source. An optical filter placed in front of the photomultiplier prevents the laser radiation from entering this PM-tube. An interference filter, tuned to the wave-length of the He-Ne-laser is positioned in front of the photomultiplier detecting the He-Ne-radiation, as can be seen in Fig. 12, and ensures optical separation of the size and velocity information.

Figure 12 also indicates, in block diagram form, the different parts of the data processing electronics. The output of the photomultiplier detecting the He-Ne-radiation can be processed in various conventional ways using frequency

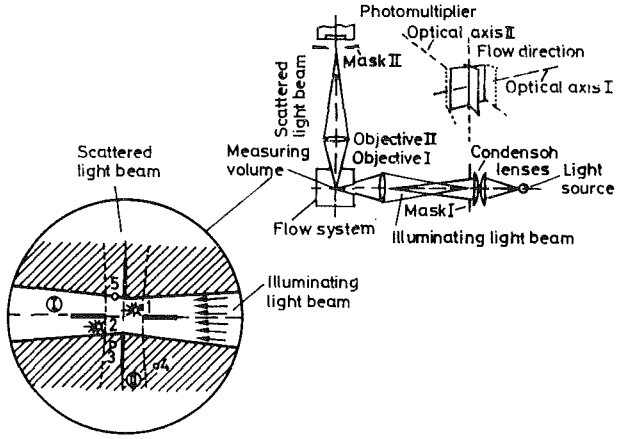

Fig. 13 Particle concentration measurements by particle counting and simultaneous velocity mesurements

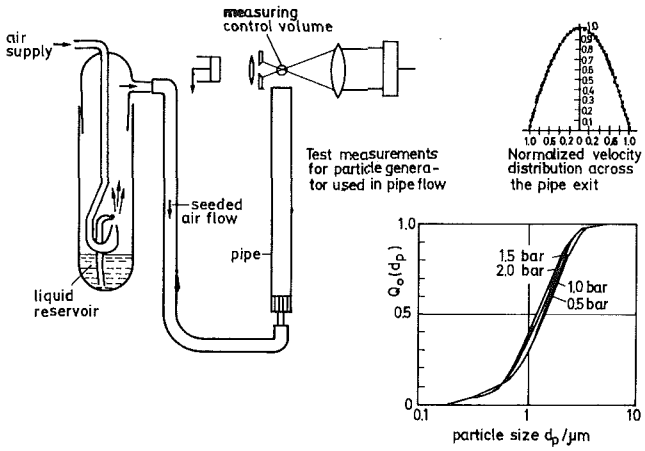

Fig. 14 Particle sizes at the pipe exit for different supply pressures

analysers, frequency trackers, or frequency counters. The author's development aims at the use of frequency counters since most of the applications envisaged are in the low particle concentration range where noncontinuous LDA-signals can be expected.

4.3 Some Applications. The combined instrument to measure the velocity of particles, size distribution, and local concentration has been extensively used to study the formation of sprays, to size atmospheric particles, to study floculations etc. and has performed satisfactorily in air and liquid systems containing particles. The instrument is set up in the author's particle laboratory as a general purpose instrument applicable to measure particle velocities, size distributions and concentrations. As it stands, it is limited to particle concentrations of less than 5.10^{11} m^{-3}, to particle sizes $d_p \leq 10^{-5}$ m, and to particle velocities $U_p \leqq 25$ m/s. Similar systems are under construction to extend the particle size range to 700 microns but this inherently reduces the particle concentration permitted. The extension to higher velocities does not present any problem.

In order to demonstrate the applicability of the combined system, measurements of the velocity profile of particles and their size distribution at the exit of a pipe are given in Fig. 14. The concentration of particles in this flow was on the order of 10^9 m^{-3} and was also obtained from the measurements. It was found to be constant across the exit of the pipe test section.

The instrument also was used by Durst and Umhauer [10] for various particle size measurements and more examples of size distribution, concentration and velocity measurements are given in their paper.

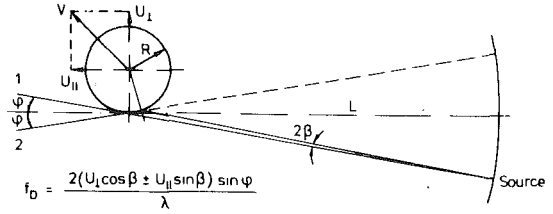

a) Reflecting Sphere

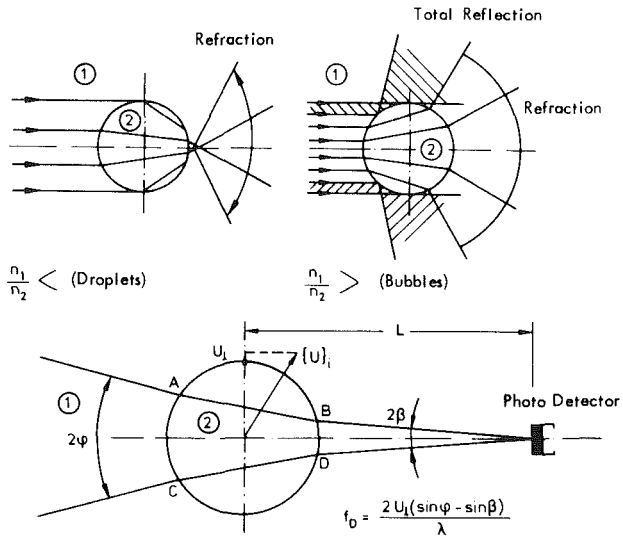

b) Transparent Sphere

Fig. 15 Configuration for spherical particle

5 A System for Measuring Properties of Large Particles

5.1 Basic Ideas of Two-Phase Flows LDA-Measurements. The basic ideas for LDA-velocity measurements in two-phase flows were brought forward by Durst and Zare (1975) who showed that the light waves produced by two laser beams, reflected by the smooth surface of a large body, interfere and produce fringes in space. The location and shape of the interference pattern is dependent on the arrangement of the incident laser beams, The shape of the body, and its location. Furthermore, the rate at which the fringes cross a detector in space is linearly related to the transverse velocity component of the reflecting body perpendicular to the symmetry line between the two incident beams.

(*a*) Reflecting Spheres. Two laser beams, reflecting from a spherical particle, interfere and produce a nonlinear fringe system. The shape and spacing of the fringes are functions of the angel between the incident laser beams and their wave length, as well as the sphere size and the direction of observation. The fringes are, of simple shape, however – namely, parallel planes – in the backward direction. The fringe separation distance in this region, for large ratios L/R and small angles φ, can be formulated as:

$$\Delta x = \left[\frac{2(L-R)}{R \cdot \cos\varphi}\right] \cdot \frac{\lambda}{2\tan\varphi} \tag{31}$$

This relationship indicates that the radius of the sphere R can be obtained by measuring the fringe distance Δx in the backward direction. The author has used a double element photodiode, with elements spaced 2 mm apart, to obtain information on the sphere diameter through phase measurements between the two detected signals. Examples of such measurements are given by Durst and Zaré [19].

As shown in Fig. 15(*a*), when the sphere moves across the two laser beams, the fringes appear to originate from a point along the direction of one of the beams, move around the entire space and then disappear into a point along the direction of the second beam.

The rate at which fringes cross any point, when produced by a moving nondeformable sphere, is the same at all points in the surrounding space, and is equal to the rate of fringe appearance at the source line or the rate of their disappearance at the sink line. The Doppler frequency detected at the source, resulting from the movement of the sphere, can be formulated as:

$$f_D = \frac{2(U_i \cos\beta \pm U_{11} \sin\beta)\sin\varphi}{\lambda} \tag{32}$$

The angle β is a function of L/R and φ. For large values of ratio L/R and small angles β, equation (32) tends toward the universal equation of laser Doppler anemometry for single phase measurements. In the case of a deforming particle, the rate of change of fringes would not remain the same all over space, and this fact allows measurement of the particle deformation through the use of proper multidetection systems.

(*b*) Transparent Spheres. As the light beam passes through a transparent particle, the relative refractive index of the particle plays a role in the characteristics of the propagated light. Two cases are distinguishable, Fig. 15(*b*): (*i*) $n_1/n_2 < 1$; the light propagates from an optically lighter medium to a denser medium. All of the light incident on the sphere passes through it and the sphere acts as a positive lens. An example of this case occurs in the measurements of water drops falling in air. (*ii*) $n_1/n_2 > 1$; the light propagates from an optically denser medium to a lighter medium. The sphere acts as a negative lens, and at a certain region total reflection occurs on the sphere surface. Such a case happens in the measurement of gas bubble-liquid flows and insoluble liquid-liquid flows. The partly or totally reflected light from the interface of the spherical particle can be treated in a manner similar to part (*a*) of this section.

When two beams are transmitted through a sphere, the shape of the fringes produced by the beams is linear in the vicinity of the optical axis in the forward direction, and for large ratios L/R and small angles φ one may show the fringe distance to be:

$$\Delta X = \left[1 + \left(\frac{2n_1}{n_2} - 2\right)\frac{L}{R}\right]\frac{\lambda}{2n_1 \sin\varphi} \tag{33}$$

For constant geometrical and physical conditions, the fringe distances are functions of sphere radius R. Consequently, spherical particle size measurements can be performed using a double photo-detector.

When transmitted through a moving particle, each of the beams is refracted at both interfaces (entering and leaving) and therefore Doppler-shifted twice. The general motion of the sphere and its surface movements all contribute to the rate of passage of the interference fringes. For a simple case of a solid sphere with no rotational movements (so that the four points A, B, and D in Fig. 15(*b*) have equal velocities), the Doppler frequency detected in the forward direction can be formulated as

$$f_D = \frac{2U_i(\sin\varphi - \sin\beta)}{\lambda} \tag{34}$$

For large ratios L/R and small beam crossing angle β, equation (34) tends towards the universal equation of laser-Doppler anemometry for single phase movements.

5.2 Optical Systems and Data Processing Electronics. Continuing the work by Durst and Zaré [19] the author and his collaborators have pursued the development of suitable

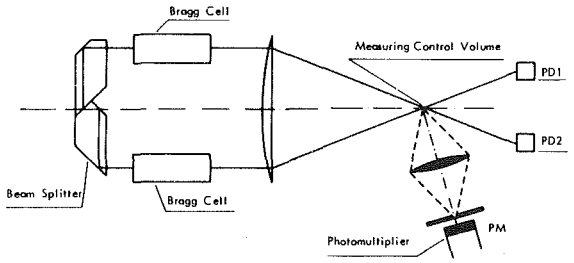

Fig. 16 Optical arrangement I for two phase flow LDA-measurements

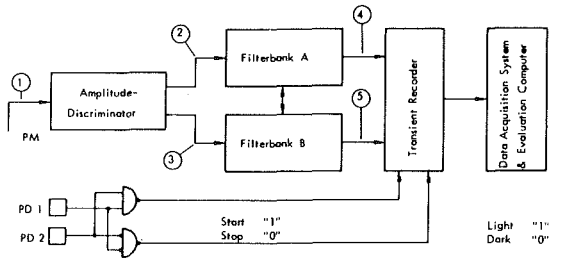

Fig. 17 Block diagram of signal processing system I for two-phase flow LDA-measurements

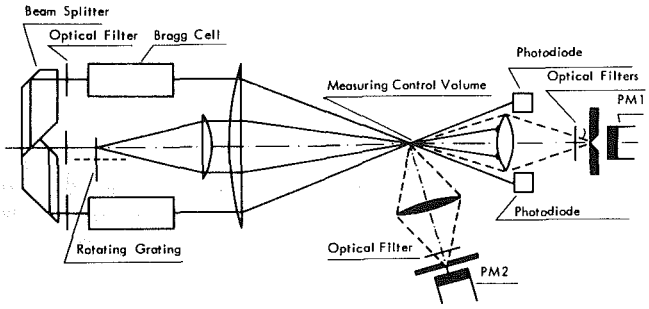

Fig. 18 Optical arrangement II for two-phase flow LDA-measurements

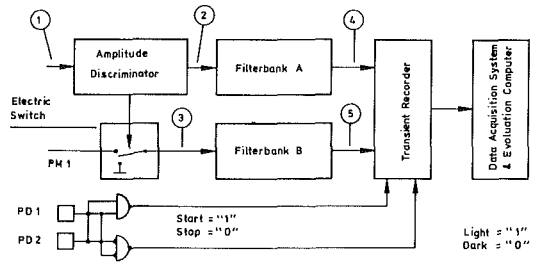

Fig. 19 Block diagram of signal processing system II for two-phase flow LDA-measurements

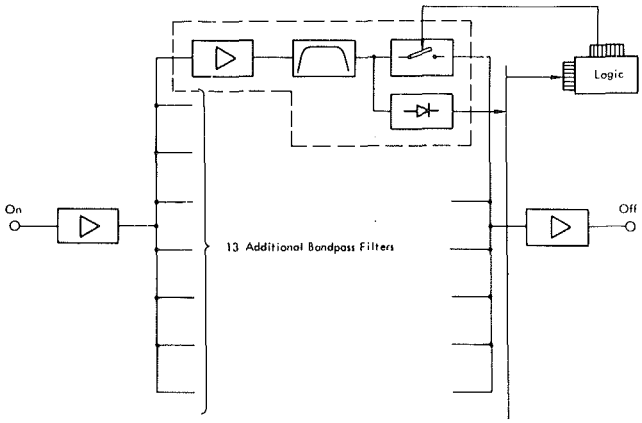

Fig. 20(*a*) Blockdiagram of automatic filterbank

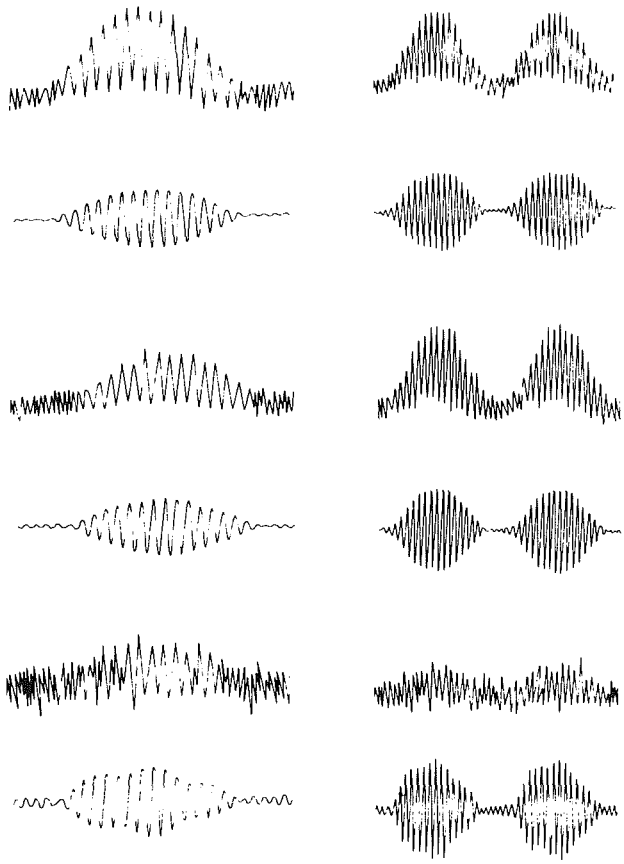

Fig. 20(*b*) Noisy signals at input and output of automatic filterbank

optical and electronic systems to carry out LDA-measurements in particulate two-phase flows. This development work resulted in two systems that are presently in use at the Sonderforschungsgereich 80 at the University of Karlsruhe. They represent extensions of LDA-systems that have been built for single-flow measurements. Figures 16 to 19 show the appropriate optical and signal processing systems in the form of diagrams. These diagrams show automatic filters banks which are used in conjunction with amplitude discriminators in order to separate those signals that are obtained from the small particles in the fluid and from the large particles.

The aforementioned filter banks have been designed for LDA-measurements in single-phase flows and have been extended to two-phase flow applications as described by Durst and Heidbreder [20]. These filter banks consist of 15 band pass filters that permit automatic selection of the optimum filter for LDA signals within a range between 500 Hz and 50 MHz. An internal logic uses the output of the filters in order to select the optimum filter. This yields filtered signals as indicated in Fig. 20. This figure shows that signals of very low signal-to-noise ratio are recognized by the filter logic and that correct decisions of the optimum band pass filter are made.

As pointed out by Durst and Heidbreder [20], LDA-optical and electronic systems for single-phase flow measurements can be extended for two-phase flow applications. In particulate two-phase flows, signals are obtained that differ in amplitude and modulation depth dependent on whether they are obtained from small paticles that follow the fluid motion or whether they are recorded from large particulates. The signals indicated in Fig. 21 and Fig. 22 demonstrate the

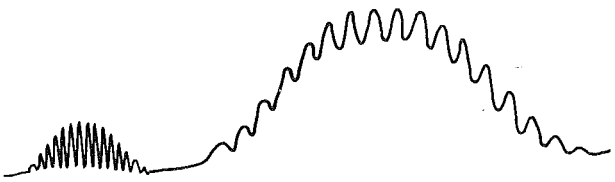

Fig. 21 Typical signals from particular two-phase flow system

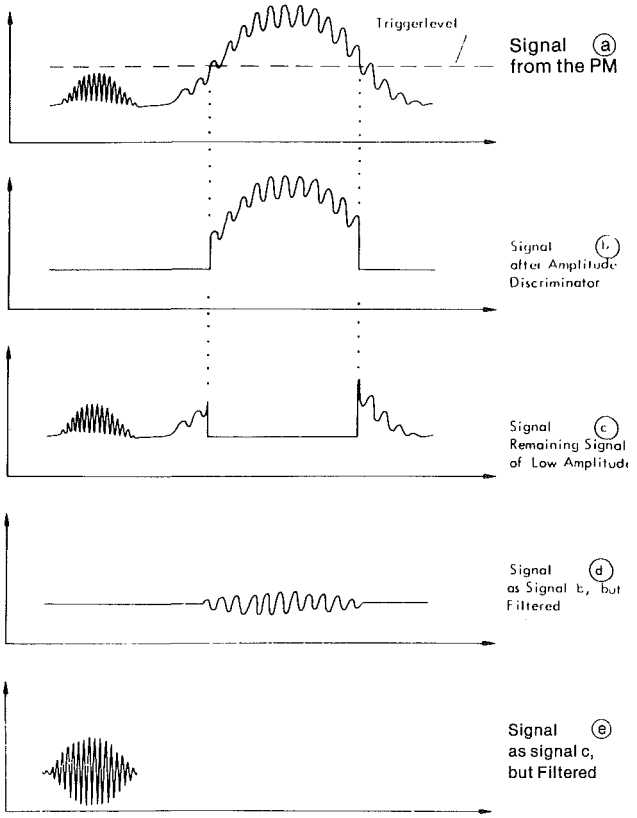

Fig. 22 Separation of signals by amplitude discriminator and automatic filterbanks

separation of the signals by amplitude discrimination and filtering. This sequence of signals indicates the functioning of the amplitude control in the electronic system given in Fig. 7 and also shows the functioning of the automatic filter banks A and B to produce the resulting signals d and e. These signals can be processed to obtain local information on the velocity fields of the two phases. In addition to the amplitude discrimination, the signals from the two photo-diodes are used to separate the signals of large and small particles. The combined usage of the amplitude discrimination and the photo-diodes permits the cross talk between signals from the small and large particles to be reduced.

In order to test the signal processing electronics, simulated signals were applied to the input of the signal processing systems. Such simulated signals are shown in Fig. 23 and consisted of bursts of different frequencies but of equal amplitude. In such a case, the amplitude discriminator would not be able to distinguish between the contributions from the two phases but the employment of the automatic filter banks in a so-called "slave-operation" permits the two contributions to be separated. It is only the employment of different controls like the amplitude discriminator, "slave-control" of the filter bank, photodiodeselection control, etc. that permits the cross talk between signals from small and large particles to be reduced.

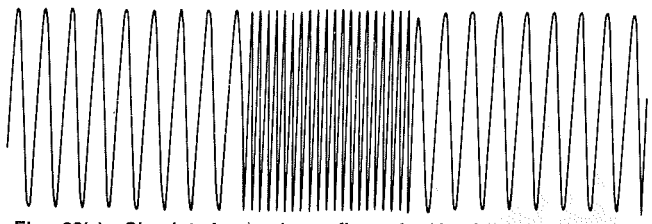

Fig. 23(a) Simulated two-phase flow signals; bursts of different frequency

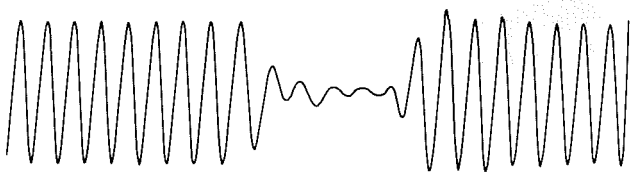

Fig. 23(b) Output of automatic filterbank A

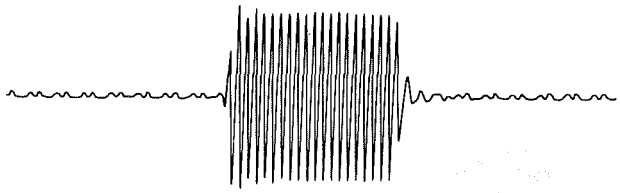

Fig. 24(c) Output of automatic filterbank B

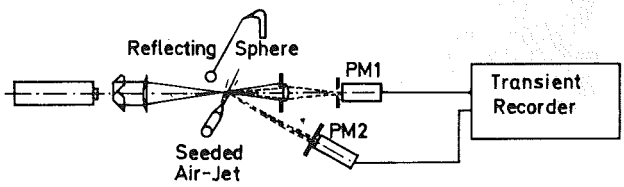

Fig. 24 Schematic of optical system and data recording for model two-phase experiment

5.3 Some Applications. The processing of laser-Doppler signals by digital computer became possible with the development of high speed analog-to-digital converters with storage capability and with digitizing rates of 100 MHz and faster. Devices of this kind permit Doppler bursts to be digitized and stored with sufficient accuracy to allow Doppler frequencies to be calculated by digital computers following the a-d-converter. The evaluation of the Doppler frequency from the recorder signals is controlled by software programs and, hence, differences in signal qualities can be accounted for easily by introducing suitable data validation schemes.

The a-d converter which was used in the present study was the 8 bit "Biomation Transient Recorder" model 8100. This model is particularly suited to record signal bursts as obtained in laser-Doppler anemometry because of its ability to operate in a "delayed-trigger" mode which allows the recording of the signals that occur prior to the triggering event. Hence, the recorder can be triggered on the high amplitude peaks in the center of the Doppler bursts and still record the entire bursts in the 2048 word memory of the transient recorder. The Biomation 8100 also offers input attenuation and amplification, and proper adjustment of these input parameters of the transient recorder permits optimal usage of the 8 bits of amplitude resolution.

In the present investigations, the contents of the 2048 word memory were transferred directly to the core memory of an available Hewlett Packard computer (HP 2116C). Once in the core, the data either can be directly analyzed (on-line operation) or stored on disk for further processing to obtain information on the Doppler frequency. Reading the data in and storing them on disk can be carried out at approximately

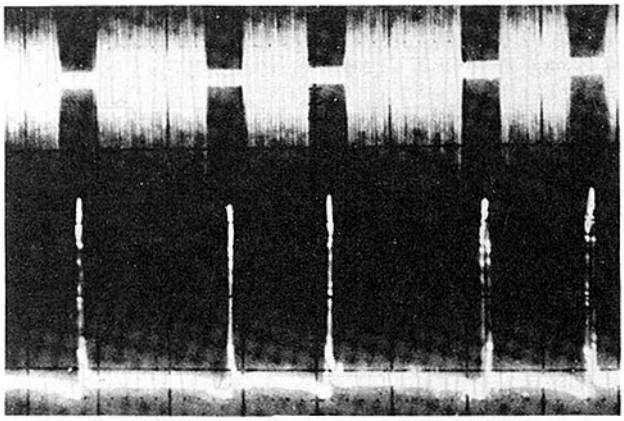

Fig. 25(a) Laser-doppler signals from the two photomultipliers of the optical arrangement shown in Fig. 24

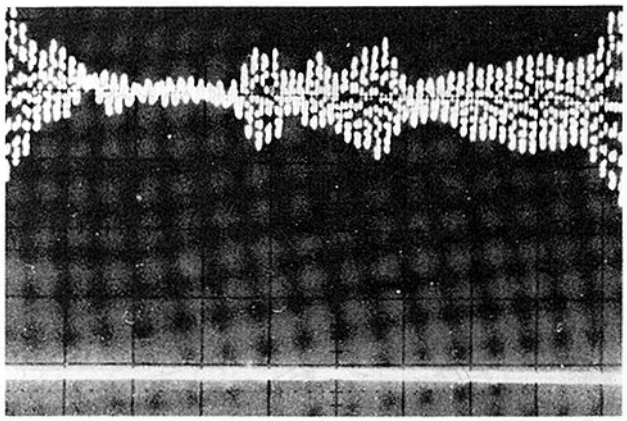

Fig. 25(b) Signals from photomultipliers: photomultiplier 1 shows the signal from small silicon oil particles, whereas no signals on photomultiplier 2

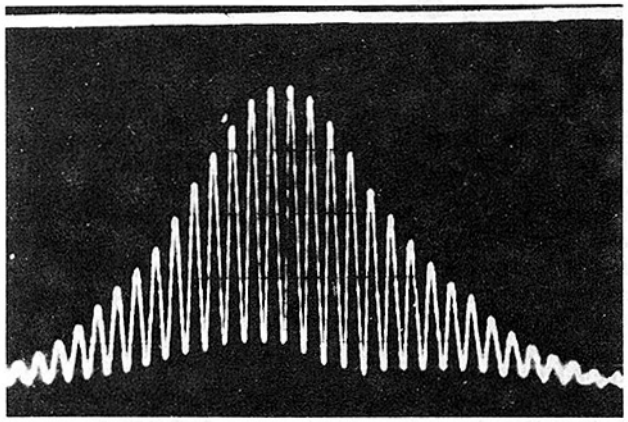

Fig. 25(c) Signals form photomultipliers: no signals are shown on photomultiplier 1 when the sphere penetrates the measuring control volume. Photomultiplier 2 shows the LDA-signal obtained from the sphere.

1000 words/s (5 complete memories), and the on-line processing rate depends entirely on the evaluation method used, as discussed by Durst and Tropea [21]. If the entire 2048 word memory is not required for analysis then a smaller portion of it may be read, thus allowing more Doppler bursts to be scanned per second. However, this modification means fewer points to describe the Doppler bursts and its application is therefore restricted to the processing of good quality signals.

During several stages of their experimental program, the author and his collaborators have verified the correct functioning of the optical and electronic systems of their two-phase flow LDA-instruments. Such verifications are best

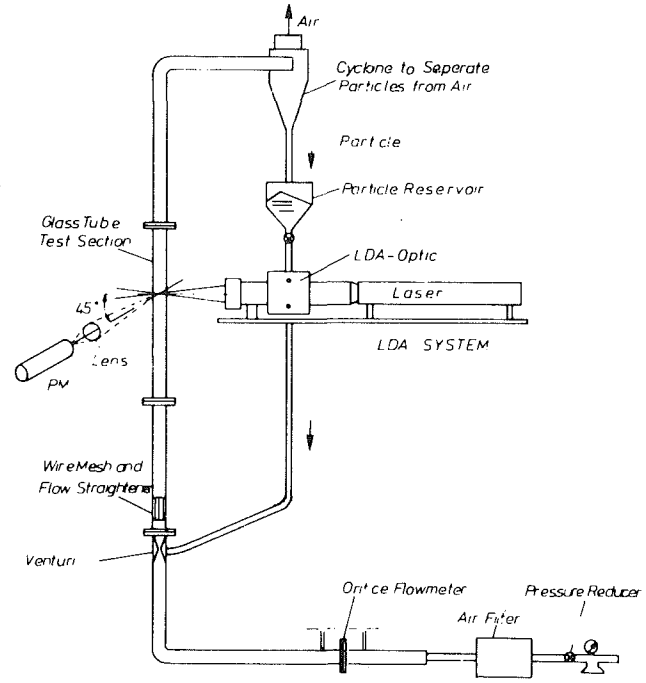

Fig. 26 Schematic diagram of the test section and the LDA-system for two-phase flow measurements

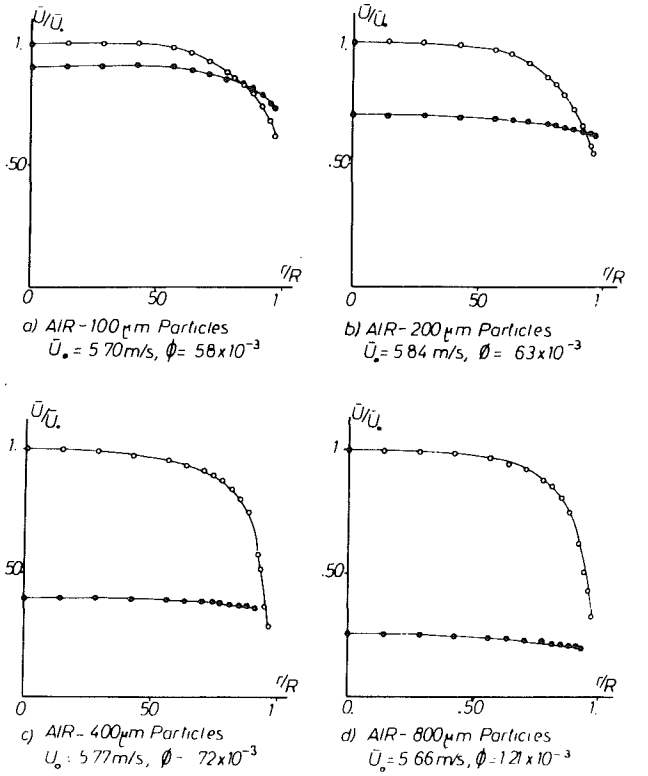

Fig. 27 LDA-measurements in two-phase flows. Mean velocity profiles of airflow and glass spheres in upward direction pipe flow.

carried out in simple two-phase flows and/or simulated flows that can be set up to emphasize particular features of the more complex flow situations in which the final instruments have to be applied. The present section describes examples of such verification experiments that clearly demonstrate the correct functioning of the two-phase flow LDA-systems described in this paper.

5.3.1 Model-Two-Phase-Flow. The present section

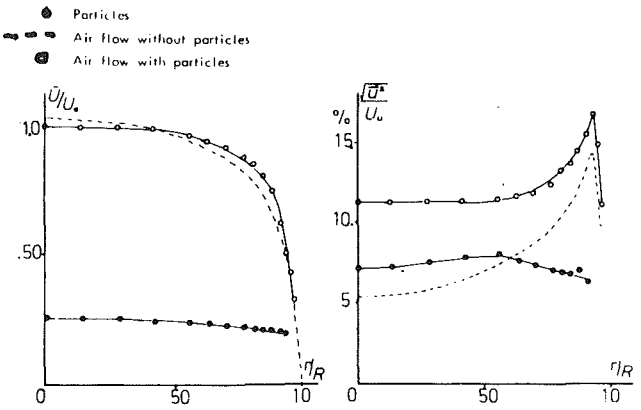

Fig. 28 Variations of the airflow due to the presence of particles

describes a model two-phase flow situation that was set up in the way proposed by Durst and Zaré [19]. This model two-phase flow is shown schematically in Fig. 24 and consists of a low velocity air jet. The second phase, i.e., the large particles in the flow, is simulated by a highly reflecting steel sphere which is made to swing through the measuring control volume. The optical and electronic system tested in this particular flow situation are also shown in Fig. 24 and are self-explanatory.

Figure 25(*a*) shows the signals that were recorded by the two channels of the transient recorder and replayed onto a scope for photographing purposes. The two signals originating from the airflow and the reflecting spheres are given on the scope display and it is shown that the signal from the airflow is interrupted when the signal from the reflecing sphere is displayed. There is a time gap between the signal from the small particles in the fluid and the large particles which is due to the spatial displacement between the two photodetectors used to record the signals; when the reflecting spheres enter the measuring control volume, it interrupts the signal on the first photodetector but some time is required until the moving fringe pattern has reached the second detector.

Figures 25(*b*) and (*c*) show the same signals as provided in Fig. 25(*a*) but with a higher time resolution on the transient recorder. It can be seen clearly that there is no signal from small particles in the air flow when the signal from the reflecting sphere is recorded and vice versa. This clearly demonstrates that the electronic system is able to separate the information from the two phases simulated in this way. There can be cross talk between the channels, however, if the particles do not move through the center of the measuring control volume but only touch the two laser beams. The combined usage of the automatic filterbank and the photodiode control circuit helps to avoid this kind of crosstalk. Nevertheless, more development work is required to improve the signal separation in complex flow cases.

5.3.2 Turbulent Pipe Flow With Solid Particles. As a further demonstration that LDA-measurements can be carried out in particulate two-phase flow systems, the present section describes measurements in a turbulent air flow with solid particles of different diameters. These measurements were performed in the test section shown in Fig. 26. It consists of a vertical pipe flow test section through which was driven filtered air supplied from a regulated pressure system. The supplied air contained enough particles to measure the air flow in the vertical glass tube so that no seeding problem existed. Glass particles of different diameters were added to this air flow via a venturi orifice that supplied the subpressure to suck the particles into the flow. A wire mesh and a flow straightener ensured an equal distribution of the particles and also helped to regulate the disturbed flow from the venturi orifice. A cyclone at the end of the test section separated the solid particles from the air flow and re-used these as indicated in Fig. 26. Particles of diameters $d_1 = 100$ μm, $d_2 = 200$ μm, $d_3 = 400$ μm and $d_4 = 800$ μm were employed in the present experiments.

Figure 27 shows examples of the results obtained in the aforementioned test section. Mean velocity distributions are shown across the entire test section for the air flow and the stream of suspended particles. The increasing velocity difference between particles and the fluid with increasing particle diameter is clearly given. With increasing particle diameter, the particle velocity profile becomes constant across the pipe diameter. At smaller particle diameters, the results show lower mean velocities of the particle in the center of the pipe but higher velocities at the pipe walls. This seems to indicate that the action of turbulent flows on solid particles shows basic differences that are dependent on the particle diameter. This is presently under study by the author and one of his colleagues, Professor R.S.L. Lee, State University of New York at Stony Brook.

Figure 28 shows the effect which solid particles have on the properties of the air flow. The velocity profiles for the axial velocity fluctuations are shown in this figure with and without particles. With particles, the mean velocity profile flattens in the center of the pipe but becomes steeper in the region near to the wall. The figure also shows that the turbulence intensities in the air flow are increased due to the particle motion. These are typical results for large particles. For small particles, reversed actions can be observed.

6 Conclusions and Final Remarks

A summary of developments in the field of laser Doppler anemometry was given with particular attention to combined systems that permit particle velocity, size distributions and concentrations to be measured locally. For small particles in the size range up to 10 microns, a combined system was described that utilizes a white light particle sizer and a laser Doppler anemometer to obtain information on particulate flow fields. In this size range, the particles are sufficiently small to follow subsonic flow and, hence, fluid measurements can be carried out with an instrument of this type. The combined measurements of size and velocity also permit correct measurements of fluid velocity; only those velocities are taken for measurements which were obtained from sufficiently small particles to follow the flow.

The fringe model has been used extensively in laser Doppler anemometry to reduce the frequency of LDA-signals. In addition, it has been employed to yield the evaluation equations for the modulation depth of LDA-signals and their dependence on the particle diameter. The present paper points out that this deduction is incorrect. The fringes do not exist in the measuring control volume as far as the scattering action of the particle is concerned. Postulating their existence is equivalent to attributing the properties of the photodetectors to the properties of the scattering particles.

The extension of laser Doppler anemometry to measure the velocity and size of large particles has been described and verification experiments have been given. Optical and electronic systems have been introduced that permit such measurement to be carried out for complex particulate two-phase flows.

Acknowledgments

The present report summarizes work on measurements of particle properties using optical techniques carried out by the author and his collaborators in the Sonderforschungsbereich 80 at the Universität Karlsruhe. Financial support was given by the Deutche Forschungsgemeinschaft to develop these techniques and to use them in particulate two-phase flows.

The author is very thankful to Mrs. G. Musiyan for the typing of the manuscript and to the staff of the drawing office of the Institute fur Hydromechanik of the Universität Karlsruhe for their help with the figures.

References

1 Durst, F., and Whitelaw, J. H., "Optimization of Optical Anemometers," *Proceedings of the Royal Society*, London, series A324, 1971, pp. 157–181.

2 Rudd, M. J., "A New Theoretical Model for the Laser Doppler Meter," *Journal of Physics E: Scientific Instruments*, Vol. 2, 1969, pp. 723–726.

3 Durst, F., and Stevenson, W. H., "Influence of Gaussian Beam Properties on Laser Doppler Signals," *Journal of Applied Optics*, Vol. 18, 1979, pp. 516–517.

4 Dopheide, D., and Durst, F., "Einfluß der Axialmoden von CW-Laser auf Laser-Doppler-Messungen bei rohen Frequenzen," *Technisches Messen*, (TM), 1981.

5 Dändliker, R., and Eliason, B., "A Theoretical Analysis of Laser-Doppler Flowmeters," *Optica Acta*, Vol. 21, No. 2, 1974, pp. 119–149.

6 Adrian, R. J., and Earley, W. L., "Evaluation of LDV Performance using Mie Scattering Theory," (in reference [19]), 1976, pp. 426–454.

7 Cherdron, W., Durst, F., and Richter G., "Computer Programs to predict the Properties of Scattered Laser Radiation," SFB 80/TM/121, 1978, Soderforschungsbereich 80, University of Karlsruhe.

8 Mie, G., "Beiträge zur Optik trüber Medien, speziell killoidaler Metalllösungen," *Ann. Physik 25*, IV. Folge, Nr. 3, 1908, pp. 377.

9 Durst, F., and Eliason, B., "Properties of Laser-Doppler Signals and Their Exploitation for Particle Size Measurements," *Proceedings of the LDA-Symposium*, University of Denmark, 1975.

10 Durst, F., and Umhauer, H., "Local Measurement of Particle Velocity, Size Distribution and Concentration with a Combined Laser-Doppler Particle Sizing System," *Proceedings of the LDA-Symposium*, University of Denmark, 1975.

11 Adrian, R. J., and Orloff, K. L., "Laser Anemometer Signals: Visibility Characteristics and Application to Particle Sizing," *Journal of Applied Optics*, Vol. 16, 1977, pp. 677–684.

12 Farmer, W. M., "Measurement of Particle Size, Number Density and Velocity using a Laser Interferometer," *Journal of Applied Optics*, Vol. 11, 1972, pp. 2603–2609.

13 Durst, F., "Scattering Phenomena and Their Application in Laser Doppler Anemometry," *Journal of Applied Mathematics and Physics* (*ZAMP*), Vol. 24, No. 4, 1973, pp. 619–643.

14 Robinson, D. M., and Chu, W. P., "Diffraction Analysis of Doppler Signal Characteristics for a Cross Beam Laser Doppler Velocimeter," *Journal of Applied Optics*, Vol. 14, 1975, pp. 2177–2181.

15 Roberds, D. W., "Particle Sizing using Laser Interfereometry," *Journal of Applied Optics*, Vol. 16, 1977, pp. 1861–1865.

16 Stümke, A., and Umhauer, H., "Local Particle Velocity Distributions in Two-Phase Flows Measured by Laser-Doppler Velocimetry," *Proceedings of the Dynamic Flow Conference*, Marseille, France, 1978.

17 Kerker, M., *The Scattering of Light and Other Electromagnetic Radiation*, Academic Press, 1969.

18 Van de Hulst, H. C., "Light Scattering by Small Particles."

19 Durst, F., and Zaré, M., "Laser-Doppler Measurements in Two-Phase Flows," *Proceedings of the LDA-Symposium*, 1975, University of Denmark.

20 Durst, F., and Heidbreder, J., "Eline automatische Filterbank für LDA-Signals," SFB 80/M/140, 1979, University of Karlsruhe.

21 Durst, F., and Tropea, C., "Processing of Laser-Doppler Signals by Means of a Transient Recorder and a Digigal Computer," SFB 80/E/118, 1977, University of Karlsurhe.

REVIEW—Numerical Models for Dilute Gas-Particle Flows

C. T. Crowe
Washington State University,
Pullman, Wash. 99164

The rapidly increasing capability of computers has led to the development of numerical models for gaseous flows and, in turn, gas-particle and gas-droplet flows. This paper reviews the essential features of gas-particle flows from the point of view of model development. Various models that have appeared for one-dimensional and two-dimensional flows are discussed. The advantages and disadvantages of the trajectory and two-fluid models are noted.

Introduction

Dilute gas-particle flows are found in many industrial applications such as cyclone separators and classifiers, pneumatic transport of powder, droplet combustion systems, spray drying and cooling, as well as sandblasting. Gas-particle flows are characterized by coupling between phases. For example, a spray, issuing into a hot gas stream, exemplifies thermal coupling through heat transfer to the droplet, momentum coupling through aerodynamic drag responsible for droplet motion, and mass coupling through evaporation. Inclusion of these coupling mechanisms complicates the analysis of gas-particle flows.

Another difference between the flow of a single phase and gas-particle[1] flow lies in the mechanism of information transfer between the elements of the particulate phase. There is no analog for pressure in a particle cloud and no information transfer between particles except through the conveying phase. These peculiarities affect the development of numerical models for gas particle flows.

The purpose of this paper is to define the significant nondimensional parameters relating to dilute gas-particle flows, to point out physical features germaine to model development and, finally to review some of the models which have appeared in the literature.

Characteristics of Gas-Particle Flows

The relative volume and mass of a component in a gas-particle mixture are quantified by the volume fraction and bulk density. Specifically, the volume fraction is the volume of a phase (gas phase, for example) per unit volume of mixture. The bulk density is the mass of a phase in the mixture per unit volume of mixture. The volume fractions of each phase sum to unity while the sum of the bulk densities yields the density of the mixture. The ratio of the bulk density of the particles to the bulk density of the gas is the loading, which is simply the ratio of the mass of the dispersed phase to the mass of the conveying phase in a mixture.

For pneumatic transport of coal in a pipe with average loading of unity, the volume fraction of particles is .001 so the corresponding volume fraction of air is .999. Under these conditions, one can assume the bulk density of the air is equal to material density of the air. This assumption is generally true for dilute gas-particle flows.

In order to define properties such as density, it is necessary to take average values over a volume. The definition of density in a continuum is the limit of the ratio of mass per unit volume as the volume approaches zero. That is, density is defined at a point. In a real gas, the limiting volume must contain a sufficient number of molecules to yield a stationary average. A volume containing 10^4 molecules will ensure a variation of less than 1 percent [1]. For a gas at standard conditions this volume would be a .1 micrometer cube. For the majority of applications this dimension is many times smaller than the characteristic flow dimension so the volume may be regarded as a "point" and the gas treated as a continuum.

In order to define properties in a gas-particle mixture, the limiting volume must be large enough to contain sufficient particles for a stationary average. For coal particles suspended in air with a loading of unity, the side of a cube which would contain 10^4 particles would be $L/D \sim 10^2$ where L is the cube dimension and D is the particle diameter. For 100 micrometer particles, L would be approximately one centimeter. Thus, the particle cloud could not be treated as a continuum in a flow system of comparable dimensions. The use of differential equations to relate property changes of a particle cloud (and mixtures) through application of the conservation equations would be cautioned in this situation [2].

Dilute Versus Dense. A dilute gas-particle flow is a flow in which the particle motion is controlled by local aerodynamic forces. In a dense gas-particle flow, particle motion is governed by particle-particle collisions. The delineation between dilute and dense flows is qualitatively established by the ratio of aerodynamic response (τ_A) time to the time between collisions (τ_C). The aerodynamic response time is the time required for a particle, released from rest in flowing stream, to achieve 63 percent of the free stream velocity. Thus, if $\tau_A/\tau_C < 1$, a particle has time to respond to the local

[1] In this paper, "gas-particle flow" refers to the flow of a gas particle or a gas-droplet suspension.

Contributed by the Fluids Engineering Division and based on a Keynote Address presented at the ASME Polyphase Flow and Technology Symposium, San Francisco, Calif., August 14-20, 1980, of THE AMERICAN SOCIETY OF MECHANICAL ENGINEERS. Manuscript received by the Fluids Engineering Division, September 26, 1980.

gas velocity field before the next collision so its motion is dominated by aerodynamic forces. This condition constitutes a dilute flow. On the other hand, if $\tau_A/\tau_C > 1$, the particle has insufficient time to respond to aerodynamic forces before the next collision so the particle motion is collision controlled and the flow is dense.

The dilute (or dense) nature of the flow will obviously depend on loading, with decreased loading leading to a dilute flow. In addition, the time between collisions depends on the mechanism responsible for developing a relative velocity (and thereby the potential for collision) between particles. In a gas-particle flow through a venturi, the smaller particles will accelerate more readily than the larger particles as the flow proceeds from the pipe to the throat region. Thus, a relative velocity between particles of different sizes is created by the response of particles to a gas velocity gradient. This particular example is analyzed in reference [3] in which it is demonstrated that the τ_A/τ_C ratio depends on loading, gas velocity gradient and the spread (standard deviation) of the particle size distribution.

Information Transfer. Another important difference between a continuum and a dilute particle cloud is the mechanism for information transfer. In a continuum, information is transmitted by pressure waves; that is, through molecular interaction. Also, information is transmitted by property diffusivity such as viscosity and thermal conductivity. In a dilute particle cloud, there is no analog to pressure and particle information is not transmitted by particle-particle collisions but only along particle trajectories. This particular feature leads to the predominantly parabolic nature of the equations for dilute particle clouds. The diffusivity of the properties of particle clouds is primarily due to the turbulence effects produced by the conveying phase which, at the present time, are not well understood.

Stokes Number. An important parameter in classifying special cases for numerical, as well as analytic, solutions is the Stokes number. The Stokes number is defined as the ratio of the aerodynamic response time to some characteristic time for the flow system, such as a nominal length divided by a gas-phase velocity. The Stokes number, then, is

$$\mathrm{St} = \tau_A/\tau_S$$

where τ_S is the flow system time. If the Stokes number is very small, the particles have ample time to respond to property changes in the conveying phase. In this case, one may assume that the particle velocities and temperatures are equal to those of the conveying gas and treat the mixture as a single-phase flow with modified properties. On the other hand, if the Stokes number is very large, then the particles are not able to respond to changes in the gas flow and the mixture may be treated again as a single-phase flow but with a distributed resistance and thermal source. Numerical methods applicable to single phase flows can be applied to these limiting cases.

Another special case is low loading in which the presence of the particles does not change the velocity or temperature fields of the conveying gas, but the conveying gas is responsible for the particle trajectories and property changes along trajectories. This condition is identified as one-way coupling.[2] The assumption of one-way coupling was used frequently in the early numerical and analytic models for gas-particle flows.

Two-Fluid Equations. One approach in modeling gas-particle flows is to start with the "two-fluid" equations. The two-fluid approach is to regard the conveying and particulate phase as two interactive fluids in much the same way as one would regard the two species of a flowing binary mixture. The two-fluid equations are obtained by averaging the conservation equations over a volume (as discussed above) and expressing the equations in differential form.

The continuity equations are similar to those for the flow of a single phase with the exception of source terms which represent mass exchange between phases. These equations for a single particle size in steady flow are [4]

$$\partial(\rho_p' v_i)/\partial x_i = -S_m \tag{1}$$

for the particulate phase and

$$\partial(\rho_g' u_i)/\partial x_i = S_m \tag{2}$$

for the continuous phase where ρ_p' and ρ_g' are the bulk densities of the particle and gas phases, v_i is the particle phase velocity and u_i is the gas phase velocity. The term S_m represents the mass addition to the continuous phase per unit volume of mixture caused by such phenomena as evaporation and burning. These equations do not include particle dispersion due to turbulence.

An alternative form of the continuity equations is to use the volume flow rate of the fluid instead of the mass flow rate as the dependent variable. In this manner, the continuity equation for the particle phase becomes

$$\partial(\alpha_p v_i)/\partial x_i = -S_v \tag{3}$$

when α_p is the volume fraction of the particulate phase and S_v is the volume source to the gaseous phase per unit volume of mixture.

The corresponding two-fluid momentum equations for a dilute gas-particle flow are (4)

$$\rho_p' v_j \partial v_i/\partial x_j = f_i \tag{4}$$

for the particles and

$$\rho_g' u_j \partial u_i/\partial x_j = -\partial P/\partial x_i - S_m(u_i - v_i) + \partial(\tau_{g,ij})/\partial x_j - f_i \tag{5}$$

for the gas phase where f_i is the aerodynamic force (including the force due to gas pressure gradient) on the particle cloud per volume of mixture and P is continuous phase pressure. $\tau_{g,ij}$ is the net shear stress tensor for the continuous phase. Body forces, such as gravity, are not included. One notes the absence of a "particle pressure" in the particle phase equations. Also, there is no equation of state for the particle cloud as there is for the conveying gas phase. In fact, the particle cloud is analogous to compressible fluid with no equation of state.

Several derivations of the two-fluid equations have ap-

[2] This condition is frequently used in the literature to classify dilute flows.

Nomenclature

D = particle diameter
E = error in volume fraction
F,G,H = dependent variables in conservative formulation of equations
L = cube dimension
P = pressure
S_m = gaseous mass source per unit volume of mixture
S_v = gaseous volume source per unit volume of mixture
u_i = gas-phase velocity
v_i = particle-phase velocity
x_i = distance vector
α_p = volume fraction of particulate phase
α_g = volume fraction of gaseous phase
ρ_p' = bulk density of particle
ρ_g' = bulk density of gas
τ_A = aerodynamic response time
τ_C = time between particle-particle collision
τ_S = flow system time
$\tau_{g,ij}$ = net gas shear stress tensor

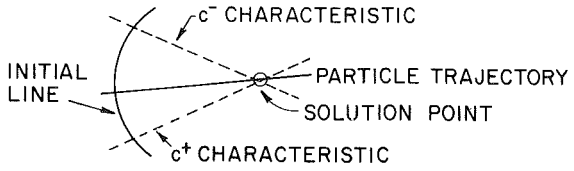

Fig. 1 Method of characteristics for gas-particle flows

peared in the literature. The equations cited most frequently are those presented by Drew [2] and Ishii [5]. Other derivations include those by Soo [6], Nigmatulin [7] and, more recently, Immich [8]. The resulting equations differ in various ways such as the formulation for the pressure gradient term, the nature of the momentum source terms and the convection terms for particle momentum. Arguments over the correct form of these equations persist in the literature. Many of the formulations include a shear stress term of the particle cloud although no general constitutive equations relating stress and flow properties have yet been developed. Numerical models based on the two-fluid equations generally do not include shear stress for the particle cloud. Either it is simply neglected or arguments are made that it is unimportant. Presently there is no quantitative justification for excluding this term, especially near a boundary where the particle can exchange momentum with the wall.

Numerical Models

The early models developed for gas-particle flows were based on one-way coupling. The assumption of one-way coupling is generally valid if the loadings are low (less than 10 percent). These models require the specification of the flow field for the conveying fluid either from experimental results or from the results of a numerical or analytic model. Particle trajectories are calculated by integrating the particle motion equations as the particle proceeds through the flow field. Mass and temperature history along the trajectory may also be calculated by integration of the appropriate rate equations. One-dimensional models with one-way coupling have appeared in the literature for a wide variety of applications from spray drying [9] to performance of a venturi scrubber [10]. Numerous two- and three-dimensional models also have appeared for several applications such as cyclone separators [11] and turbine blade erosion [12]. Recently Laitone [13] has used the flow field generated by the discrete vortex method for unsteady flow over a cylinder to calculate particle trajectories in the wake of a cylinder. The implementation of such models is, in principle, straightforward.

Interactive coupling in which the mutual effects of both the particles and gas are included is referred to as "two-way" coupling. The majority of the discussion in this paper focuses on models which incorporate two-way coupling.

The parabolic nature of the particle cloud suggests numerical solutions based on marching techniques as most appropriate for the integration of the particle cloud equations. Such techniques are also used for the solution of unsteady compressible flows and two dimensional steady supersonic flows. In these cases marching techniques for each phase can be combined to yield a numerical model for the gas-particle mixtures.

Two-Dimensional Supersonic Gas-Particle Flows. The method of characteristics is well established for supersonic, two-dimensional flows. Pairs of characteristic lines are drawn from an initial line, as shown in Fig. 1. The compatability conditions between the dependent variables yield the values of the dependent variable at the points where the characteristic lines cross. The particle trajectory simply constitutes a third characteristic. The integration of the equations for particle properties along the trajectory yields the particle compatability condition which, combined with the gas-phase compatability conditions, yields the gas and particle properties at the intersection point. This approach was first used by Kliegel [14] in the analysis of gas-particle flow in rocket nozzles. It has been, and continues to be, used in the optimal design of rocket nozzles.

Another numerical scheme for supersonic gas-particle flows has been recently developed by Dash and Thorpe [15]. In this case the two-dimensional flow equations are written in conservative form amenable to Lax-Wendorff methods; namely,

$$\partial F/\partial \zeta + \partial G/\partial \eta + H = 0 \tag{6}$$

where F and G are variables representing combinations of gas flow properties and ζ and η are the marching and transverse directions respectively. The effects of the particles are contained in the term H. The particle cloud equations are also written in conservation form. For example, the F and G for the gas continuity equation are the component mass fluxes and H is the mass addition term due to the particles. The momentum and energy equations are written in the same form. The coupled system of equations are solved using the two-step explicit MacCormack scheme [16]. The advantage of this approach is that the calculation can be extended through shock waves due to the conservative formulation of the governing equations.

One-Dimensional Unsteady Flows. In principle, the same approach based on the method of characteristics for supersonic steady flow can be used for compressible, unsteady one-dimensional flows. Recently, Low et al. [17, 18] used the method of characteristics for one-dimensional air-droplet flow with the intention of modeling charge transport into the cylinder of a spark ignition engine. Besides the gas flow characteristics and the particle trajectories, Low et al. used the gas-phase streamlines to obtain the entropy and mole fraction of fuel vapor.

Marching solutions based on Lax-Wendorff formulations have been used for unsteady steam-water flow in a Laval nozzle [19]. In this case the equations are the same form as equation (1) with the independent variables being space and time. The calculations were continued until steady flow was achieved in order to compare the numerical predictions with experimental results. Reasonably good agreement was obtained.

Marching solutions encounter difficulties when the conveying fluid becomes incompressible and information is transmitted in the continuous phase instantaneously in all directions. The characteristic lines collapse onto the spatial coordinates and the technique becomes inoperative.

One-Dimensional Steady Flows. Several numerical models have been published for one-dimensional, and quasi one-dimensional steady gas-particle flows. In this case, information is confined to travel in one direction only, and solutions can be obtained by integrating the governing equations in this direction. This approach was used by Kleigel [20] in 1961 to model gas-particle flow in a Laval nozzle. The equations for the particles and the gas were integrated explicitly accounting for momentum and thermal coupling. The correct initial conditions were unknown apriori so the upstream velocity was varied until the solution proceeded smoothly through the sonic region near the throat. This technique was used extensively [21, 22, 23] to predict performance loss due to particles in rocket exhausts and as starting conditions for the method of characteristics solution in supersonic diffusers [4].

An implicit formulation for gas-particle flow in venturis has been developed by Sharma [24]. In this case the equations are written in conservative form for the gas using mass flow,

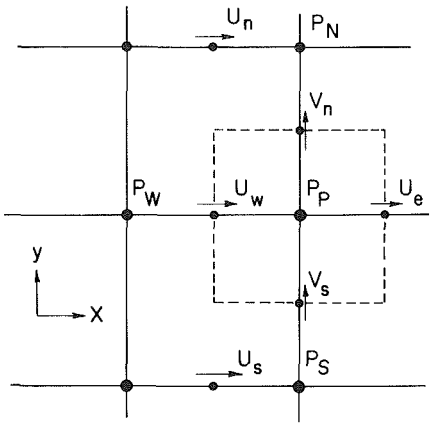

Fig. 2 Staggered-grid coordinate system for primitive variables

momentum flux plus pressure, and total energy flux as the dependent variables. The mass, momentum, and energy coupling terms due to the particles appear as source terms to the gaseous phase. The procedure for each computational cell begins by assuming a downstream pressure and solving for the primitive gas variables, including the pressure, and particle properties at the downstream station. The calculated pressure is used as a new estimate and iteration continues until the pressure converges within acceptable limits. This scheme is conceptually simple and computationably efficient. The results show good agreement with experiment.

A quasi one-dimensional numerical model for gas-particle flow which is based on a system of equations for the entire field and solved using relaxation methods has been developed by Baghdadi [25]. This model is the one-dimensional analog of the multidimensional model proposed by Spalding [26] and discussed more fully in the following section. This model was applied to gas-particle flow in a venturi as studied by Sharma [27] and good agreement with experimental data is reported. The calculation, however, was limited to one particle size. The question as to the adequacy of an "average" particle size to represent a distribution of sizes was not addressed.

Two-Dimensional Subsonic Flows. In order to review two-dimensional models for gas-particle flows, it is helpful to make a cursory summary of numerical models for single-phase flows. Basically, two approaches have been used to model the flow of single-phase fluids; the vorticity-stream function and primitive variable approach.

The vorticity stream function approach was popularized by Gosman et al. [28] in 1969. The governing equations are formulated using vorticity and stream function as the dependent variables which reduces the number of equations by one and eliminates pressure as a dependent variable. The equations are written in finite difference form using upwind differencing and solved by relaxation techniques such as Gauss-Seidel successive substitution. This approach has the advantage of eliminating the troublesome variable, pressure. However, the numerical scheme has characteristically slow convergence because of coupling of the boundary conditions. Also the scheme is at a disadvantage for applications where pressure is required, such as modeling compressible flows. For these reasons, the vorticity stream function formulation is used infrequently.

The primitive variable approach uses velocity and pressure (as well as density, temperature, etc.) as the dependent variables. The fact that a pressure gradient is primarily responsible for fluid motion leads to a technique whereby the pressures and velocities are not defined at the same physical locations. This leads to the "staggered grid" arrangement or designating the velocity field by fractional indices. Consider the grid system shown in Fig. 2. The x and y component of

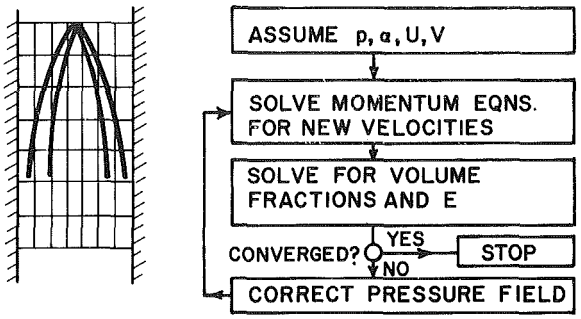

Fig. 3 Flow diagram for two-fluid models

velocities are defined midway between grid lines and pressures are defined at the nodal points. The pressure gradient between a pair of nodal points is responsible for the motion of the fluid at the midnodal points. The velocity component at the point w, for example, can be obtained by writing the momentum equation in finite difference form as a function of the pressure pair and the neighboring velocities,

$$u_w = f(P_p, P_w, u_n) \tag{7}$$

where u_n represents the velocities surrounding the point w. The effect of a pressure change on the velocity is approximated by the first term of a Taylor series expansion

$$u_w = u_w^* + (\partial u_w/\partial P_p)\Delta P_p + (\partial u_w/\partial P_w)\Delta P_w \tag{2}$$

where u_w^* is the previous velocity. Applying this equation to the velocity components surrounding a computational cell (dotted line in Fig. 2) and setting the net mass flux equal to zero (for steady flow) yields an equation for the pressure change. Thus the continuity equation is replaced by an equation for pressure change. The algebraic difference equations for velocities and pressure are solved by relaxation methods reflecting the elliptical nature of the governing equations. This approach was originated at Los Alamos Scientific Laboratories [29] and utilized in different forms in subsequent numerical models developed by others. This is known as the SIMPLE algorithm [30, 31] in the programs developed at Imperial College in London.

One notes that, independent of the approach used, relaxation methods are employed to solve the gas flow field which contrasts with the marching methods natural to solution of particle cloud equations.

There are basically two schemes that have been used in the literature to model two-dimensional subsonic gas-particle flows; the two fluid method and the trajectory method.

Two-Fluid Model. The basic equations, or equations similar thereto, used for the two fluid models are equations (1) through (5). The approach developed by Harlow and Amsden [32] is to manipulate the momentum equations into a form to yield the component mass fluxes. These mass fluxes are then incorporated into the continuity equations for each phase to yield a "mass residue." A mass residue of zero signifies continuity is satisfied. These mass residues are then used in a Newton-Raphson formulation to increment pressure in the same manner as for single-phase flows. The volume fractions of each phase are then adjusted to locally equilibrate the pressure. Lee [33] has used this scheme with some modifications, to model the impingement of a steam-water jet on a flat plate. He reports good agreement between predicted and measured stagnation pressures although stability problems were encountered for weak momentum and thermal coupling.

A somewhat similar approach to modeling gas-particle flows has been developed by Spalding [26]. The volume formulation of the continuity equation, equation (3), is written in finite difference form using upwind differencing to

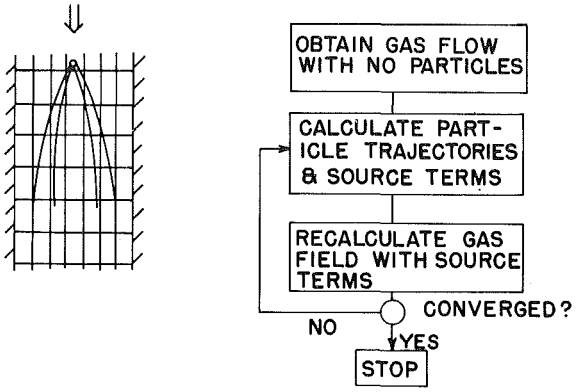

Fig. 4 Flow diagram for trajectory models

yield the volume fraction of each phase. The "volume residue" is then calculated in each computational cell; namely.

$$E = 1 - \alpha_g - \alpha_p \tag{9}$$

when α_g and α_p are the volume fractions of the gaseous and particulate phases, respectivley. This equation is subjected to a Newton-Raphson procedure to yield an equation for pressure change analogous to that used for single phase flows. A simple flow diagram outlining the steps in the two-fluid model is shown in Fig. 3. Repeated iterations continue to update the velocities and volume fractions until E becomes acceptably small. If there are several particle sizes being considered, the volume fraction of the particulate phase is the sum of the volume fractions of each size class. Pun [34] has applied this scheme to predict the raindrop field produced by flow over an obstacle.

Recently Di Giancinto et al. [35] have presented a numerical model for gas-particle flow through a constriction (like an orifice) based on the two-fluid equations. The time unsteady equations were used and integrated implicitly to yield gas and particle phase velocities and particle volume fraction. Gas phase pressures were determined by an iteration over relaxation scheme which updates the velocities as well. The method appears very similar to that developed by Harlow and Amsden [32] but specialized to dilute flows. The steady flow solution is obtained by performing the integration until the flow field fails to change with time. The calculations were performed with a single particle size. The stress term for the particle cloud is discarded because the authors argue that it is negligible for dilute flows.

Chang [36] has also used the unsteady two-fluid equations in conservative form and MacCormack's scheme [16] to predict gas and particle fields in planar and axisymmetric nozzles. Using a body-fitted coordinate system, he was able to obtain solutions for submerged nozzles and for nozzles with small radii of curvature. The calculations were limited to single-size particles but the scheme appears to have considerable potential for solving complex gas-particle flow fields.

Although the two fluid models applied to dilute gas-particle flows have the advantage of using numerical procedures already established for single-phase flow, there are some difficulties. The use of upwind differencing introduces numerical diffusion which requires the use of finer grid spacing (more expensive) for control. When treating more than one particle size, one must regard each size category as a separate fluid which demands considerably more computer storage. It has also been found that prohibitively small time steps must be used when strong gas-particle momentum coupling is encountered.

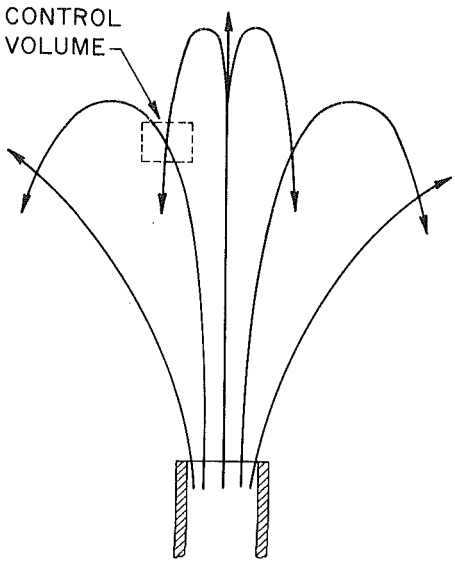

Fig. 5 Control volume with two particle velocities

Trajectory Models. The other approach to modeling gas-particle flow is the trajectory approach pioneered at Washington State University [37] in 1972. This approach, called the PSI Cell (Particle-Source-in-Cell) model [38], is based on treating the particles as sources of mass, momentum and energy to the gaseous phase. A single flow diagram for the method is illustrated in Fig. 4. The procedure begins by solving the gas flow field using a numerical scheme [30] developed at Imperial College in London. The first calculation assumes that no particles are present in the flow field. Particle trajectories, and the mass and temperature history on each trajectory, are then calculated through the gas flow field. The particle properties on crossing the boundaries of computational cells yields the mass, momentum, and energy source terms for the gas in each cell. The gas flow field is recalculated, incorporating these source terms. New trajectories are calculated and source terms reevaluated. The process is continued until the flow field fails to change with repeated iteration.

This approach incorporates the most natural computational scheme for each phase, namely, a relaxation method for the continuous (gas) phase and marching method for the dispersed (particle or droplet) phase. Thus, the elliptic nature of gas flow and the parabolic nature of the dilute cloud equations are retained. This approach was originally used for gas-particle flow in a cyclone separator [39] with the vorticity-stream function formulation. Since then the scheme has been used extensively with the TEACHT code [30], which uses the primitive variables, and has been applied to several problems such as spray drying (40), fire suppression [41], liquid fuel combustors [42] and pneumatic transport [43]. A similar scheme has been used by Palaszewski et al. [44] to model spray units.

One interesting feature of the trajectory approach is the absence of numerical diffusion of the particle cloud. In fact, this feature turns out to be a shortcoming of this approach. There are two methods by which particle dispersion due to turbulence can be modeled. One technique, pioneered by Jurewicz [45] and subsequently utilized by others [46, 47], is to use an effective diffusion velocity (or diffusion "force") in the particle motion equation which is dependent on the particle concentration gradient. An effective diffusion coefficient must be chosen for which no reliable information is currently available. Even though this approach has the same problem as the two-fluid model; that is, the choice of an

appropriate value for the effective diffusion coefficient, it does preserve the parabolic nature of the particle cloud.

Dukowicz [48] has extended the SOLA code developed by Los Alamos [32] for single-phase gas flows to treat gas-particle flows using the trajectory approach. The model was applied to liquid fuel sprays. The droplets were treated in a Lagrangian fashion by integrating the droplet motion equations to locate new positions as a function of time. By time splitting, the droplet-gas coupling phenomena is carried out noniteratively. Particle dispersion due to turbulence is modeled by diffusion "force" requiring selection of a diffusion coefficient. Good agreement with measured and predicted fuel spray penetration was achieved although mass coupling was not included.

Two-dimensional models [49, 50] of gas-particle flow in electrostatic precipitators have also treated particle dispersion due to turbulence as a Fickian diffusion process. These models are based on "one-way" coupling (which is valid for the low loadings characteristic of electrostatic precipitators) with the mean particle velocity field differing from the gas flow field by the drift velocity due to the Coulomb force. Some questions have existed for the appropriate formulation for the concentration boundary conditions [50].

The selection of appropriate diffusion coefficients and boundary conditions must await an improved understanding and mathematical description of the turbulence-particle interaction. Such studies are currently underway by Reeks [51] and others.

The other technique is based on the Monte Carlo method in which the turbulent gas flow field is modeled as a steady flow plus a random velocity fluctuation [52]. Many particles must be used to simulate the cloud, requiring extensive run time. Provided the turbulent field is adequately modeled, this procedure precludes the need for an effective diffusion coefficient.

A point of interest with regard to the two-fluid and trajectory approaches to modeling gas-particle flows lies in the nature of the equations. The incorporation of particle diffusion (and/or viscosity) into the steady two-fluid formulation for the particle cloud changes the equations from parabolic to elliptic. This means that the solution to the particle cloud equations becomes a boundary value problem which is in contrast to the basic nature of particulate motion. Also, this means that a particle "viscosity" must be defined for the motion of a particle cloud adjacent to a wall and the particle velocity at the wall (slip velocity) must be established. The trajectory approach, on the other hand, preserves the basic nature of the particulate flow and poses no problem with boundary conditions (rebounds or sticks) provided particle rebound information is available.

A vivid contrast between the two-fluid and trajectory models is provided by the problem shown in Fig. 5. Assume a stream of particles is emitted from a vertical source. Two possible particle trajectories are shown which traverse the same computational volume. The particle velocity in the computational cell would not be unique and definable in a two-fluid model and consideration would have to be given to upward moving and downward moving particles. This configuration would offer no problem, however, to the trajectory approach.

The relative advantages and disadvantages of the two-fluid and trajectory approaches to modeling gas-particle flow can be summarized as follows. The two-fluid models can easily incorporate particle diffusion effects (if data are available) and can be extended easily to multidimensional flows. However, numerical instabilities, numerical diffusion and large storage requirements for multiple particle sizes are inherent difficulties. The trajectory approach embodies the "natural" solution schemes for each phase and exhibits no numerical diffusion of the particulate phase. Also, storage requirements for multiple particle sizes are not excessive. Particle dispersion must be incorporated through an empirical diffusion velocity or more expensive Monte Carlo methods.

Conclusion

A wide variety of models have appeared in the literature for gas-particle flows. These models can be categorized according to coupling (one-way or two-way), dimensional capability (one-dimensional, quasi one-dimensional and two- and three-dimensional) and approach (two-fluid and trajectory). The most difficult aspect of model development for gas-particle flows is the adequate description of particle dispersion due to turbulence. Considerably more experimental and complementary numerical work are needed in this area.

Acknowledgment

The author acknowledges the invitation of R. Bajura to prepare this paper. The partial support of NSF Grant CPE-7925077 as well as the Mechanical Engineering Department of Washington State University are appreciated.

References

1 Reif, F., *Fundamentals of Statistics and Thermal Physics*, McGraw-Hill, 1965.

2 Drew, D. A., "Averaged Field Equations for Two-Phase Media," *Studies in Applied Mathematics*, Vol. 1, No. 2, 1971.

3 Crowe, C. T., "On the Relative Importance of Particle-Particle Collisions in Gas-Particle Flows," Paper C78—81, Conf. on Gas-Borne Particles, Inst. of Mech. Engr., Oxford, England, 1981, pp. 135–137.

4 Crowe, C. T., "On the Vapor Droplet Flows Including Boundary Droplet Effects," *Two-Phase Transport and Reactor Safety*, Vol. 1, Hemisphere Publishing Co., 1978, pp. 385–405.

5 Ishii, M., *Thermo-Fluid Dynamic Theory of Two Phase Flow*, Eyrolles, 1975.

6 Soo, S. L., "On One-Dimensional Motion of a Single Component in Two Phases," *Int. Jnl. Multiphase Flow*, Vol. 3, 1976, pp. 79–82.

7 Nigmatlin, R. I., "Spatial Averaging of Heterogenous and Dispersed Phase Systems," *Int. Jnl. Multiphase Flow*, Vol. 5, 1979, pp. 353–385.

8 Immich, H., "Zweiphasen-kontinuumstheorie einer Suspension starrer, kugelformiger Teilchen unter Berucksichtigung der Teilchenrotation," *Zeit ange Math Mech*, Vol. 60, 1980, Part I, pp. 99–107, Part II, pp. 153–160.

9 Marshall, W. R., and Seltzer, E., "Principles of Spray Drying, part 1. Fundamentals of Spray Dryers Operation, *"Chemical Engineering Science*, Vol. 46, No. 10, 1950, pp. 501–508.

10 Boll, R. H., "Particle Collection and Pressure Drop in Venturi Scrubbers," *Industrial Engineering Chemistry Fundamentals*, Vol. 12, No. 1, 1973, pp. 40–50.

11 Trow, M., "Particle Trajectories in Uni-Flow Cyclones," Paper C64/81, Conference on Gas Borne Particles, Inst. of Mech. Engr., Oxford, England, 1981, pp. 31–36.

12 Tabakoff, W., and Hamed, A., "Three Dimensional Particles Trajectories in Turbomachinery," Conference on Gas-Borne Particles, The Institution of Mechanical Engineers, Oxford, 1981 pp. 21–25.

13 Laitone, J. A., "A Numerical Solution for Gas-Particle Flow at High Reynolds Numbers," ASME *Journal of Applied Mechanics*, Vol. 48, 1981, pp. 465–471.

14 Kliegel, J. R., "Gas-Particle Nozzle Flows," *Ninth (Int'l) Symposium on Combustion*, Academic Press, 1963, pp. 811–826.

15 Dash, S. M., and Thorpe, R. D., "Shock-Capturing Model for One- and Two-Phase Supersonic Exhaust Flows," *AIAA Journal*, Vol. 19, No. 7, 1981, pp. 842–851.

16 MacCormack, R. W., "The Effect of Viscosity in Hypervelocity Impact Cratering," AIAA Paper No. 69-354, 1969.

17 Low, S. C., Baruah, P. C., and Winterbone, D. E., "One-Dimensional Air and Droplets Flow Model Which Includes Evaporation, Heat Transfer and Drag," Conference on Gas-Borne Particles, Inst. of Mech. Engr., Oxford, England, 1981, pp. 37–46.

18 Low, S. C., and Baruah, P. C., "Liquid Fuel Droplets Entrained in Transient Unidimensional Gas-Flow in a Pipe," *Int. Jnl. Multiphase Flow*, Vol. 7, 1981, pp. 293–309.

19 Comfort, W. L., et al., "Calculation of Two-Phase Dispersed Droplet-in-Vapor Flows Including Normal Shock Waves," ASME JOURNAL OF FLUIDS ENGINEERING, Vol. 100, No. 3, 1979, pp. 355–362.

20 Kiegel, J. R., "One-Dimensional Flow of a Gas-Particle System," Paper No. 60-S, IAS 28th meeting, New York, 1960.

21 Nelson, J. H., and Gilchrist, A., "An Analytic and Experimental Investigation of the Velocity of Particles Entrained by a Gas Flow in Nozzles," *Journal of Fluid Mechanics*, Vol. 33, Part 1, 1968, pp. 131–149.

22 Hoglund, R. F., "Recent Advances in Gas-Particle Nozzle Flows," *Journal of the American Rocket Society*, Vol. 32, 1962, p. 662.

23 Holtberg, J. A., and Soo, S. L., "Two-Phase Flow Through a Nozzle," *Astronautica Acta*, Vol. 11, 1965, p. 207.

24 Sharma, M. P., and Crowe, C. T., "A Novel Physico-Computational Model for Quasi One-Dimensional Gas-Particle Flows," ASME JOURNAL OF FLUIDS ENGINEERING, Vol. 100, No. 3, 1978, pp. 343-349.

25 Baghdadi, A. H. A., "Numerical Modeling of Two-Phase Flow with Interphase Slip," Ph.D. thesis, Imperial College of Science and Technology, London, England, 1979.

26 Spalding, D. B., "Numerical Computation of Multiphase Flows, "Workshop Lecture Notes, Purdue University, 1978.

27 Sharma, M. P., "Numerical and Experimental Study of Gas-Particle Flows in Orifices and Venturis: Application to Flow Meter Design," Ph.D. thesis, Washington State University, 1977.

28 Gosman, A. D., et al., *Heat and Mass Transfer in Recirculating Flows*, Academic Press, 1969.

29 Hirt, C. W., Nichols, B. D., and Romer, N. C., "SOLA-A Numerical Solution Algorithm for Transient Fluid Flows," Los Alamos Scientific Laboratory Report LA-5852, 1975.

30 Gosman, A. D., and Pun, W. M., "Calculation of Recirculating Flow," Lecture Notes, Imperial College of Science and Technology, London, England, 1973.

31 Patankar, S. V., *Numerical Heat Transfer and Fluid Flow*, McGraw-Hill, 1980.

32 Harlow, F., and Amsden, A., "Numerical Calculation of Multiphase Fluid Flow," *Journal of Computational Physics*, Vol. 17, 1975, pp. 19-52.

33 Lee, W. H., "A Pressure Iteration Scheme for Two-Phase Flow Modeling," Los Alamos Scientific Laboratory Report, LA-UR-79-975, 1979.

34 Pun, W. M., et al., "Calculation of Two-Dimensional Steady Two-Phase Flow," *Two-Phase Momentum and Heat Transfer in Chemical, Process and Energy Engineering Systems*, Vol. 2 ed. F. Durst et al., Hemisphere Pub. 1979, pp. 461-470.

35 Di Giacinto, M., Sabetta, F., and Piva, H., "Two-Way Coupling Effects in Dilute Gas-Particle Flow," ASME JOURNAL OF FLUIDS ENGINEERING, (in press).

36 Chang, I., "One- and Two-Phase Nozzle Flows," *AIAA Journal*, Vol. 18, No. 12, 1980, pp. 1455-1461.

37 Crowe, C. T., and Pratt, D. T., "Two Dimensional Gas-Particle Flow," *Proceedings of 1972 Heat Transfer and Fluid Mechanics Institute*, Stanford University Press, 1972, pp.

38 Crowe, C. T., Sharma, M. P., and Stock, D. E., "The Particle-Source-in-Cell Method for Gas Droplet Flow," ASME JOURNAL OF FLUIDS ENGINEERING, Vol. 99, No. 2, 1977, pp. 325-332.

39 Crowe, C. T., and Pratt, D. T., "Analysis of the Flow Field in Cyclone Separators," *Computers and Fluids*, Vol. 2, 1974, pp. 249-260.

40 Crowe, C. T., "On Modeling Spray Air Contact in Spray-Drying Systems," Chapter 3, *Advances in Drying*, Hemisphere Pub. 1980.

41 Alpert, R. L., and Mathews, M. K., "Calculation of Large Scale Flow Fields Induced by Droplet Sprays," *Proceedings of Polyphase Flow and Transport Technology*, ASME, ed. R. Bajura, 1980, pp. 115-127.

42 El-Bainhawy, V., and Whitelaw, J. H., "The Calculation of the Flow Properties of a Confined Kerosine-Spray Flame," *AIAA Journal*, Vol. 18, No. 12, 1980, pp. 1503-1510.

43 Lee, J., and Crowe, C. T., "Scaling Laws for Metering the Flow of Gas-Particle Suspension through Venturi," *Proceedings of Polyphase Flow and Transport Technology Conference*, ASME, edited by R. Bajura, San Francisco, 1980, pp. 245-249.

44 Palaszewski, S. J., Jiji, L. M., and Weinbaum, S. "A Three Dimensional Air-Vapor-Droplet Local Interaction Model for Spray Units," *Jnl Heat Transfer*, Vol. 103, 1981, pp. 514-521.

45 Jurewicz, J. T., and Stock, D. E., "A Numerical Model for Turbulent Diffusion in Gas-Particle Flows," Paper 76-WS/FE-33, ASME Winter Annual Meeting, New York, 1976.

46 Smith, P. J., Fletcher, T. H., and Smoot, L. D., "Two-Dimensional Model for Pulverized Flow Combustion and Gasification," Paper WSS 80-7, Western States Section, Combustion Institute, Irvine, CA, 1980.

47 Abbas, A. S., Koussa, S. S., and Lockwood , F. C., "The Prediction of Particle-Laden Gas Flows," 18th (Int'l) Symposium on Combustion, Combustion Institute, 1981, pp. 1427-1438.

48 Dukowicz, J. K., "A Particle-Fluid Numerical Model for Liquid Sprays," *Journal of Computational Physics*, Vol. 35, 1980, pp. 229-253.

49 Eschbach, E. J., and Stock, D. E., "Optimization of Collection Efficiency by Varying Plate Spacing with an Electrostatic Precipitator," *Proceedings of the 2nd EPA Conference on Transfer and Utilization of Particulate Control Technology*, Denver, 1979.

50 Leonard, G., et al., "Particle Transport in Electrostatic Precipitators," *Atmosphere Environment*, Vol. 14, No. 11, 1980, pp. 1289-1299.

51 Reeks, M. W., "The Transport of Discrete Particles in Turbulent Shear Flow," Paper C71/82, Conference on Gas-Borne Particles, Inst. of Mech. Engr., Oxford, England, 1981, pp. 87-92.

52 Gosman, A. D., and Ioannides, E., "Aspects of Computer Simulation of Liquid-Fueled Combustors," AIAA paper 81-0323, 19th Aerospace Sciences Meeting, St. Louis, 1981.

Two-Way Coupling Effects in Dilute Gas-Particle Flows[1]

M. Di Giacinto
Assistant Professor,
Istituto di Propulsione Aerospaziale,
Università di Roma,
00184 Rome, Italy

F. Sabetta
Professor,
Istituto di Fisica Generale,
Università di Ancona,
60100 Ancona, Italy

R. Piva
Professor,
Istituto di Meccanica Applicata,
Università di Roma,
00184 Rome, Italy

A general analysis of gas-particle flows, under the hypotheses of number of particles large enough to consider the solid phase as a continuum and of volume fraction small enough to consider the suspension as dilute, is presented. The Stokes number Sk and the particle loading ratio β are shown to be the basic parameters governing the flow. Depending on the values of these two parameters, in one case the reciprocal interaction of the fluid and solid phases must be considered (two-way coupling), in the second case only the effect of the fluid field on the particle motion is relevant (one-way coupling). In the more general case of two-way coupling, the flow is governed by two sets of Navier-Stokes equations, one for each phase, which are coupled together through the particle volume fraction and the momentum interchange forces. The two systems of equations, expressed in the variables velocity, pressure, and particle volume fraction, are solved numerically by a finite difference scheme. The model has been applied to a duct with a sudden restriction, simulating a flow metering device. The coupling effect both on fluid and solid phase fields, the increase of pressure drop, and the energy dissipated in the fluid-solid interaction have been determined as functions of the governing parameters, Sk and β. The parametric study also indicates the ranges of β and Sk in which simplified formulations may be assumed.

1 Introduction

Gas-particle flows are intended to be a particular class of two-phase flows in which small particles are suspended in a gas. Momentum and energy interchange may occur between the two phases by viscous interaction and convective heat transfer if other sources of interchange, like mass transfer by evaporation and condensation or chemical reactions, are not considered. The amount of particles may be so small that the gas flow field is not affected by the presence of the particles, while the trajectories of the particles are determined by the motion of the supporting fluid. In this case we are concerned with a "one-way" – from fluid to particles – physical coupling between the two phases.

On the contrary, the amount of particles may be large enough to modify the gas flow field significantly or even to require the volume fraction occupied by the particles to be accounted for. We have now a "two-way" – from fluid to particles and viceversa – physical coupling between the two phases. In the latter case also, the mixture may maintain the characteristics of a dilute suspension, that is average distance between particles large compared with their linear dimensions.

Depending on the volume fraction of the mixture occupied by the particles, different kinds of gas-particle flows are encountered in engineering applications, going from atmospheric dust and particulate deposition concerning air pollution control of industrial emissions, to transport of pulverized material in pipelines or fluidized beds for improving combustion processes. Intermediate conditions between the two above extreme cases occur for gas-particle flows in machine ducts, such as turbomachines operating with dusty gases, combustion chambers with powdered fuel injection, rocket propulsion nozzles with metallic powder. In all these applications an accurate knowledge of the interaction between the two phases is essential in order to determine and control the phenomena of wall friction, erosion, pressure drop, and deposition, which are of basic importance for all the above applications.

Computational models are a very useful tool for a deeper understanding and a higher level design in this field, considering both the inability of the analytical methods to account for all the complicacies involved in the real problems, and the intrinsic difficulty of experimental investigations and measurement techniques. As above mentioned, many different conditions may occur and rather than trying to set up a numerical model valid in general [1, 2], we think it is better to single out the characteristic parameters which govern such phenomena, to analyze their influence in the various conditions of interest, and thereafter to select for each class of problems the more suitable physical and computational model. This approach allows us to have a better insight into the physical aspects, and to build less time consuming computational models, easier to handle for parametric investigations. Following this line, particular attention must be given to the definition of the validity range and the corresponding accuracy of the set of hypotheses the models are built on.

[1] This paper was prepared while the three authors were members of the Istituto di Aerodinamica, Universita di Roma, 00184 Rome, Italy.

Contributed by the Fluid Engineering Division of THE AMERICAN SOCIETY OF MECHANICAL ENGINEERS and presented at the Winter Annual Meeting, Phoenix, Ariz., November 14–19, 1982. Manuscript received by the Fluids Engineering Division, November 20, 1980. Paper No. 82-WA/FE-1.

A first way to face the problem is to assume dynamic and thermal equilibrium between the two phases in order to consider the suspensions as a single homogeneous fluid, with modified properties with respect to the ambient supporting fluid to account for the presence of the suspended particles [3, 4, 5]. In this approach the suspension is usually assumed to be dilute – that is composed of noninteracting particles – and the effective transport coefficients are calculated from the disturbance flow field generated by a single particle. First order effects of the interaction between two close particles may be considered to obtain more approximate corrective terms [4].

Coming back to the more physical assumption of two separate phases, many one-way coupling studies are available in literature, either based on a Lagrangian approach for the trajectories of the particles considered as solid bodies embedded in the fluid [6, 7], or based on the Eulerian approach considering the particles as a continuum [8, 9]. Particularly in previous papers we presented a model for translational quasi-equilibrium between the solid and fluid phases [10], and a model for strong nonequilibrium conditions, but restricted to small values of the loading ratio [11].

Two-way coupling models are less frequent in the literature, apart from the general models mentioned before [1, 2], which are though general, limited to the description of a numerical procedure. Quasi-one-dimensional models have been developed to predict performance losses in rocket nozzles with condensed combustion products or to evaluate the effects of the inclusion of metallic powder in solid rockets [12, 13] and more recently [14] for gas-particle flow metering through a Venturi tube. In the latter application, since the measuring technique is based on a precise evaluation of the throat pressure drop and hence of the interaction between the two phases, the quasi-one-dimensional model seems to be not sufficiently accurate to study a problem particularly sensible to two-dimensional effects. Some interesting analytical solutions of fully coupled fields in two dimensions have been obtained in the past for specific problems and for particular conditions [15, 16, 17]. Several two-dimensional computational models have been recently presented [18, 19]. In the first, [18], the particles are regarded as a source of mass, momentum and energy for the supporting fluid and their trajectories are determined by the Lagrangian approach. The different description, Eulerian for fluid and Lagrangian for particles, seems not quite suitable for a two-way coupling solution, and requires in any case a toilsome computation for the source terms. In the second, [19], both fields are described by an Eulerian approach, but several ad hoc simplifications of equations and boundary conditions for the specific investigated problem (flow between corotating disks) have been introduced.

The purpose of the present paper is the formulation of an Eulerian two-dimensional model for dilute suspensions, which accounts for two-way coupling between the solid and the fluid phases. The model is valid in a range of the characteristic parameters in which a large loading ratio and any relaxation of the particles may be considered while the volume fraction occupied by the particles can be neglected in the fluid equations. The latter hypothesis, reasonable for many problems of practical interest, allows us to use a simpler model, making a parametric study of pressure drop and particles relaxation feasible in fully two-dimensional configurations. The following sections describe the basic parameters which govern the physical phenomena, the system of conservation equations with particular attention to the interaction terms, the numerical procedure and finally a test application for the prediction of pressure and velocity fields in a drastic duct restriction.

2 Physical Model and Characteristic Parameters

Different physical models may be assumed as more appropriate in correspondence to different conditions and different values of the characteristic parameters which appear in the governing equations. First we consider these parameters in connection with the physical conditions of interest in the present study.

Let the solid particles be spherical with diameter D, constant material density ρ_p' and hence with identical volume V and mass m.

Let the number density of the particles N be sufficiently large to consider the solid phase as a continuum. That is, if we consider a volume of the order $0(\delta^3)$ with $D<<\delta<<L$, where L is the characteristic length scale of the flow field, average values of the particles properties evaluated on this volume must be continuous together with their derivatives.

The volume fraction occupied by the solid phase is

$$\alpha_p = V \cdot N = \frac{\rho_p}{\rho_p'} \tag{1}$$

where ρ_p' is the particle material density and ρ_p is the mass of the solid phase per unit volume of the suspension. The actual value of α_p depends on the problem, going from values less than 10^{-3} (e.g., for combustion processes or atmospheric dust) up to values of the order of 10^{-1} for pulverized material transport or fluidized beds. In the present study we assume values of α_p small enough (at most of the order of one percent) to verify the assumption of dilute suspension, but at the

Nomenclature

f = drag coefficient
$\mathbf{g}$ = gravity acceleration vector
m = particle mass
p = pressure
D = particle diameter
E_D = dissipated energy between inlet and outlet due to fluid-particle interaction
$\mathbf{F}_p$ = solid-fluid interaction force
Fr = Froude number $= (u^2/gL)^{1/2}$
I = enthalpy
L = flow field characteristic length
N = particle number density
$\mathbf{Q}$ = heat flux vector
Re = flow Reynolds number
Re_p = particle Reynolds number $= \rho_f D\,|\mathbf{V}_f - \mathbf{V}_p|/\mu_f$
Sk = Stokes number
U = flow characteristic velocity
V = particle volume
$\mathbf{V}$ = velocity vector
α = volume fraction
α_{p0} = reference value for particle volume fraction
β = loading ratio as defined by (4)
γ = solid to fluid material density ratio
λ = bulk viscosity
μ = viscosity coefficient
ρ = mass per unit volume of the suspension
ρ' = material density
τ_p = particle relaxation time
τ_f = flow field characteristic time
Φ = dissipation function
Δ_p = pressure drop between inlet and outlet
Δ_{p_T} = total pressure drop between inlet and outlet
Δ_{p_θ} = pressure drop between inlet and throat

Subscripts

f = fluid
i = inlet section
0 = unloaded fluid ($\beta = 0$)
p = particle

same time large enough to keep satisfied the condition required by the continuum approach. The following relation holds for the volume fractions of the two phases

$$\alpha_p + \alpha_f = 1 \tag{2}$$

The ratio between the material density of the solid and fluid phases

$$\gamma = \frac{\rho_p'}{\rho_f'} \tag{3}$$

is taken in the present study to be a constant and its value is assumed of the order of 10^3 (e.g., coal particles in air).

The loading ratio of the flow is defined as the ratio between the mass concentration of the solid and the fluid phase

$$\beta = \frac{\rho_p}{\rho_f} \tag{4}$$

The loading ratio may be expressed as a funciton of α_p and γ

$$\beta = \frac{\rho_p}{\rho_p'}\,\frac{\rho_p'}{\rho_f'}\,\frac{\rho_f'}{\rho_f} = \frac{\alpha_p}{1-\alpha_p}\,\gamma \tag{5}$$

Among the three quantities α_p, β, and γ, two are independent characteristic parameters of the gas-particle mixture together with the particle relaxation time τ_p which is given by [20]

$$\tau_p = \frac{\rho_p' D^2}{18\,\mu_f f} \tag{6}$$

where $f = (1 + 1/6\ \mathrm{Re}_p^{2/3})$ is the drag coefficient, a function of the particle Reynolds number. The suspension relaxation time τ_p must be evaluated in comparison with the characteristic time of the supporting flow field

$$\tau_f = \frac{L}{U}$$

In the flow equations the ratio of these characteristic times, that is the Stokes number

$$\mathrm{Sk} = \frac{\tau_p}{\tau_f} \tag{7}$$

will then appear.

In conclusion the parameters which characterize the suspension flow, beside the ones, such as Re and Pr, governing the supporting flow, are α_p, β, and Sk. The numerical values of these parameters are not arbitrary, being interrelated by the values of D and ρ_p'. They must be chosen in the numerical applications in such a way as to satisfy the conditions required by the continuum approach.

3 Conservation Equations

In the hypothesis, discussed in the previous section, that both fluid and solid phases are considered as a continuum, a set of mass and momentum conservation equations may be written for each phase. Assuming a constant value for the viscosity coefficients λ and μ and substituting $\alpha_p = 1 - \alpha_f$, the two sets of equations are written [11] as

$$\rho_f'\left\{\frac{\partial(1-\alpha_p)}{\partial t} + \nabla\cdot[(1-\alpha_p)\,\mathbf{V}_f]\right\} = 0 \tag{8a}$$

$$\rho_f'\left\{\frac{\partial(1-\alpha_p)\,\mathbf{V}_f}{\partial t} + \nabla\cdot[(1-\alpha_p)\,\mathbf{V}_f\mathbf{V}_f]\right\} = -\nabla p_f + \mu_f \nabla^2 \mathbf{V}_f + (\lambda_f + \mu_f)\,\nabla(\nabla\cdot\mathbf{V}_f) + \mathbf{g}\rho_f'(1-\alpha_p) - \mathbf{F}_p \tag{8b}$$

for the fluid phase, and

$$\rho_p'\left\{\frac{\partial \alpha_p}{\partial t} + \nabla\cdot(\alpha_p \mathbf{V}_p)\right\} = 0 \tag{9a}$$

$$\rho_p'\left\{\frac{\partial \alpha_p \mathbf{V}_p}{\partial t} + \nabla\cdot(\alpha_p \mathbf{V}_p \mathbf{V}_p)\right\} = -\nabla p_p + \mu_p \nabla^2 \mathbf{V}_p + (\lambda_p + \mu_p)\,\nabla(\nabla\cdot\mathbf{V}_p) + \mathbf{g}\rho_p'\,\alpha_p + \mathbf{F}_p \tag{9b}$$

for the solid phase.

The two sets of equations are coupled through the momentum interchange force $\mathbf{F}_p$ and the volume fraction α_p. The interaction force per unit volume $\mathbf{F}_p$, in the considered case of $\gamma >> 1$, is mainly due to the viscous drag, which in the hypothesis of dilute suspension is approximately given by the sum of the drag forces applied to each of the N particles [11]

$$\mathbf{F}_p = \frac{18\,\mu f}{D^2}\,\alpha_p\,(\mathbf{V}_f - \mathbf{V}_p) \tag{10}$$

The lift component of the interaction force, resulting from particle rotation, may, become relevant in shear flows and particularly near to solid walls, but is not considered in the present study. The other contributions to the interaction force given, for example, by buoyancy or by the effect of flow pattern deviation from the steady state, as discussed by Corrsin and Lumley [21] for turbulent flows, are proportional to the fluid density ρ_f' and therefore become important only if ρ_f' is comparable to ρ_p', which is not the present case.

Moreover, the viscous and pressure terms in the solid phase momentum equations may be neglected for dilute suspensions. In fact they would account for the effects of the field interaction between two or more particles (the effect of individual particles being given by the drag force $\mathbf{F}_p$) which are inversely proportional to the ratio between the particle distance and their diameter and therefore small for dilute suspensions. However the presence of particles increases the rate of dissipation, when nonequilibrium conditions between particles and fluid velocities occur. In fact, when the two components of the system have different velocity, the mechanical energy gained by one of the two phase, let say $\mathbf{F}_p\mathbf{V}_p$, does not equal the mechanical energy lost by the other phase, that is $\mathbf{F}_p\mathbf{V}_f$. The magnitude of this additional dissipation term may be evaluated by considering the energy equation of the total system, which is written in its general form [15, 22]

$$(1-\alpha_p)\left[\rho_f'\frac{DI_f}{Dt} - \frac{Dp_f}{Dt} - \nabla\cdot\mathbf{Q}_f - \Phi_f\right] + \alpha_p\left[\rho_p'\frac{DI_p}{Dt} - \frac{Dp_p}{Dt} - \nabla\cdot\mathbf{Q}_p - \Phi_p\right] = \mathbf{F}_p\cdot(\mathbf{V}_f - \mathbf{V}_p) \tag{11}$$

where I, $\mathbf{Q}$, and Φ are the enthalpy, the heat flux and the dissipation function, respectively. The last term in equation (11) leads to a rate of dissipation per unit volume due to the presence of the particles, also in absence of the particle viscous term Φ_p.

The volume fraction α_p, which also couples the two sets of equations, has been assumed to be, for the dilute suspension hypothesis, sufficiently small to neglect α_p in all the equation terms containing $(1-\alpha_p)$, that is

$$\alpha_p << 1 \tag{12}$$

With all the above assumptions the set of equations for the fluid phase, when written in nondimensional form taking as reference values U, L, τ_f, and α_{p0} for velocities, lengths, time, and particle volume fraction, respectively, becomes

$$\nabla\cdot\mathbf{V}_f = 0 \tag{13a}$$

$$\frac{\partial \mathbf{V}_f}{\partial t} + \nabla\cdot(\mathbf{V}_f\mathbf{V}_f) = -\nabla p + \frac{1}{\mathrm{Re}}\nabla^2\mathbf{V}_f + \frac{1}{\mathrm{Fr}^2} - \frac{\beta}{\mathrm{Sk}}\,\alpha_p\,(\mathbf{V}_f - \mathbf{V}_p) \tag{13b}$$

where the expression $\beta = \alpha_{p0}\,\gamma$ has been used as a consequence of the assumption (12). In the above equations we used the

same symbols used before for the dimensional quantities having the same physical meaning.

Analogously the set of conservation equations for the solid phase becomes in nondimensional form

$$\frac{\partial \alpha_p}{\partial t} + \nabla \cdot (\alpha_p \mathbf{V}_p) = 0 \tag{14a}$$

$$\frac{\partial \alpha_p \mathbf{V}_p}{\partial t} + \nabla \cdot (\alpha_p \mathbf{V}_p \mathbf{V}_p) = \frac{1}{\mathrm{Fr}^2} \alpha_p + \frac{\alpha_p}{\mathrm{Sk}} (\mathbf{V}_f - \mathbf{V}_p) \tag{14b}$$

It is worth noting that in the fluid momentum equation the interaction term is β times larger than in the particle momentum equation.

With the same assumptions and neglecting here the heat flux, the energy equation in nondimensional form is written as

$$\frac{D}{Dt}(I_f + \beta I_p) - \frac{Dp}{Dt} = \Phi + \frac{\beta}{\mathrm{Sk}} \alpha_p (\mathbf{V}_f - \mathbf{V}_p)^2 \tag{15}$$

The boundary conditions, associated with the system of equations (13) and (14), will be examined in the next section together with the numerical approximation.

As shown by equations (13), (14), and (15), the parameters β and Sk, introduced in the previous section, govern the flow of the particle suspension and depending on their values a different reciprocal influence between the two phases and a different level of coupling is experienced. The Stokes number is proportional to the translational nonequilibrium of the particles, that is a small value of Sk means a small difference between particle and fluid velocities but a large coupling effect, at least for the particle flow. For Sk going to zero the interaction force assumes a finite value, corresponding to its maximum, while the energy dissipation term goes to zero. For Sk going to infinity both the interaction force and the energy dissipation terms go to zero. The energy dissipation term, being always positive, must then have a maximum for intermediate values of Sk.

The loading ratio β multiplies the effects of the Stokes number on the momentum and energy equations, increasing the coupling of the fluid with the particle field. Let us examine in more detail the phenomena for two extreme values of β. For very small values of β the fluid phase is independent from the solid phase and only a one-way coupling occurs between the two equation systems. The value of the Stokes number indicates whether it is appropriate to consider the particles to be in equilibrium with the fluid flow. As was shown in a previous paper [11], for $\mathrm{Sk} < 10^{-2}$ the flow is only slightly out of equilibrium which allows us to assume that the particle velocity field is a superposition of the fluid flow field and of the particle settling velocity. For $\mathrm{Sk} > 10^{-2}$ the nonequilibrium effects become significant and imply large relaxation between the particles and the fluid.

For large values of the loading factor β a two-way coupling occurs between the two equation systems and they must be solved simultaneously. The effect of the particles on the fluid flow field cannot be neglected anymore, becoming more relevant at smaller Stokes number. In the present case, with γ of the order of 10^3, we focus our attention on cases with strong two-way coupling (that is large values of β) even maintaining small the values of α_{p0}, as required by the assumption (12).

4 Numerical Procedure

The two sets of equations (13) and (14) have been discretized by a finite difference scheme, and solved simultaneously by a time marching implicit technique. The dependent variables for the fluid system, namely the velocity components u, v, and the pressure p, have been placed, as in the MAC method, on a staggered grid with velocities at the cell midside and pressure at the center of the cell. The pressure is determined by an iterative over-relaxation routine which updates the pressure modifying at the same time the velocity components toward the satisfaction of the continuity equation [23]. The dependent variables for the particle system (velocity components u_p, v_p, and volume fraction α_p) have been placed in analogous way with u_p, v_p at the cell midside and α_p at the center of the cell. The new values of u_p, v_p, α_p, obtained by time integration, are used to update the momentum interaction force in the fluid equation.

At each time step the following sequence of operations determines all the dependent variables at the new time $n+1$:

1. All dependent variables are known from time step n;
2. New values of local Re_p are estimated;
3. Fluid velocity components u, v are computed from implicit time integration of momentum conservation equations;
4. Pressure p is determined by the over-relaxation iterative routine;
5. Particle velocity components and volume fraction are computed from mass and momentum conservation equations with the new values of u, v in the interaction force.

The computation proceeds up to the steady state, which is considered to be reached for a relative change of the field variables, from one time step to the other, less than a certain small value ϵ, assumed 10^{-4} in our computations.

The initial conditions are relevant for the computer time required to converge. In the parametric study, the final results of the closer case – with regard to the values of the parameters β and Sk – have been assumed as initial conditions.

The boundary conditions associated with the equation system (13) and (14) for a flowing stream in a general two-dimensional field have been assumed as follows:

– at the inflow boundary identical velocity profiles for both phases and a uniform value of α_p have been assigned

$$u = u_p = \bar{u}(y)$$
$$v = v_p = 0$$
$$\alpha_p = 1$$

– at the solid walls zero velocity for fluid, slip condition for particle velocity and zero flux for α_p have been assumed

$$u = v = 0$$
$$\mathbf{V}_{pn} = 0 \qquad \frac{\partial \mathbf{V}_{pt}}{\partial n} = 0$$
$$\frac{\partial \alpha_p}{\partial n} = 0$$

– at the outflow boundary first or second derivatives of the variables have been assumed to be zero, as the less constrictive approximation for the internal field

$$\frac{\partial u}{\partial x} = \frac{\partial v}{\partial x} = \frac{\partial u_p}{\partial x} = \frac{\partial v_p}{\partial x} = 0 \qquad \frac{\partial^2 \alpha_p}{\partial x^2} = 0$$

The effect on the flow field of the arbitrariness of the latter condition is further on reduced, without a prohibitive increase of the node number, by a numerical mapping which enlarges the grid toward the outflow region.

5 Application to a Duct Sudden Restriction

The physical and computational model described in the previous sections has been applied to a simple two-dimensional configuration, in order to evaluate quantitatively the effects of the loading ratio and of the Stokes number on the interaction phenomena between the two phases.

In the considered geometrical configuration (Fig. 1), which may schematically represent a flow metering system, the sudden throat restriction generates substantial accelerations

Table 1

Sk = 10^{-2}		$D = 27\ \mu m$				Re = 10^2
β	α_{p0}	N cm^{-3}	Δp	Δp_θ	Δp_T	E_D
0	0	0	.83	.78	.88	0
.1	10^{-4}	10^4	.85	.84	.91	.0012
1	10^{-3}	10^5	1.09	1.33	1.16	.012
2.5	$2.5 \cdot 10^{-3}$	$2.5 \cdot 10^5$	1.36	2.07	1.47	.025
5	$5 \cdot 10^{-3}$	$5 \cdot 10^5$	1.95	3.21	2.07	.054
10	10^{-2}	10^6	3.57	5.51	3.54	.11

and translational non-equilibrium between the two phases, giving more evidence to the coupling effects. In flow metering ducts, with a characteristic dimension of few centimeters, the flow is laminar with a Reynolds number of the order of 10^4, while the Froude number is of the order of 10. In the numerical simulation we may therefore neglect the gravity term, which is proportional to $1/Fr^2$. For the Reynolds number we consider a maximum value of 10^3. In fact larger Reynolds numbers would require an excessive computer effort both in time and storage, due to the finer mesh to be used for a sufficiently accurate solution. Moreover the extension of the recirculating regions behind the throat becomes larger as the Reynolds number increases and therefore more extended ducts must be considered in order to avoide an excessive influence of the outflow conditions on the flow field solution in the throat region. For instance, a distance between the throat and the outflow boundary of five duct diameters is required for the case of Re = 10^2, while the same distance must be increased up to 30 duct diameters for Re = 10^3.

For both the above reasons the parametric study, which requires the simulation of many different conditions, has been performed with a Reynolds number of 10^2 and only few cases at Re = 10^3 have been considered, to show the influence of an increase in the reference velocity.

In Fig. 1 the characteristic lengths and the computational grid are shown for the case of Re = 100.

Let us first analyze the effect of the loading ratio β for a value of Sk which has been chosen small (Sk = 10^{-2}) to emphasize the coupling effect on the fluid flow field. The values assumed for β in the computation are listed in Table 1 together with the values of α_{p0} and N.

For each value of β the following overall quantities have been computed:

- The pressure drop between the inlet and the throat section: Δp_θ;
- The pressure drop for the entire length of the duct: Δp;
- The drop of total pressure for the entire length of the duct: Δp_T;
- The energy dissipated due to the nonequilibrium between the two phases, for the entire length of the duct: E_D.

As the loading factor becomes larger, all pressure drops increase since the fluid bulk has to accelerate and drag a larger amount of particles which, for the given Stokes number, are in close translational equilibrium with the fluid. Besides the pressure drop magnitude, the pressure distribution is also affected by the value of β. As shown in Fig. 2, for larger values of β the minimum of the pressure diagram becomes deeper and moves downstream. In presence of the solid phase the fluid reaches the throat section with a smaller velocity since part of the energy has been spent to accelerate the particles, which on the other hand, due to their large inertia, retain a larger velocity (Fig. 3) after the throat. In a section downstream of the throat the velocity profile of both fluid and particle phases becomes sharper, as shown in Fig. 4. Side by side with such modification of the velocity profile for growing β, an enlargement of the recirculating regions behind

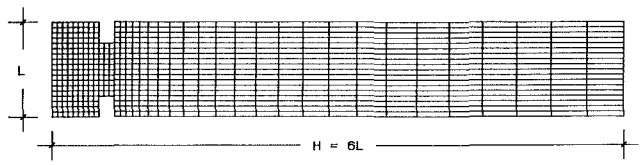

Fig. 1 Sketch of the duct and computational grid (Re = 10^2)

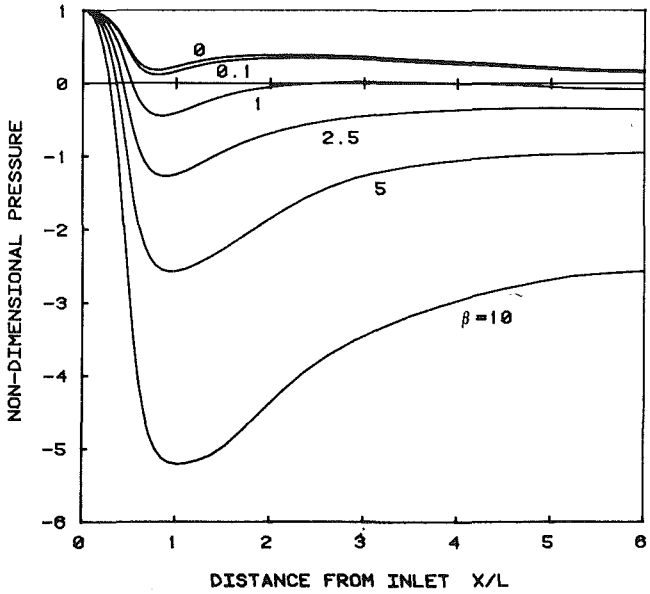

Fig. 2 Nondimensional pressure profiles along duct axis (Sk = 10^{-2})

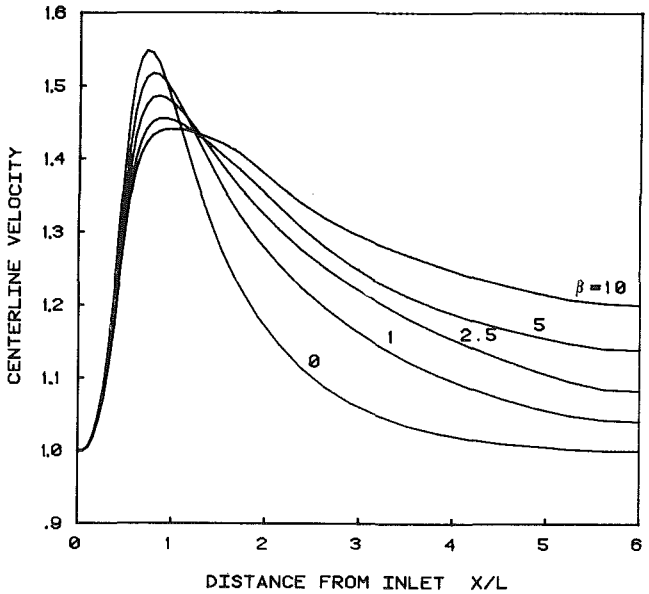

Fig. 3 Profiles of nondimensional axial velocity along duct axis (Sk = 10^{-2})

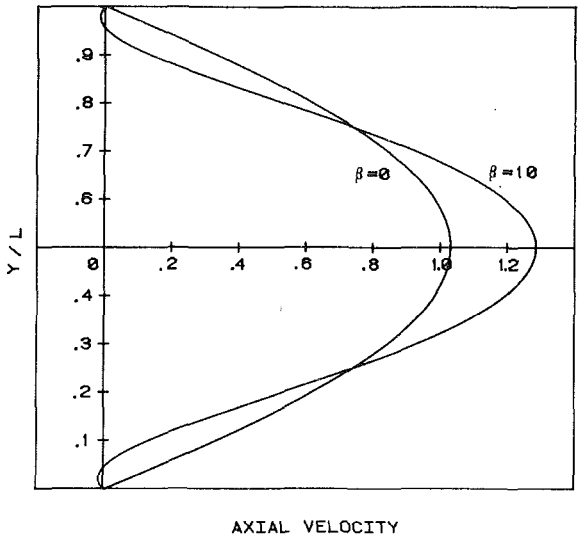

Fig. 4 Vertical profiles of axial velocity (Sk = 10^{-2}, x = 3.5)

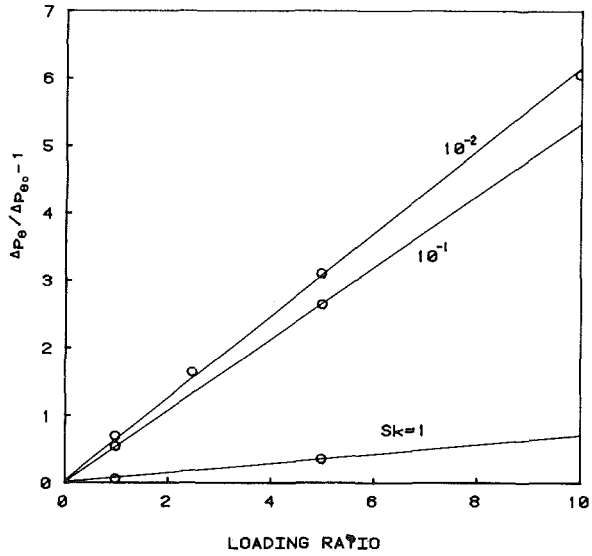

Fig. 5 Nondimensional increase of throat pressure drop versus loading ratio

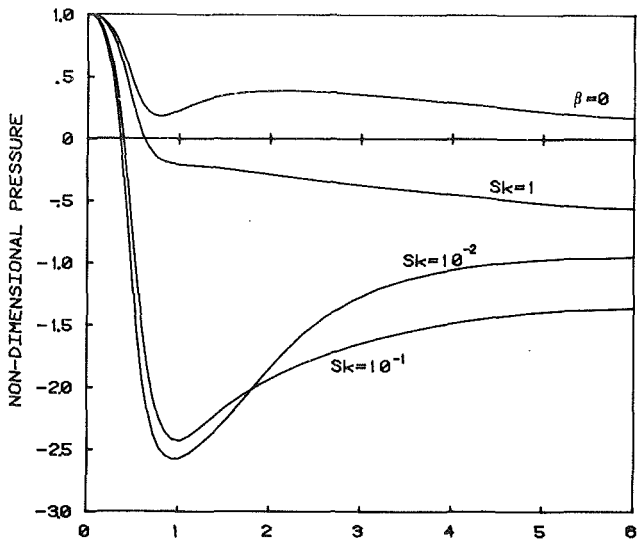

Fig. 6 Nondimensional pressure profiles along duct axis (β = 5)

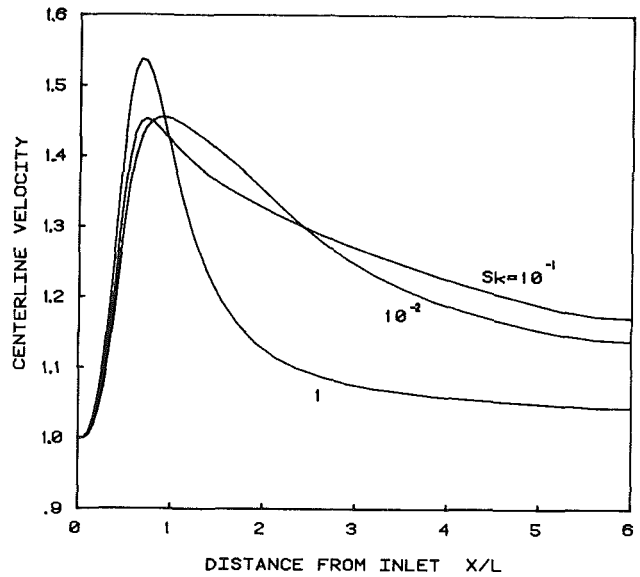

Fig. 7 Profiles of nondimensional fluid phase axial velocity along duct axis (β = 5)

the throat, analogous to the one experimented for growing Reynolds number, may be observed.

The rise of the pressure drop Δp_θ due to the particle loading, which is of particular importance for flow metering applications, is shown to be with good approximation linearly dependent on the loading ratio (Fig. 5) and the following correlation may be assumed

$$\frac{\Delta p_\theta}{\Delta p_{\theta_0}} = 1 + C\beta$$

where Δp_{θ_0} is the pressure drop for $\beta = 0$.

As shown in Fig. 5, the value of the coefficient C is strongly dependent on the considered value of the Stokes number. Therefore if a mixture of different size particles is considered, as in the experiments by Farbar [24], the value of C will assume an average value between those corresponding to the largest and smallest particles and its magnitude will be affected by the mass distribution in the various size classes. For this reason only a qualitative agreement can be observed with the results obtained by Crowe and Sharma [14] who considered the particle mixture used in Farbar's experiments.

The numerical values reported in Table 1 indicate that the increase with β of the energy dissipated in the interaction between the two phases (E_D) is lower than the corresponding increase of the total energy losses ($\Delta p_T - \Delta p_{T0}$). Such apparent discrepancy may be explained considering the larger viscous energy dissipation Φ occurring as a consequence of the above described larger velocity gradients induced by the coupling.

Let us analyze now the effect of the Stokes number. The nondimensional pressure along the duct for β = 5 and three different values of Sk (1, 10^{-1}, 10^{-2}) is plotted in Fig. 6 together with the case β = 0. While the pressure drop at the throat is continuously increasing for decreasing values of Sk, the pressure drop for the entire length of the duct reaches a maximum for a certain value of Sk, which in the case shown in Fig. 6 is close to Sk = 10^{-1}. This behaviour may be attributed to the viscous dissipation after the throat section, which increases for larger velocity gradients and hence for larger axial velocities. In fact, due to the different influence of the coupling, both for Sk = 1 and Sk = 10^{-2} the axial velocity in the outlet region results smaller than that for Sk = 10^{-1}, as it is shown in Fig. 7. In more detail, for large Sk the fluid is slightly affected by the particles, which due to their large inertia tend to keep the velocity reached at the throat

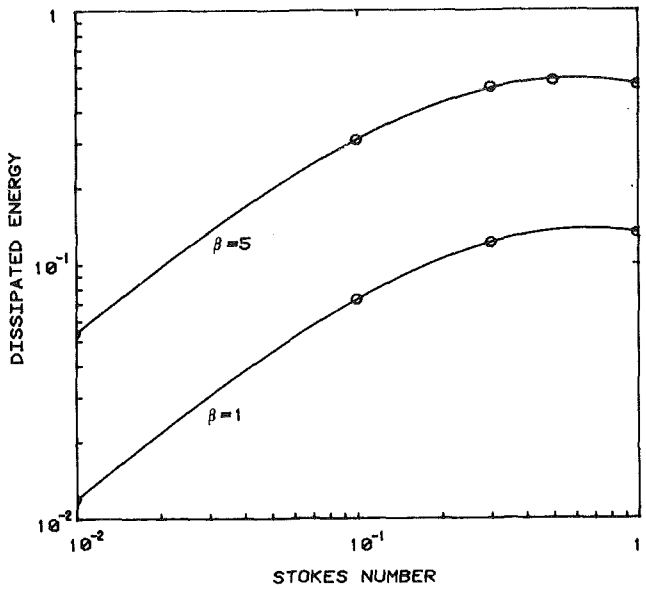

Fig. 8 Nondimensional dissipated energy versus Stokes number

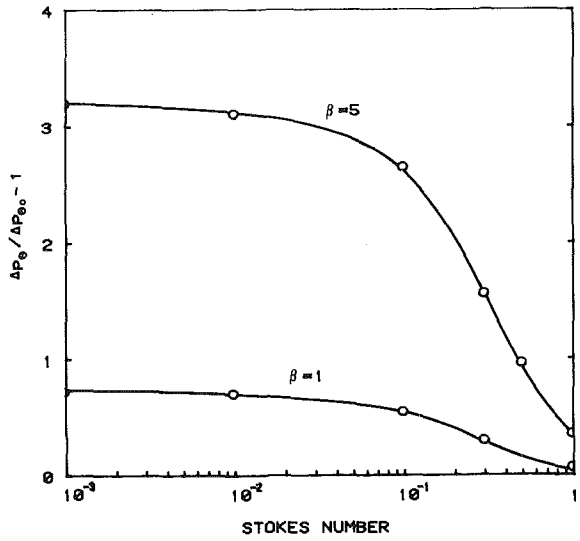

Fig. 9 Increase of throat pressure drop due to particle loading versus Stokes number

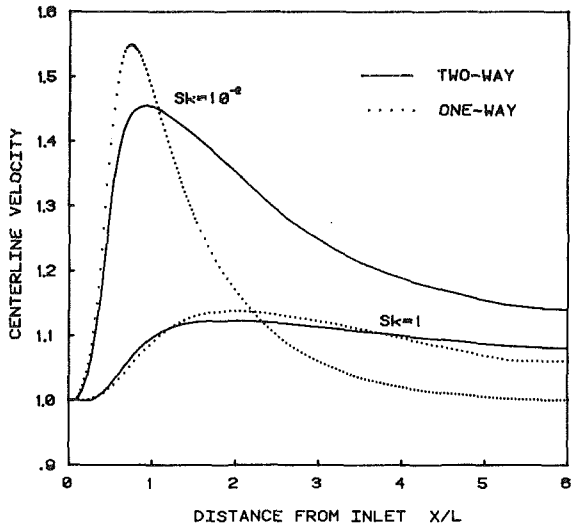

Fig. 10 Two-way coupling effect on axial velocity of the solid phase (β = 5)

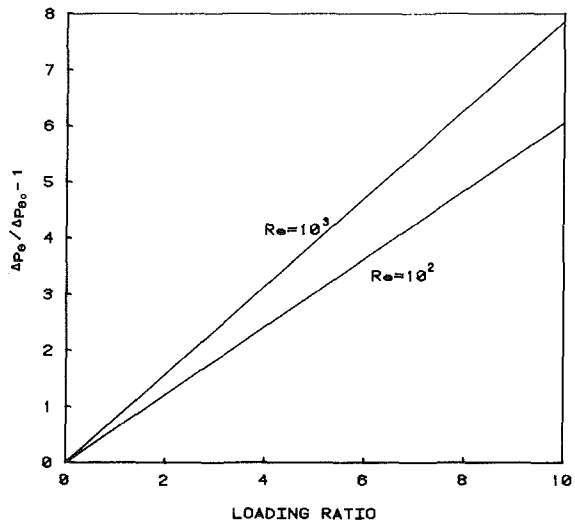

Fig. 11 Effect of Reynolds number on throat pressure drop (Sk = 10^{-2})

section. On the contrary for small Sk the fluid is strongly influenced by the particles which, however, due to the small inertia, present a rapidly decreasing velocity. This explains the presence of a maximum for the fluid velocity in the region after the throat for intermediate values of Sk.

Also the energy dissipated in the interaction between the two phases reaches a maximum for a certain value of Sk, as predicted in Section 3. Figure 8 shows that the maximum of E_D is shifted toward lower Sk values as the loading ratio increases.

The increase of the throat pressure drop due to particle loading, plotted as function of the Stokes number in Fig. 9, shows an asymptotic trend for Sk→0, with the asymptotic maximum value increasing together with β. It is worth noting that, for a constant loading, the influence of the particles on the flow field undergoes a drastic reduction as the Stokes number becomes larger than 10^{-1}.

For the analysis of the coupling effect on the solid phase field two extreme conditions may be considered. For Sk very small, the particle and fluid flow fields are practically coincident and significant differences in the computed values for the particle velocity are observed, whether or not two-way coupling is accounted for, as shown in Fig. 10 by dashed and solid lines for Sk = 10^{-2}. For large values of Sk, the particle velocity considerably deviates from the fluid one, but in this case the difference between one-way and two-way coupling tends to vanish.

The above parametric study has been performed, as previously discussed, for low Reynolds number (Re = 100) to understand and classify the physical phenomena without a prohibitive amount of computer time. A more realistic value of the Reynolds number (Re = 1000) is now considered to evaluate the influence of this last parameter. As indicated in Fig. 11, for Re = 1000 the relative increase of the throat pressure drop is larger for a given value of the loading factor. From these few results at Re = 1000, a larger influence of the coupling phenomena with increasing Reynolds numbers may be deduced.

6 Conclusions

The loading ratio and the Stokes number have been shown to be the basic parameters governing gas-solid flows. For small values of β and large values of Sk it is possible to neglect the effect of the particles on the fluid field and simpler numerical models based on a one-way coupling may be ap-

propriate. On the other hand for larger β (for instance $\beta >$ 0.1) and lower Sk (for instance Sk $< 10^{-1}$) both the fluid and the solid phase flow fields (and as a consequence overall quantities such as pressure drop and energy dissipation) are substantially affected by the interphase coupling. In this case computational models accounting for two-way coupling, such as the one presented here, are required for an accurate simulation.

Correlations have been developed in this paper for pressure drop which increases as a function of β and Sk. These correlations may be of practical interest for the investigation of flow metering systems, even if an extension of the model to multi-size mixtures would be required for a better comparison with experiments, and an accurate calibration of the model.

References

1 Harlow, F. H., and Amsden, A. A., "Numerical Calculation of Multiphase Fluid Flow," *J. Comp. Phys.*, Vol. 17, 1975, p. 440.

2 Gosman, A. D., Li, K. H., and Samaraweera, D. S. A., "A Numerical Calculation Procedure for Two-Phase Recirculating Flows," *Proc. 5th Intern. Conf. on Numerical Methods in Fluid Dynamics*, Springer Verlag, 1976, p. 212.

3 Cox, R. G., and Mason, S. G., "Suspended Particles in Fluid Flow Through Tubes," *Annual Rev. of Fluid Mech.*, Vol. 3, 1971, p. 291.

4 Batchelor, G. K., "Transport Properties of Two-Phase Materials with Random Structure," *Annual Rev. of Fluid Mech.*, Vol. 6, 1974, p. 227.

5 Herczynski, R., and Pienkowska, I., "On the Effective Transport Coefficients," IFTR Report, Polskiej Akademii Nauk, 1976.

6 Morsi, S. A., and Alexander, A. J., "An Invesigation of Particles Trajectories in Two-Phase Flow System," *J. Fluid Mech.*, Vol. 55, 1972, p. 193.

7 Hotchkiss, R. S., and Harlow, F. H., "Air Pollution Transport in Street Canyons," EPA-R4-73-029, 1973.

8 Eldighidy, S. M., Chen, R. Y., and Comparin, R. A., "Deposition of Suspensions in the Entrance of a Channel," ASME JOURNAL OF FLUIDS ENGINEERING, Vol. 99, 1977, p. 365.

9 Hamed, A., and Tabakoff, W., "Solid Particle Demixing in a Suspension Flow of Viscous Gas," ASME JOURNAL OF FLUIDS ENGINEERING, Vol. 97, 1975, p. 106.

10 Sabetta, F., Piva, R., and Di Giacinto M., "Navier Stokes Flows with Suspended Particles: Mathematical Modelling and Numerical Simulation," *Theor. and Appl. Mech.*, W. T. Koiter ed., North Holland Publ. Co., 1976, p. 425.

11 Piva, R., Sabetta, F., and Di Giacinto M., "Relaxation of Dilute Suspensions in Non-Uniform Flows" L'Aerotecnica Missili e Spazio, Vol. 57, No. 4, 1978, p. 207.

12 Hoglund, R. F., "Recent Advances in Gas-Particle Nozzle Flows," *ARS Journal*, Vol. 32, 1962, p. 662.

13 Hultberg, J. A., and Soo, S. L., "Two-Phase Flow Through a Nozzle," *Astronautica Acta*, Vol. 11, 1965, p. 207.

14 Sharma, M. P., and Crowe, C. T., "A Novel Physico-Computational Model for Quasi One-Dimensional Gas-Particle Flows," ASME *Journal of Fluids Engineering*, Vol. 100, 1978, p. 343.

15 Murray, J. D., "On the Mathematics of Fluidization Part I. Fundamental Equations and Wave Propagation," *J. Fluid Mech.*, Vol. 21, 1965, p. 465.

16 Marble, F. E., "Some Gasdynamics Problems in the Flow of Condensing Vapors," *Astronautica Acta*, Vol. 14, 1969, p. 585.

17 Soo, S. L., *Fluid Dynamics of Multiphase Systems*, Blaisdell Publ. Co., Waltham, Mass., 1967.

18 Crowe, C. T., Sharma, M. P., and Stock, D. E., "The Particle-Source-In Cell (PSI-CELL) Model for Gas-Droplet Flows," ASME JOURNAL OF FLUIDS ENGINEERING, Vol. 99, 1977, p. 325.

19 Truman, C. R., Rice, W., and Jankowski, D. F., "Laminar Through-flow of a Fluid Containing Particles Between Corotating Disks," ASME JOURNAL OF FLUIDS ENGINEERING, Vol. 101, 1979, p. 87,

20 Rudinger, G., "Flow of Solid Particles in Gases," AGARD-AG-222, 1976.

21 Corrsin, S., and Lumley, J., *Appl. Sc. Res.*, Vol. 6, 1956.

22 Gidaspow, D., "Fluid-Particle Systems," *Proc. of Two-Phase Flow Conf.*, Turkey, 1976.

23 Viecelli, J. A., "A Computing Method for Incompressible Flows Bounded by Moving Walls," *J. Comp. Physics*, Vol. 8, 1971, p. 119.

24 Farbar, L., "The Venturi as a Meter for Gas-Solids Mixtures," Trans. ASME, 1953, p. 943.

propriate. On the other hand for larger β (for instance $\beta > 0.1$) and lower Sk (for instance $Sk < 10^{-1}$) both the fluid and the solid phase flow fields (and as a consequence overall quantities such as pressure drop and energy dissipation) are substantially affected by the interphase coupling. In this case computational models accounting for two-way coupling, such as the one presented here, are required for an accurate simulation.

Correlations have been developed in this paper for pressure drop which increases as a function of β and Sk. These correlations may be of practical interest for the investigation of flow metering systems, even if an extension of the model to multi-size mixtures would be required for a better comparison with experiments, and an accurate calibration of the model.

References

1 Harlow, F. H., and Amsden, A. A., "Numerical Calculation of Multiphase Fluid Flow," *J. Comp. Phys.*, Vol. 17, 1975, p. 440.

2 Gosman, A. D., Li, K. H., and Samaraweera, D. S. A., "A Numerical Calculation Procedure for Two-Phase Recirculating Flows," *Proc. 5th Intern. Conf. on Numerical Methods in Fluid Dynamics*, Springer Verlag, 1976, p. 212.

3 Cox, R. G., and Mason, S. G., "Suspended Particles in Fluid Flow Through Tubes," *Annual Rev. of Fluid Mech.*, Vol. 3, 1971, p. 291.

4 Batchelor, G. K., "Transport Properties of Two-Phase Materials with Random Structure," *Annual Rev. of Fluid Mech.*, Vol. 6, 1974, p. 227.

5 Herczynski, R., and Pienkowska, I., "On the Effective Transport Coefficients," IFTR Report, Polskiej Akademii Nauk, 1976.

6 Morsi, S. A., and Alexander, A. J., "An Invesigation of Particles Trajectories in Two-Phase Flow System," *J. Fluid Mech.*, Vol. 55, 1972, p. 193.

7 Hotchkiss, R. S., and Harlow, F. H., "Air Pollution Transport in Street Canyons," EPA-R4-73-029, 1973.

8 Eldighidy, S. M., Chen, R. Y., and Comparin, R. A., "Deposition of Suspensions in the Entrance of a Channel," ASME JOURNAL OF FLUIDS ENGINEERING, Vol. 99, 1977, p. 365.

9 Hamed, A., and Tabakoff, W., "Solid Particle Demixing in a Suspension Flow of Viscous Gas," ASME JOURNAL OF FLUIDS ENGINEERING, Vol. 97, 1975, p. 106.

10 Sabetta, F., Piva, R., and Di Giacinto M., "Navier Stokes Flows with Suspended Particles: Mathematical Modelling and Numerical Simulation," *Theor. and Appl. Mech.*, W. T. Koiter ed., North Holland Publ. Co., 1976, p. 425.

11 Piva, R., Sabetta, F., and Di Giacinto M., "Relaxation of Dilute Suspensions in Non-Uniform Flows" L'Aerotecnica Missili e Spazio, Vol. 57, No. 4, 1978, p. 207.

12 Hoglund, R. F., "Recent Advances in Gas-Particle Nozzle Flows," *ARS Journal*, Vol. 32, 1962, p. 662.

13 Hultberg, J. A., and Soo, S. L., "Two-Phase Flow Through a Nozzle," *Astronautica Acta*, Vol. 11, 1965, p. 207.

14 Sharma, M. P., and Crowe, C. T., "A Novel Physico-Computational Model for Quasi One-Dimensional Gas-Particle Flows," ASME *Journal of Fluids Engineering*, Vol. 100, 1978, p. 343.

15 Murray, J. D., "On the Mathematics of Fluidization Part I. Fundamental Equations and Wave Propagation," *J. Fluid Mech.*, Vol. 21, 1965, p. 465.

16 Marble, F. E., "Some Gasdynamics Problems in the Flow of Condensing Vapors," *Astronautica Acta*, Vol. 14, 1969, p. 585.

17 Soo, S. L., *Fluid Dynamics of Multiphase Systems*, Blaisdell Publ. Co., Waltham, Mass., 1967.

18 Crowe, C. T., Sharma, M. P., and Stock, D. E., "The Particle-Source-In Cell (PSI-CELL) Model for Gas-Droplet Flows," ASME JOURNAL OF FLUIDS ENGINEERING, Vol. 99, 1977, p. 325.

19 Truman, C. R., Rice, W., and Jankowski, D. F., "Laminar Throughflow of a Fluid Containing Particles Between Corotating Disks," ASME JOURNAL OF FLUIDS ENGINEERING, Vol. 101, 1979, p. 87,

20 Rudinger, G., "Flow of Solid Particles in Gases," AGARD-AG-222, 1976.

21 Corrsin, S., and Lumley, J., *Appl. Sc. Res.*, Vol. 6, 1956.

22 Gidaspow, D., "Fluid-Particle Systems," *Proc. of Two-Phase Flow Conf.*, Turkey, 1976.

23 Viecelli, J. A., "A Computing Method for Incompressible Flows Bounded by Moving Walls," *J. Comp. Physics*, Vol. 8, 1971, p. 119.

24 Farbar, L., "The Venturi as a Meter for Gas-Solids Mixtures," Trans. ASME, 1953, p. 943.

DISCUSSION

C. C. Crowe[1]

The authors provide an interesting application of the two-fluid model to gas-particle flow in an orifice. The two fluid equations are simplified to model dilute flows thereby avoiding the troublesome particle shear stress terms which are common to the particle-phase equations. Also, the material density of gas phase (as well as the particulate phase) is assumed constant precluding the need for a gas-phase energy equation and equation of state. These assumptions are reasonable for the application addressed in this paper.

Another point of interest is the assumed boundary condition for the particulate phase at the wall, namely, that the normal component of velocity is zero and that the tangential velocity is unchanged. This corresponds to perfectly elastic collisions of the particles with the wall. The validity of the assumption is questionable, especially for non-spherical particles. It is not known how important this assumption is.

The authors state that the nominal Reynolds number for "flow metering ducts" is 10^4 and that this condition corresponds to laminar flow. With this argument, the authors assumed laminar flow throughout and performed calculations at Re = 10^2 and 10^3. Transition to turbulence in a duct nominally occur at 3000. However, the recirculative flow and adverse pressure gradient downstream of an orifice will likely induce turbulence at Reynolds numbers significantly lower than 3×10^3. A Reynolds number of 10^4 represents the lower limit of Reynolds numbers of interest in flow metering.

The various trends predicted by the model appear reasonable. The predicted trends for axial velocity distribution (Fig. 4) and centerline pressure distribution (Fig. 6) are similar to those obtained in reference 1. Unfortunately, insufficient information is given to compare the orifice flow coefficient at zero loading with the commonly accepted results. Data obtained[2] for gas-particle flow through an orifice at a nominal Reynolds number of 3000 indicate a pressure ratio of

$$\left(\frac{\Delta P_\theta}{\Delta P_{\theta 0}} - 1\right)/\beta \cong 0.4$$

Using the predictions from Figs. 9 and 11, one estimates the value to be 0.2. The agreement is not as good as that obtained by the trajectory model but this may be due to the laminar flow assumption used for the two fluid model.

At low Stokes numbers ($Sk = 10^{-2}$) the particles and gas achieve dynamic equilibrium and the two-phase mixture behaves like a gas with a density of $\rho_g(1+\beta)$. If the velocity field for the "heavy" gas is the same as that for the gas alone (a reasonable assumption here), then the pressure ratio $\Delta P_\theta / \Delta P_{\theta 0}$ should vary as $1+\beta$ or

$$\frac{\Delta P_\theta}{\Delta P_{\theta 0}} - 1 \simeq \beta$$

The line for $Sk = 10^{-2}$ in Fig. 5 falls well below this

[1] Department of Mechanical Engineering, Washington State University, Pullman, Wash. 99164

[2] Sharma, M. P., Crowe, C. T., and Stock, D. E., "A Numerical Model for Gas-Particle Flows through an Orifice," *Proceedings of the 17th National Heat Transfer Conference*, AIChE, HT&EC Division, Salt Lake City, 1977, pp. 111-117.

relationship. Also, the limits of the pressure ratio for decreasing Stokes number in Fig. 9 fall below this value as well. The reason for this discrepancy is unclear.

The paper provides no information on nominal run times. Also, comments on the feasibility of extending the model to multiple particle sizes and including gas-phase turbulence effects would have been instructive.

Authors' Closure

The authors thank Professor Crowe for his interest in the present paper and for his stimulating remarks. We agree with Professor Crowe's comments about the arbitrariness of the assumed boundary condition for the solid phase and about the fact that turbulence is already established in the range of Reynolds numbers of interest in the flow metering systems.

However this was taken just as a sample case to test the various modelling approximations for dilute suspensions, while the simulation of an actual flow metering device was not the main purpose of the paper. In fact even the assumption of uniform size particles is far from the actual conditions. The insertion of a turbulence model and the extension to multiple particle sizes may be considered as further steps to complete the model, whose main features remain nevertheless valid in this more general case.

Due to the different working conditions (Reynolds number, particle size and geometrical configuration), strict quantitative comparison with the results obtained by Sharma et al, are not really feasible. We should however notice that from our results (Figs. 5 and 11) the ratio

$$\left(\frac{\Delta_{p_\theta}}{\Delta_{p_{\theta 0}}} - 1\right)/\beta$$

has approximately the value 0.8 at low Stokes numbers, and decreases for larger particle sizes.

Finally Professor Crowe's statement that for low Stokes numbers the suspension should behave like a heavier gas is valid only when the suspension is not dilute and the particle size is tendentially of the same order of magnitude as the gas molecules. These conditions are out of the validity range of the model, which is based on the assumption that the solid particles are not interacting, and therefore they are studied as a continuum without pressure and viscosity. Moreover the assumption of the particle interaction with the supporting fluid given by the aerodynamic force is not valid, of course, in the case of particles having approximately the gas molecular size.

It is, thus, not surprising that, for $Sk \to 0$, the suspension doesn't behave exactly as a gas mixture and that the model gives a limiting value of the parameter $(\Delta p_\theta / \Delta p_{\theta 0} - 1)$ which is approximately 25 percent lower than the value predicted for the "heavy" gas suggested by Crowe.

J. M. Tishkoff

D. C. Hammond, Jr.

Staff Research Engineers,
Fluid Dynamics Department.

A. R. Chraplyvy[1]
Associate Senior Research Scientist,
Physics Department.

General Motors Research Laboratories,
Warren, Mich. 48090-9055

Diagnostic Measurements of Fuel Spray Dispersion

Plume shape, vaporization, droplet-size distribution, and number density of a solid-cone fuel spray were studied with both conventional and novel measurement techniques. Minor differences in spray plume shape were observed by measurements with photography, pulsed laser shadowgraphy, and in-line infrared spectroscopy. Laser Mie scattering showed the dispersion of small numbers of droplets beyond spray boundaries as determined by other measurements. A new optical method for nonintrusive, local, time-averaged measurement of vapor concentration, droplet-size distribution and number density within an axisymmetric spray is introduced. For the spray studied this method showed that vapor is confined to the spray plume and that vapor concentration and the concentration of small-diameter droplets exhibit analogous behavior.

Introduction

Recent entries to the literature have stressed the interaction between the liquid and gas phases in controlling fuel spray vaporization [1–5] and combustion [5–13]. These articles have been primarily theoretical with a limited number of experimental efforts [6–7, 12–13] oriented exclusively toward combustion.

This paper will describe measurement techniques and results for an experiment on spray vaporization. The experiment has been undertaken to study the physics of air-fuel spray interactions, develop instrumentation for spray measurements and provide experimental support for the formulation of fuel spray models.

Description of the Experiment

Airflow. The flow facility in which measurements were made is pictured in Fig. 1. In this facility a vacuum system draws air at room temperature and pressure downward through a bellmouth inlet and honeycomb straightener into a transparent plastic test section. The test section is square, 0.3 m on a side, and 1.8 m long. The airflow rate was constant at 0.224 kg/s. Hot wire anemometer measurements without a nozzle, spray, or other obstruction in the test section showed that the velocity was close to uniform at any horizontal plane, with an associated turbulence intensity of approximately 0.01.

Sprays. n-Heptane sprays were injected co-axially downward in the airflow from a Delavan Type B-4.00 GPH-80 deg. nozzle. Sprays injected from this nozzle have an axially symmetric solid cone geometry which is representative of conical sprays found in many industrial and transportation combustion systems. The nozzle was covered by a teardrop fairing mounted at the end of a horizontal airfoil tube (as shown in Fig. 2) extending into the test section through a slot in the sidewall. This tube was mounted on a traverse which could be adjusted vertically and in one horizontal dimension. The horizontal spread of disturbances to the airflow mean velocity caused by the nozzle holder was narrower than those of the spray plumes. Associated turbulence intensities were less than those observed through limited measurements near the edges of sprays, so the nozzle holder should not affect

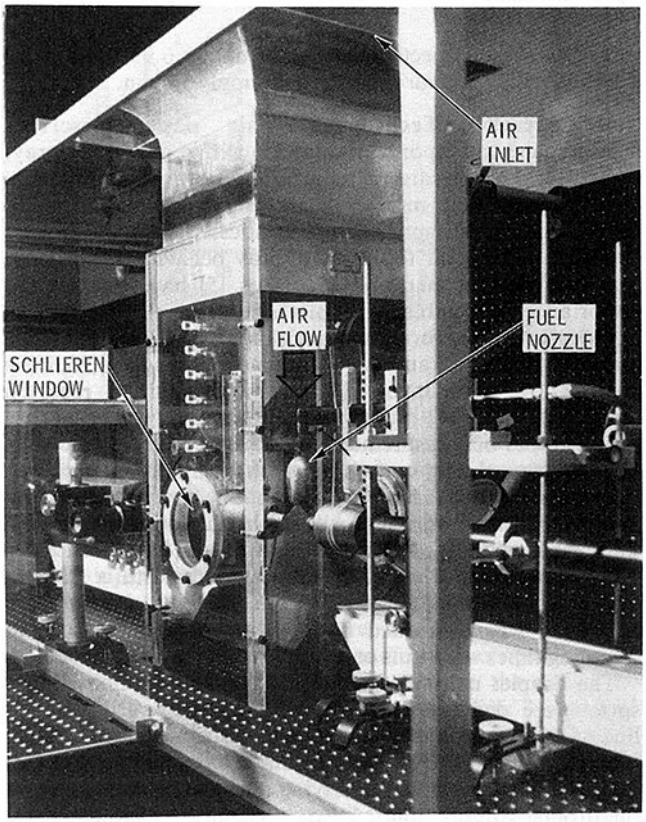

Fig. 1 Atmospheric pressure spray test facility

[1] Current address: Bell Laboratories, Holmdel, N.J. 07733.

Contributed by the Fluids Engineering Division for publication in the JOURNAL OF FLUIDS ENGINEERING. Manuscript received by the Fluids Engineering Division, July 23, 1980.

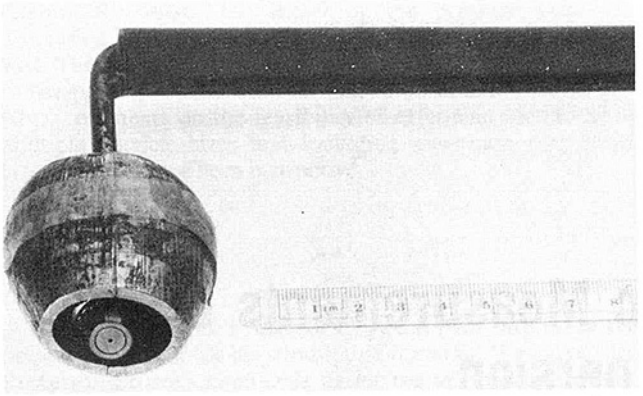

Fig. 2 Teardrop nozzle holder fairing

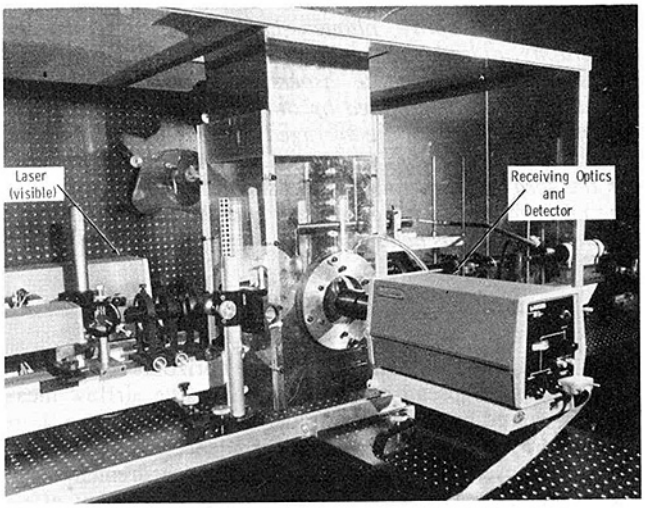

Fig. 3 Installation of 633 nm optical scattering instrument for particle size measurements

spray behavior. Injection pressures up to 6.99 MPa were achieved with a pressurized nitrogen supply system.

Measurement Techniques. This paper describes measurements of vapor concentration within a volatile spray, spray plume shape, droplet number density, and droplet-size distribution. These measurements as a group yield useful information about spray characteristics, but should not be considered sufficient to describe spray behavior completely. For example, Gosman and Ioannides [5] have stressed the importance of combined droplet size and velocity data as input information for spray modeling. This measurement is an objective of the authors' experimental program, but the amount of work involved dictates that it be reported separately.

Four types of measurements were made to locate the edge of the spray plume: conventional photography, laser beam scattering, in-line infrared absorption spectroscopy and pulsed laser shadowgraphy. All but the shadowgraphs, which were made with 10 ns duration laser pulses, produced time-averaged results. Photographs were made with a 35 mm camera using Kodak Plus-X-Pan Film. The duration of film exposures was controlled by the camera shutter, so that sampling times were 1 ms or longer.

The droplet number density and size distributions in the spray were deduced from the measured forward-scattered line-of-sight average light energy distributions. A commercially available Malvern ST-1800 spray analyzer (see [14] for a description of the underlying theory) was used to make the droplet-size distribution measurements; its installation is shown in Fig. 3. A 0.8 mm beam diameter, 633 nm

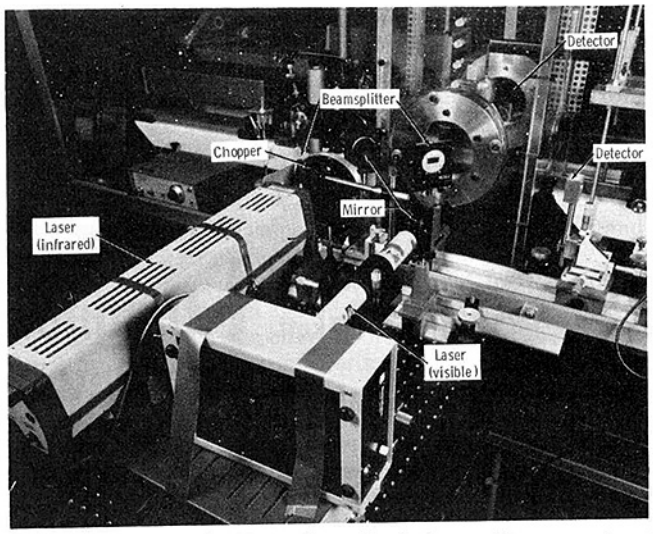

Fig. 4 Installation of 3.39 μm absorption instrument for vapor-phase measurements

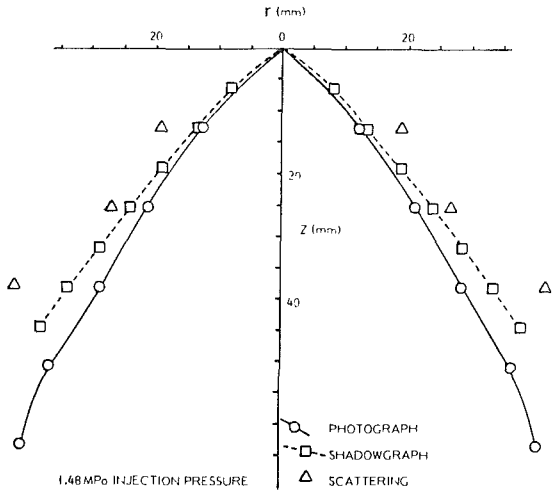

Fig. 5 Spray boundaries at 1.48 MPa injection pressure

wavelength helium-neon laser was used, and, as a result, the measurements were not affected by the presence of vapor since n-heptane exhibits negligible absorption at that wavelength. With the assumption of axial symmetry for the spray, a deconvolution technique developed by Hammond [15] was used to transform these line-of-sight average measurements into the actual radial variations of droplet number density and size distribution. Statistical examination of replicate measurements yielded uncertainty intervals for the data (at 95 percent confidence level) of ± 2.5 percentage points for extinction and ± 20 percent in any category of the 15-category histogram representation of the droplet-size distribution.

Figure 4 shows infrared absorption instrumentation. In this figure two collimated laser beams (0.8 mm in diameter), one at a wavelength of 633 nm (visible) and the other at 3.39 μm (infrared) are projected along the same optical path through the middle of the flow facility. Two detectors, not shown in Fig. 4, sample the beam strength on opposite sides of the flow duct to separate laser intensity variations from attenuation due to the spray. The visible laser beam is attenuated only by the droplets while the infrared beam is attenuated both by the droplets and the hydrocarbon vapor. The attenuation of the infrared beam by the droplets can be calculated from Mie theory using the measured attenuation of the visible beam and the associated droplet-size distribution. Subtraction of the attenuation due to droplets from the total attenuation of the

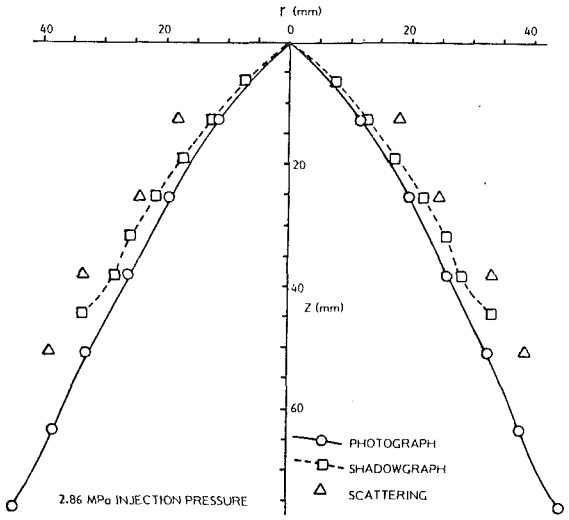

Fig. 6 Spray boundaries at 2.86 MPa injection pressure

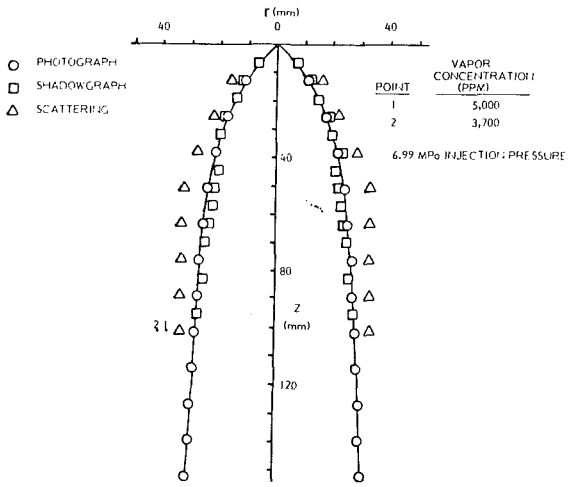

Fig. 7 Spray boundaries at 6.99 MPa injection pressure

infrared beam permits calculation of the vapor concentration. The Gaussian transverse intensity variation present in the 3.39 μm beam produces, at most, a 0.2 percent error in the measured attenuation. These line-of-sight average vapor concentration measurements can then be deconvoluted into the actual radial variation of vapor concentration in a particular axial plane. The vapor measurement technique is described more completely in [16].

Composite Measurements of Spray Plume Shape

Figures 5–7 show outlines of heptane spray plumes at three injection pressures. The plume shape of each spray is given as a vertical coordinate, z, plotted against a horizontal radial coordinate, r. The same scales are used on both axes to preserve the geometrical appearance of the plumes, and the origin of the axes represents the nozzle tip. The shadowgraph results, represented by the square data points, and the photographic results, given by circular points, are the averages of five trials. An upper limit for the average deviations of the radii for both types of measurements increases with increasing distance below the nozzle tip up to a maximum of ± 3 mm. For each type of measurement the edge of the spray plume is defined as the maximum radius at which either droplets or vapor can be detected.

In Figs. 5 and 6, representing heptane absolute injection pressures of 1.48 and 2.86 MPa, respectively, conventional photography defined the narrowest plume diameter, followed by shadowgraphy and laser scattering. The difference between

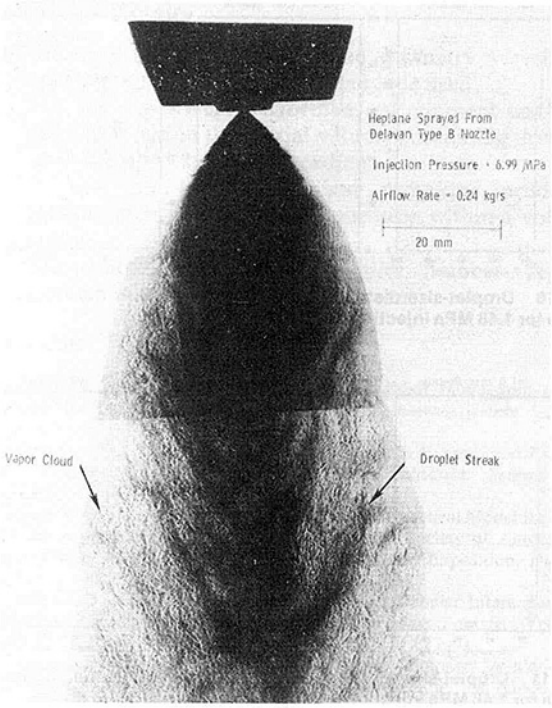

Fig. 8 Shadowgraphs at 6.99 MPa injection pressure

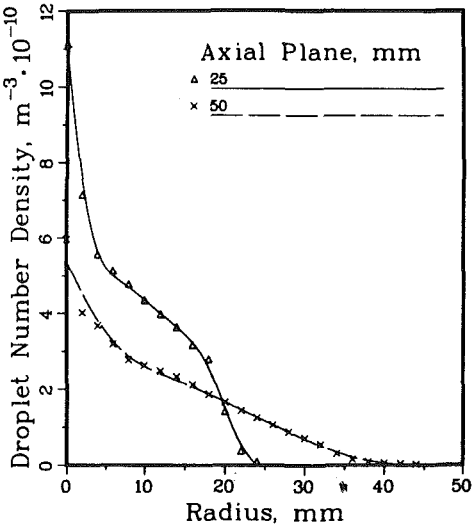

Fig. 9 Radial variations of droplet number density at 1.48 MPa injection pressure

the photographs and shadowgraphs results from the higher sensitivity of the shadowgraphs to combinations of low number densities of droplets and vapor concentrations. Scattering by small numbers of droplets, undetectable with the other measurement techniques, determines the largest plume diameter. Figure 7 shows the spray outline at 6.99 MPa absolute injection pressure. In this figure the photograph and shadowgraph data show only small differences. At each height, z, the scattering measurements indicated larger r values than do the corresponding photograph and shadowgraph data, which is consistent with the results of Figs. 5–6. The two numbered data points in Fig. 7 represent infrared measurements of vapor concentration in the absence of droplets. For the injection pressures of Figs. 5–6 no region of vapor without droplets could be found, and in Fig. 7 vapor dispersion is confined to a narrow spatial volume at the edge of the spray plume.

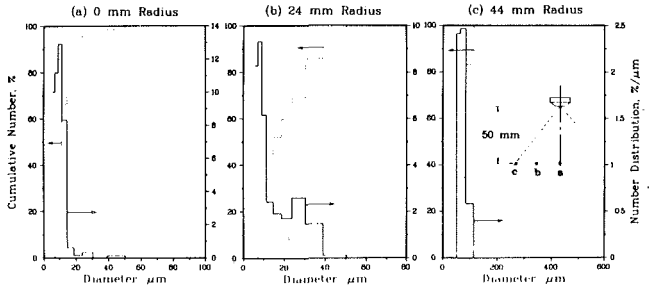

Fig. 10 Droplet-size distributions at various radii in the 25 mm axial plane for 1.48 MPa injection pressure

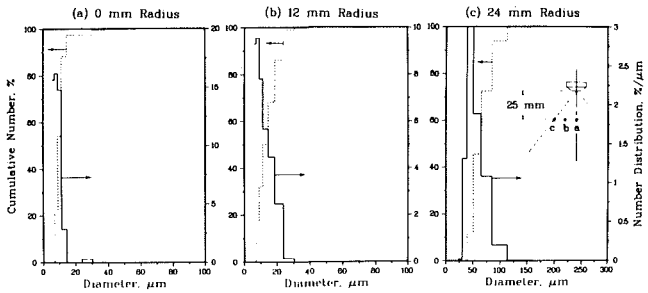

Fig. 11 Droplet-size distributions at various radii in the 50 mm axial plane for 1.48 MPa injection pressure

Figure 8 clarifies the nature of vaporization in the spray. The figure combines two pulsed laser shadowgraphs to show an "instantaneous" view of heptane spray at 6.99 MPa absolute injection pressure. Thin dark streaks, representing droplets, are interspersed with translucent clouds of vapor. In a time-averaged representation the vapor clouds and droplet streaks would be blurred together, so only a measurement of very short time duration will give an accurate representation of the vaporization process.

Measurements Within the Spray Plume

Figures 5–7 show that vapor is bounded by the spray plume, so that measurements of vapor concentration must be made in the presence of large numbers of droplets in order to study the vaporization process. The optical technique for measuring time-averaged local vapor concentration based on scattering of infrared and visible laser beams introduced in an earlier section of this paper not only accounts for droplets, but also provides time-averaged number density and size distribution data as additional information. The technique also is non-intrusive. Measurements are time-averaged, rather than instantaneous, but they provide information which was unattainable previously and is suitable for comparison with the predictions of current spray models [3, 5, 9, 10].

Droplet Number Density and Size Distribution. Measurements of the liquid-phase behavior were made in axial planes 25 and 50 mm below the atomizer tip at a single injection pressure of 1.48 MPa. The line-of-sight averaged extinction and droplet-size distributions were deconvoluted into the actual radial variations of droplet number density and droplet-size distribution in those planes under the assumption of axial symmetry. This assumption was checked by comparing data taken at identical radii on opposite sides of the centerline. The radial variations of the two sets of data were identical, and the numerical values (extinction and line-of-sight average distribution) were essentially the same if the "center" of the spray was shifted 5 percent of its diameter from the geometric nozzle centerline. The uncertainty intervals for these results were estimated as ±25 percent for

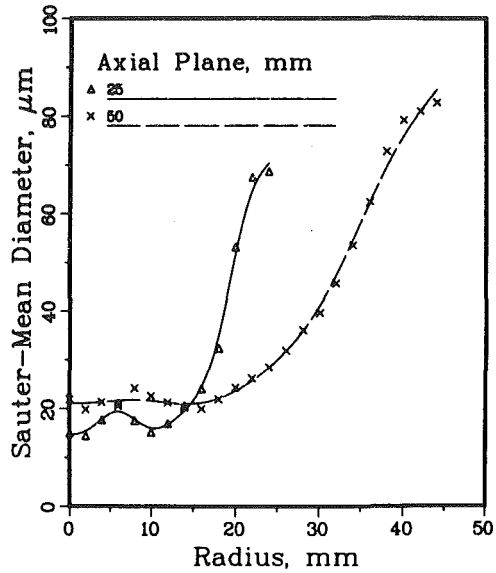

Fig. 12 Radial variations of Sauter-mean diameter at 1.48 MPa injection pressure

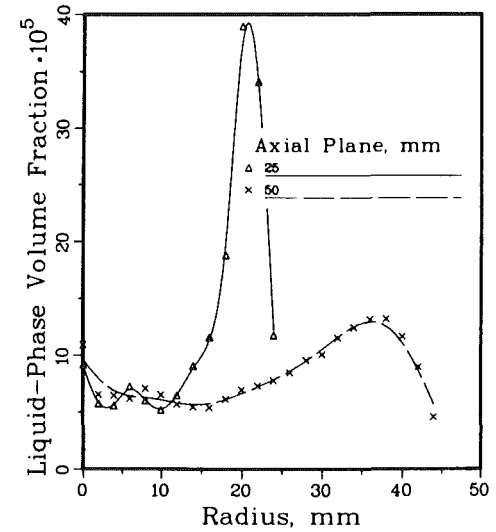

Fig. 13 Radial variations of liquid-phase volume fraction at 1.48 MPa injection pressure

number density and ±20 percent for size distribution (at the 95 percent confidence level).

The radial variations of droplet number density are shown in Fig. 9. Both axial planes exhibited rapid decreases in number density with increasing radius. Droplet-size distributions at three selected radii in the 25 mm plane are shown in Fig. 10 and similar results for the 50 mm plane in Fig. 11. The radial variations of Sauter-mean diameter calculated from the droplet size distribution at each radius are shown in Fig. 12. These results reveal the nature of the spray, i.e., the interior of the spray contains relatively large numbers of small droplets (diameters from 10 to 25 μm) while the outer edge contains considerably fewer but larger droplets (diameters from 60 to 85 μm). Combining these results into the liquid-phase volume fraction presented in Fig. 13 clearly shows the bulk of the liquid is confined to the outer region. Mixing is evidenced by the increase of the width and decrease in magnitude of the high volume fraction region in moving from the 25 to the 50 mm axial plane.

Vapor Concentration. Measurements of vapor concentrations were made in the 25 and 50 mm axial planes at a

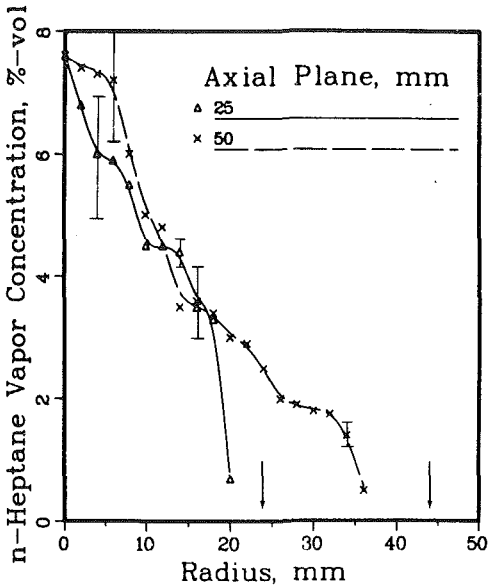

Fig. 14 Radial variations of vapor concentration for 1.48 MPa injection pressure

single injection pressure of 1.48 MPa. Line-of-sight average droplet-size distribution measurements combined with infrared attenuation measurements permitted calculation of the actual radial variations of n-heptane vapor concentrations in the two planes under the assumption of axial symmetry.

The radial variations of fuel vapor concentration are shown in Fig. 14. Arrows denote the edges of the spray. The vapor concentrations increase monotonically toward the center of the spray. At both heights the vapor pressure on the axis of the spray is slightly less than the saturation vapor pressure at 300 K.

A striking analogy appears in a comparison between the radial variations of droplet number density in Fig. 9 and vapor concentration in Fig. 14; both of these quantities decrease almost linearly with distance from the axis of symmetry of the spray. Because droplet sizes inside the spray are small, with Sauter-mean diameters of 20 μm (except close to the edge of the plume), negligible relative velocity with respect to local gaseous flow should be expected, and the droplets behave like molecules of a gaseous species to be mixed with the surrounding gaseous flow. Thus, in the interior region of the spray droplet concentrations are affected by the same fluid transport processes which control the dispersion of vapor, providing a rationale for the similar appearance of Figs. 9 and 14. At the periphery of the spray entrained air convects both vapor and smaller droplets inward without similarly affecting the relatively large droplets. Thus, no vapor appears exterior to the droplet region.

Summary of Results

1. Measurements of spray plume geometry varied according to the measurement technique used.
2. For the experiment performed, entrainment confined the vapor within the spatial volume containing droplets until the spray stopped spreading.
3. A new non-intrusive optical technique produced measurements of vapor concentration within a volatile spray.
4. The radial variation of droplet number density mirrored that of vapor concentration.

References

1 Labowsky, M., "The Effects of Nearest Neighbor Interactions on the Evaporation Rate of Cloud Particles," *Chemical Engineering Science*, Vol. 31, 1976, pp. 803-818.

2 Labowsky, M., "A Formalism for Calculating the Evaporation Rates of Rapidly Evaporating Interacting Particles," *Combustion Science and Technology*, Vol. 18, 1978, pp. 148-151.

3 Haselman, L. C., and Westbrook, C. K., "A Theoretical Model for Two-Phase Fuel Injection in Stratified Charge Engines," Society of Automotive Engineers Paper 780318 presented at the Congress and Exposition, Detroit, Mich., Feb. 27-Mar. 3, 1978.

4 Tishkoff, J. M., "A Model for the Effect of Droplet Interactions on Vaporization," *International Journal of Heat and Mass Transfer*, Vol. 22, 1979, pp. 1407-1415.

5 Gosman, A. D., and Ioannides, E., "Aspects of Computer Simulation of Liquid-Fuelled Combustors," Paper 81-0323 presented at the AIAA 19th Aerospace Sciences Meeting, St. Louis, Mo., Jan. 12-15, 1981.

6 Chigier, N. A., and McCreath, C., "Combustion of Droplets in Sprays," *Acta Astronautica*, Vol. 1, 1974, pp. 687-710.

7 Chigier, N. A., "The Atomization and Burning of Liquid Fuel Sprays," Progress in Energy and Combustion Science, Vol. 2, 1976, pp. 1-18.

8 Labowsky, M., and Rosner, D., "Conditions for 'Group' Combustion of Droplets in Fuel Clouds: I. Quasi-Steady Predictions," Paper presented at the ACS-Div. Petroleum Chemistry Symposium, San Francisco, California, August 29-Sept. 3, 1976.

9 Chiu, H. H., and Liu, T. M., "Group Combustion of Liquid Droplets," *Combustion Science and Technology*, Vol. 17, 1977, pp. 127-142.

10 Chiu, H. H., Ahluwalia, R. K., Koh, B., and Croke, E. J., "Spray Group Combustion," Paper 78-75 for presentation at the AIAA 16th Aerospace Sciences Meeting, Huntsville, Alabama, Jan. 16-18, 1978.

11 Labowsky, M., "Calculations of the Burning Rates of Interacting Fuel Particles," Paper presented at the Combustion Institute Central States Section Meeting, West Lafayette, Ind., Apr. 3-5, 1978.

12 Brzustowski, T. A., Twardus, E. M., Wojcicki, W., and Sobiesiak, A., "Interaction of Two Burning Fuel Droplets of Arbitrary Size," *AIAA Journal*, Vol. 17, No. 11, Nov. 1979, pp. 1234-1242.

13 Sangiovanni, J. J., and Dodge, L. G., "Observations of Flame Structure in the Combustion of Monodispersed Droplet Streams," *Seventeenth Symposium (International) on Combustion*, The Combustion Institute: Pittsburgh, 1979, pp. 455-465.

14 Swithenbank, J., Beer, J. M., Taylor, D. S., Abbot, D., and McCreath, G. C., "A Laser Diagnostic Technique for the Measurement of Droplet and Particle Size Distribution," *Progress in Astronautics and Aeronautics*, Vol. 53, Experimental Diagnostics in Gas Phase Combustion Systems, Edited by B. T. Zinn, New York: American Institute of Aeronautics and Astronautics, 1977.

15 Hammond, D. C., Jr., "Deconvolution Technique for Line-of-Sight Optical Scattering Measurements in Axisymmetric Sprays," *Applied Optics*, Vol. 20, No. 3, Feb. 1981, pp. 493-499.

16 Chraplyvy, A. R., "Nonintrusive Measurements of Vapor Concentrations Inside Sprays," *Applied Optics*, Vol. 20, No. 15, August 1981, pp. 2620-2624.

F. J. Hatfield
Associate Professor.

D. C. Wiggert
Professor.

R. S. Otwell
Graduate Research Assistant.

Department of Civil Engineering,
Michigan State University,
East Lansing, Mich. 48824

Fluid Structure Interaction in Piping by Component Synthesis

Pipe vibrations can be induced by internal liquid pulsations which propagate throughout the piping system and create unbalanced oscillatory pressure forces at locations where either flow area or direction changes. The fluid motion is set up by a source of mechanical excitation or flow instability. Dynamic interaction of the liquid and piping may be modelled by separate analyses of liquid and solid components followed by synthesis of the component solutions. In contrast to other formulations that correctly represent interaction, the technique presented herein has the computational advantage of decomposing the anaysis into steps. The most time-consuming step is structural analysis, which may be delegated to existing, efficient computer algorithms. The synthesis method is outlined, the advantages discussed and application illustrated with numerical examples.

Introduction

Pipe vibrations caused by internal liquid pulsation may exhibit displacements of relatively large amplitude and the system may subsequently fail through fatigue of piping or supports. As an example, modern petrochemical processes, such as certain steps in the production of synthetic fuels, require higher temperatures and pressures than were commonly encountered in the past. Higher pressures necessitate the use of reciprocating pumps, which produce large amplitude, low-frequency flow pulsation. Higher temperatures necessitate minimal structural restraint of the piping in order to avoid excessive thermal stress. Because of the resulting low stiffness, the piping exhibits structural resonance at relatively low frequencies. If one of the first few harmonics of pump pulsation coincides with a resonant frequency of the piping, severe vibration results, which can damage supports and secondary piping.

In engineering practice the phenomenon typically is analyzed by using a transfer function procedure or electrical analog to predict oscillatory pressures in the liquid, followed by a finite element solution to estimate response of the pipe structure to those pressures. The fluid analysis includes reduction in sonic velocity due to compliance of pipe walls, but assumes that pipes do not bend, twist or elongate. The only liquid property considered in the structural analysis is mass. Resonant frequencies of the fluid-structure system are assumed to be the union of resonant frequencies of the liquid and structure as determined by the separate analyses.

Previous investigators have noted that resonant frequencies of liquid-filled piping generally are not the same as would be predicted by fluid and structural analyses conducted indepedently. There is the danger that analysis as currently performed will fail to predict resonance of compliant piping at a particular frequency. If that frequency coincides with a low-order harmonic of the exciter to which the piping is connected, destructive vibrations will result when the system is operated. Various formulations have been proposed that correctly couple the liquid to the pipe structure and therefore predict resonant frequencies accurately. The present paper offers an accurate alternative method based on separate analyses of the pipe structure and liquid components, followed by imposition of continuity and force constraints that couple the results of the separate analyses. Because dynamic response of the structural component is expressed in modal parameters, the method may be considered as an extension of the modal synthesis technique of structural engineering. That method is approximate because the response of a continuous system is represented by a finite number of modes; however, any degree of precision may be achieved by including a sufficient number of modes.

Advantages of component synthesis over one-step procedures for analysis of fluid-structure interaction in piping are:

1 Decomposition of a single, typically large, system matrix into smaller matrices which are solved independently of one another. This can save considerable computation cost since the time required to solve a matrix is proportional to the square of its dimension.

2 Utilization of existing progams for dynamic structural analysis so that their considerable efficiency and sophistication is exploited directly without having to incorporate them into a more comprehensive fluid-structural analysis program.

3 Providing a way to incorporate in the analysis data from field test on pipe structures. For example, a newly-constructed empty pipe system could be tested before start up to determine its structural modal parameters. If these differ appreciably from design values, the synthesis step of analysis is repeated using the modal parameters derived from test results to predict interactive response of the piping as actually con-

Contributed by the Fluids Engineering Division and presented at the Joint Applied Mechanics, Fluids Engineering, and Bioengineering Conference, Boulder, Colo., June 22-24, 1981, of THE AMERICAN SOCIETY OF MECHANICAL ENGINEERS. Manuscript received by the Fluids Engineering Division, October 31, 1981.

structed. Necessary revisions can be designed and implemented before the new system is operated.

Previous Studies

The present paper is concerned with pipe vibrations induced by internal fluid pulsations which propagate throughout the system and create unbalanced oscillatory pressure forces at locations where either flow area or direction changes. The fluid motion is caused by a source of harmonic excitation such as a reciprocating pump or oscillating valve. Literature on transient as well as oscillatory motion is cited herein in order to provide a more comprehensive perspective. The references portray a progression from axial wave and single degree of freedom pipe motion, through multidimensional wave equations, to finite element and modal approximations.

Reduction of the acoustic wave speed by circumferential and axial deformation of a pipe is described in numerous sources, e.g., the text by Wylie and Streeter [1]. This modification has been used traditionally in the prediction of waterhammer and oscillatory flows in fluid-filled lines where pipe motion is insignificant. For downstream load rejection, i.e., rapid valve closure, on a straight pipe Skalak [2], Thorely [3], and Williams [4], among others, coupled the longitudinal wave equations of the fluid and the pipe to predict the presence of a tension wave in the piping material, which is a precursor to the primary waterhammer, or acoustic, wave. Skalak [2] gives a review of this type of analysis, in which the pipe motion is primarily in the axial direction and is due entirely to elastic elongation. Regetz [5], D'Souza and Oldenburger [6], and Jones and Wood [7] have dealt with oscillatory flow setting up a vibratory, axial pipe motion for a single line. As in the transient case, no pipe translation was taking place, so that the pipe movement was of small magnitude and due only to elastic elongation. For the pipeline investigated by Regetz [5] and in one experiment by D'Souza and Oldenburger [6], the natural frequency of the pipe motion was sufficiently low to interfere with a lower mode of vibration of the fluid column.

In related studies Wood [8, 9] coupled unsteady flow with a single degree of freedom spring-mass component located at the end of a rigid, relatively immobile pipe. Significant fluid-structure interaction was demonstrated. That analysis also is valid for pipe systems exhibiting single degree of freedom vibration. Blade et al. [10] investigated the vibrational motion of a long hydraulic line with a right-angle bend at the midpoint. The system was constrained to allow only longitudinal motion in the downstream section, thus creating a single degree of freedom system. The coupled fluid-structural analysis was corroborated by experimental data.

Fully coupled fluid-structure interaction for piping with multiple structural degrees of freedom has not been analyzed extensively. Typically, in both transient and vibrational situations, the piping is assumed rigid and the fluid motion is predicted using conventional characteristics or impedance methods. Subsequently the hydrodynamic loads are applied to pipe components to determine the structural response. An example of this technique of noninteractive analysis is given by Mahoney et al. [11]. Uncoupled fluid vibrational analysis for complex piping networks has been developed by Zielke and Hack [12], Wylie and Streeter [1], and Chaudhry [13].

Analysis with interactive coupling can be effected by considering wave motion in the pipe walls as well as in the fluid component. Davidson and Smith [14] developed a combined liquid-structure transfer matrix for a pipe bend and experimentally demonstrated the validity of their analysis. As an extension of that work, Davidson and Samsury [15] developed a more accurate solution, analyzed a non-planar pipe system incorporating three bends, and validated the results experimentally. Wilkinson [16] outlined a method to predict general piping system vibrational response using the transfer matrix approach: equations in physical coordinates couple five wave families, one in the fluid and four in the piping structure. In a later work Wilkinson [17] presented a simplified theory for transient, solitary wave propagation in the close vicinity of tees, bends, etc., to show the basic mechanisms involved at such discontinuities. Ellis [18]

Nomenclature

A = vector of pipe cross-sectional areas
a = acoustic or pressure pulse wave speed of fluid component
D = complex number for fluid displacement
D_F = complex-valued vector of absolute fluid displacements at points
D_S = complex-valued vector of absolute structural displacements of points on the pipe walls and supports
F = complex-valued vector of forces at points on the pipe walls and supports
F' = complex-valued vector of applied external forces at points on the pipe walls and supports
G_0 = characteristic compliance
$[G_F]$ = complex-valued matrix of fluid compliances
$[G_s]$ = complex-valued matrix of structural compliances
$[G_V]$ = matrix of valve compliances
i = imaginary unit $\sqrt{-1}$
k = structural stiffness
l = length of fluid component between points
m = mass
P = complex-valued vector of fluid pressures at points
ΔP = instantaneous pressure drop across orifice
$\Delta \bar{P}$ = mean pressure drop across orifice
Q = complex number for pipe discharge
$\bar{Q}$ = mean discharge through orifice
$[R],[S],[T],[U]$ = connectivity matrices
t = time
$\mathbf{V}$ = complex-valued vector of fluid volumetric displacements into pipe network at points
x,y,z = Cartesian coordinates
Z_0 = characteristic impedance
α = pipe slope
β = ratio of orifice area to pipe area
γ = complex propagation constant
ξ = structural damping ratio
ρ = mass density of fluid
ω = angular frequency
ω_i = resonant angular frequency for ith mode

analyzed the transient behavior of a pumping station pipe network. By assuming release of certain force components at elbows and tees, he was able to utilize the method of characteristics for coupled fluid and pipe motion. Gibert et al. [19] described an experimental study of piping with an inverted U configuration which exhibited low-frequency resonance. Vibrations were induced by a stationary, partially closed gate valve creating downstream flow instabilities. Included was a finite element technique to couple liquid and structure and obtain modal parameters of the combined system, plus discussions of the various sources of vibrational excitation in piping systems and the use of power spectra to characterize them. Olson [20] devised structural analogs for unsteady flow in a variety of acoustic components. The formulations suggest the possibility of modelling both piping and contained liquid as solid elements, appropriately linked, and then analyzing the combined system with a structural finite element algorithm. Schwirian and Karabin [21] recently have implemented this type of analysis.

Analysis of dynamic behavior of structures typically is accomplished by matrix transformation that uncouples the equations of motion. The transformation vectors consist of displacements corresponding to modes of the undamped structure. These, together with the natural frequencies, transformed mass, stiffness and damping matrices, are termed "modal parameters." Modal superposition is the technique of expressing response of the structure to a particular dynamic load as a linear combination of modal parameters. Discussion of uncoupling the equations of motion, and subsequent response estimation by modal superposition, may be found in most contemporary texts on structural dynamics [22].

Modal synthesis is an extension of modal superposition in which the response of a structural system is expressed as a linear combination of modal parameters of two or more physical components of the system. Much of the pioneering work on modal synthesis is credited to Hurty [23] and is discussed in his survey paper [24]. Specific derivation for sinusoidal forcing functions is given by Klosterman and Lemon [25]. A later paper by Klosterman et al. [26] presents techniques for improving numerical accuracy achieved with a limited number of modes.

Karnopp [27] applied modal synthesis to oscillatory flows and pressures in linear acoustic filters. The motivation was to extend the frequency range over which lumped parameter models are valid. A combined structural-acoustic system representing a vehicle passenger compartment was analyzed by Wolf [28], using modal synthesis, to determine interior acoustical response.

Theoretical Development

The fundamental concept of the synthesis technique is that the dynamic response of a system may be expressed as a linear combination of responses of components of the system. For fluid-structure interaction in piping, the solid portion of the system, augmented by the mass of the liquid, is considered a single component. It includes not only the pipes, but hangers, guides, rack, and other flexible support structures as well. Modal parameters, i.e., natural frequencies, apparent mass, stiffness, damping, and mode shapes, provide a concise description of dynamic behavior of the structural components from which approximate response at any frequency may be computed. Modal parameters are determined by test of the actual pipe structure or by analysis using a finite element program such as ANSYS [29].

Oscillatory pressures in the liquid exert forces on the piping at velocity discontinuities such as elbows, tees, reducers and blind ends, and at pressure discontinuities such as orifices and nozzles. The liquid in each reach of pipe between adjacent

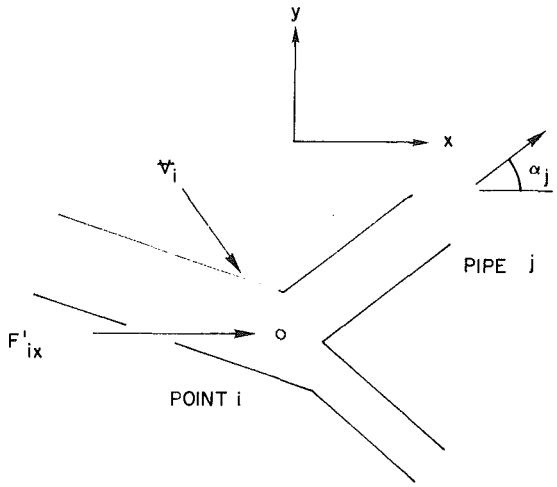

Fig. 1 Pipe junction

discontinuities is considered a separate distributed parameter component. Oscillatory behavior of each of these components may be expressed approximately as a linear combination of modal parameters. Alternatively, transfer functions can be derived that are exact and concise, and hence are preferable.

Associated with each velocity and pressure discontinuity is a displacement continuity constraint and a set of fluid forces acting on the piping. Structural force-displacement relations for degrees of freedom corresponding to discontinuities are derived from modal parameters and, together with the fluid force expressions and fluid transfer functions, are substituted into the continuity constraints to produce the system matrix equation. The resulting unknowns are pressures at discontinuities. Input excitations are oscillatory flow and oscillatory force. Inclusion of the latter permits the method to simulate a field test in which resonant frequencies are determined by vibrating the pipe at a velocity discontinuity while monitoring pressures at various points.

Assumptions. Assumptions necessary for synthesis of liquid and structural components are:

1 Linear relationships for force and displacement. Included in this assumption is the accepted condition of oscillatory flow in which fluid particle displacements are sufficiently small that linearization of the wave equations is appropriate.

2 Structural displacements are small relative to the wave lengths of the fluid pulsations.

3 Axial strain in the piping is at least several orders of magnitude less than unity.

4 Cross-sectional deformations of the pipe are negligible compared to the other displacements. The sonic velocity of the liquid is reduced to account for pipe wall compliance, but these deformations do not appear in the continuity and equilibrium constrants.

5 Wave lengths of fluid pulsations are much larger than pipe diameters so that pulsations may be considered one-dimensional.

6 Mean velocity of the liquid is much smaller than sonic velocity.

7 Structural modes are not coupled by damping.

8 Forces are transmitted from the liquid to the pipe walls at discrete locations termed points. Implicit in this assumption is the condition that friction forces exerted by the liquid on the pipe walls are negligible, or can be lumped at points.

9 Acceleration forces of fluid on pipe walls are negligible compared to pressure forces.

10 Structural damping is viscous and proportional to mass and stiffness.

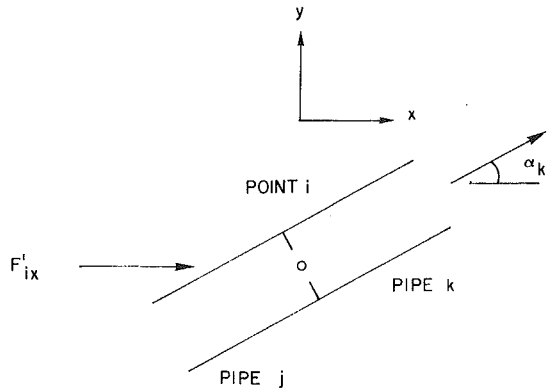

Fig. 2 Orifice at an interior point

System Equations for Synthesis. Let points on a pipe network and its supporting structure be selected such that there is a point at each fluid velocity discontinuity, one at each pressure discontinuity, and one at each location where external forces are applied directly to the structure. Additional points may be selected at other locations where computation of pressures and displacements is desired. The displacement of each point is expressed as a linear combination of x, y and z translations and rotations, giving six structural degrees of freedom for each point. However, restrained degrees of freedom and those for which there are no fluid force components may be omitted. In general, the number of degrees of freedom needed for component synthesis will be much smaller than the number of degrees of freedom needed for the structural finite element analysis of the same pipe network and supports.

Compliance for a linearly elastic structure is expressed by

$$D_S = [G_S]F \tag{1}$$

in which the vectors and matrix are dimensioned by the reduced number of structural degrees of freedom associated with points. For sinusodial forces the compliance terms may be expressed in modal parameters [25].

Two linearized equations, derived in the Appendix, may be written for each pipe to relate fluid displacements at the upstream and downstream ends to upstream and downstream pressures. These equations are combined into a fluid compliance equation:

$$D_F = [G_F]P \tag{2}$$

Associated with each fluid velocity discontinuity are a displacement or continuity constraint and forces acting on the piping. For example, the continuity constraint for the generalized junction i shown in Fig. 1 is

$$\mathcal{V}_i = \sum_j A_j D_{Fji} - D_{Six} \sum_j A_j \cos\alpha_j - D_{Siy} \sum_j A_j \sin\alpha_j \tag{3}$$

This generalization of an expression suggested by Wood [8] has been simplified by omission of translation in the z direction and of rotations, which have little effect on fluid displacements into the nearly concentric junctions of practical pipe networks. The expression for forces applied to the piping in the x direction in Fig. 1 is

$$F_{ix} = F'_{ix} - \sum_j P_{ji} A_j \cos\alpha_j \tag{4}$$

which is subject to the identity

$$P_{ji} = P_{ki} \tag{5}$$

for all pipes $j \neq k$ incident on point i.

Associated with each pressure discontinuity are a pressure constraint, a continuity constraint, and forces acting on the piping. For example, the pressure constraint for the orifice i shown in Fig. 2 is

$$G_{Vi}[P_{ji} - P_{ik}] - D_{Fji} + D_{Six}\cos\alpha_k + D_{Siy}\sin\alpha_k = 0 \tag{6}$$

An expression for G_V is derived in the Appendix. The continuity constraint at the pressure discontinuity is given by the identity

$$D_{Fik} = D_{Fji} \tag{7}$$

The forces applied to the piping in the x direction in Fig. 2 are

$$F_{ix} = F'_{ix} + [P_{ji} - P_{ik}]A_j[1 - \beta_i]\cos\alpha_k \tag{8}$$

The identities given by equations (5) and (7) are used to identify the independent vector bases for pressure and fluid displacement, P and D_F. The force expression, equations (4) and (8), may be combined to form a matrix function in terms of the pressure vector:

$$F = F' + [R]P \tag{9}$$

The continuity constraints, equation (3), are combined with relations for pressure discontinuities, equation (6), to form a matrix function in terms of the displacement and pressure vectors:

$$\mathcal{V} = [S]D_F + [T]D_S + [U]P \tag{10}$$

Note that $\mathcal{V}_i = 0$ if point i is a pressure discontinuity, and that unknown volumetric displacements into the network have been eliminated from the expression by replacing them with corresponding unknown fluid displacements at pipe ends. Equation (9) is substituted into equation (1), and the resulting expression along with equation (2) is substituted into equation (10) to produce the system equation

$$\mathcal{V} - [T][G_S]F' = \{[S][G_F] + [T][G_S][R] + [U]\}P \tag{11}$$

This expression is solved to find the unknown pressures, given known volumetric displacement inputs and applied external forces. Subsequently, equations (2) and (9) are employed to compute fluid displacements and forces on the pipe walls, and equation (1) is used to compute structural displacements.

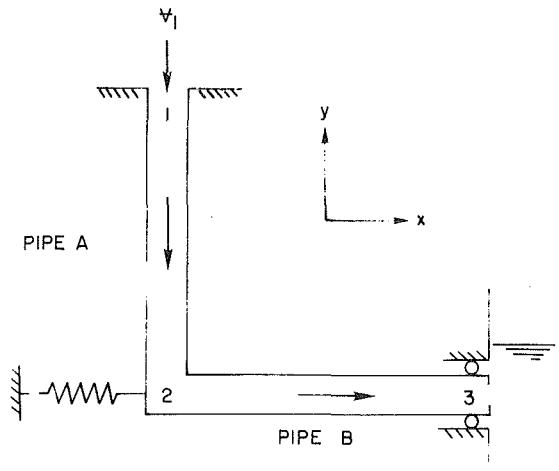

Fig. 3 Experimental system of Blade et al, (10). Parameters are: l = 10.35m, A = 3.8cm^2, a = 1143m/s, ρ = 773kg/m^3, β = 0.072, ξ = 0.16, m = 12kg.

Application

The piping illustrated in Fig. 3 was investigated by Blade et al. [10] to determine the effect of displacement response of the elbow on oscillatory pressures in the liquid. Their results have been used to validate the synthesis method for this elementary pipe system.

Because all forces are in the xy plane and the structure is symmetric about this plane, no z- translational nor x- and y-rotational degrees of freedom need to be considered. The z-

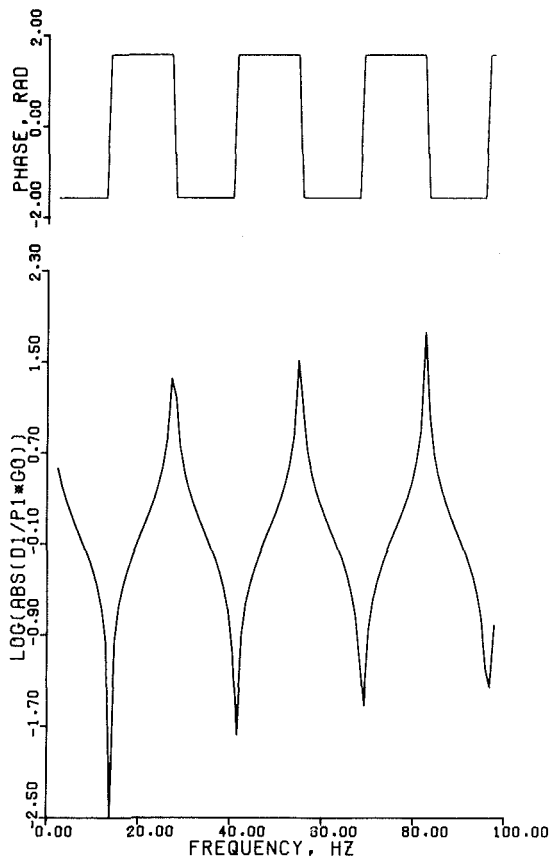

Fig. 4 Driving point compliance versus frequency for $G_V/G_0 \to \infty$, $k \to \infty$, $\omega_1 \to \infty$

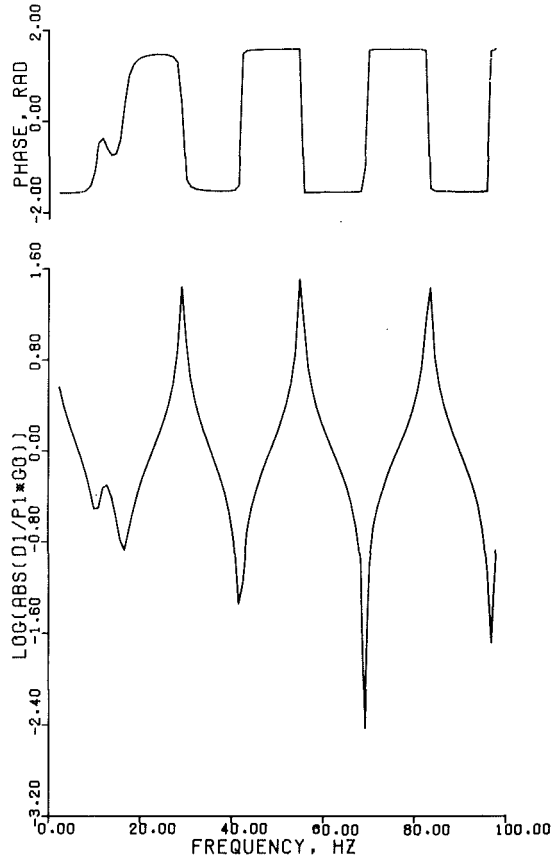

Fig. 5 Driving point compliance versus frequency for $G_V/G_0 \to \infty$, κ = 79.5kN/m, ω_1 = 82 rad/s (13 Hz)

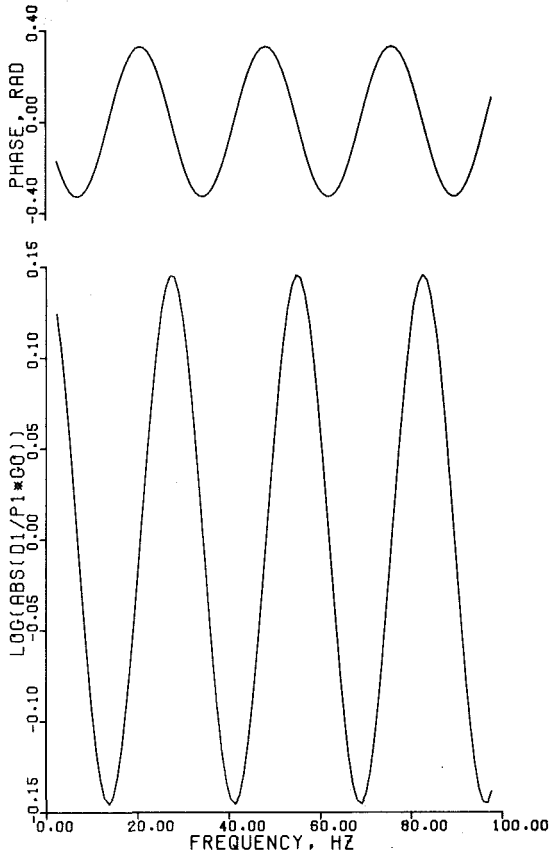

Fig. 6 Driving point compliance versus frequency for G_V/G_0 = 1.40, $k \to \infty$, $\omega_1 \to \infty$

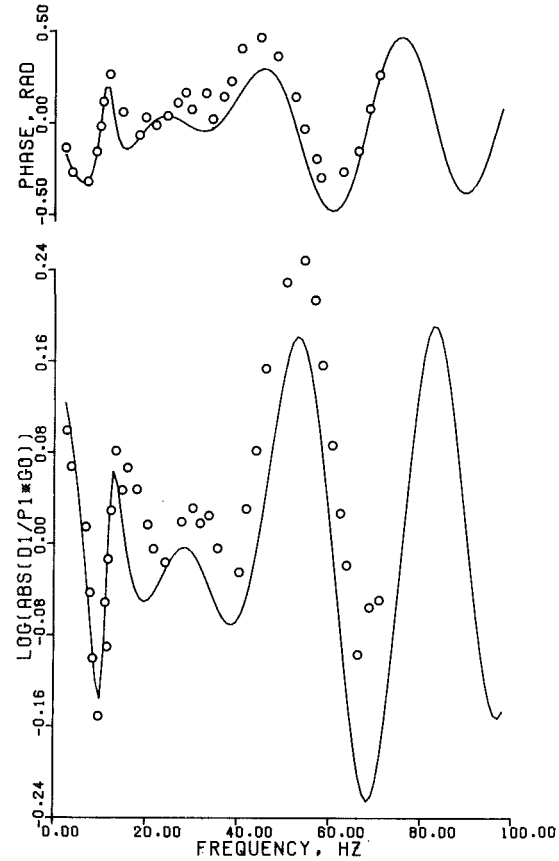

Fig. 7 Driving point compliance versus frequency for G_V/G_0 = 1.40, k = 79.5 kN/m, ω_1 = 82 rad/s (13 Hz). Circles are experimental data of Blade et al. [10].

rotational degrees of freedom do not enter into fluid-structure coupling because there are no applied moments nor flow axes eccentric to points. The pipe is supported such that translations in the y direction are negligible compared to translations in the x direction. Because the axial stiffness of the pipe is much greater than that of the spring, the x-translational degrees of freedom of points 2 and 3 may be considered identical. Therefore, the system has only one structural degree of freedom. The structural compliance expression is

$$D_{Sx2} = G_S(F_{x2} + F_{x3}) \tag{12}$$

in which

$$G_S = \frac{1}{k\{[1-(\omega/\omega_1)^2] + 2i\xi(\omega/\omega_1)\}} \tag{13}$$

Fluid compliance is given by the expression

$$\begin{bmatrix} D_{FA1} \\ D_{FA2} \\ D_{FB2} \\ D_{FB3} \end{bmatrix} = \begin{bmatrix} G_{FA11} & G_{FA12} & 0 \\ G_{FA21} & G_{FA22} & 0 \\ 0 & G_{FB22} & G_{FB23} \\ 0 & G_{FB32} & G_{FB33} \end{bmatrix} \begin{bmatrix} P_1 \\ P_2 \\ P_3 \end{bmatrix} \tag{14}$$

Forces on the piping are

$$\begin{bmatrix} F_{x2} \\ F_{x3} \end{bmatrix} = \begin{bmatrix} 0 & -A_B & 0 \\ 0 & 0 & (1-\beta)A_B \end{bmatrix} \begin{bmatrix} P_1 \\ P_2 \\ P_3 \end{bmatrix} \tag{15}$$

Continuity and pressure constraints are

$$\begin{bmatrix} V_1 \\ 0 \\ 0 \end{bmatrix} = \begin{bmatrix} A_A & 0 & 0 & 0 & 0 & 0 & 0 & 0 \\ 0 & -A_A & A_B & 0 & -A_B & 0 & 0 & 0 \\ 0 & 0 & 0 & -A_B & A_B & 0 & 0 & A_B G_V \end{bmatrix} \begin{bmatrix} D_{FA1} \\ D_{FA2} \\ D_{FB2} \\ D_{FB3} \\ D_{Sx2} \\ P_1 \\ P_2 \\ P_3 \end{bmatrix} \tag{16}$$

Equation (15) is substituted into equation (12), and the result, together with equation (14), is substituted into equation (16) to form the following system equation:

$$\begin{bmatrix} V_1 \\ 0 \\ 0 \end{bmatrix} = \begin{bmatrix} A_A G_{FA11} & A_A G_{FA12} & 0 \\ -A_A G_{FA21} & A_B G_{FB22} - A_A G_{FA22} + A_B^2 G_S & A_B G_{FB23} - A_B^2 G_S(1-\beta) \\ 0 & -A_B G_{FB32} - A_B^2 G_S & A_B^2 G_S(1-\beta) + A_B G_V - A_B G_{FB33} \end{bmatrix} \begin{bmatrix} P_1 \\ P_2 \\ P_3 \end{bmatrix} \tag{17}$$

This equation was solved for pressures corresponding to a unit volumetric displacement at point 1. Driving point compliances $D_1/(P_1 G_0)$ are shown in Figs. 4 through 7. In Figs. 4 and 5 the compliance at location 3 (Fig. 3) is infinite, that is, the orifice is removed. In Figs. 6 and 7 the orifice compliance at location 3 is equal to 1.40 times the characteristic compliance. The effect of a rigid pipe structure, $k \to \infty$, in Figs. 4 and 6 is contrasted with a compliant one, $k = 79.5$ kN/m, in Figs. 5 and 7. The natural frequency of the compliant pipe structure is $\omega_1 = 82$ rad/s, or 13 Hz. Figure 7 corresponds to the configuration analyzed by Blade et al. [10], and their experimental data are shown for comparison. Their theoretical impedance solution, not shown here, is identical to the component synthesis analysis shown in Fig. 7.

The first four resonant modes of the fluid column occur at frequencies of approximately 14, 42, 70, and 98 Hz; these are seen in Figs. 4 or 6 for the stiff piping. An orifice placed at the downstream end of the pipe damps the compliance response, as seen by comparing either Figs. 4 and 6, or Figs. 5 and 7. The effect of pipe motion has a profound impact on the system response. For both the open-ended and orifice configurations, two resonances replace the fundamental fluid resonance of 14 Hz. Generally, higher modes are relatively unaffected, although the mode at 70 Hz increases in amplitude, as shown by Figs. 6 and 7.

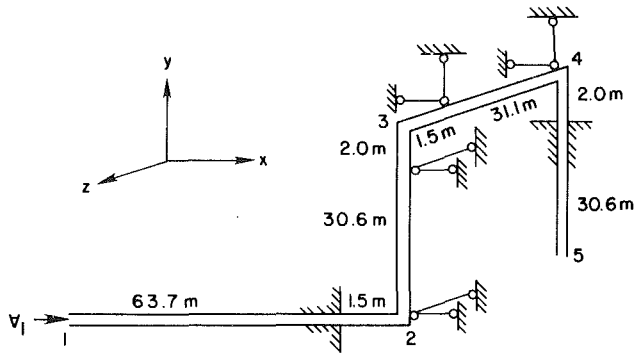

Fig. 8 Piping system with two structural degrees of freedom. Parameters are: A = 181.5cm^2, a = 1280m/s, ρ = 998kg/m^3, ω_1 = 45.9 rad/s (7.3Hz), ω_2 = 61.6 rad/s (9.8 Hz).

An example piping system in three dimensions and with multiple degrees of freedom is shown in Fig. 8. The first structural mode is translation of segment 2-3 in the y direction; the second structural mode is translation of segment 3-4 in the z direction. Excitation is provided at location 1 by a forced sinusoidal volumetric input. The frequency response of the driving point compliance D_1/P_1 is shown in Fig. 9. The dashed lines show the noninteractive (uncoupled) analysis and the solid lines relate the interactive (coupled) analysis. It is apparent that significant shifting of resonant frequencies occurs when coupling is included. Figure 10 shows the

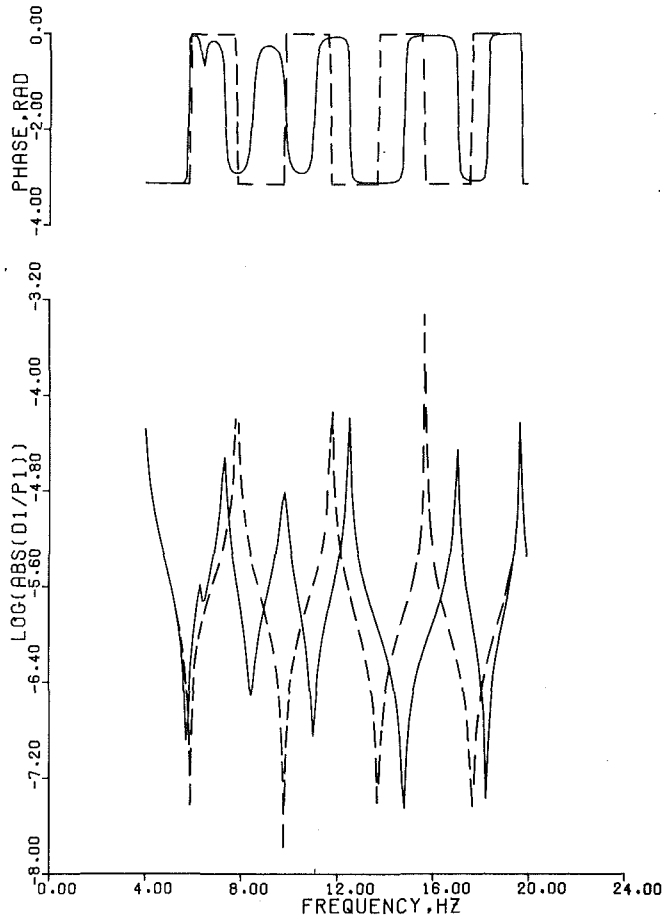

Fig. 9 Driving point compliance versus frequency. D1/P1 in ft/(lb/ft^2); 1 ft = .3048m, 1 lb/ft^2 = 47.88Pa.

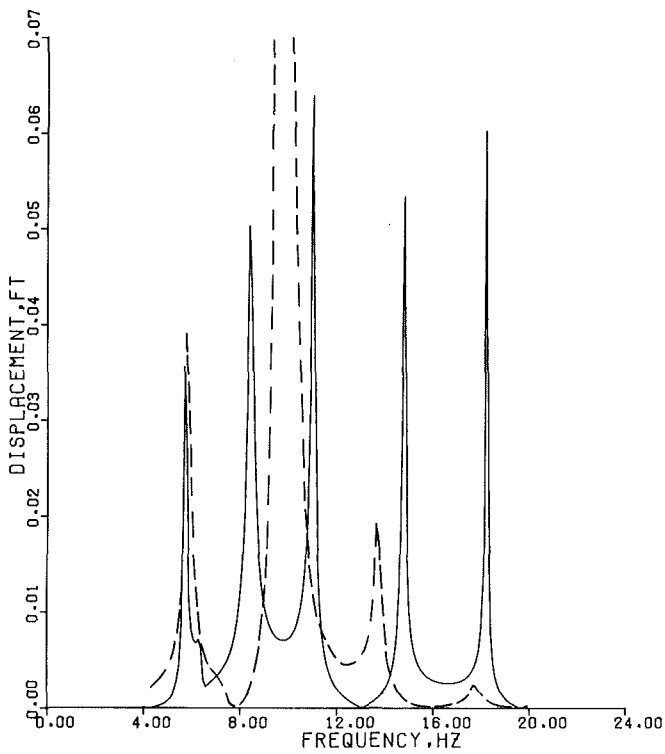

Fig. 10 Displacement in Y-direction of point 3; 1 ft = .3048m.

translation in the y direction of point 3. The dashed lines are the displacement predicted by applying the uncoupled dynamic pressure forces (represented by the uncoupled response in Fig. 9) to the structure and subsequently determining its response. In contrast, the solid lines show the interactive displacement response predicted by component synthesis. Both Figs. 9 and 10 illustrate the severe drawback of uncoupled analysis, namely, it does not accurately predict resonant frequencies of the combined fluid-structure system.

In general, analyses that do not consider coupling of fluid and structure may produce such dangerously inaccurate estimates of lower resonant frequencies when both the structural stiffness is low and the mass of the piping is not much greater than the mass of the contained fluid.

Summary and Conclusions

Pipe vibrations induced by internal fluid pulsations are encountered in industrial piping systems. Resonant frequencies of such piping are not estimated reliably by separate analysis of fluid and structure; the result can be severe vibration not predicted by design analysis. Formulations exist that correctly couple liquid and structural behavior. Unfortunately, they require solving a matrix that is necessarily larger than the system matrix for a purely structural analysis. Compared to these single-step formulations, component synthesis offers the computational advantages of solving two matrices instead of a single larger one, and of using existing structural analysis programs for the larger of the solutions. The necessary assumptions are valid within the frequency range corresponding to the first several harmonics of reciprocating pumps.

Modal description uses the parameters of a finite number of modes to represent behavior of systems that have an infinite number of modes. One must ask how many modes of the structural component should be included to achieve given precision within a given frequency range. Guidelines cannot be established until additional theoretical and experimental work is completed. For purely structural applications, inertia restraint and residual flexibility terms [25] may be incorporated to compensate for omitted modes. It is probable that utilization of these terms could increase the efficiency of the synthesis technique for fluid-structure systems as well.

The piping systems analyzed herein have up to two coupled degrees of freedom. Clearly, experimental validation of component synthesis for fluid-structure interaction in more complicated piping is needed. In addition, studies are necessary to incorporate acceleration forces, to determine numerical precision as a function of number of structural modes included, and to incorporate factors that compensate for omitted modes. With further development, the method may have application to higher frequency oscillation and to fluid transients, where nonperiodic loading could be represented in the frequency domain by Fourier transformation.

Acknowledgments

This study was supported in part by the Division of Engineering Research, Michigan State University. The authors are indebted to the reviewers for their helpful suggestions.

References

1 Wylie, E. B., and Streeter, V. L., *Fluid Transients*, McGraw-Hill, Inc., 1978.

2 Skalak, R., "An Extension of the Theory of Water Hammer, *Trans. ASME*, Vol. 78, No. 1, 1956, pp. 105-116.

3 Thorley, A. R. D., "Pressure Transients in Hydraulic Pipelines," ASME *Journal of Basic Engineering*, Vol. 91, Sept. 1969, pp. 453-461.

4 Williams, D. J., "Waterhammer in Non-Rigid Pipes: Precursor Waves and Mechanical Damping," *Journal of Mechanical Engineering Science, Institute of Mechanical Engineers*, Vol. 19, No. 6, 1977, pp. 237-242.

5 Regetz, J. D., Jr., "An Experimental Determination of the Dynamic Response of a Long Hydraulic Line," NASA Technical Note D-576, Dec. 1960.

6 D'Souza, A. F., and Oldenburger, R., "Dynamic Response of Fluid Lines," ASME *Journal of Basic Engineering*, Vol. 86, Sept. 1964, pp. 589-598.

7 Jones, S. E., and Wood, D. J., "The Effect of Axial Boundary Motion on Pressure Surge Generation," ASME *Journal of Basic Engineering*, Vol. 94, June 1972, pp. 441-446.

8 Wood, D. J., "A Study of the Response of Coupled Liquid Flow-Structural Systems Subjected to Periodic Disturbances," ASME *Journal of Basic Engineering*, Vol. 90, Dec. 1968, pp. 532-540.

9 Wood, D. J., "Influence of Line Motion on Waterhammer Pressures," *Journal of the Hydraulics Division, Proceedings of the American Society of Civil Engineers*, Vol. 95, No. HY3, May 1969, pp. 941-959.

10 Blade, R. J., Lewis, W., and Goodykoontz, J. H., "Study of a Sinusoidally Perturbed Flow in a Line Including a 90 deg Elbow with Flexible Supports," NASA Technical Note D-1216, 1962.

11 Mahoney, J. B., Ramchandani, M., and Hsu, S. T., "Steady State Vibration in Condensate Piping due to Pump Operation," ASME Paper No. 80-C2/PVP-46, Aug. 1980.

12 Zielke, W., and Hack, H. P., "Resonance Frequencies and Associated Mode Shapes of Pressurized Piping Systems," *Proceedings of the First International Conference on Pressure Surges*, BHRA Fluid Engineering, Cranfield, Bedford, England, Sept. 1972, pp. G1-1-13.

13 Chaudhry, M. H., *Applied Hydraulic Transients*, VanNostrand Reinhold Co., 1979.

14 Davidson, L. C., and Smith, J. E., "Liquid-Structure Coupling in Curved Pipes," *The Shock and Vibration Bulletin*, No. 40, Part 4, Dec. 1969, pp. 197-207.

15 Davidson, L. C., and Samsury, D. R., "Liquid-Structure Coupling in Curves Pipes—II," *Shock and Vibration Bulletin*, No. 42, Part 1, Jan. 1972, pp. 123-135.

16 Wilkinson, D. H., "Acoustic and Mechanical Vibrations in Liquid-Filled Pipework Systems," *Proceedings of the BNES Vibration in Nuclear Plant Conference*, Paper No. 8:5, Keswick, England, May 1978.

17 Wilkinson, D. H., "Dynamic Response of Pipework Systems to Water Hammer," *Proceedings of the Third International Conference on Pressure Surges*, Vol. 1, BHRA Fluid Engineering, Canterbury, England, Mar. 1980, pp. 185-202.

18 Ellis, J., "A Study of Pipe-Liquid Interaction Following Pump Trip and Check-Valve Closure in a Pumping Station," *Proceedings of the Third International Conference on Pressure Surges*, Vol. 1, BHRA Fluid Engineering, Canterbury, England, Mar. 1980, pp. 203-220.

19 Gibert, R. J., Axisa, F., and Villard, B., "Flow Induced Vibrations of Piping System (Vibration Sources-Mechanical Response of the Pipes)," *Proceedings of the BNES Vibration in Nuclear Plant Conference*, Paper No. 6:2. Keswick, England, May 1978.

20 Olson, H. F., *Dynamical Analogies*, D. VanNostrand Co., Inc., 1943.

21 Schwirian, R. E., and Karabin, M. E., "Use of Spar Elements to Simulate Fluid-Solid Interaction in the Finite Element Analysis of Piping System Dynamics," *Proceedings of the Symposium on Fluid Transients and Structural Interactions in Piping Systems*, American Society of Mechanical Engineers, June 1981, pp. 1-11.

22 Clough, R. W., and Penzien, J., *Dynamics of Structures*, McGraw-Hill, 1975.

23 Hurty, W. C., "Dynamic Analysis of Structural Systems Using Component Modes," *AIAA Journal*, Vol. 3, No. 4, Apr. 1965, pp. 678-685.

24 Hurty, W. C., "Introduction to Modal Synthesis Techniques," *Synthesis of Vibrating Systems*, Neubert, V. H., and Raney, J. P., eds., ASME, 1971, pp. 1-13.

25 Klosterman, A. L., and Lemon, J. R., "Building Block Approach to Structural Dynamics," *Proceedings of the Vibrations Conference*, Design Engineering Division, ASME, Philadelphia, 1969

26 Klosterman, A. L., McClelland, W. A., and Sherlock, J. E., "Dynamic Simulation of Complex Systems Utilizing Experimental and Analytical Techniques," *Proceedings of the Winter Annual Meeting*, Aerospace Division, ASME, Houston, 1975.

27 Karnopp, D., "Lumped Parameter Models of Acoustic Filters Using Normal Modes and Bond Graphs," *Journal of Sound and Vibration*, Vol. 42, No. 4, 1975, pp. 437-446.

28 Wolf, J. A., Jr., "Modal Synthesis for Combined Structural-Acoustic Systems," *AIAA Journal*, Vol. 15, No. 5, 1977, pp. 743-745.

29 DeSalvo, G., and Swanson, J. A., *ANSYS Engineering Analysis System, User's Manual*, Swanson Analysis Systems, Inc., Houston, Penn., Aug. 1978.

APPENDIX

Derivation of Fluid Compliance Functions

For forced oscillations in a pipe, the equations of motion and continuity can be linearized and solved for the instantaneous pressure and flow expressed in the form $P(x)\exp(i\omega t)$ and $Q(x)\exp(i\omega t)$, respectively [1]. The function $P(x)$ and $Q(x)$ are given by

$$P(x) = P_1 \cosh\gamma x - Z_0 Q_1 \sinh\gamma x \tag{18}$$

$$Q(x) = -\frac{P_1}{Z_0}\sinh\gamma x + Q_1 \cosh\gamma x \tag{19}$$

in which P_1 and Q_1 are complex pressure and discharge at the upstream location 1, and γ is the complex propagation constant. The characteristic impedance is

$$Z_0 = \gamma\rho a^2/(i\omega A) \tag{20}$$

The fluid displacement $D(x)$ is related to $Q(x)$ in the manner

$$D(x) = Q(x)/(i\omega A) \tag{21}$$

Note that the displacement is $\pi/2$ radians out of phase with respect to discharge. Replacing $Q(x)$ and Q_1 in equations (18) and (19) by $D(x)$ and D_1 results in

$$P(x) = P_1\cosh\gamma x - \frac{D_1}{G_0}\sinh\gamma x \tag{22}$$

$$D(x) = -G_0 P_1 \sinh\gamma x + D_1 \cosh\gamma x \tag{23}$$

in which G_0 is a "characteristic compliance"

$$G_0 = 1/(\gamma\rho a^2) \tag{24}$$

Transfer functions which relate conditions at the upstream location 1 to those a distance l downstream at location 2 are:

$$P_2 = P_1\cosh\gamma l - \frac{D_1}{G_0}\sinh\gamma l \tag{25}$$

$$D_2 = -G_0 P_1 \sinh\gamma l + D_1 \cosh\gamma l \tag{26}$$

Equation (25) and (26) can be rearranged in the transfer matrix form

$$\begin{bmatrix} D_1 \\ D_2 \end{bmatrix} = \begin{bmatrix} G_0\,\mathrm{ctnh}\gamma l & -G_0/\sinh\gamma l \\ G_0/\sinh\gamma l & -G_0\,\mathrm{ctnh}\gamma l \end{bmatrix} \begin{bmatrix} P_1 \\ P_2 \end{bmatrix} \tag{27}$$

For an assumed frictionless flow the complex propagation constant reduces to $i\omega a$, and the compliance matrix becomes

$$[G_F] = \begin{bmatrix} -\dfrac{\mathrm{ctn}(\omega l/a)}{\rho a\omega} & \dfrac{1}{\rho a\omega\sin(\omega l/a)} \\ -\dfrac{1}{\rho a\omega\sin(\omega l/a)} & \dfrac{\mathrm{ctn}(\omega l/a)}{\rho a\omega} \end{bmatrix} \tag{28}$$

Equation (27) relates to a column of fluid in a single pipe reach. For a piping system the overall compliance matrix, given by equation (2), is composed of individual compliances for each reach; an example is given by equation (14).

The fixed orifice boundary condition in linearized form is given by [1]

$$Q_V = \frac{\bar{Q}}{2\overline{\Delta P}}\Delta P_V \tag{29}$$

in which $\bar{Q}$ and $\overline{\Delta P}$ are the mean discharge and pressure drop across the orifice, respectively, and Q_V and ΔP_V are the complex instantaneous discharge relative to the moving valve and pressure drop. With equation (21) Q_V can be replaced by D_V, the fluid displacement relative to the valve, so that equation (29) becomes

$$D_V = G_V \Delta P_V \tag{30}$$

wherein the valve compliance is

$$G_V = \bar{Q}/(2i\omega A\overline{\Delta P}) \tag{31}$$

Additional boundary conditions can be related to point compliances in a similar manner. Examples include a rotating valve, and accumulator, and a lumped capacitance element.

The Form Drag of Three-Dimensional Bluff Bodies Immersed in Turbulent Boundary Layers

H. Sakamoto

M. Moriya

S. Taniguchi

Department of Mechanical Engineering,
Kitami Institute of Technology,
Kitami, 090, Japan

M. Arie

President, Hokkaido University
Sapparo, 060, Japan

Measurements of the pressure distributions on the three-dimensional bluff bodies are correlated with the characteristics of the smooth-wall turbulent boundary layers in which the bodies are immersed. The bluff bodies selected for measurement were a cube and a vertical circular cylinder which can be considered as typical examples of three-dimensional bluff bodies. Experimental data were collected to investigate the effects of (1) the variation of the height of bluff bodies h, (2) the characteristics of the smooth-wall boundary layers in which they are immersed, on the form drag acting on the three-dimensional bluff bodies. For flow with zero-pressure gradient, the form drag coefficients of the cube and the vertical circular cylinder defined by $C_{D\tau}=D/(1/2\rho u_\tau^2 h^2)$ *are found to be expressed as a power-law function of* hu_τ/ν *in the range of* h/δ *less than about 1.0, where D is the form drag,* u_τ *the shear velocity,* ν *the kinematic viscosity and* δ *the thickness of the undisturbed boundary layer at the location of the bluff bodies. For* $h/\delta > 1.0$*, the drag coefficients are independent of the parameter* u_τ/U_0*, being uniquely related to* h/δ*. Further, the pressure distributions along the front centerline of each bluff body can be expressed by a single curve irrespective of both the height of the bluff body and the boundary layer characteristics and show a good agreement with the dynamic pressure in an undisturbed boundary layer at the location of the bluff bodies in the range of about* $0.2 < y/h < 0.7$*, where y is the distance from the wall.*

1 Introduction

The flow of an incompressible fluid over bluff bodies is one of the basic problems repeatedly drawing the attention of many research workers. Especially, the prediction of the drag and lift forces acting on a body concerned is of great importance for practical purposes, and hence, a considerable amount of effort has been devoted to this subject. However, a major part of this effort is concerned with two-dimensional bluff bodies located in a uniform stream of infinite extent. Because of its complex nature, the flow around the bluff bodies which are attached to a plane wall still remains in the category of difficult and interesting problems to be investigated further. The flow around the bluff bodies attached to a plane wall is also of great practical importance in connection with such diverse applications as the wind load on the man-made structures, the oscillation characteristics and noise of the high-speed vehicles, the effect of roughness on the boundary layer characteristics, and the effectiveness of the spoilers on an airfoil, etc.

Recently, experimental investigations on the flow around the bluff bodies attached to a long plane wall on which a turbulent boundary layer develops have been reported by several authors. Good and Joubert [1] measured in detail the pressure and mean-velocity profiles around normal flat plates immersed in an equilibrium turbulent boundary layer with zero-pressure gradient to show that the drag coefficient obeys a wall-similarity law with respect to the plate height, which is similar to the wall-similarity law of the mean velocity profile in the turbulent boundary layers. Arie et al. [2] and Sakamoto et al. [3] showed that the same type of wall-similarity law is also valid for the rectangular cylinders with various width-to-height ratio and the flat plate at various angles of inclination respectively. More recently, Ranga Raju et al. [4] demonstrated that the form drag coefficient of a two-dimensional fence placed in the rough-wall turbulent boundary layer under zero-pressure gradient is a unique function of h/y', where y' is the roughness length.

All the investigations mentioned above are concerned with the form drag of the two-dimensional bluff bodies attached to a plane wall. However, since the hydrodynamics characteristics between the two-dimensional and three-dimensional bluff bodies attached to a plane wall are considerably different, the values of the form drag of the three-dimensional bluff bodies such as the man-made structures on the ground and the roughness elements on the boundary surface, cannot

Contributed by the Fluids Engineering Division for publication in the JOURNAL OF FLUIDS ENGINEERING. Manuscript received by the Fluids Engineering Division, April 6, 1981.

accurately be estimated based on the experimental results of the two-dimensional cases of bodies.

This study intends to experimentally clarify the form drag acting on a cube and a vertical circular cylinder in correlation with the characteristics of the smooth-wall boundary layer in which they are immersed. Among the possible types of three-dimensional obstacles, a cube and a vertical circular cylinder were selected as the most suitable ones to establish the model law. Since many natural obstacles like man-made structures, roughness elements on the surface of solid wall, spurs in river, etc., exhibit similar configurations, structural engineers calculating wind loads, hydraulic engineers designing spur dikes for river drainage and agricultural engineers dealing with shelter belts will find information on these drags useful.

2 Parameters to be Included

The physical parameters governing the flow around the three-dimensional bluff bodies set on a plane wall will be considered first. It has been well established that a fully-developed turbulent boundary layer becomes self-preserving. The mean velocity and turbulent properties in the boundary layer have similar nondimensional profiles at each station downstream of a certain point, where the boundary layer attains its fully developed form, when flowing along a smooth floor under zero pressure gradient. The properties of the turbulent boundary layer can be specified by free-stream velocity U_0, shear velocity u_τ, kinematic viscosity ν, density of the fluid ρ and thickness of the boundary layer δ.

The variables characterizing the geometrical shape of the two bodies dealt in the present paper are determined as follows: the height h in the case of the cube, and the height h and diameter d in the vertical circular cylinder, respectively. Since the diameter d of the cylinder selected for measurements was equal to its height h, we finally chose only the height h as the variable characterizing the geometrical shape of these bodies.

Accordingly, the functional relationship for the variation of form drag D of the three-dimensional bluff bodies placed in a turbulent boundary layer may be written as

$$D=f(h,u_\tau,U_0,\delta,\rho,\nu) \tag{1}$$

By dimensional analysis, one gets the following functional relationships from equation (1):

$$C_D=\frac{D}{\frac{1}{2}\rho U_0^2h^2}=f_1\left(\frac{u_\tau}{U_0},\frac{h}{\delta},\frac{hU_0}{\nu}\right) \tag{2}$$

$$C_{D\tau}=\frac{D}{\frac{1}{2}\rho u_\tau^2h^2}=f_2\left(\frac{u_\tau}{U_0},\frac{h}{\delta},\frac{hu_\tau}{\nu}\right) \tag{3}$$

Further, there exists the following relation [5] in the turbulent boundary layer adopted in the present experiment:

$$\frac{U_0}{u_\tau}=\frac{1}{\kappa}\log_e\frac{\delta u_\tau}{\nu}+C+\frac{\Pi}{\kappa}w(1) \tag{4}$$

where Coles obtained $\Pi=0.55$ by assuming that $\kappa=0.4$ and $C=5.1$ for a boundary layer with zero pressure-gradient. Since these parameters included in the right-hand side of equations (2) and (3) are directly related by equation (4), the functional relationship of equations (2) and (3) can finally be put in a proper form of the correlation:

$$C_D=f_3\left(\frac{u_\tau}{U_0},\frac{h}{\delta}\right) \tag{5}$$

$$C_{D\tau}=f_4\left(\frac{u_\tau}{U_0},\frac{hu_\tau}{\nu}\right) \tag{6}$$

The main objective of the present investigation is to determine the functional forms of equations (5) and (6) by experimental measurements.

3 Experimental Equipment and Procedure

The experimental work was carried out in two closed-circuit wind tunnels installed at the Kitami Institute of Technology. All the measurements for the cubes were undertaken in a wind tunnel with a uniform test section of 0.6 meter high, 0.6 meter wide, and 5.4 meter long. A series of four turbulence-reducing screens are installed in the settling section upstream of the contraction (9:1), and the free-stream turbulence level in the test section is about 0.2 percent at the free-stream velocity of 25 m/s which was employed in the present experiment. All the measurements for the vertical circular cylinders were made in a wind tunnel which has a contraction ratio of 14:1. The test section of the tunnel has a uniform cross-section of 0.4 meter $\times$ 0.4 meter and the length is 4.0 meters. The free-stream turbulence level in the test section of this tunnel was about 0.2 percent at the free-stream velocity of 20 m/s.

The ceiling of the test section of each of the tunnels is made of a flexible sheet of stainless steel so that its shape can be adjusted to remove the longitudinal pressure gradient. Also, the test section floor of the tunnels is covered with a smooth plastic plate of 10 mm thickness in order to eliminate the effect of the roughness of the surface. The floor itself is used as the plane boundary along which the turbulent boundary layer develops.

Nomenclature

C_D = pressure drag coefficient = $D/(1/2\rho U_0^2h^2)$
$C_{D\tau}$ = pressure drag coefficient = $D/(1/2\rho u_\tau^2h^2)$
$C_{Db\tau}$ = contribution of base pressure to $C_{D\tau}$
$C_{Df\tau}$ = contribution of front pressure to $C_{D\tau}$
C_p = pressure coefficient = $(p-p_0)/(1/2\rho U_0^2)$
C_{psg} = pressure coefficient on the front stagnation line of the cube and the cylinder
D = pressure drag
d = diameter of the cylinder
H = shape factor of the boundary layer = δ^*/θ
h = height of the cube and the cylinder
p = pressure on the surface of the cube and the cylinder
p_0 = static pressure of the free stream
p_{sg} = pressure on the front stagnation line of the cube
q = nondimensional dynamic pressure in the turbulent boundary layer = $(u/U_0)^2$
R_θ = Reynolds number = $U_0\theta/\nu$
U_0 = velocity of the free stream
u = longitudinal mean velocity component in the boundary layer
u_τ = shear velocity
x,y,z = Cartesian coordinate system
δ = thickness of the boundary layer
δ^* = displacement thickness of the boundary layer
θ = momentum thickness of the boundary layer, circumferential angle of the cylinder
ρ = density of the fluid
ν = kinematic viscosity of the fluid

In the present experiment, the height h of the test bluff bodies was taken up to about 1.5 times the boundary layer thickness. In the case of the cube, the height h selected for measurement were 7, 10, 15, 20, 25, 30, 35, 40, 50, 60, and 70 mm. The cubes tested were made of acrylic-resin. A number of 0.5 mm piezometer holes were drilled on one side-face of the cube, the number of holes increasing with the size of the cube. In this manner, a fairly detailed measurement of the pressure distribution on the surface could be obtained, even for a cube height of 7 mm, which had 25 exposed pressure taps. The cube was mounted on a disk so that it could be rotated to attain the purpose of measuring the pressure distributions on the other side-face of the cube. These pressure taps were connected to a Betz type of manometer through 1.0 mm I.D. stainless tube and polyvinylchloride tubes of various diameters.

The vertical circular cylinders were made of brass with the same height and diameter. The heights selected for measurement were 5, 7.5, 10, 12.5, 15, 20, 25, 30, 40, and 46 mm. A large number of 0.5 mm piezometric holes were drilled on the surface along its height with a spacing which was increased progressively with distance from the top. The cylinders could again be rotated about their axis so that the pressure distributions on their entire surface could be measured. Figure 1 shows the definition sketch of the test bodies placed in a turbulent boundary layer.

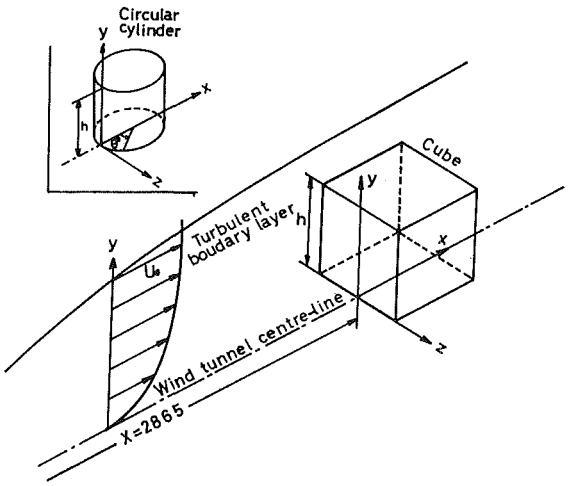

Fig. 1 Definition sketch for a test body placed in the turbulent boundary layer

4 Characteristics of the Turbulent Boundary Layer

The turbulent boundary layer developing along the floor of the test section of the wind tunnels was adopted in the present investigation. The characteristics of the boundary layer are examined to ascertain whether or not a fully-developed equilibrium boundary layer was achieved at the location of the bluff body.

The mean velocity profiles in the boundary layer flow agreed well with the experimental data of Klebanoff and Diehl [6]. Also, the mean velocity profiles in the region near the wall were confirmed as following the logarithmic law suggested by Coles [5]:

$$\frac{u}{u_\tau} = 5.75 \log\left(\frac{yu_\tau}{\nu}\right) + 5.1 \tag{7}$$

The distribution of the longitudinal turbulence intensity in the boundary layer at the location of the body corresponded well with the data of Klebanoff and Diehl [6].

The two-dimensionality of the flow field in the test section of the two wind tunnels was examined by measuring velocity profiles in the direction normal to the xy-plane at various distances from the wall. The results showed that a satisfactory two-dimensionality was realized in the region of about 300 mm in width containing the centerline in the 0.6 m × 0.6 m wind tunnel and in the region about 150 mm in width in the 0.4 m × 0.4 m wind tunnel.

From the foregoing considerations, it was concluded that the turbulent boundary layers along the floors of the two test

Table 1(*a*) Characteristics of the undisturbed turbulent boundary layer at the location of a cube (X = 2865 mm)

RUN	U_0 m/s	δ mm	δ^* mm	θ mm	R_θ	u_τ/U_0	H
1	15	48.6	7.5	5.4	5164	0.0371	1.40
2	20	51.6	7.9	5.8	7396	0.0360	1.36
3	25	50.4	7.6	5.6	8926	0.0353	1.34

Table 1(*b*) Characteristics of the undisturbed turbulent boundary layer at the location of a vertical circular cylinder (X = 2355 mm)

RUN	U_0 m/s	δ mm	δ^* mm	θ mm	R_θ	u_τ/U_0	H
1	12	30.0	4.9	3.5	2523	0.0408	1.40
2	16	39.0	6.3	4.5	4286	0.0384	1.38
3	20	44.8	6.6	4.9	5904	0.0376	1.34

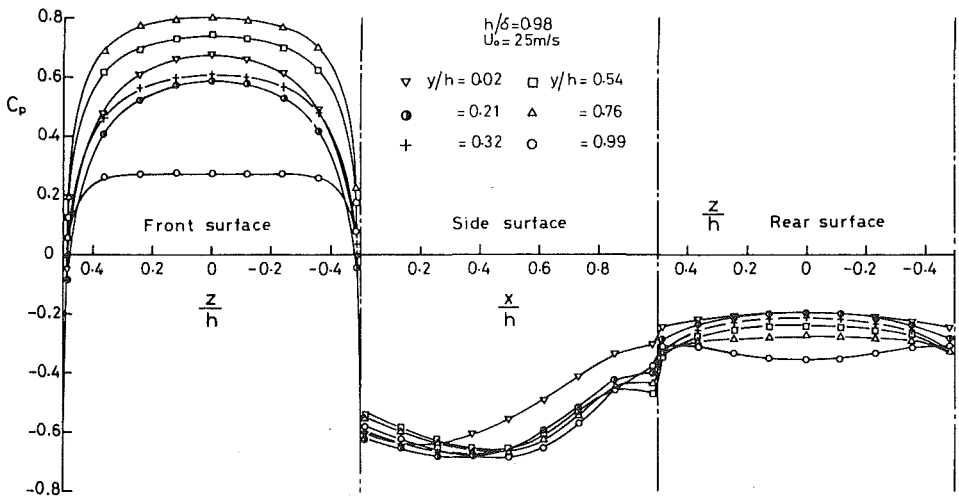

Fig. 2 Pressure distributions on the surface of a cube. The uncertainty in the ordinate is ±0.01 and that in the abscissa is less than ±0.005. Lines for visual aid only.

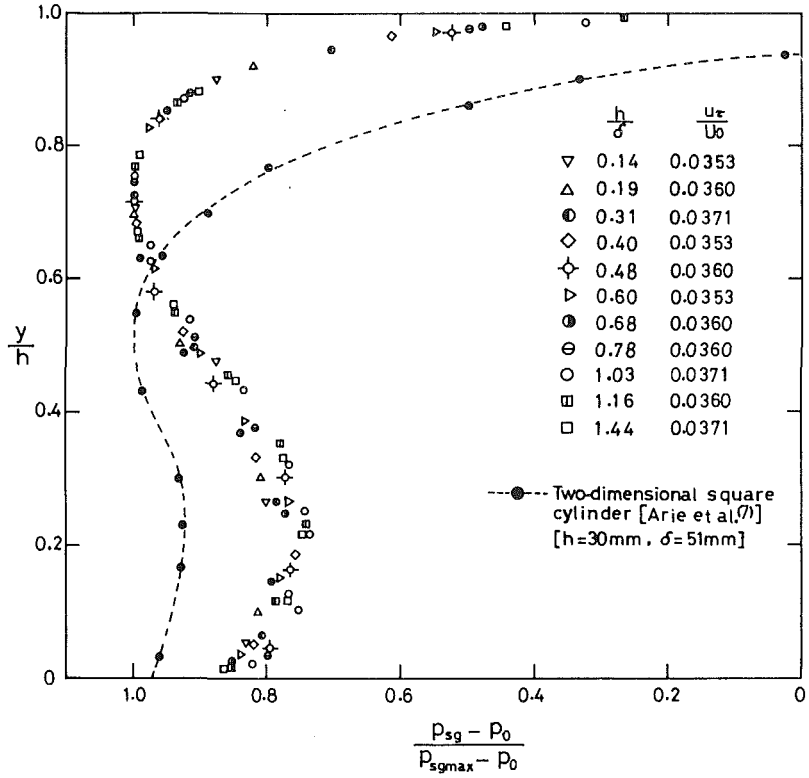

Fig. 3 Similarity of pressure distributions along the front centerline of a cube. The uncertainty in the ordinate is less than ±0.005 and that in the abscissa is ±0.01.

sections had the same characteristics as a fully-developed equilibrium turbulent boundary layer with zero-pressure gradient developing along a smooth flat plate. The boundary layer characteristics at the location of the cube and the vertical circular cylinder are summarized in Tables 1(*a*) and (*b*), respectively.

5 Results and Discussion

5.1 Pressure Distribution on the Cube. Figure 2 shows the general shape of the pressure distribution on the upstream surface, the downstream surface and the side surfaces of the cube for the case of $U_0 = 25$ m/s and $h/\delta = 0.98$. All the results are plotted non-dimensionally in the form of a pressure coefficient C_p defined by

$$C_p = (p - p_0)/\left(\frac{1}{2}\rho U_0^2\right)$$

where p is the surface pressure and p_0 and U_0 are the static pressure and the free-stream velocity, respectively.

The results of the pressure distribution on the upstream surface will first be examined. The profiles of the pressure distribution at the relative height y/h exhibit a reasonably systematic trend except in the neighborhood of the top of the cube. However, it may be noticed that the value of C_p at $y/h = 0.02$ is considerably larger than the values at $y/h = 0.21$ and 0.32, although the dynamic pressure at $y/h = 0.02$ in the approaching boundary layer is smaller than that at $y/h = 0.21$ and 0.32. The result is presumably caused by the existence of a horseshoe vortex which wraps itself around the base of the body. This vortex undoubtedly promotes extra turbulent mixing in the vicinity of the base of the body entraining fluid into the base region, thereby increasing the pressure at the vicinity of the body.

Regarding the pressure distribution on the side surfaces and the rear surface, on the other hand, it can be seen that the pressure variation for each value of y/h shows almost similar shape on each surface, and the difference of pressure itself is less pronounced except near base and the top of the body as is observed by the pressure distribution along $y/h = 0.02$ and 0.99.

Figure 3 shows the variation of the pressure distributions along the centerline of the front face of the cube ($z/h = 0$), which is normalized by the maximum pressure on the centerline of the front face for various values of the parameters u_τ/U_0 and h/δ, respectively. The results of the experiments plotted in this figure include the change of the velocity of main flow which means the changes of the value of parameters u_τ/U_0 as tabulated in Table 1(*a*) and h/δ, i.e., the height of the cube nondimensionalized with the boundary layer thickness δ. As can be seen in this figure, the profiles of the pressure distributions for three different values of u_τ/U_0 and h/δ are the same. Particularly, it should be noted that the individual pressure distributions exhibit an approximately similar profile which shows its own maximum value somewhere at about $y/h = 0.75$. This result suggests that the individual flow fields upstream of the cube are similar to each other regardless of the variation of the two parameters u_τ/U_0 and h/δ. Arie et al. [7] have shown experimentally that, when normalized by the maximum pressures, the pressure distributions on the two-dimensional square cylinders, of which Fig. 3 is typical, exhibit approximately similar profiles which have a maximum at about $y/h = 0.55$. The difference between the positions where the pressure attains its maximum value in the cube and in the two-dimensional square cylinders may be caused by the following reason. In the case of a square cylinder, the boundary layer in the approaching flow is forced to separate from the tunnel wall and it reattaches to the front surface at about $y/h = 0.55$, where the pressure distribution on the front surface attains maximum value. On the other hand, the variation of the flow velocity in the boundary layer approaching the cube caused by its blockage itself is com-

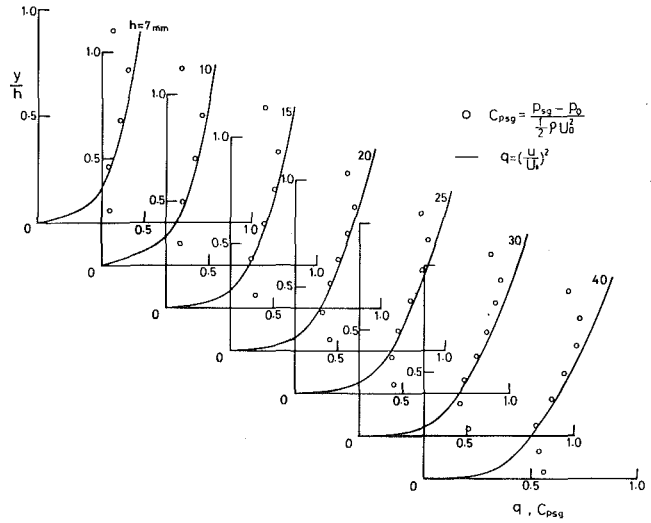

Fig. 4 Comparison of pressure distributions on the front centerline of a cube with the dynamic pressure in the undisturbed turbulent boundary layer. The uncertainty in the ordinate is less than ±0.005 and that in the abscissa is ±0.01.

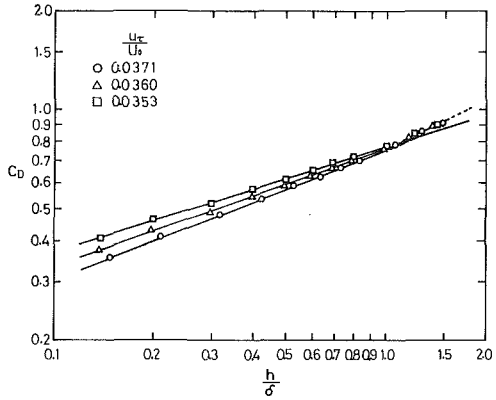

Fig. 5 Relation between C_D and h/δ for a cube. The uncertainty in the ordinate is ±0.02 and that in the abscissa is ±0.01. Lines are the best-fit line obtained by the least-square averaging of the data.

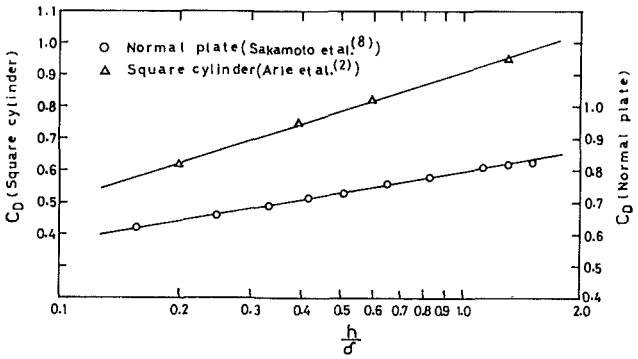

Fig. 6 Relation between C_D and h/δ for a two-dimensional normal plate and square cylinder. For further information, see the caption of Fig. 5.

paratively small. Thus, the dynamic pressure $1/2\rho u^2$ at a distance y from the wall in the approaching boundary-layer flow may almost directly be transformed into stagnation pressure at the corresponding position on the centerline of the front face of the cube, except in the region influenced by the horseshoe vortex, where the flow swirls around the base. Thus, the value of the pressure along the centerline of the front face rises gradually with increasing y/h. However, when y/h is larger than about 0.75, the pressure becomes influenced by the high negative suction around the top edge and starts to decrease towards the negative value at the top edge.

When the pressure distribution along the centerline of the front face is compared with the dynamic pressure in the undisturbed boundary layer, one can more clearly understand the flow field around the cube. The results of the experiment are shown in Fig. 4. As can be seen in this figure, the pressure and the dynamic pressure agree fairly well in the range of about $0.2<y/h<0.7$. Accordingly, it may be judged that the dynamic pressure of the flow is converted into the pressure on the centerline of the front face except in the two distinct ranges of y/h which are less than about 0.2 where the flow is influenced by the horseshoe vortex and larger than about 0.7 where the flow is influenced by prevailing negative suction along the top surface of the cube.

5.2 Drag Force Acting on the Cube. The drag acting on the cube consists of two forces; one is pressure drag due to a pressure difference between the front and the rear surface of the cube, and the other is viscous drag due to the surface shear stress acting on the upper surface and the two side surfaces. Of the two, however, we take up only the former in the present investigation. It may be considered that the upper surface and the side surfaces are exposed almost entirely to low velocity reverse flow caused by separation of flow at the top edge of the upper surface and at the front edges of the side surfaces. In this case the contribution of the viscous drag to the total drag can safely be neglected.

Measurements of the pressure distributions on the cubes were made for the conditions shown in Table 1(*a*). The values of the drag coefficients, C_D, were obtained by mean of the equation given by

$$C_D=\int_0^1\int_{-0.5}^{0.5}(C_{pf}-C_{pb})\,d\left(\frac{z}{h}\right)d\left(\frac{y}{h}\right) \tag{8}$$

where C_{pf} and C_{pb} are the pressure coefficients on the upstream and downstream surfaces of the cube defined by $C_{pf}=(p_f-p_0)/(1/2\rho U_0^2)$ and $C_{pb}=(p_b-p_0)/(1/2\rho U_0^2)$, respectively.

Figure 5 shows the relation between C_D and h/δ with u_τ/U_0 as a parameter. It is apparent that the drag coefficient C_D depends on u_τ/U_0, except possibly in the range $h/\delta>1.0$, in accordance with the general correlation

$$C_D=f_3\left(\frac{u_\tau}{U_0},\frac{h}{\delta}\right)$$

given before as equation (5). It can be still seen that the drag coefficient C_D plotted on a logarithmic scale can well be expressed as a linear function of $\log_{10}(h/\delta)$ with a slope which is different depending on the value of u_τ/U_0 in the range $h/\delta\leqq 1.0$. In the range of h/δ much larger than 1.0, the drag coefficient is no longer dependent on the parameter u_τ/U_0 but depends only on h/δ. Accordingly, the log-log plot between C_D and h/δ shows that the variation of the drag coefficient can be expressed well by

$$C_D=A_1\left(\frac{h}{\delta}\right)^n \tag{9}$$

where A_1 and n are functions of u_τ/U_0 alone.

On the other hand, Fig. 6 shows the relation between C_D and h/δ for a two-dimensional normal plate and square cylinder measured by Arie et al. [2], [8]. As will be seen in this figure, the drag coefficients for these two bluff bodies be expressed as a linear function of $\log_{10}(h/\delta)$ in the range of h/δ less than about 1.3 or 1.4. Arie et al. [2], [8] found that the drag coefficient of the two-dimensional bluff bodies can be expressed by the following equation:

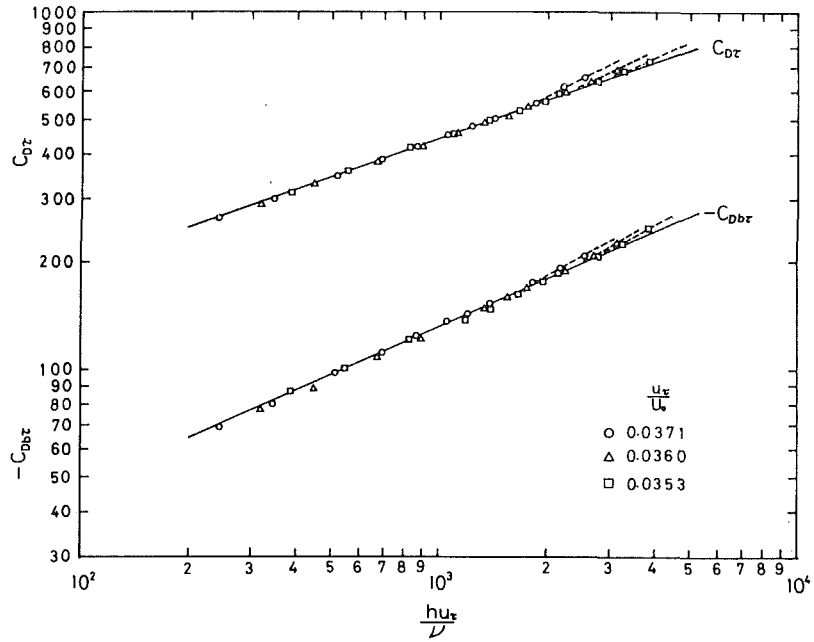

Fig. 7 Relation between $C_{D\tau}$ and hu_τ/ν for a cube. The uncertainty in the ordinate is ± 0.02 and that in the abscissa is ± 0.01. Lines are the best-fit line obtained by the least-square averaging of the data.

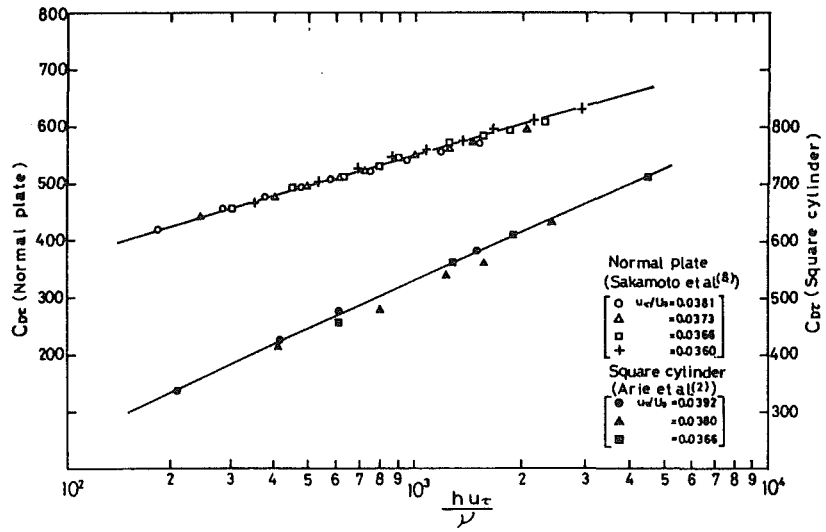

Fig. 8 Relation between $C_{D\tau}$ and hu_τ/ν for a two-dimensional normal plate and square cylinder. For further information, see the caption of Fig. 7.

$$C_D = A_2 \log_{10}\left(\frac{h}{\delta}\right) + B_2 \tag{10}$$

where A_2 and B_2 are functions of u_τ/U_0 alone.

As a result, the variations of the drag coefficient C_D can be written in a logarithmic law in terms of h/δ for a two-dimensional bluff body and in a power law with exponent n of h/δ for a three-dimensional bluff body, respectively. The difference of variations between the drag coefficients of two- and three-dimensional bluff bodies may perhaps be based on the different feature of the approaching velocity field caused by the bluff bodies themselves.

The drag coefficient $C_{D\tau}$ defined by $C_{D\tau} = D/(1/2\rho u_\tau^2 h^2)$ is plotted in Fig. 7 in log-log form based on equation (6). Figure 7 clearly shows that $C_{D\tau}$ is uniquely related to hu_τ/ν at least in the range $h/\delta \leqq 1.0$. In other words, the parameter u_τ/U_0 has no influence on the drag coefficient of the cube in this range. This simply implies that the free-stream velocity U_0 has no direct influence on the drag of the cube, so that

$$C_{D\tau} = f_5\left(\frac{hu_\tau}{\nu}\right) \tag{11}$$

Therefore, the drag coefficient of the cube in the range $h/\delta \leqq 1.0$ can empirically be expressed by a power law with exponent $n = 0.351$ by the following equation:

$$C_{D\tau} = 39.2\left(\frac{hu_\tau}{\nu}\right)^{0.351} \quad (h/\delta \leqq 1.0) \tag{12}$$

The solid line indicated in Fig. 7 is the best-fit line using the least-squares-method for the experimental data obtained.

Arie et al. [2], [8] measured in detail the drag coefficients $C_{D\tau}$ of the two-dimensional normal plates and rectangular cylinders with various width-to-height ratios immersed in an equilibrium turbulent boundary layer with zero-pressure

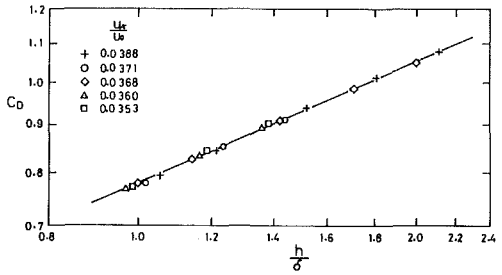

Fig. 9 Variation of C_D with h/δ for a cube in the range $h/\delta > 1.0$. For further information, see the caption of Fig. 5.

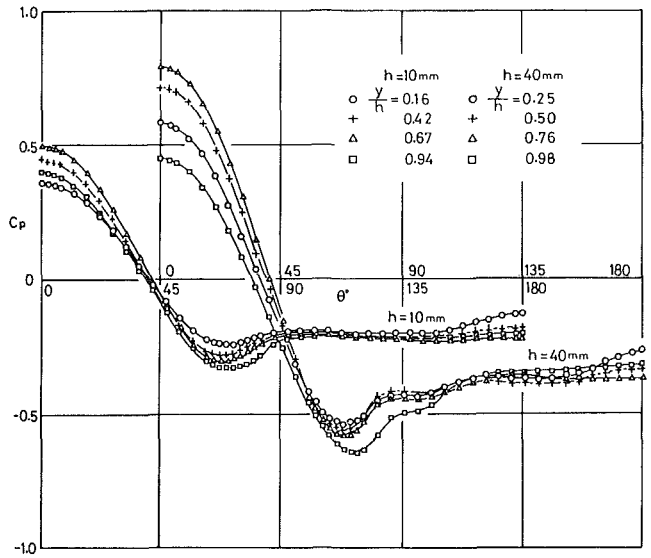

Fig. 10 Pressure distributions around a vertical circular cylinder. The uncertainty in the ordinate is ±0.01 and that in the abscissa is ±0.5 deg. Lines for visual aid only.

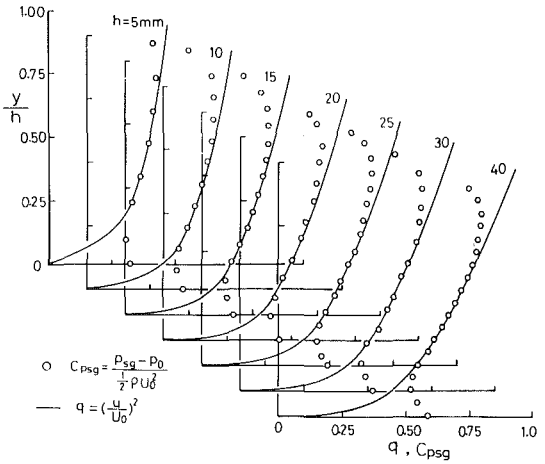

Fig. 11 Comparison of pressure distributions on the front centerline of a vertical circular cylinder with the dynamic pressure in the undisturbed turbulent boundary layer. For further information, see the caption of Fig. 4.

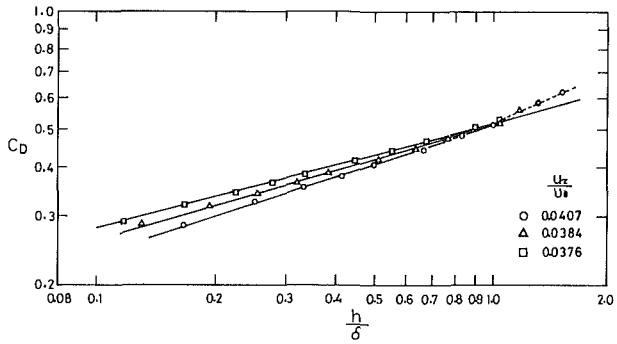

Fig. 12 Relation between C_D and h/δ for a vertical circular cylinder. For further information, see the caption of Fig. 5.

gradient. They demonstrated that $C_{D\tau}$ could be written by the logarithmic law in terms of hu_τ/ν. The results for the normal plate and a rectangular cylinder of the width-to-height ratio $b/h=1.0$, i.e., the square cylinder are shown in Fig. 8 on semi-log plot. It is noticeable that the correlation obtained for drag coefficient of three-dimensional bluff body, i.e., the power law with exponent n of hu_τ/ν, is different from that of the two-dimensional bluff bodies.

Figure 7 also shows the contribution of the base pressure acting on the rear surface to the drag coefficient. $C_{Db\tau}$ is defined as

$$C_{Db\tau}=\int_0^1\int_{-0.5}^{0.5}\frac{p_b-p_0}{\frac{1}{2}\rho u_\tau^2}\,d\left(\frac{z}{h}\right)d\left(\frac{y}{h}\right) \tag{13}$$

which is always negative in value. $C_{Db\tau}$ also follows a power law with exponent $n=0.446$ in the range of h/δ less than about 1.0 as follows:

$$-C_{Db\tau}=6.07\left(\frac{hu_\tau}{\nu}\right)^{0.446}\quad(h/\delta\leqq 1.0) \tag{14}$$

If one designates the contribution of the pressure on the front surface to the total drag coefficient $C_{D\tau}$ as $C_{Df\tau}$,

$$C_{Df\tau}=C_{D\tau}+C_{Db\tau} \tag{15}$$

this equation provides a mean to evaluate $C_{Df\tau}$.

For a zero pressure-gradient boundary layer, the correlation given by equation (12) permits the prediction of the pressure drag of the cube in terms of the wall shear stress of an otherwise undisturbed boundary layer at the location of the cube, provided the relative height of the cube is in the range $h/\delta\leqq 1.0$. If h/δ becomes much larger than 1.0, the drag coefficient will not properly be expressed by equation (12). The data plotted in Fig. 5 do indicate strongly that the drag coefficient of the cube is independent of the parameter u_τ/U_0 and is simply related to h/δ alone. But, it is difficult to find a functional relationship betwen C_D and h/δ from the present results because the data plotted in Fig. 5 do not cover a sufficiently wide range.

For the purpose of supplementing data for a wide range, additional results of measurements are given in Fig. 9. The trend in this figure clearly shows that C_D is uniquely related to h/δ in the present range of h/δ less than about 2.2, so that the drag coefficient can be expressed as

$$C_D=0.78\left(\frac{h}{\delta}\right)^{0.437}\quad(1.0<h/\delta<2.2) \tag{16}$$

5.3 Drag Force Acting on the Vertical Circular Cylinder. Measurements of the pressure distributions on the vertical circular cylinders were made for the conditions shown in Table 1(*b*). The typical pressure distributions around the cylinder at various heights of the cylinders for the case of $U_0=20$ m/s are given in Fig. 10. The curves in this figure were obtained by plotting the measured values of $(p-p_0)/(1/2\rho U_0^2)$ against the angle θ at several heights from the bottom of the cylinder.

A comparison of the pressure distributions along the centerline of the front face of the cylinder and the dynamic pressure in the undisturbed boundary layer at respective height are given in Fig. 11. There is a good agreement between the two in the range $0.2<y/h<0.7$. Accordingly, the flow direction in the boundary approaching the cylinder, which is

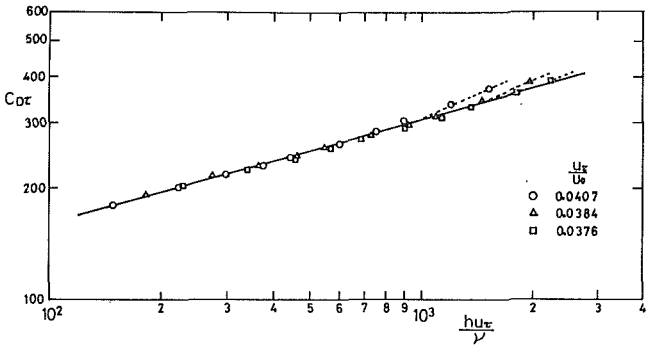

Fig. 13 Relation between C_{D_τ} and hu_τ/ν for a vertical circular cylinder. For further information, see the caption of Fig. 7.

parallel to the plane boundary, may be judged to be well conserved in the neighborhood of the centerline of the front face in this range. However, a horseshoe vortex is dominant in the range of y/h less than about 0.2, and the negative suction pressure at the top of the cylinder prevails in the range of y/h larger than about 0.7.

The drag coefficient of the cylinder integrated from the measurements of the pressure on the surface is given in Fig. 12. The drag coefficient is defined as

$$C_D = \int_0^1 \int_0^\pi \frac{p - p_0}{\frac{1}{2}\rho U_0^2} \cos\theta d\theta d\left(\frac{y}{h}\right) \tag{17}$$

It can be seen in this figure that the results exhibit the same features as those of the cube shown in Fig. 5, i.e., the drag coefficient of the cylinders is also dependent on u_τ/U_0 within the range of h/δ which is less than about 1.0. The drag coefficient plotted on a log-log sheet shows a linear trend against the height in this range, the slope of the straight lines being different for each value of u_τ/U_0. It is worth nothing that the drag coefficients of both the cubes and the cylinders tested in the present study are dependent on the parameter u_τ/U_0 in the same range of h/δ. The drag coefficient C_{D_τ} of the cylinders defined by $C_{D_\tau} = D/(1/2\rho u_\tau^2 h^2)$ is plotted in Fig. 13 in the form given by equation (6). It can clearly be seen that a relationship between C_{D_τ} and hu_τ/ν, which is similar in form to that of the cube mentioned in Section 5.2, may be applied in the range $h/\delta \leqq 1.0$. The drag coefficient C_{D_τ} of the cylinders can be expressed by

$$C_{D_\tau} = 44.8\left(\frac{hu_\tau}{\nu}\right)^{0.279} \quad (h/\delta \leqq 1.0) \tag{18}$$

If h/δ becomes much larger than 1.0, the drag coefficient will not be expressed by equation(18) and it may be expressed in a different form. Probably, the drag coefficient of the cylinders for $h/\delta > 1.0$ is independent of the parameter u_τ/U_0 and is uniquely related to h/δ in much the similar way as the case of the cubes which are shown in Fig. 9. The determination of such a relationship is left for future study, since the data in Fig. 12 are not sufficient in their coverage.

6 Concluding Remarks

The present paper has described an experimental investigation on the form drag of the three-dimensional bluff bodies attached to a long plane boundary along which a turbulent boundary layer is fully developed. The bluff bodies selected for measurement were a cube and a vertical circular cylinder which may be considered as typical examples of three-dimensional bluff bodies. Measurements of the pressure distributions were carried out to obtain the drag forces acting on these bluff bodies by systematically changing both the body height h and the characteristics of the smooth-wall boundary layer in which they were immersed. The primary results of these investigations will be summarized as follows:

(1) The pressure distributions along the centerline of the front face of each bluff body may be expressed by a single curve irrespective of both the body height and the boundary layer characteristics. Further, the pressure distributions along the centerline of the front face show a good agreement with the dynamic pressure in an undisturbed boundary layer at the location of the bluff bodies, except in the two distinct ranges of y/h which are less than about 0.2 where the flow is influenced by the horseshoe vortex and larger than about 0.7 where the prevailing flow is influenced by the suction pressure along the top surface of the bluff body.

(2) The pressure drag of these bluff bodies was experimentally correlated with the thickness and wall shear stress of the boundary layer at the location of the bodies which would be measured if they were absent. It was found that the drag coefficient in the form $\log_{10} C_D$ can be expressed as a linear function of $\log_{10}(h/\delta)$ with the gradient depending on the parameter u_τ/U_0 in the range $h/\delta \leqq 1.0$. Further, the drag coefficient of these bluff bodies in this range as defined by $C_{D_\tau} = D/(1/2\rho u_\tau^2 h^2)$ was found to be expressed by a power law formula.

(3) If h/δ becomes much larger than 1.0, the drag coefficient C_D is independent of the parameter u_τ/U_0 and uniquely related to h/δ. A functional relationship between C_D and h/δ is found for the case of the cubes. However, it is difficult to find a similar functional relationship between C_D and h/δ from the present results because the data is not sufficient for the vertical circular cylinders.

References

1 Good, M. C., and Joubert, P. N., "The Form Drag of Two-dimensional Bluff Plates Immersed in Turbulent Boundary Layers," *Journal of Fluid Mechanics*, Vol. 31, Part 3, 1968, pp. 547-582.

2 Arie, M., Kiya, M., Tanuma, H., and Kanayama, Y., "Flow over Rectangular Cylinders Immersed in a Turbulent Boundary Layer (Part 1)," *Bulletin of the JSME*, Vol. 18, No. 125, 1975, pp. 1260-1268.

3 Sakamoto, H., Moriya, M., and Arie, M., "A Study on the Flow around Bluff Bodies Immersed in Turbulent Boundary Layers (Part 2)," *Bulletin of the JSME*, Vol. 20, No. 139, 1977, pp. 71-78.

4 Raju, R. K. G., Loeser, J., and Plate, E. J., "Velocity Profiles and Fence Drag for a Turbulent Boundary Layer Along Smooth and Rough Flat Plates," *Journal of Fluid Mechanics*, Vol. 76, Part 2, 1976, pp. 383-399.

5 Coles, D., "The Law of the Wake in the Turbulent Boundary Layer," *Journal of Fluid Mechanics*, Vol. 1, 1956, pp. 191-226.

6 Klebanoff, P. S., and Diehl, Z. W., "Some Features of Artificially Thickened Fully Developed Turbulent Boundary Layer with Zero Pressure Gradient," NACA TR, No. 1110, 1952.

7 Arie, M., Kiya, M., Tanuma, H., Kosugi, M., and Takaoka, K., "Flow over Rectangular Cylinders Immersed in a Turbulent Boundary Layer (Part 2)," *Bulletin of the JSME*, Vol. 18, No. 125, 1975, pp. 1269-1276.

8 Sakamoto, H., Moriya, M., and Arie, M., "A Study on the Flow Around Bluff Bodies Immersed in Turbulent Boundary Layers (Part 1)," *Bulletin of the JSME*, Vol. 18, No. 124, 1975, pp. 1126-1133.

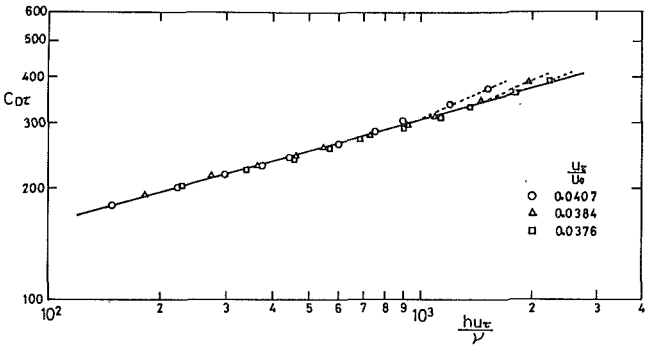

Fig. 13 Relation between C_{D_τ} and hu_τ/ν for a vertical circular cylinder. For further information, see the caption of Fig. 7.

parallel to the plane boundary, may be judged to be well conserved in the neighborhood of the centerline of the front face in this range. However, a horseshoe vortex is dominant in the range of y/h less than about 0.2, and the negative suction pressure at the top of the cylinder prevails in the range of y/h larger than about 0.7.

The drag coefficient of the cylinder integrated from the measurements of the pressure on the surface is given in Fig. 12. The drag coefficient is defined as

$$C_D = \int_0^1 \int_0^\pi \frac{p - p_0}{\frac{1}{2}\rho U_0^2} \cos\theta d\theta d\left(\frac{y}{h}\right) \tag{17}$$

It can be seen in this figure that the results exhibit the same features as those of the cube shown in Fig. 5, i.e., the drag coefficient of the cylinders is also dependent on u_τ/U_0 within the range of h/δ which is less than about 1.0. The drag coefficient plotted on a log-log sheet shows a linear trend against the height in this range, the slope of the straight lines being different for each value of u_τ/U_0. It is worth nothing that the drag coefficients of both the cubes and the cylinders tested in the present study are dependent on the parameter u_τ/U_0 in the same range of h/δ. The drag coefficient C_{D_τ} of the cylinders defined by $C_{D_\tau} = D/(1/2\rho u_\tau^2 h^2)$ is plotted in Fig. 13 in the form given by equation (6). It can clearly be seen that a relationship between C_{D_τ} and hu_τ/ν, which is similar in form to that of the cube mentioned in Section 5.2, may be applied in the range $h/\delta \leqq 1.0$. The drag coefficient C_{D_τ} of the cylinders can be expressed by

$$C_{D_\tau} = 44.8\left(\frac{hu_\tau}{\nu}\right)^{0.279} \quad (h/\delta \leqq 1.0) \tag{18}$$

If h/δ becomes much larger than 1.0, the drag coefficient will not be expressed by equation(18) and it may be expressed in a different form. Probably, the drag coefficient of the cylinders for $h/\delta > 1.0$ is independent of the parameter u_τ/U_0 and is uniquely related to h/δ in much the similar way as the case of the cubes which are shown in Fig. 9. The determination of such a relationship is left for future study, since the data in Fig. 12 are not sufficient in their coverage.

6 Concluding Remarks

The present paper has described an experimental investigation on the form drag of the three-dimensional bluff bodies attached to a long plane boundary along which a turbulent boundary layer is fully developed. The bluff bodies selected for measurement were a cube and a vertical circular cylinder which may be considered as typical examples of three-dimensional bluff bodies. Measurements of the pressure distributions were carried out to obtain the drag forces acting on these bluff bodies by systematically changing both the body height h and the characteristics of the smooth-wall boundary layer in which they were immersed. The primary results of these investigations will be summarized as follows:

(1) The pressure distributions along the centerline of the front face of each bluff body may be expressed by a single curve irrespective of both the body height and the boundary layer characteristics. Further, the pressure distributions along the centerline of the front face show a good agreement with the dynamic pressure in an undisturbed boundary layer at the location of the bluff bodies, except in the two distinct ranges of y/h which are less than about 0.2 where the flow is influenced by the horseshoe vortex and larger than about 0.7 where the prevailing flow is influenced by the suction pressure along the top surface of the bluff body.

(2) The pressure drag of these bluff bodies was experimentally correlated with the thickness and wall shear stress of the boundary layer at the location of the bodies which would be measured if they were absent. It was found that the drag coefficient in the form $\log_{10} C_D$ can be expressed as a linear function of $\log_{10}(h/\delta)$ with the gradient depending on the parameter u_τ/U_0 in the range $h/\delta \leqq 1.0$. Further, the drag coefficient of these bluff bodies in this range as defined by $C_{D_\tau} = D/(1/2\rho u_\tau^2 h^2)$ was found to be expressed by a power law formula.

(3) If h/δ becomes much larger than 1.0, the drag coefficient C_D is independent of the parameter u_τ/U_0 and uniquely related to h/δ. A functional relationship between C_D and h/δ is found for the case of the cubes. However, it is difficult to find a similar functional relationship between C_D and h/δ from the present results because the data is not sufficient for the vertical circular cylinders.

References

1 Good, M. C., and Joubert, P. N., "The Form Drag of Two-dimensional Bluff Plates Immersed in Turbulent Boundary Layers," *Journal of Fluid Mechanics*, Vol. 31, Part 3, 1968, pp. 547-582.

2 Arie, M., Kiya, M., Tanuma, H., and Kanayama, Y., "Flow over Rectangular Cylinders Immersed in a Turbulent Boundary Layer (Part 1)," *Bulletin of the JSME*, Vol. 18, No. 125, 1975, pp. 1260-1268.

3 Sakamoto, H., Moriya, M., and Arie, M., "A Study on the Flow around Bluff Bodies Immersed in Turbulent Boundary Layers (Part 2)," *Bulletin of the JSME*, Vol. 20, No. 139, 1977, pp. 71-78.

4 Raju, R. K. G., Loeser, J., and Plate, E. J., "Velocity Profiles and Fence Drag for a Turbulent Boundary Layer Along Smooth and Rough Flat Plates," *Journal of Fluid Mechanics*, Vol. 76, Part 2, 1976, pp. 383-399.

5 Coles, D., "The Law of the Wake in the Turbulent Boundary Layer," *Journal of Fluid Mechanics*, Vol. 1, 1956, pp. 191-226.

6 Klebanoff, P. S., and Diehl, Z. W., "Some Features of Artificially Thickened Fully Developed Turbulent Boundary Layer with Zero Pressure Gradient," NACA TR, No. 1110, 1952.

7 Arie, M., Kiya, M., Tanuma, H., Kosugi, M., and Takaoka, K., "Flow over Rectangular Cylinders Immersed in a Turbulent Boundary Layer (Part 2)," *Bulletin of the JSME*, Vol. 18, No. 125, 1975, pp. 1269-1276.

8 Sakamoto, H., Moriya, M., and Arie, M., "A Study on the Flow Around Bluff Bodies Immersed in Turbulent Boundary Layers (Part 1)," *Bulletin of the JSME*, Vol. 18, No. 124, 1975, pp. 1126-1133.

DISCUSSION

E. Plate[1]

The authors of the above-mentioned paper are to be congratulated on the excellent experimental data which they have obtained. The extensive experimentation took a great deal of patience and a long term program. The results are a useful addition to the still rather limited literature on the resistance of three-dimensional bodies immersed in turbulent boundary layers. In addition, the writer believes that the study is a valuable contribution to the theory for modelling of wind forces on structures.

Present technique of wind tunnel modelling consists of establishing a boundary layer along the wind tunnel floor with a distribution of mean velocity obeying a power law with an

exponent which is the same in model and prototype (for example Plate, 2). It is assumed that under this condition the nondimensional forces, as expressed by the drag and lift coefficients, are the same in model and prototype, provided the Reynolds number based on the building height exceeds in the model a value of about 10^4, and provided that the corners of the building are sharp-edged. This modelling law is independent of the boundary layer height δ, supposedly as long as the structure is embedded in the boundary layer. An alternate way of stating this modelling law is to say that only the parameters of the well-known "inner law," or "law of the wall" of the velocity distribution are important for modelling purposes, a statement which can be expressed differently as saying that the ratio of h/z_0 is the same, where h is the building height and z_0 is the roughness height, which for a smooth wall is $z_0 \sim \nu/u$. The argument is completed by assuming that a unique relationship exists between the exponent of the power law and a suitably dimensionless ratio z_0/L where L is a characteristic length of the rough boundary.

The question is unresolved of how thick δ has to be in order to obtain independence of h/δ. The disturbing possibility exists that this is valid only over the height of the validity of the "inner law" of the velocity distribution, which is only about 0, 15 δ and thus makes it very difficult to model high buildings at a reasonable scale. For the case of a fence Ranga Raju et al. [4] have shown that inner law scaling is valid up to values of $h/\delta \approx 1$, but experiments of Castro and Robins (1) have revealed a more complex relationship between pressure distribution and approach velocity profile. It is therefore most gratifying that the excellent results of the authors establish firmly that at least for the drag coefficient of cubical bodies in smooth surface boundary layers "inner law" scaling is valid also up to $h/\delta \approx 1$ as is evident in equation (12), and in Fig. 7. The writer would be most interested in hearing if the authors found this scaling confirmed also for rough boundaries.

Additional References

1 Castro, J. P., and Robins, A. G., "The Flow Around a Surface-Mounted Cube in Uniform and Turbulent Streams," *J. of Fluid Mechs.*, Vol. 79, Part 2, pp. 307–335.

2 Plate, E. J., *Engineering Meteorology*, Elsevier Publishing Company, Amsterdam, The Netherlands, 1982.

Authors' Closure

It is within only about 15 percent at most of δ, the thickness of the boundary layer, that the inner law holds in the distribution of velocity in a turbulent boundary layer developing along a plane wall. However, C_{D_τ}, the drag coefficient, of the two- or the three-dimensional body immersed in a turbulent boundary layer is represented, in a range up to about $h/\delta \approx 1.0$, by the same form of hu_τ/ν as the case in which the distribution of velocity of an inner layer is represented by the form of hu_τ/ν. The reason for it remains not so clear except that the result from the following is considered to provide a support that the coefficient of drag of a body measured by the present experiment by a function of hu_τ/ν in a range up to about $h/\delta \approx 1.0$. Namely, attached Fig. 1 shows the coefficient, $\tilde{q}_h = \tilde{q}/(\frac{1}{2}\rho u_\tau^2)$, of the mean dynamic pressure given by the following and made dimensionless by $\frac{1}{2}\rho u_\tau^2$

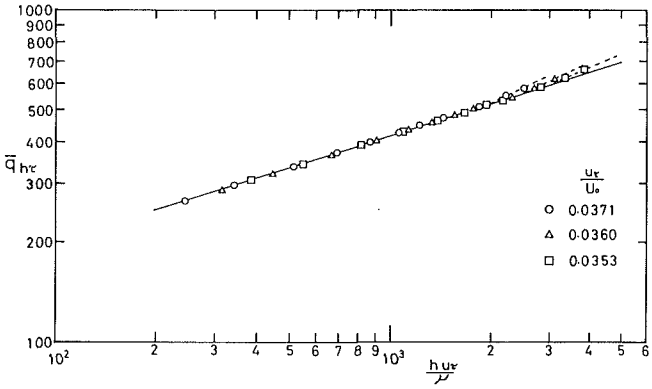

Fig. 1

$$\tilde{q} = \frac{1}{h}\int_0^h \frac{1}{2}\rho u^2 dy$$

similarly to the case of C_{D_τ}, in a range $y = 0 \sim h$, in an undisturbed boundary layer at the location of a body which is looked on as governing the drag of the body; similarly to C_{D_τ} independently of u_τ/Uo, in a range up to $h/\delta \approx 1.0$, $\tilde{q}_{h_T}$ is represented by a function of only hu_τ/ν.

Measurements have not been made of drag of a body on a rough wall, but $\tilde{q}_{h_\tau}$, the coefficient of mean dynamic pressure, in a boundary layer developing on a rough wall is also considered to be represented by a function of hu_τ/ν similarly to the case using a smooth wall. Accordingly, C_{D_τ} of a body on a rough wall is conjectured to be represented also by a function of hu_τ/ν in a rnge up to about $h/\delta \approx 1.0$.

ERRATA

"A Four Hole Pressure Probe For Fluid Flow Measurements in Three Dimensions," by I. C. Shepherd, Journal of Fluids Engineering, Vol. 103, Dec. 1981, pp. 590–594.

Page 594, Second Column

Additional References as follows:

5 Perry, J. H., "Calibration and Comparison of Cobra Probe and Hot Wire Anemometer for Flow Measurements in Turbomachinery," CSIRO Division of Mechanical Engineering, Tech. Rep. No. TR1, 1974, Melbourne, Australia.

6 Raghava, A. K., et al., "A Probe for the Measurement of the Velocity Field," ASME JOURNAL OF FLUIDS ENGINEERING, March, 1979, Vol. 101.

7 Becker, H. A., and Brown, A. P. C., "Response of Pitot Probes in Turbulent Streams," *J. Fluid Mech.*, Vol. 62, Part 1, 1974, pp. 85–114.

8 Dixon, S. L., "Measurement of Flow Direction in a Shear Flow," *J. Phys. E.: Sci. Inst.*, Vol. 11, 1978.

9 Kline, S. J., and McClintock, F. A., "Describing Uncertainties in Single-Sample Experiments," ASME *Mechanical Engineering*, Vol. 75, No. 1, 1953.

Transient Response of Fluid Viscoelastic Lines

E. Rieutord
Professor,
Laboratoire d'Hydraulique et Dynamique des Gaz,
Institut National des Sciences Appliquées de Lyon,
69 621 Villeurbanne, Cédex, France

Basic relations and method of solution are given for laminar transient flows in linear viscoelastic circular fluid transmission lines. Using a numerical method to invert the Laplace-Carson transforms, basic step response plots are given for semi-infinite liquid-lines. The method can be immediately applied to any practical problem with linear or explicitly time dependent boundary conditions. Analytical expressions are given for the behavior at the wave front and for large values of time. Also derived are classical parameters characterizing the frequency response.

Introduction

The transient and frequency responses of a viscous fluid line, including associated problems such as waterhammer, have been treated extensively for the cases of rigid and elastic tube walls. References include the pioneer works of Iberall [1], Nichols [2], Brown [3,4], Zielke [5]; a valuable review on viscous fluid transients is given in a more recent paper of Goodson and Leonard [6]. Studies assuming viscoelastic walls, which can be applied to plastic pipes, blood vessel, etc., are scarce and consider principally waterhammer problems. For the plastic pipes, one of the first investigations, performed in 1958 by Tison [7] on polyethylene pipes showed the "storage effect" due to wall creep. Later Zeller, Talukder, and Lorentz [8,9], studied wave propagation in viscoelastic pipes and gave some experimental results on the attenuation of a pressure wave in PVC[1] and rubber pipes. Simultaneously more general basic equations of unsteady flow in viscoelastic pipes were developed by Blanchard and the author [10]. More recently, this work has been extended [11] and was confirmed by experimental data obtained on polyethylene pipes [12]. As for blood flow, in spite of the fact that the viscoelastic properties of the arterial wall are well known, most authors consider the wall to be elastic. However, some researchers such as Klip [13], Westherhoff and Noordergraff [14] and more recently Flaud, Geiger, Oddou, and Quemada [15,16] attempted to take into account the viscoelasticity of the wall.

The present paper is intended as an extension of the classical work on transient response of viscous fluid transmission lines to the case where the pipe is taken to be viscoelastic.

Formulations

The formulation is based on the following assumptions: the flow is laminar and one-dimensional but with a varying velocity profile; the momentum equation is linearized; the thermodynamical aspects of dissipation are negligible; the boundary conditions are linear or explicitly time dependent.

(a) Elastic Case. With these assumptions and the use of the integral transform $f^*(s) = s\int_0^\infty f(t)\, e^{-ts}dt$ for the time dependent functions $f(t)$, the continuity and momentum equations together with the laws of behavior of the fluid and of the wall lead to the following classical set of equations [3,6],

$$\frac{\partial p^*(x,s)}{\partial x} + Z_s q^*(x,s) = 0 \tag{1}$$

$$\frac{\partial q^*(x,s)}{\partial x} + Y_s p^*(x,s) = 0 \tag{2}$$

in which p and q are pressure and volume flow rate disturbances relative to the initially steady flow, i.e., p and $q \equiv 0$ for $t < 0$.

Also, Z_s and Y_s are the series impedance and the shunt admittance per unit length:

$$Z_s = \frac{\rho s}{\pi R^2} \frac{I_0\left(\sqrt{\frac{sR^2}{\nu}}\right)}{I_2\left(\sqrt{\frac{sR^2}{\nu}}\right)} \tag{3}$$

$$Y_s = \frac{\pi R^2 s}{\rho a^2}\left(1+(\gamma-1)\left(1-\frac{I_2\left(\sqrt{\mathrm{Pr}\frac{sR^2}{\nu}}\right)}{I_0\left(\sqrt{\mathrm{Pr}\frac{sR^2}{\nu}}\right)}\right)\right) \tag{4}$$

where a, corresponds to the speed of propagation of disturbances,

$$a = \frac{1}{\sqrt{\rho\left(\frac{1}{\kappa}+\frac{\zeta D_m}{eE}\right)}} \tag{5}$$

in which ζ is a dimensionless parameter that describes the effect of pipe constraint conditions on the wall deformation [17].

These results are exactly the same as those obtained from the standard Laplace transform $\hat{f}(s)$ since $f^*(s) = s\hat{f}(s)$. However the choice of the s-multiplied Laplace transform,

[1] Polyvinylchlorid.

Contributed by the Fluids Engineering Division for publication in the JOURNAL OF FLUIDS ENGINEERING. Manuscript received by the Fluids Engineering Division, January 30, 1980.

also called Laplace-Carson transform [18], was made, as shown later, to keep the same equation forms in both the elastic and viscoelastic cases.

By introducing the characteristic impedance $Z(s)$ and the propagation operator $\Gamma(s)$ per unit length, such as,

$$Z(s) = \left(\frac{Z_s}{Y_s}\right)^{1/2} \qquad \Gamma(s) = (Z_s Y_s)^{1/2},$$

the solution of simultaneous equations (1), (2) may be written as:

$$p^*(x,s) = A_1(s)e^{-\Gamma(s)x} + A_2(s)e^{\Gamma(s)x} \tag{6}$$

$$q^*(x,s) = \frac{1}{Z(s)}\left(A_1(s)e^{-\Gamma(s)x} - A_2(s)e^{\Gamma(s)x}\right) \tag{7}$$

where $A_1(s)$ and $A_2(s)$ are constants of integration with respect to x. They are to be determined from boundary conditions.

(b) Viscoelastic Case. It is well known that the L.C. transform[2] of the constitutive equation for an isotropic linear viscoelastic material has the same form [19],

$$\sigma_{ij}^* = \lambda^* \epsilon_{kk}^* \delta_{ij} + 2\mu^* \epsilon_{ij}^*$$

as for an elastic material, λ^* and μ^* being the L.C. transforms of the viscoelastic functions that correspond to the λ and μ Lame's coefficients of the elastic case.

This leads to the classical result that the L.C. transform of the solution for a linear viscoelastic problem can be obtained directly from the L.C. transform of the solution for the corresponding linear elastic problem by replacing the elastic moduli λ and μ by the L.C. transform $\lambda^*(s)$ and $\mu^*(s)$ of the relaxation functions $\lambda(t)$ and $\mu(t)$.

For the problems considered here, λ and μ appear only in (5) where ζ is usually expressed [17] through Poisson's ratio $\xi = 0.5\lambda/(\lambda+\mu)$ and where $E = \mu(3\lambda+2\mu)/(\lambda+\mu)$. In the usual cases where ξ can be assumed constant the viscoelasticity of the pipe is characterized only by the relaxation function $E(t)$ that correspond to Young's modulus E and is related to $\lambda(t)$ and $\mu(t)$ through its transform as $E^* = \mu^*(3\lambda^* + 2\mu^*)/(\lambda^* + \mu^*)$.

From this, by replacing E by $E^*(s)$ in (5) and by introducing this new value of a, i.e.,

$$a(s) = \frac{1}{\sqrt{\rho\left(\frac{1}{\kappa} + \frac{\zeta D_m}{e\,E^*(s)}\right)}} \tag{8}$$

into $Z(s)$ and $\Gamma(s)$, we obtain from (6) and (7) the transformed solution for a linear viscoelastic pipe. If instead of $E(t)$, we introduce the creep function $J(t)$ such as $J^*(s) = 1/E^*(s)$, we can write for $a(s)$,

$$a(s) = a_0\left(1 + \frac{\rho a_0^2 \zeta D_m}{e}\left(J^*(s) - J(0)\right)\right)^{-1/2} \tag{9}$$

where

$$a_0 = \frac{1}{\sqrt{\rho\left(\frac{1}{\kappa} + \frac{\zeta D_m}{e}J(0)\right)}} \qquad (a_0 = \lim_{s\to\infty} a(s))$$

We shall see that a_0 corresponds to the speed of propagation of disturbances.

In the particular case where the wall material can be represented by a generalised Kelvin-Voigt model:

$$J(t) = J_0 + \sum_{i=1}^{n} J_i(1 - e^{-t/\tau_i})$$

[2] Abbreviation for Laplace-Carson transform.

Nomenclature

A_1, A_2 = integration constants
$a, a(s)$ = parameters defined by (5) and (8)
a_0 = propagation speed
$C^{-1} f^*(s)$ = inverse Laplace-Carson transform of $f^*(s)$
B_1, B_2 = functions defined by (17) and (18)
C_1, C_2, C_3 = coefficients of the asymptotic development in (17)
D_m = mean diameter of the pipe
e = pipe wall thickness
erfc = complementary error function
E = Young's modulus
$E(t)$ = relaxation function corresponding to E
$i^n \operatorname{erfc} x = \int_x^\infty i^{n-1} \operatorname{erfc} t\, dt$ $\quad (i^0 \operatorname{erfc} = \operatorname{erfc})$
I_0, I_2 = modified Bessel function of 1st kind of order 0 and 2
j = $\sqrt{-1}$
$J(t)$ = creep function
J_0 = $J(0)$ instantaneous compliance
J_i = compliance associated to ith Kelvin-Voigt element
k = $1 + \bar{J}(\infty) - \bar{J}(0)$
p = pressure
p_0 = transmitted pressure step
Pr = Prandtl number
q = volume flow rate
q_0 = transmitted volume flow rate step
R = inner radius of pipe
s = Laplace-Carson variable
t = time
v = phase velocity
x = axial coordinate
Y_s = shunt admittance
Z_0 = $\rho a_0/\pi R^2$
Z_s = series impedance
$Z(s)$ = characteristic impedance
α = $\bar{J}'(0)/2$
β = $(\bar{J}''(0) - J'^2(0)/4)/2$
γ = ratio of specific heat
Γ = propagation operator
δ_{ij} = Kronecker symbol
ϵ_{ij} = component of the strain tensor
ζ = coefficient which is dependent on the pipe constraints
κ = bulk modulus of fluid
λ, μ = Lame's coefficients
ν = kinematic viscosity
ξ = Poisson's ratio
ρ = density
σ_{ij} = component of stress tensor
τ = dimensionless time ($= t\nu/R^2$)
$\tilde{\tau}$ = $\tau - \tau_0$
τ_0 = dimensionless delay time ($= x\nu/R^2 a_0$)
τ_i = relaxation time of the ith Kelvin-Voigt element
Υ = Heaviside unit step function
ω = angular velocity
Ω = dimensionless angular velocity

Superscripts

$-$ = nondimensional value
$*$ = Laplace-Carson transform
$\hat{}$ = Laplace transform
$', ''$ = 1st, 2nd derivative

we obtain for $a(s)$:

$$a(s) = a_0 \left(1 + \frac{\rho\, a_0^2\, \zeta D_m}{e} \sum_{i=1}^{n} \frac{J_i}{1 + s\,\tau_i}\right)^{-1/2} \tag{10}$$

Furthermore, as in the elastic case, the substitution of the imaginary angular frequency $j\omega$ for s gives immediately the classical parameters characterizing the frequency response of any viscoelastic fluid line (see Appendix).

Results and Discussion

For given boundary conditions and with $a(s)$ from (8) in $Z(s)$ and $\Gamma(s)$, relations (6) and (7) provide, after inversion of L.C. transforms, the pressure and volume flow rate solutions for a viscoelastic pipe. To invert the L.C. transforms, we have used a numerical method based on an algorithm developed by F. Veillon [20] to compute an inversion formula proposed by Dubner and Abarth [21].

This procedure can be applied to solve any viscoelastic pipe problem provided the Carson transform of the solution for the corresponding elastic problem is known. However, as the main purpose of this paper is to present a method for the analysis and the calculation of laminar transient flow in viscoelastic pipes, we have studied here only the step response of a semi-infinite line to illustrate the effects of the viscoelasticity.

In order to compare with the classical results obtained by Brown and Nelson [4], we have considered the three following main cases:

1. the pressure (or flow) response downstream p (or q) to an upstream step of pressure p_0 (or flow q_0),
2. the flow response q to a step of pressure p_0,
3. the pressure response p to a step of flow q_0.

Introducing in (6) and (7) the classical dimensionless variables $\tau_0 = x\nu/(a_0 R^2)$, $\bar{s} = s\,R^2/\nu$, $\bar{a} = a/a_0$, $\bar{Z} = Z/Z_0$ and $\bar{\Gamma} = \Gamma\, a_0\, R^2/\nu$ and setting $\mathrm{C}^{-1} f(s)$ the inverse transform of $f(s)$, we obtain the following solutions, function of the dimensionless time $\tau = t\nu/R^2$:

$$\frac{p(\tau)}{p_0}\left(\text{or } \frac{q(\tau)}{q_0}\right) = \mathrm{C}^{-1} e^{-\bar{\Gamma}(\bar{s})\tau_0} \tag{11}$$

$$\frac{p(\tau)}{q_0\, Z_0} = \mathrm{C}^{-1} \bar{Z}(\bar{s})\; e^{-\bar{\Gamma}(\bar{s})\tau_0} \tag{12}$$

$$\frac{Z_0\, q(\tau)}{p_0} = \mathrm{C}^{-1} \frac{e^{-\bar{\Gamma}(\bar{s})\tau_0}}{\bar{Z}(\bar{s})} \tag{13}$$

where $Z_0 = \rho a_0/\pi R^2$. In these relations the viscoelasticity of the pipe is characterized by the dimensionless value of $a(s)$,

$$\bar{a}(\bar{s}) = (1 + \bar{J}^*(\bar{s}) - \bar{J}(0))^{-1/2} \tag{14}$$

in which the relaxation function and its transform are made dimensionless by multiplication by $\rho\, a_0^2\, \zeta\, D_m/e$.

For a generalised Kelvin-Voigt model:

$$\bar{a}(s) = \left(1 + \sum_{i=1}^{n} \frac{\bar{J}_i}{1 + \bar{s}\bar{\tau}_i}\right)^{-1/2} \tag{15}$$

where $\bar{\tau}_i = \tau_i\, \nu/R^2$ is the dimensionless time related to the dimensionless compliance $\bar{J}_i = J_i\, \rho\, a_0^2\, \zeta\, D_m/e$ of the ith element.

With this last model, (11), (12), and (13) give, for a liquid such as water where $\gamma \approx 1$, the results shown in Figs. 1, 2, and 3. For clarity, we have only plotted the curves corresponding to four values of τ_0. Further for the simplicity of the interpretation, we have chosen a case for which $\bar{J}(\tau)$ is represented by one Kelvin-Voigt element $(\bar{J}_1, \bar{\tau}_1)$ associated to an elastic element, i.e., $n = 1$ in (15).

As was to be expected, the delayed deformation of the wall results in an attenuation of the pressure response to a step of flow rate but an increase of the flow rate response to a step of pressure. Also, one can observe, in Figs. 2 and 3, that the difference between elastic and viscoelastic cases is significant only when time $\tau > \tau_0 + \bar{\tau}_1$. This delay with respect to the arrival of the wave front corresponds, roughly, to the relaxation time of the wall material.

Limit Cases

In the case where $\tau \to \tau_0$ or $\tau \to \infty$, we can obtain an explicit formulation illustrating the behavior of the wave front or the evolution of the disturbance for large values of time.

(a) Wave Front ($\tau \to \tau_0$). First, it is easy to see, through the use of Mellin-Fourier inversion integral[3] that, for $\tau < \tau_0$ i.e., $t < x/a_0$, $p(\tau)$ in (11), (12) and $q(\tau)$ in (13) are zero.

Consequently, a_0 is the speed of propagation of disturbances and,

$$\mathrm{C}^{-1} f^*(s) = \frac{1}{2\pi j} \int_{\sigma - j\infty}^{\sigma + j\infty} \frac{f^*(s)}{s} e^{st}\, ds$$

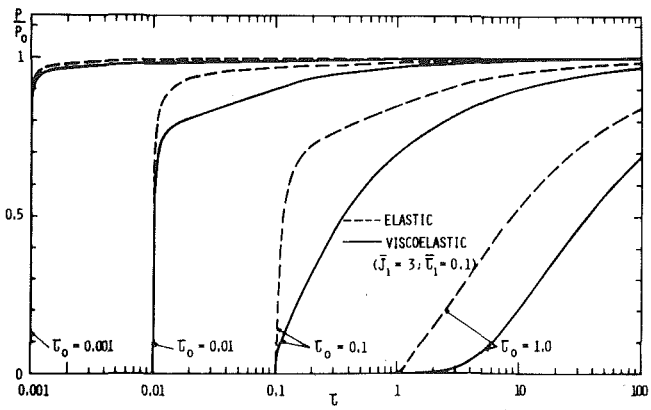

Fig. 1 Pressure (flow) responses to step of pressure (flow)

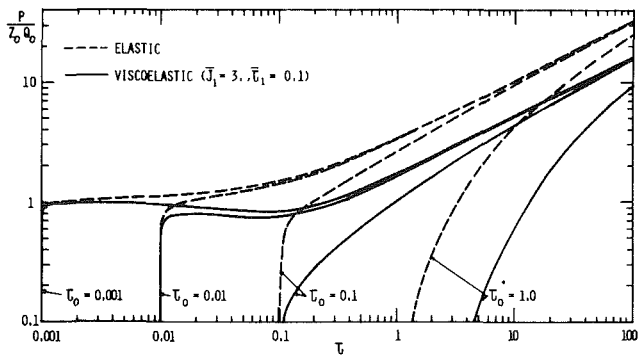

Fig. 2 Pressure responses to step of flow

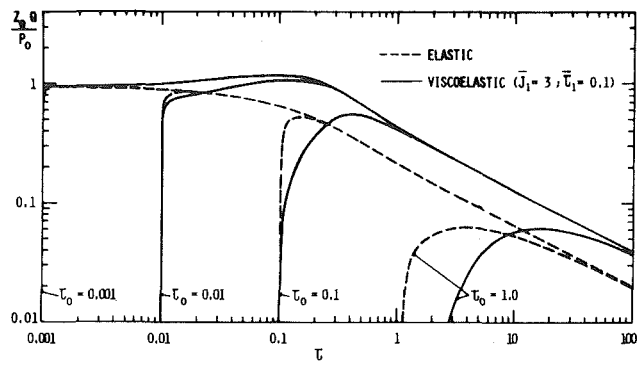

Fig. 3 Flow responses to step of pressure

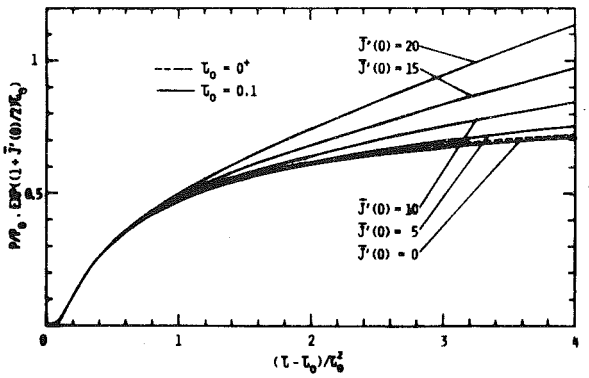

Fig. 4 Front portions of step responses, pressure for pressure or flow for flow

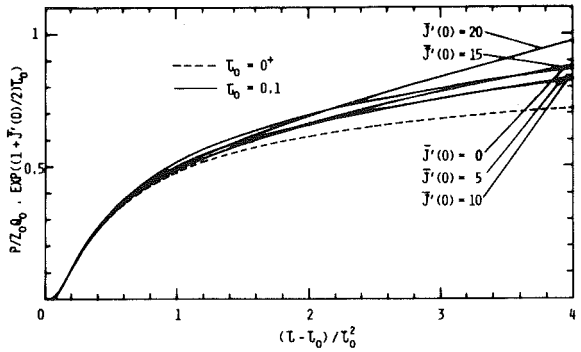

Fig. 5 Front portions of step responses, pressure for flow

$$\lim_{\tau \to \tau_0} p(\tau) \text{ (or } q(\tau)) = \lim_{\bar{s} \to \infty} p^*(\bar{s}) e^{\tau_0 \bar{s}} \text{ (or } q^*(\bar{s}) e^{\tau_0 \bar{s}})$$

From this, through an asymptotic development (see Appendix), we get the following expression valid immediately behind the wave front, i.e., for $\tau - \tau_0 \neq 0$ but positive.

$$\frac{p(\tau)}{p_0} = e^{-(1+\bar{J}'(0)/2)\tau_0} \left\{ B_1 \ \text{erfc}\left(\frac{\tau_0}{2\sqrt{\tau - \tau_0}}\right) + B_2 \ \exp\left(\frac{-\tau_0^2}{\tau - \tau_0}\right) \right\} \tag{16}$$

with

$$\bar{J}(0) = \frac{d\bar{J}(\tau)}{d\tau}\bigg|_{\tau=0}$$

and where B_1 and B_2 are functions of τ_0 and $\tau - \tau_0$ given in Appendix.

In the same way, we obtain two identical forms for $p(\tau)/Z_0 q_0$ and $Z_0\, q(\tau)/p_0$ but with other values for B_1 and B_2 (see also Appendix).

These expressions show that, as in the elastic case, the wave front has the behavior of the erfc function. Expanding in (16) the first exponential factor as follows:

$$e^{-\frac{x}{a_0}\left(\frac{\nu}{R^2} + \frac{\rho\, \zeta a_0^2 D_m}{2e} J'(0)\right)}$$

we can see that the wave front attenuation increases with travelling time x/a_0, kinematic viscosity ν of the fluid and also with the value $J'(0)$ of the so-called memory function $dJ(t)/dt$ at $t = 0$.

For an elastic pipe, we have $J'(0) \equiv 0$ and the damping only comes from the viscosity of the fluid. On the other hand, for an inviscid fluid only the viscoelasticity of the wall takes place, and, in this case, the relation (16) has, in first approximation, the following form as $t \to x/a_0$:

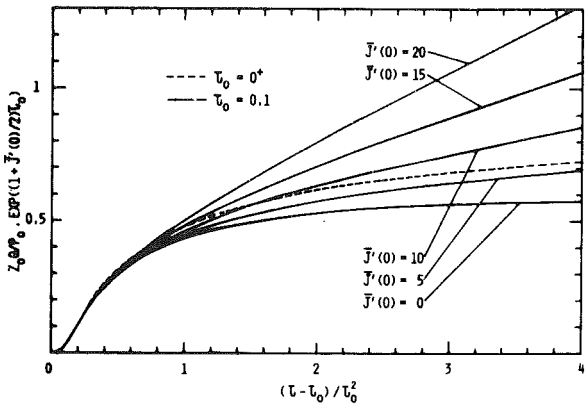

Fig. 6 Front portions of step responses, flow for pressure

$$\frac{p(\tau)}{p_0} \simeq e^{-\frac{\rho\, \zeta a_0 D_m}{2e} J'(0) x} \Upsilon\left(t - \frac{x}{a_0}\right)$$

which expresses the classical exponential step front attenuation [11]. Here $\Upsilon(t - x/a_0)$ is the unit step function of Heaviside.

Figures 4, 5, and 6 give a plot of these expressions for small values of $\tau - \tau_0$. If τ_0 is also very small and $\bar{J}'(0)$ not too large, we have a single curve (erfc $\tau_0/2\sqrt{\tau - \tau_0}$) with the representation chosen, the same as in elastic case [4], for the three functions p/p_0, $p/Z_0 q_0$ and $Z_0 q/p_0$.

(b) Asymptotic Behavior ($\tau \to \infty$). The classical relation,

$$\lim_{\tau \to \infty} f(\tau) = \lim_{s \to 0} f^*(s),$$

applied to equations (11), (12) and (13) enables us to obtain the asymptotic forms given in Appendix. Retaining in each development only the main part, we have

$$\frac{p(\tau)}{p_0} \sim 1 - 2\tau_0 \sqrt{\frac{2(1 + \bar{J}(\infty) - \bar{J}(0))}{\pi\tau}}$$

$$\frac{p(\tau)}{Z_0 q_0} \sim 4\sqrt{\frac{2\tau}{\pi(1 + \bar{J}(\infty) - \bar{J}(0))}} - 8\tau_0$$

$$\frac{Z_0 q(\tau)}{p_0} \sim \frac{1}{2}\sqrt{\frac{1 + \bar{J}(\infty) - \bar{J}(0)}{2\pi\tau}}$$

showing that:

– for a step in pressure (or flow), the pressure (or flow) response (Fig. 1) approaches its limiting value more slowly than in the elastic case, because the equilibrium value $\bar{J}(\infty)$ of the wall compliance is always greater than its instantaneous value $\bar{J}(0)$ (in the elastic case $\bar{J}(\infty) \equiv \bar{J}(0)$)

– for a step in flow the pressure response increases indefinitely as $\sqrt{\tau}$ but, given τ and τ_0, the pressure for a viscoelastic pipe is always lower than for an elastic pipe with a limiting value of the pressure ratio equal to $\sqrt{1 + \bar{J}(\infty) - \bar{J}(0)}$. This leads, in logarithmic coordinates (Fig. 2), to the same slope 0.5 for the asymptotes but with an ordinate difference equal to $0.5 \log(1 + \bar{J}(\infty) - \bar{J}(0))$.

– for a step pressure the flow response decreases to zero as $1/\sqrt{\tau}$. This gives, as shown in Fig. 3, a behavior opposite to that found in the previous case, the slope and the ordinate difference of the asymptotes having the same magnitude but with opposite signs.

It is interesting to note that all these approximations are very close to the exact value over a large range.

Conclusions

Basic equations and step responses in newtonian fluid-filled laminar-flow viscoelastic circular lines have been given. In

most cases, wall viscoelasticity attenuates flow disturbances. However, owing to the creep deformation, flow rate perturbations associated to pressure disturbances are increased.

The use of Laplace-Carson transform gives a method well suited to study laminar transient flows in linear viscoelastic pipes. This was confirmed by some technical applications where we compared the theoretical results given by this method to those given by the method of characteristics in which the fluid viscosity was taken into account through the Zielke procedure [5]. These applications concerned:

– pressure surges induced by valve closure at the end of a polyethylene pipe for which some theoretical and experimental results are published elsewhere [12].

– pressure fluctuations at the exit of a reciprocating-pump connected to a PVC conduit.

In both cases, the two methods gave approximately the same results. For the reciprocating-pump, these results were also in good agreement with those obtained by Meissner [22], in spite of simplifying assumptions made to applied his mathematical model based on the impulse response of pipe.

Compared to the method of characteristics or to others finite-difference methods, this procedure enables one to perform direct calculation for a given parameter at any time and at any distance along the pipe. Further, one can note that most of the studies and results on linear elastic lines can be extended, in a similar manner, to linear viscoelastic lines, the solution being obtained by numerical inversion of Laplace-Carson transforms.

References

1 Iberall, A. S., "Attenuation of Oscillatory Pressures in Instrument Lines," *Journal of Research*, National Bureau of Standards, Vol. 45, July 1950, R.P. 2115.

2 Nichols, N. B., "The Linear Properties of Pneumatic Transmission Lines," submitted to the Instrument Society of American for presentation at the Joint Automatic Control Conference, June, 28-30, 1961, Boulder, Colo.

3 Brown, F. T., "The Transient Response of Fluid Lines," ASME *Journal of Basic Engineering*, Vol. 84, No. 4, Dec. 1962, pp. 547–553.

4 Brown, F. T., and Nelson, S. E., "Step Responses of Liquid Lines with Frequency-Dependent Effects of Viscosity," *Journal of Basic Engineering*, Vol. 87, No. 2, June 1965, pp. 504–510.

5 Zielke, W., "Frequency-Dependent Friction in Transient Pipe Flow," ASME *Journal of Basic Engineering*, Vol. 90, No. 1, Mar. 1968, pp. 109–115.

6 Goodson, R. E., and Leonard, R. G., "A Survey of Modeling Techniques for Fluid Line Transients," ASME *Journal of Basic Engineering*, Vol. 94, June 1972, pp. 474–482.

7 Tison, G., "Le mouvement non permanent succédant à l'ouverture d'une vanne sur une conduite en polyéthylène," Communication No. 3, Becetel, Université de Gand, 1958.

8 Zeller, H., Talukder, N., and Lorentz, J., "Model Studies of Pulsating Flow in Arterial Branches and Wave Propagation in Blood Vessels," AGARD Conf. "Fluids Dynamics of Blood Circulation and Respiratory Flow," Naples, Paper 15, AGARD CP 65, 1970.

9 Lorentz, J., and Zeller, H., "An Analogous Treatment of Waves Propagation in Liquid Filled Elastic Tubes and Gas Filled Rigid Tubes," Int. Conf. on Pressures Surges, Paper B 5, B.H.R.A. Fluid Engineering, Canterbury, England, Sept. 1972.

10 Rieutord, E., and Blanchard, A., "Influence d'un comportement viscoélastique de la conduite dans le phénomène du coup de bélier," Compte-Rendu Académie des Sciences, Paris, tome 274, 1972, pp. 1963–1966.

11 Rieutord, E., and Blanchard, A., "Ecoulement non permanent en conduite viscoelastique - Coup de bélier," *Journal of Hydraulic Research*, Vol. 17, No. 3, 1979, pp. 217–229.

12 Gally, M., Güney, M., and Rieutord, E., "An Investigation of Pressure Transients in Viscoelastic Pipes," ASME JOURNAL OF FLUIDS ENGINEERING, Vol. 101, Dec. 1979, pp. 495–499.

13 Klip, W., Van Loon, P., and Klip, D. A., "Formulas for Phase Velocity and Damping of Longitudinal Waves in Thick-Walled Viscoelastic Tubes," *Journal of Applied Physics*, Vol. 38, No. 9, Aug. 1967, pp. 3745–3755.

14 Westerhof, N., and Noordergraaf, A., "Arterial Viscoelasticity: a Generalized Model. Effect on Input Impedance and Wave Travel in the Systematic Tree," *J. Biomechanics*, Vol. 3, 1970, pp. 357–379.

15 Flaud, P., Geiger, D., Oddou, E., and Quemada, D., "Ecoulements pulsés dans les tuyaux viscoélastiques, applications à l'étude de la circulation sanguine," *Le Journal de Physique*, tome 35, Nov. 1974, pp. 869–882.

16 Flaud, P., Geiger, D., Oddou, E., and Quemada, D., "Experimental Study of Wave Propagation through Viscous Fluid Contained in Viscoelastic Cylindrical Tube under Static Stresses," *Biorheology*, Vol. 12, 1975, pp. 347–354.

17 Wylie, E., and Streeter, *Fluid Transients*, McGraw-Hill, 1978.

18 Ditkine, V., and Proudnikov, A., "Integral transforms and operational calculus," MIR publication, 1978.

19 Mandel, J., "Mécanique des milieux continus," Tome II, Gauthier-Villars, Paris, 1966, pp. 812–813.

20 Veillon, F., "Numerical Inversion of Laplace Transform," Communication of the ACM, Vol. 17, No. 10, Oct. 1974, pp. 587–590 (revised ACM Vol. 2, No. 4, Sept. 1976 and ACM, Vol. 3, No. 1, Mar. 1977).

21 Dubner, H., and Abarth, J., "Numerical Inversion of Laplace Transform and the Finite Fourier Transform," *J. ACM*, Vol. 15, No. 1, Jan. 1968, pp. 115–123.

22 Meissner, E., "Das Impulsantwortverfahren - ein mathematisches Modell zur Berechnung instationärer Strömungsvorgänge in Druckleitungen," Forsch. Ing.-Wes., 43, Nr. 4, 1977, pp. 115–125.

APPENDIX

A. Approximation for the Wave Front ($\tau \to \tau_0$)

The behavior of equations (11), (12), and (13) in the neighborhood of the wave front can be obtained by considering the asymptotic development of:

$$\bar{\Gamma}(\bar{s}) = \frac{\bar{s}}{\bar{a}(\bar{s})}\left(\frac{I_0(\sqrt{\bar{s}})}{I_2(\sqrt{\bar{s}})}\right)^{1/2} \quad \text{and} \quad \bar{Z}(\bar{s}) = \bar{a}(\bar{s})\left(\frac{I_0(\sqrt{\bar{s}})}{I_2(\sqrt{\bar{s}})}\right)^{1/2}$$

$$\text{As } \bar{a} = (1 + \bar{J}^*(\bar{s}) - \bar{J}(0))^{-1/2}$$

and, for large value of $\bar{s}$,

$$\bar{J}^*(\bar{s}) = \bar{J}(0) + \frac{\bar{J}'(0)}{\bar{s}} + \frac{\bar{J}''(0)}{\bar{s}^2} + 0\left(\frac{1}{\bar{s}^3}\right)$$

with

$$\bar{J}''(0) = \left.\frac{d^2\bar{J}(\tau)}{d\tau^2}\right|_{\tau=0}$$

we obtain:

$$\frac{1}{\bar{a}(\bar{s})} = 1 + \frac{\bar{J}'(0)}{2\bar{s}} + \frac{1}{2\bar{s}^2}\left(\bar{J}''(0) - \frac{1}{4}\bar{J}'^2(0)\right) + 0\left(\frac{1}{\bar{s}^3}\right)$$

In the same manner:

$$\left(\frac{I_0(\sqrt{\bar{s}})}{I_2(\sqrt{\bar{s}})}\right)^{1/2} = 1 + \frac{1}{\bar{s}^{1/2}} + \frac{1}{\bar{s}} + \frac{7}{8}\frac{1}{\bar{s}^{3/2}} + \frac{1}{2}\frac{1}{\bar{s}} - \frac{41}{128}\frac{1}{\bar{s}^{5/2}} + 0\left(\frac{1}{\bar{s}^3}\right)$$

Substituting for $\bar{a}$ and $(I_0/I_2)^{1/2}$ their asymptotic development in $\bar{\Gamma}(\bar{s})$ and $\bar{Z}(\bar{s})$, we find an expression for equation (11), (12), and (13) in the following form:

$$f(\bar{s}) = e^{-\bar{s}\tau_0}\, e^{-(1+\bar{J}'(0))\tau_0}\, e^{-\tau_0\sqrt{\bar{s}}}\left\{1 + \frac{C_1}{\bar{s}^{1/2}} + \frac{C_2}{\bar{s}} + \frac{C_3}{\bar{s}^{3/2}} + 0\left(\frac{1}{\bar{s}^2}\right)\right\}$$

where for:

$$(a)\quad f(\bar{s}) = \frac{p(\bar{s})}{p_0}\left(\text{or } \frac{q(\bar{s})}{q_0}\right)$$

$$C_1 = -\left(\frac{7}{8} + \alpha\right)\tau_0$$

$$C_2 = -\left(\frac{1}{2} + \alpha + \beta\right)\tau_0 + \frac{1}{2}\left(\frac{7}{8} + \alpha\right)^2\tau_0^2$$

$$C_3 = \left(\frac{41}{128} - \frac{7}{8}\alpha - \beta\right)\tau_0 + \left(\frac{1}{2} + \alpha + \beta\right)\left(\frac{7}{8} + \alpha\right)\tau_0^2 - \frac{1}{6}\left(\frac{7}{8} + \alpha\right)^3\tau_0^3$$

$$(b)\quad f(\bar{s}) = \frac{p(\bar{s})}{Z_0 q_0}$$

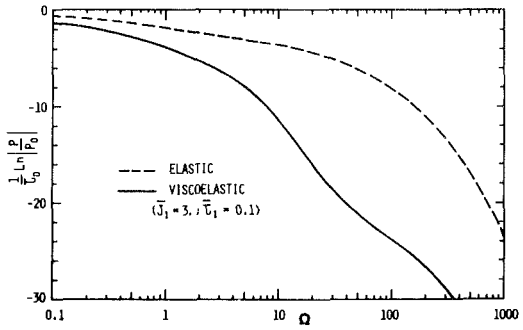

Fig. 7 Attenuation of pressure (or flow) sinusoidal disturbances

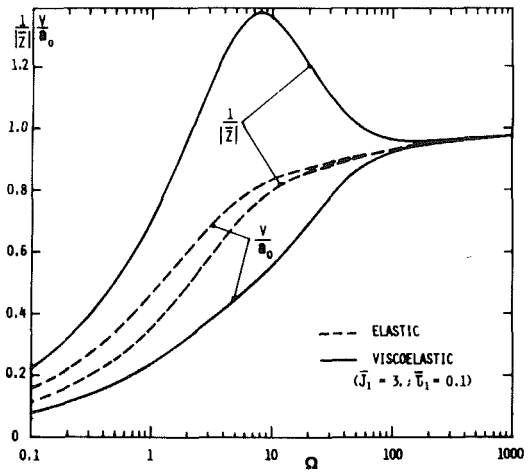

Fig. 8 Phase velocity and magnitude of characteristic admittance

$$C_1 = 1 - \left(\frac{7}{8} + \alpha\right)\tau_0$$

$$C_2 = 1 - \left(\frac{11}{8} + 2\alpha + \beta\right)\tau_0 - \alpha + \frac{1}{2}\left(\frac{7}{8} + \alpha^2\right)^2 \tau_0^2$$

$$C_3 = \frac{7}{8} - \alpha - \left(\frac{135}{128} + 2(\alpha+\beta) - \alpha^2\right)\tau_0 + \frac{1}{2}\left(\frac{7}{8} + \alpha\right)^2 \tau_0^2 + \left(\frac{1}{2} + \alpha + \beta\right)\left(\frac{7}{8} + \alpha\right)\tau_0^2 - \frac{1}{6}\left(\frac{7}{8} + \alpha\right)^3 \tau_0^3$$

(c) $f(\bar{s}) = \dfrac{Z_0 q(\bar{s})}{p_0}$

$$C_1 = -1 - \left(\frac{7}{8} + \alpha\right)\tau_0$$

$$C_2 = \alpha + \left(\frac{11}{8} - \beta\right)\tau_0 + \frac{1}{2}\left(\frac{7}{8} + \alpha\right)^2 \tau_0^2$$

$$C_3 = \frac{1}{8} - \alpha + \left(\frac{105}{128} - \frac{3}{4}\alpha - \alpha^2\right)\tau_0 + \left(\frac{1}{2} + \alpha + \beta\right)\left(\frac{7}{8} + \alpha\right)\tau_0^2 - \frac{1}{2}\left(\frac{7}{8} + \alpha\right)^2 \tau_0^2 - \frac{1}{6}\left(\frac{7}{8} + \alpha\right)^3 \tau_0^3$$

In these expressions, we have put $\alpha = \bar{J}'(0)/2$ and

$$\beta = \frac{1}{2}\left(\bar{J}''(0) - \frac{\bar{J}'^2(0)}{4}\right).$$

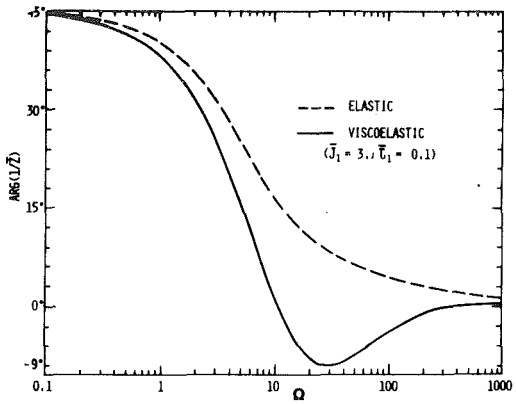

Fig. 9 Phase of characteristic admittance

If we consider a generalized Kelvin-Voigt model where

$$\alpha = \frac{1}{2}\sum_{i=1}^{n}\frac{\bar{J}_i}{\bar{\tau}_i} \quad \text{and} \quad \beta = -\frac{1}{2}\sum_{i=1}^{n}\left(\frac{\bar{J}_i}{\bar{\tau}_i^2} + \frac{\bar{J}_i^2}{4\bar{\tau}_i^2}\right)$$

The inverse transform of $f^*(\bar{s})$ can be written,

$$C^{-1} f^*(\bar{s}) = e^{-(1+\bar{J}'(0)/2)} \sum_{n=0}^{3} C_n (4\tilde{\tau})^{n/2} i^n \operatorname{erfc}\frac{\tau_0}{2\sqrt{\tilde{\tau}}}$$

with $C_0 = 1$ and $\tilde{\tau} = \tau - \tau_0 \qquad (\tau > \tau_0)$

Developing the integral error function i^n erfc, we obtain relation (16) in which B_1 and B_2 have the following values:

$$B_1 = 1 + \tilde{\tau}(C_2 - \tau_0 C_3) + \tau_0(C_2/2 - \tau_0 C_3/6) - C_1\tau_0 \quad (17)$$

$$B_2 = \sqrt{\frac{\tilde{\tau}}{\pi}}\left(2C_1 + \frac{C_3}{3}\tau_0^3 - C_2\tau_0 + \frac{4}{3}C_3\tilde{\tau}\right) \quad (18)$$

B. Approximations for Large Value of τ

The approximation of equations (11), (12), and (13) as $\tau \to \infty$ can be obtained from series development of these expressions for $s \to 0$.

We have:

$$\left(\frac{I_0(\sqrt{\bar{s}})}{I_2(\sqrt{\bar{s}})}\right)^{1/2} = \sqrt{\frac{8}{\bar{s}}}\left(1 + \frac{1}{12}\bar{s} - \frac{1}{16^2}\bar{s}^2 + 0(\bar{s}^3)\right)$$

and

$$\frac{1}{\bar{a}(\bar{s})} = \left(1 + \bar{J}^*(0) - \bar{J}(0) + \bar{J}^{*\prime}(0)\bar{s} + \bar{J}^{*\prime\prime}(0)\frac{\bar{s}^2}{2}\right)^{1/2}$$

where

$$\bar{J}^*(0) = \lim_{\bar{s}\to 0}\bar{J}^*(\bar{s}) = \lim_{\tau\to\infty}\bar{J}(\tau) = \bar{J}(\infty)$$

and

$$\bar{J}^{*\prime}(0) = \frac{d\bar{J}^*(s)}{d\bar{s}}\bigg|_{\bar{s}=0}; \quad \bar{J}^{*\prime\prime}(0) = \frac{d^2\bar{J}^*(\bar{s})}{d\bar{s}^2}\bigg|_{\bar{s}=0}$$

Putting $k = 1 + \bar{J}(\infty) - \bar{J}(0)$, we can write for small values of $\bar{s}$:

$$\frac{1}{\bar{a}(\bar{s})} = \sqrt{k}\left(1 + \frac{1}{2}\frac{\bar{J}^{*\prime}(0)}{k}\bar{s} + \frac{1}{4}\left(\frac{\bar{J}^{*\prime\prime}(0)}{k} - \frac{1}{2}\frac{\bar{J}^{*\prime\prime}(0)^2}{k^2}\right)\bar{s}^2 + 0(\bar{s}^3)\right)$$

In the case of a generalized Kelvin-Voigt model

$$k = 1 + \sum_{i=1}^{n}\bar{J}_i \quad \bar{J}^{*\prime}(0) = -\sum_{i=1}^{n}\bar{J}_i\bar{\tau}_i \quad \text{and} \quad \bar{J}^{*\prime\prime}(0) = 2\sum_{i=1}^{n}\bar{J}_i\bar{\tau}_i^2$$

Substituting for $\bar{a}$ and $(I_0/I_2)^{1/2}$ their development in Taylor's series about $s = 0$, in $\bar{\Gamma}(\bar{s})$ and $\bar{Z}(\bar{s})$, we obtain for equations (11), (12), and (13):

$$\frac{p^*(\bar{s})}{p_0} = \left\{1 - \sqrt{2k}\tau_0\left(\frac{1}{6} + \frac{\bar{J}^{*\prime}(0)}{k}\right)\bar{s}^{3/2} + 0(\bar{s}^{5/2})\right\} e^{-2\tau_0\sqrt{2k\bar{s}}}$$

$$\frac{p^*(\bar{s})}{Z_0 q_0} = \left\{2\sqrt{\frac{2}{ks}} + \left(\frac{1}{6} - \frac{\bar{J}^{*\prime}(0)}{k}\right)\sqrt{\frac{2\bar{s}}{k}} - 4\tau_0\left(\frac{1}{6} + \frac{\bar{J}^{*\prime}(0)}{k}\right)\bar{s} + 0(\bar{s}^{3/2})\right\} e^{-2\tau_0\sqrt{2k\bar{s}}}$$

$$\frac{Z_0 q^*(\bar{s})}{p_0} = \frac{\sqrt{k}}{2}\left\{\sqrt{\frac{\bar{s}}{2}} - \frac{\bar{s}^{3/2}}{2\sqrt{2}}\left(\frac{1}{6} - \frac{\bar{J}^{*\prime}(0)}{k}\right) - \tau_0\sqrt{k}\left(\frac{1}{6} + \frac{\bar{J}^{*\prime}(0)}{k}\right)\bar{s}^2 + 0(\bar{s}^{5/2})\right\} e^{-2\tau_0\sqrt{2k\bar{s}}}$$

and after inversion,

$$\frac{p^*(\tau)}{p_0} \sim \operatorname{erfc}\frac{\sqrt{2k}\ \tau_0}{\sqrt{\tau}} + \left(\frac{1}{6} + \frac{\bar{J}^{*\prime}(0)}{k}\right)\frac{\sqrt{k}\ \tau_0}{\sqrt{2\pi}\ \tau^{3/2}}\left(1 - \frac{4k\ \tau_0^2}{\tau}\right) e^{-\frac{2k\tau_0^2}{\tau}}$$

$$\frac{p(\tau)}{Z_0 q_0} \sim -8\tau_0 \operatorname{erfc}\frac{\sqrt{2k}\ \tau_0}{\sqrt{\tau}} + \sqrt{\frac{2}{\pi k}}\left\{4\sqrt{\tau} + \left(\frac{1}{6} - \frac{\bar{J}^{*\prime}(0)}{k}\right)\frac{1}{\sqrt{\tau}} - \left(\frac{1}{6} + \frac{\bar{J}^{*\prime}(0)}{k}\right)\frac{4k\ \tau_0^2}{\tau^{3/2}}\right\} e^{-\frac{2k\tau_0^2}{\tau}}$$

$$\frac{Z_0 q(\tau)}{p_0} \sim \frac{1}{2}\sqrt{\frac{k}{2\pi\tau}}\left\{1 + \frac{1}{4\tau}\left(\frac{1}{6} - \frac{\bar{J}^{*\prime}(0)}{k}\right)\left(1 - \frac{4\tau_0^2 k}{\tau}\right)\right\} e^{-\frac{2k\tau_0^2}{\tau}}$$

C. Frequency Response

Putting $\bar{s} = j\Omega$ and $\Omega = \omega R^2/\nu$, we obtain immediately the classical parameters, plotted in Figs. 7, 8, 9, and characterizing the frequency response i.e.,:

– attenuation: $\frac{1}{\tau_0}\operatorname{Ln}\left|\frac{p}{p_0}\right| = -\operatorname{Re}\bar{\Gamma}(j\Omega)$,

– phase velocity: $\frac{v}{a_0} = \frac{\Omega}{\operatorname{Im}\ \bar{\Gamma}(j\Omega)}$

– modulus and argument of the characteristic transmittance:

$$\frac{1}{\bar{Z}} = \frac{j\Omega}{\bar{a}^2\bar{\Gamma}(j\Omega)}$$

As expected from values of $\bar{a}(j\Omega)$, the viscoelasticity increase the attenuation and the magnitude of the characteristic admittance, but decreases the phase velocity and the phase of the characteristic admittance.

M. P. Paidoussis
Professor and Chairman.
Mem. ASME

LI. R. Curling
Research Assistant.

J. O. Gagnon
Research Assistant.

Department of Mechanical Engineering,
McGill University,
Montreal, Quebec, H3A 2K6
Canada

Experiments on Fluidelastic Instability of Cylinder Clusters in Axial Flow

This paper presents a summary of the general behavior of cylinder clusters in axial flow and especially of the fluidelastic instabilities which occur at high flow velocities. Experiments were conducted in a water tunnel with three- and four-cylinder clusters, and the behavior was monitored either optically or by instrumenting one of the cylinders with strain gauges. With increasing flow, the amplitude of small random vibrations of the cylinders increased; simultaneously, the natural frequencies, as a group, decreased, which is in good agreement with theory. The cylinders eventually lost stability by buckling (divergence), and at higher flow by flutter. Agreement between theoretical and experimental critical flow velocities for these fluidelastic instabilities has been found to be good.

1 Introduction

The dynamics of a single cylinder in axial flow have been studied fairly extensively, e.g. [1-4], and reviewed, e.g. [5,6]. It was firmly established [3] that the cylinders are subjected to small random vibrations at low flow velocities, induced by random perturbations in the mean flow; the effect of the mean flow itself is to generate flow-induced damping and to lower the natural frequencies of the cylinder. At sufficiently high flow velocities, however, the system loses stability, first by buckling (divergence) and then by flutter [1,2]. It was also shown that in most ordinary industrial systems the cylinders are not sufficiently flexible nor the flow velocities sufficiently high for these instabilities to materialize [6].

In 1975, S.-S. Chen's remarkable work on fluidelastic coupling in the motions of closely-spaced cylinders [7,8] opened the way to the study of the dynamics of *clusters of cylinders*, as opposed to solitary ones, in axial flow. A number of significant theoretical papers on the dynamics of such systems followed, e.g. [9,10], the latter of which studied at some length the stability of the system. It was found that the critical flow velocity was substantially reduced in the case of closely packed cylinder arrays, as compared to a solitary cylinder in unconfined flow.

The theoretical model for hydrodynamic coupling in still fluid was found to be in excellent agreement with experiment [11]. Finally, recent experiments [12] have shown that the stability characteristics of clusters in axial flow are in broad agreement with the theoretical model developed by Paidoussis and Suss [10]. The experiments to be described here complement and extend the work of reference [12], mainly in two ways: (*a*) by pinpointing the onset of instabilities much more accurately, either through optical measurements, or by using instrumented cylinders; (*b*) by studying the frequency content of the flow-induced vibration and determining its functional dependence on flow velocity – from essentially zero flow to the onset of buckling.

The work in this paper is of interest mainly to applied mechanicians. Nevertheless, it is also of interest to design engineers; for, although fluid-elastic instabilities *per se* are perhaps of minor interest to them, as they lie beyond the operating range of most industrial equipment, the development of a sound theory for the dynamics of clusters of cylinders in axial flow certainly *is*. The reason is simple: in the same way that the theory for dynamics of a solitary cylinder in axial flow [1,2] served as the foundation for later work focusing on prediction of low amplitude subcritical vibration, the theory for the dynamics of clusters of cylinders in axial flow will serve an analogous role in its own way. Hence, testing the theory adequately – e.g., by high flow velocity experiments – is ultimately not only of academic but also of practical import.

2 The Experimental Setup

All experiments were conducted in a closed-loop water tunnel, shown diagrammatically in Fig. 1. The water, con-

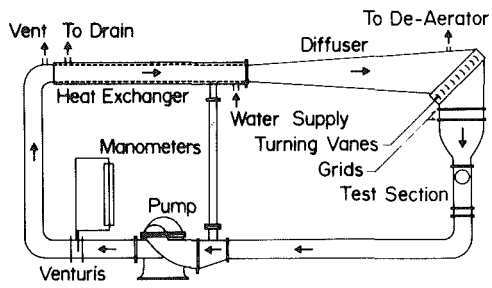

Fig. 1 Schematic of the water tunnel used in the experiments

Contributed by the Fluids Engineering Division and presented at the Joint ASME/ASCE Joint Bioengineering, Fluids Engineering and Applied Mechanics Conference, Boulder, Colo, June 22-24, 1981, of THE AMERICAN SOCIETY OF MECHANICAL ENGINEERS. Manuscript received by the Fluids Engineering Division December 30, 1980.

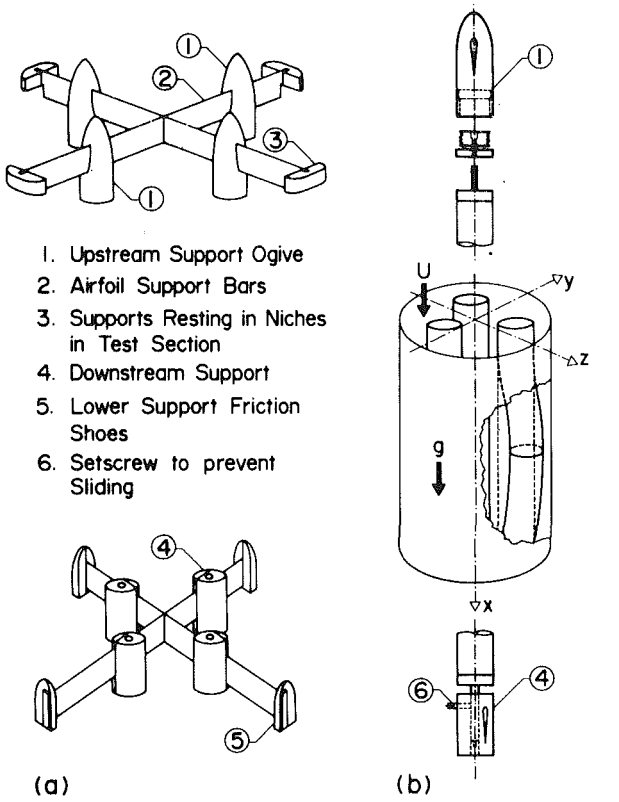

Fig. 2 (*a*) Schematic of the upper and lower supports for mounting a maximum of four cylinders in the water-tunnel test section. (*b*) Schematic of a system of three cylinders in the test section (not to scale), showing an exploded view of the arrangement for a clamped upper end and a clamped (axially sliding or fixed) lower one.

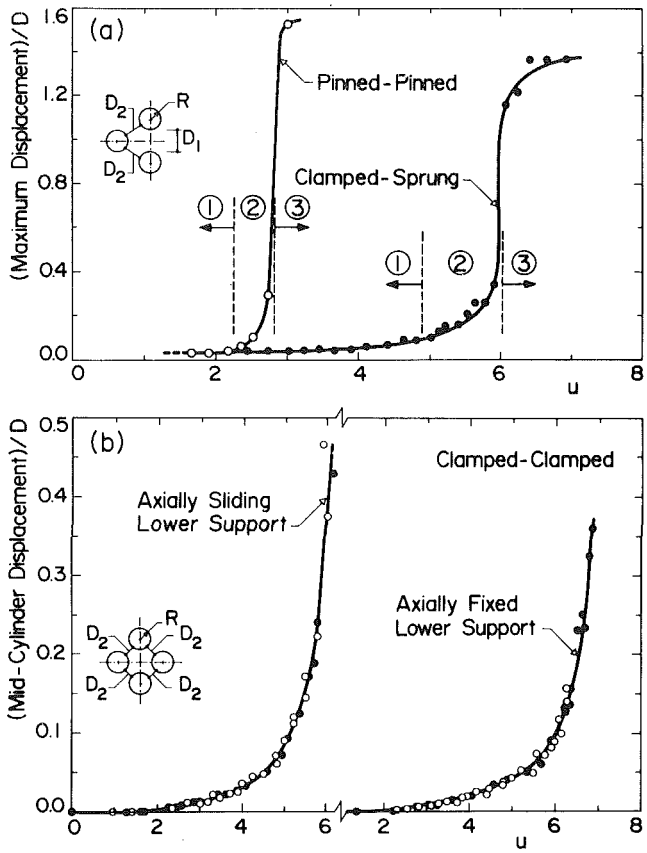

Fig. 3 (*a*) Typical well-defined thresholds of buckling for pinned-pinned and clamped-sprung three-cylinder systems with axially sliding bottom supports, obtained by optical measurements, showing also three of the regimes of dynamical behavior, 1, 2, and 3, encountered with increasing dimensionless flow velocity, u. (Dimensionless parameters: $\beta = 0.467$, $\epsilon = 16.67$, $\gamma = 1.38$, $h = 0.176$, $c_f = 0.016$, $c_b = 0.0$; for the pinned-pinned system: $D_1/R = 1.5$, $D_2/R = 1.25$; for the clamped-sprung system: $D_1/R = 1.5$, $D_2/R = 2.0$.) Maximum uncertainty in dimensionless maximum displacement, $\bar{y}/D$: ±100 percent for $\bar{y}/D <$ 0.1; ±20 percent for larger $\bar{y}/D$; uncertainty in u: ±5 percent. (*b*) Typical transition to buckling of a clamped-clamped four-cylinder instrumented system. (Dimensionless parameters: $\beta = 0.466$, $\epsilon = 20.6$, $\gamma = 1.93$, $h = 0.197$, $c_f = 0.027$, $c_b = 0.20$, $D_2/R = 0.75$, $\kappa = \infty$; for the case of an axially fixed lower support: $\Gamma = 0$, $\Pi = 141$, $\nu = 0.47$.) Uncertainty in $\bar{y}/D$: $< \pm 15$ percent in 86 percent of data points (5/6ths of cases), and $< \pm 20$ percent in 94 percent of data points (19/20ths of cases); uncertainty in u = ±5 percent.

tinuously deaerated, passes through a specially designed bend, equipped with turning vanes, and then through screens ("grids") and a contraction section, all of which ensure that at the vertical test section the flow is uniform and of relatively low turbulence. The heat exchanger maintains the fluid at a constant temperature.

Most experiments were conducted with three- or four-cylinder clusters. The cylinders were specially cast from low-viscosity silicone rubber. The upper and lower supports and the manner of mounting of cylinders between them are shown in Fig. 2. The design was such that, by sliding the supports on the support bars, different cluster configurations could be generated. The four-cylinder configurations tested were always symmetric, while the three-cylinder configurations were mostly asymmetric (see also the insets in Fig. 3). The coordinate system utilized is defined in Fig. 2(*b*). The cylinders were 25.3 mm in diameter, and the inner diameter of the test section 205 mm.

Experiments were conducted with the ends of the cylinders either clamped, as shown in Fig. 2(*b*), or "pinned" with the aid of universal ball joints at the supports. The lower support was so designed as to provide the choice of either a positively fixed end, or one in which axial sliding is permitted. In the latter case, because sliding necessitates allowing some lateral, albeit infinitesimal clearance, an imperfectly irrotational end condition was sometimes obtained, rather than a truly clamped one; this condition was considered equivalent to having a pinned end, restrained by a heavy rotational spring. Such support conditions are referred to as "clamped-sprung," to differentiate them from true clamped-clamped boundary conditions; the effective rotational spring constant was measured in such cases by simple means [12], and used in the analysis when comparing theory to experiment.

Most observations on the behavior of the cylinders were made visually through the transparent test section. However, in conjunction with the onset of buckling, optical measurements of displacement *versus* flow were made, in order to pin-point the threshold flow velocity.

More recently, experiments were also done with one of the cylinders instrumented with strain gauges, implanted in the cylinder by a special technique, and capable of determining flexure, and hence amplitude of motion, in two mutually perpendicular planes; with the aid of a rectangular-to-polar conversion circuit the total displacement vector of the cylinder could be monitored electronically. The signal was passed through filters and a digital voltmeter, and/or processed by a Fast-Fourier-Transform (FFT) signal analyzer. This permitted the detailed study of frequency content and amplitude of the flow-induced vibration, as well as the more precise determination of the onset of instability.

3 General Observed Behavior

Experiments were conducted in the range of flow velocities attainable by the water tunnel, i.e., 0 to 6 m/s. As the flow velocity was increased, at least four different regimes of dynamical behavior could be identified: (i) the subcritical

regime, where system behavior was dominated by small amplitude random vibration; (ii) a transition region to the third regime; (iii) the buckled state where the cylinders have collapsed, either toward one another or in another characteristic pattern; (iv) the region of large amplitude flutter. These regimes will be discussed in greater detail below. Typical plots of mean displacement away from the vertical equilibrium position *versus* flow velocity, shown in Fig. 3(*a*), help identify the first three regimes; flutter occurs at flow velocities higher than shown.

3.1 The Subcritical Regime. The random vibrations occur in a fairly broad frequency band (*vide* Section 5.1), in contrast to the vibrations of a single cylinder which are of the narrow-band type [3]. In axial form they are almost totally of the first-mode shape, but in terms of cross-sectional intercylinder patterns of motion, they appear to involve several, if not all, of the theoretical modal patterns ([10,12]; *vide* also Section 4) in a jumbled mixture. As the flow velocity is increased, the rms values of the vibration amplitude increase quite considerably. At the same time, the frequency band broadens by expanding on the low frequency side. This, as will be seen, is in good agreement with theoretical predictions.

3.2 The Transition Region. Here the steady-state displacement away from the vertical begins to become appreciably large [Fig. 3(*a*)]. The vibration amplitudes continue to grow; the vibration frequency band stretches to almost zero on the low side, signalling the approach of buckling. The sharpness of the onset of buckling depends on the boundary conditions; the "stiffer" they are, the more gradual it is. This may be seen in Fig. 3, where the sharpest rise in steady-state displacement is for a pinned-pinned system, where axial sliding of the lower end is allowed, and the most gradual rise is for the clamped-clamped system with an axially fixed lower support.

3.3 The Buckled State. In this state the cylinders are severely bent, often in a cross-sectional pattern where they all have moved toward the center of the channel; especially when the cylinders are free to slide at the lower support, they may even bend enough to touch one another. Vibration about this bent state is considerably abated. However, in some cases the cylinders snap back and forth from an inward collapsed form to an outward one.

3.4 The Region of Large Amplitude Flutter. As the flow velocity is increased further, large amplitude oscillations are precipitated, at first intermittently, then more regularly, of combined first- and second-axial-mode shape.

The results shown in Fig. 3 are typical of many similar ones. The repeatability of these experiments was very good, especially with the instrumented cylinders; as shown in Fig. 3(*b*) the results with the open and closed circles are very similar; indeed, each of these symbols corresponds to two or more independent runs, not differentiated here for the sake of clarity.

4 Theoretically Predicted Behavior

A brief review of the theoretically predicted behavior will be given here, mainly to aid comparison of experiment with theory. Interested readers may find greater detail in references [10,12].

For cylinders of length L, diameter D, cross-sectional area A, mass per unit length m, and flexural rigidity EI, in an axial flow of velocity U, and fluid density ρ, the dynamics of the system are found to be governed by the following parameters:

$$u = (\rho A/EI)^{1/2} UL = \text{a dimensionless flow velocity, and}$$

$$\beta = \rho A/(\rho A - m),\ \epsilon = L/D,\ \gamma = [(\rho A - m)/EI]gL^3,$$

$$h = D/D_h,\ \alpha = \{I/[E(\rho A + m)]\}^{1/2}\ \mu/L^2,$$

$$c_f = (4/\pi)C_f,\ c_b = (4/\pi)C_b,\ \kappa = c_L L/EI,$$

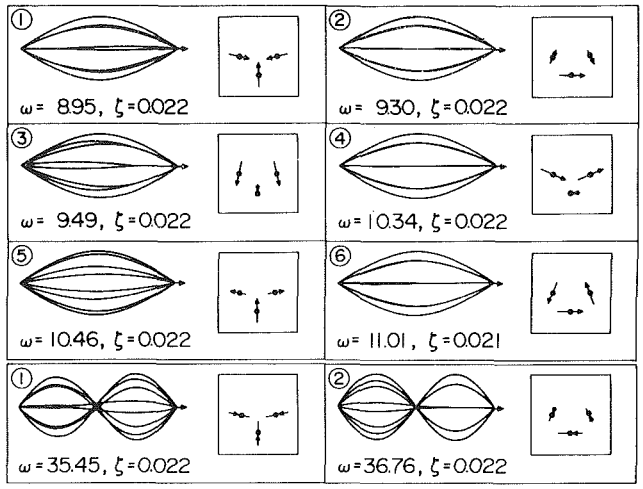

Fig. 4 Typical theoretical axial mode shapes and inter-cylinder (cross-sectional) patterns of vibration (in the squares) of the lowest six modes of the first-mode group, and of the lowest two of the second-mode group, for a three-cylinder, pinned-pinned system with the bottom ends free to slide axially, at $u = 0.5$. In each case, the associated dimensionless frequency of oscillation, ω, and the damping parameter ζ are shown. (Dimensionless system parameters: same as in Fig. 3(*a*), but $D_2/R = 1.0$; α was taken to be zero.)

where D_h is the hydraulic diameter in the channel, μ is a viscoelastic dissipative constant, C_f the frictional coefficient, and C_b a form drag coefficient at the lower (downstream) support; c_L is the rotational spring constant for an imperfectly clamped lower support ($c_L = 0$ for a pinned end). These are sufficient if the lower support is free to slide axially; in the case of a fixed end, $c_b = 0$, but one needs the additional parameters $\Pi = \bar{p}AL^2/EI$, $\Gamma = \bar{T}L^2/EI$ and Poisson's ratio ν, where $\bar{p}$ is the mean pressure, and $\bar{T}$ the mean axial tension imposed by other than the flow.

For a cluster of K cylinders one finds that the system possesses $2K$ complex conjugate pairs of "first-mode" eigenvalues, in the sense that they correspond to modes with first-beam-mode axial modal shapes (at least at low flow velocities), but each is associated with a distinctive cross-sectional pattern of inter-cylinder motions; similarly, there are $2K$ pairs of "second-mode" eigenvalues, and so on. The real part of the eigenvalues is proportional to a dimensionless damping factor, ζ, and the imaginary to a dimensionless circular frequency, ω; they are related to the circular frequency of oscillation, Ω – for any given mode – and to the corresponding modal logarithmic decrement, δ, by

$$\omega = \left\{\frac{\rho A + m}{EI}\right\}^{1/2} \Omega L^2 \quad \text{and} \quad \zeta = \frac{\omega}{2\pi}\delta.$$

Figure 4 illustrates the cross-sectional patterns of inter-cylinder motions that differentiate one mode from another within the same group of $2K$ modes, as well as the corresponding axial modal shapes of one of the cylinders, for a typical three-cylinder pinned-pinned system[1] at $u = 0.5$, which is a relatively low flow velocity (*vide* Fig. 3(*a*)). All six modes of the first mode group are shown, as well as the lowest two of the second-mode group, together with the associated ω and ζ.

With increasing flow, the values of ω decrease for all modes, but fastest for that with the lowest ω, and slowest for that with the highest. This is demonstrated in Fig. 5, where the values of ω and ζ are plotted in Argand-diagram form, (*a*) for the first (lowest) eigenmode in the first-mode group and (*b*)

[1] It should be noted that the cross-sectional modal patterns are sensitive to changes in geometry. Thus, for D_2/R, D_1/R (*vide* Fig. 3(*a*)) other than those of Fig. 4, the angles and relative amplitudes of inter-cylinder motions would be different (cf. Fig. 3 of reference [10]).

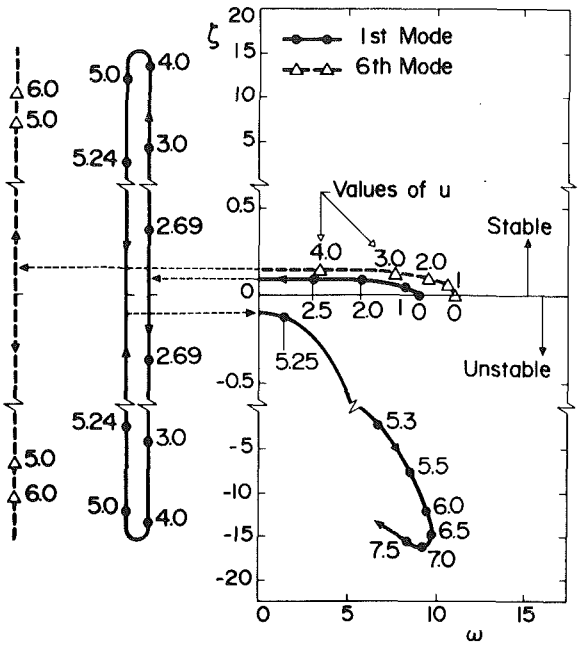

Fig. 5 The theoretical variation of ω and ζ with increasing dimensionless flow velocity, u, for the lowest (first) and the highest (sixth) mode of the first-mode group of a three-cylinder, pinned-pinned system. (Dimensionless system parameters: $\beta = 0.467$, $\epsilon = 16.67$, $\gamma = 1.38$, $h = 0.176$, $\alpha = 0$, $c_f = 0.016$, $c_b = 0.0$, $D_1/R = 1.5$, $D_2/R = 1.0$.) The diagrams on the left of the figure show the evolution of the loci while on the ζ-axis; they have been drawn separate from the main figure for clarity.

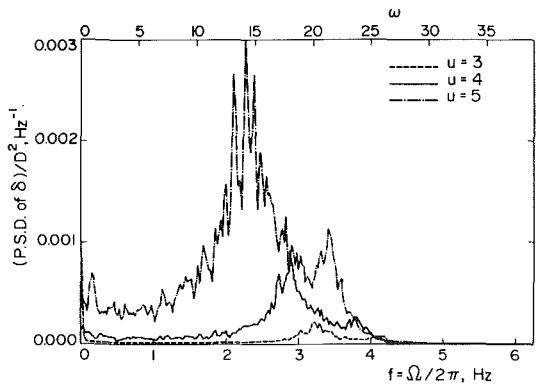

Fig. 6 Observed power-spectral-densities for the mid-cylinder displacement, δ, in the (y,x)-plane of a cylinder in a cluster of four clamped-clamped cylinders, for three different dimensionless flow velocities u. Frequency resolution. $\Delta f = 0.024$ Hz; 500 averages. System parameters: $\beta = 0.466$, $\epsilon = 18.6$, $\gamma = 1.42$, $h = 0.197$, $\Gamma = 0$, $\Pi = 115$, $\nu = 0.47$, $D_2/R = 1$.

for the highest mode of that group, It is seen that eventually, for high enough values of the dimensionless flow velocity, u, the first mode loses stability by buckling ($\omega = 0$, $\zeta < 0$) at $u = u_{cb} \simeq 2.69$, and at yet higher flow by flutter ($\omega \neq 0$, $\zeta < 0$) at $u = u_{cf} \simeq 5.25$. The other modes, exemplified here by the sixth, behave similarly, but loss of stability in these modes occurs successively at correspondingly higher flow velocities.

It should be noted that with increasing flow, the axial mode shape of each of the modes changes [12] – so that, eventually, "first-mode" axial shapes begin to look more like second-beam-mode axial shapes – but the cross-sectional patterns of inter-cylinder motions remain unaltered.

5 Comparison between Theory and Experiments

Comparing the previously described, general observed behavior of the system with that predicted theoretically, it may be concluded that the two are in broad qualitative agreement.

Some significant differences do, nevertheless, exist. For instance, the theoretically predicted succession of buckling in each of the modes of the first-mode group could not be observed. In the experiments, once the system lost stability by buckling in the manner shown in Fig. 3, presumably in one specific mode, the post-buckling behavior was both complex and not wholly repeatable; in any event, the thresholds of higher-mode buckling instabilities could not be defined. This is not surprising, as one could hardly expect linear theory to predict the behavior of the system beyond the threshold of the first instability encountered. Nevertheless, it is of interest that flutter does materialize at sufficiently high flow velocities.

Considering, next, quantitative agreement between theory and experiment, two quantities will be compared: the natural frequencies of oscillation and the critical flow velocities.

5.1 Comparison Between Theoretical and Experimental Natural Frequencies. Experiments were done with an instrumented four-cylinder system. According to theory there should be eight distinct first-mode eigenfrequencies; or, if the symmetry of the system was perfect, a maximum of two pairs of these eigenfrequencies would be repeated, yielding six distinct ones.

In the experiments, the system was allowed to be excited by the random pressure field, rather than by intrusive mechanical excitation. Observations were made by taking the power spectral density (p.s.d.) of the vibration signals, such as those shown in Fig. 6 for three different flow velocities. The experimental band of dominant vibration frequencies of Fig. 6 was found to always be in the neighbourhood of the theoretical eigenfrequencies of the first-mode group. The second- and third-mode groups of frequencies could also be discerned, but with very small energy content. Figure 6 shows clearly that with increasing flow (*a*) the amplitude of vibration is increased and (*b*) the vibration frequency band becomes broader and shifts toward lower frequencies.

Within each p.s.d. plot it was found difficult to pinpoint with certainty individual frequencies, as (i) the dominant frequency peaks within the band shifted from one experiment to the other, and (ii) the number of the dominant peaks was sometimes smaller, but usually larger than the theoretical number of six to eight[2]. However, the frequency band itself remained sensibly unchanged and well defined, and it was decided to compare theoretical and experimental *bands* of frequencies, rather than individual frequencies. A typical such comparison is made in Fig. 7, where agreement is seen to be reasonably good[3]. It should be noted that the flow velocity at which the minimum frequency within the band is essentially zero corresponds to the onset of buckling, which is in good agreement with theory (cf. Fig. 5).

5.2 Comparison of the Critical Flow Velocities. The dimensionless critical flow velocity for buckling, u_{cb}, was determined from curves, such as those of Fig. 3, by the

[2] This was found to be the case for various settings of the FFT analyzer: e.g., for various sampling times, number of ensemble averages, etc. Hence, this appears to be a characteristic of the vibration itself, rather than of the mode of signal analysis. (Similar occurrences in the case of strongly coupled vibrations of clustered cylinders in cross flow have also been reported [13].) The reasons for this behavior remain elusive. One possible reason is that the vibration is not purely planar, as supposed by theory, but contains important orbital components – as revealed by $(y-z)$-plots of the vibration; also, for larger amplitudes of motion, amplitude-dependent nonlinear fluid effects could become significant. Both effects would act to produce a broader frequency response than the six to eight distinct peaks predicted by theory. This is partly supported by the observation that, as the number of ensemble averages is increased, the prominent peaks and valleys become smoothed out, resulting in p.s.d.'s much more like that for $u = 4$ in Fig. 6 than that for $u = 5$.

[3] In comparing theory and experiment, all quantities necessary for defining the dimensionless parameters of Section 4 were measured in each case, with the exception of c_f which was estimated from information on the drag of long cylinders inclined to the flow [14,15], and c_b which was estimated from wind-tunnel data [16].

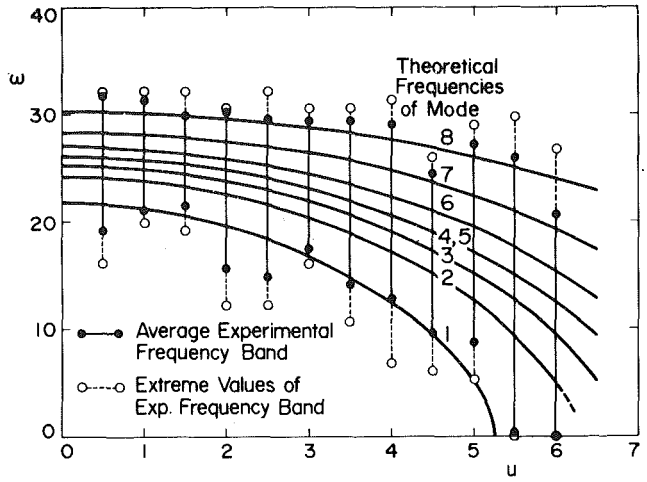

Fig. 7 Comparison of the theoretical eigenfrequencies of the first-mode group with the observed vibration frequency band, at different values of the dimensionless flow velocity, u, for a system of four clamped-clamped cylinders. (Dimensionless system parameters: $\beta = 0.466$, $\epsilon = 20.6$, $\epsilon c_f = 0.556$, $\gamma = 1.93$, $h = 0.197$, $\Gamma = 0$, $\Pi = 141$, $\nu = 0.47$, $D_2/R = 0.75$). Uncertainty in u: ±5 percent; uncertainty in ω : ±4 dimensionless units in 4/5ths of the cases, including fixed errors.

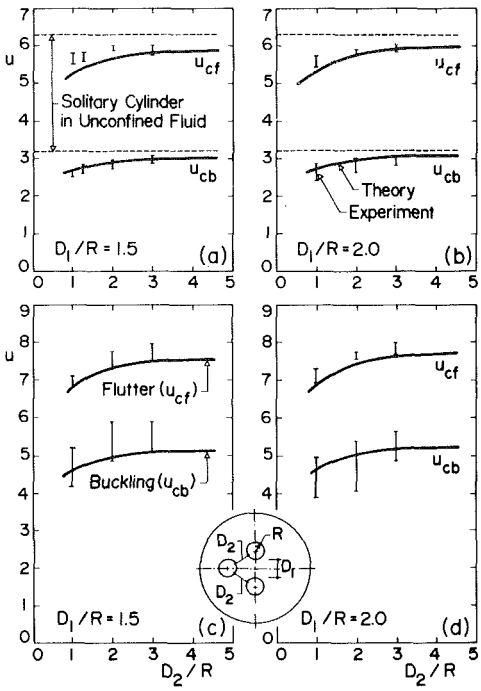

Fig. 8 Comparison between experimental and theoretical dimensionless critical flow velocities for buckling, u_{cb}, and flutter, u_{cf}, for a three-cylinder system with different values of D_1/R and D_2/R. (a),(b): Pinned-pinned ends; (c),(d): clamped-sprung boundary conditions ($\kappa = 7.6$, measured as described in reference [12]). Other system parameters: same as in Fig. 5.

"tangent method", i.e., u_{cb} is defined as the intercept on the abscissa of a tangent drawn to the steep part of the curve. Examination of Fig. 3 makes it immediately obvious that the result will depend on exactly what position of the curve the tangent is drawn to; moreover, the uncertainty is greater in some cases than others. The critical flow velocity for flutter, u_{cf}, was defined as the point of more-or-less coherent large amplitude oscillation; obviously, there is some uncertainty in pin-pointing this instability also.

The critical flow velocities for buckling and flutter are compared to theory in Fig. 8, for three-cylinder systems, where measurements were taken optically. The analogous comparison for buckling of some instrumented four-cylinder systems is made in Table 1. The theoretical critical flow velocities are those associated with the lowest mode.

The bars in Fig. 8 represent the maximum uncertainty in defining the threshold of instability for the reasons discussed above. Consistently with Fig. 3, the uncertainty in the case of cylinders with pinned ends is considerably smaller than in the case of nominally clamped (clamped-sprung) ones. Nevertheless, agreement between theory and experiment may be said to be, on the whole, satisfactorily good; this is especially true insofar as u_{cb} is concerned, which, strictly, is the only experimental quantity to which linear theory should be compared.

Some experiments with uninstrumented four-cylinder systems have already been reported [12]; hence, only new experimental data obtained with instrumented systems will be discussed here. Experimental and theoretical values of u_{cb} are compared in Table 1. The experimental values in this case were determined by drawing the tangent to the steepest, upper part of the amplitude-*versus*-flow curve; they are not deemed to be correct to better than ±10 percent, for the reasons already discussed. It should be noted that in Table 1 (as well as in Fig. 7) the critical flow velocities have been corrected for non-uniformity in flow-velocity distribution in the test section, produced, especially at small D_2/R,[4] by the presence of the cluster of cylinders in the central portion of the test section; this results in a mean flow velocity, in the neighborhood of the cylinder cluster, lower than the measured overall mean flow in the test section. The necessary correction was established by mapping the velocity distribution in the test section, with the flexible cylinders substituted by rigid ones; it amounted to a maximum of 5 percent for $D_2/R = 0.75$ and ~2 percent for $D_2/R = 1.5$.

Table 1 Comparison between theoretical and experimental critical flow velocities for buckling, u_{cb}, for four-cylinder instrumented cylinders. Experimental values are within ±10 percent. [D_2/R is defined in inset of Fig. 3(*b*).]

Support Conditions	Geometry	Values of u_{cb}	
	D_2/R	Experiment	Theory
Clamped-clamped	0.75	5.10	4.84
cylinders; axially	1.00	5.30	5.24
sliding lower support	1.50	5.45	5.78
Clamped-clamped	0.75	5.70	5.26
cylinders; axially	1.00	5.53	5.64
fixed lower support	1.50	6.04	6.12

The degree of agreement between theory and experiment in Table 1 may be considered to be reasonably good, especially when the various simplifying assumptions of the theory [10] are taken into account.

6 Conclusion

This paper presented results of two series of experiments on fluid-elastic instabilities of clusters of cylinders in axial flow. In the first set of experiments, uninstrumented three-cylinder clusters were tested, displacement measurements being taken by optical means. These experiments extend, refine, and complement those of reference [12].

In the second set of experiments, instrumented four-cylinder clusters were tested. In this case, not only the onset of instability could be defined more clearly and easily, but also the flow-induced vibration itself could be monitored and its evolution with increasing flow velocity studied. The results shown in Figs. 6 and 7 show clearly how the band of observed predominant frequencies of vibration shifts to lower frequencies as the flow velocity is increased; for sufficiently high flow velocity, the low side of the frequency band

[4] For the definition of D_2/R, see inset in Fig. 3(*b*).

vanishes, indicating that one of the vibration frequencies is essentially zero. This was found to correspond to the onset of buckling, and is in remarkable agreement with the theoretically predicted behavior of the system.

Unfortunately, although the band of flow-induced vibration frequencies could be defined, by means of power-spectral-density analysis of the vibration signal, the theoretically predicted individual frequencies within the band could not be pin-pointed. This aspect of the problem, together with others not related to the stability of the system, but rather to subcritical vibration, are under continuing study and will eventually be published as a separate paper.

Concerning the critical flow velocities for loss of stability by buckling, it has been found in Fig. 8 and Table 1 that theory is adequately successful in their prediction; agreement between theoretical and experimental threshold flow velocities is fairly good. Such comparisons are made more difficult by uncertainties associated with the experimental values, related to the definition of exactly when instability has taken place, especially in cases where divergence from the position of vertical equilibrium with increasing flow occurs gradually, rather than abruptly.

It is gratifying, if surprising, to report that the critical flow velocities for the flutter instabilities, which occur at higher flow velocities than buckling, may be predicted by theory, also reasonably well.

On the whole, it may be concluded that the theoretical model for the dynamical behavior of such systems in axial flow – at least for the boundary conditions and other parameters tested in this paper – is quite sound.

7 Acknowledgments

The authors gratefully acknowledge the Natural Sciences and Engineering Research Council of Canada and "Le programme de formation de chercheurs et d'action concertée DGES-FCAC" of Québec for supporting this research. The support by the Whiteshell Nuclear Research Establishment of Atomic Energy of Canada of the earlier components of this research programme is equally gratefully remembered.

References

1 Paidoussis, M. P., "Dynamics of Flexible Slender Cylinders in Axial Flow. Part 1: Theory," *Journal of Fluid Mechanics*, Vol. 26, 1966, pp. 717–736.

2 Paidoussis, M. P., "Dynamics of Flexible Slender Cylinders in Axial Flow. Part 2: Experiments," *Journal of Fluid Mechanics*, Vol. 26, 1966, pp. 737–751.

3 Chen, S.-S., and Wambsganss, M. W., "Parallel Flow-Induced Vibration of Fuel Rods," *Nuclear Engineering and Design*, Vol. 18, 1972, pp. 253–278.

4 Paidoussis, M. P., "Dynamics of Cylindrical Structures Subjected to Axial Flow," *Journal of Sound and Vibration*, Vol. 29, 1973, pp. 365–385.

5 Chen, S.-S., "Parallel Flow-Induced Vibrations and Instabilities of Cylindrical Structures," *Shock and Vibration Digest*, Vol. 6, 1974, pp. 1–11.

6 Paidoussis, M. P., "Vibration of Cylindrical Structures Induced by Axial Flow," ASME *Journal of Engineering for Industry*, Vol. 96, 1974, pp. 547–552.

7 Chen, S.-S., "Vibration of Nuclear Fuel Bundles," *Nuclear Engineering and Design*, Vol. 35, 1975, pp. 399–422.

8 Chen, S.-S., "Vibrations of a Row of Circular Cylinders in a Liquid," ASME *Journal of Engineering for Industry*, Vol. 97, 1975, pp. 1212–1217.

9 Chung, H., and Chen, S.-S., "Vibration of a Group of Circular Cylinders in Confined Fluid," ASME *Journal of Applied Mechanics*, Vol. 44, 1977, pp. 213–217.

10 Paidoussis, M. P., and Suss, S., "Stability of a Cluster of Flexible Cylinders in Bounded Axial Flow," ASME *Journal of Applied Mechanics*, Vol. 44, 1977, pp. 401–408.

11 Chen, S.-S., and Jendrzejczyk, J. A., "Experiments in Fluidelastic Vibration of Cantilevered Tube Bundles," ASME *Journal of Mechanical Design*, Vol. 100, 1978, pp. 540–548.

12 Paidoussis, M. P., "The Dynamics of Clusters of Flexible Cylinders in Axial Flow: Theory and Experiments," *Journal of Sound and Vibration*, Vol. 65, 1979, pp. 391–417.

13 Haslinger, K. H., oral presentation at the *Heat Exchanger Tube Vibration Working Group Meeting*, Argonne National Laboratories, CT/VA 1511; Argonne, Ill., 19 Nov. 1980.

vanishes, indicating that one of the vibration frequencies is essentially zero. This was found to correspond to the onset of buckling, and is in remarkable agreement with the theoretically predicted behavior of the system.

Unfortunately, although the band of flow-induced vibration frequencies could be defined, by means of power-spectral-density analysis of the vibration signal, the theoretically predicted individual frequencies within the band could not be pin-pointed. This aspect of the problem, together with others not related to the stability of the system, but rather to subcritical vibration, are under continuing study and will eventually be published as a separate paper.

Concerning the critical flow velocities for loss of stability by buckling, it has been found in Fig. 8 and Table 1 that theory is adequately successful in their prediction; agreement between theoretical and experimental threshold flow velocities is fairly good. Such comparisons are made more difficult by uncertainties associated with the experimental values, related to the definition of exactly when instability has taken place, especially in cases where divergence from the position of vertical equilibrium with increasing flow occurs gradually, rather than abruptly.

It is gratifying, if surprising, to report that the critical flow velocities for the flutter instabilities, which occur at higher flow velocities than buckling, may be predicted by theory, also reasonably well.

On the whole, it may be concluded that the theoretical model for the dynamical behavior of such systems in axial flow – at least for the boundary conditions and other parameters tested in this paper – is quite sound.

7 Acknowledgments

The authors gratefully acknowledge the Natural Sciences and Engineering Research Council of Canada and "Le programme de formation de chercheurs et d'action concertée DGES-FCAC" of Québec for supporting this research. The support by the Whiteshell Nuclear Research Establishment of Atomic Energy of Canada of the earlier components of this research programme is equally gratefully remembered.

References

1 Paidoussis, M. P., "Dynamics of Flexible Slender Cylinders in Axial Flow. Part 1: Theory," *Journal of Fluid Mechanics*, Vol. 26, 1966, pp. 717–736.

2 Paidoussis, M. P., "Dynamics of Flexible Slender Cylinders in Axial Flow. Part 2: Experiments," *Journal of Fluid Mechanics*, Vol. 26, 1966, pp. 737–751.

3 Chen, S.-S., and Wambsganss, M. W., "Parallel Flow-Induced Vibration of Fuel Rods," *Nuclear Engineering and Design*, Vol. 18, 1972, pp. 253–278.

4 Paidoussis, M. P., "Dynamics of Cylindrical Structures Subjected to Axial Flow," *Journal of Sound and Vibration*, Vol. 29, 1973, pp. 365–385.

5 Chen, S.-S., "Parallel Flow-Induced Vibrations and Instabilities of Cylindrical Structures," *Shock and Vibration Digest*, Vol. 6, 1974, pp. 1–11.

6 Paidoussis, M. P., "Vibration of Cylindrical Structures Induced by Axial Flow," ASME *Journal of Engineering for Industry*, Vol. 96, 1974, pp. 547–552.

7 Chen, S.-S., "Vibration of Nuclear Fuel Bundles," *Nuclear Engineering and Design*, Vol. 35, 1975, pp. 399–422.

8 Chen, S.-S., "Vibrations of a Row of Circular Cylinders in a Liquid," ASME *Journal of Engineering for Industry*, Vol. 97, 1975, pp. 1212–1217.

9 Chung, H., and Chen, S.-S., "Vibration of a Group of Circular Cylinders in Confined Fluid," ASME *Journal of Applied Mechanics*, Vol. 44, 1977, pp. 213–217.

10 Paidoussis, M. P., and Suss, S., "Stability of a Cluster of Flexible Cylinders in Bounded Axial Flow," ASME *Journal of Applied Mechanics*, Vol. 44, 1977, pp. 401–408.

11 Chen, S.-S., and Jendrzejczyk, J. A., "Experiments in Fluidelastic Vibration of Cantilevered Tube Bundles," ASME *Journal of Mechanical Design*, Vol. 100, 1978, pp. 540–548.

12 Paidoussis, M. P., "The Dynamics of Clusters of Flexible Cylinders in Axial Flow: Theory and Experiments," *Journal of Sound and Vibration*, Vol. 65, 1979, pp. 391–417.

13 Haslinger, K. H., oral presentation at the *Heat Exchanger Tube Vibration Working Group Meeting*, Argonne National Laboratories, CT/VA 1511; Argonne, Ill., 19 Nov. 1980.

14 Taylor, G. I., "Analysis of the Swimming of Long and Narrow Animals," *Proceedings of the Royal Society (London)*, Vol. 214(A), 1952, pp. 158–183.

15 Hoerner, S. F., *Fluid-Dynamic Drag*, published by the author; Brick Town, N.J., 1965.

16 Hannoyer, M. J., "Instabilities of Slender, Tapered Tubular Beams Induced by Internal and External Axial Flow," Ph.D. thesis, 1977, Department of Mechanical Engineering, McGill University, Montreal, Québec, Canada.

DISCUSSION

D. S. Weaver[1]

Professor Paidoussis and his coworkers are to be congratulated on their careful examination of the stability behavior of a cluster of cylinders in axial flow. The theoretical and physical modelling of flow induced vibration problems is generally quite difficult and the agreement found by the authors is excellent by standards in this field. The results have importance beyond the particular application dealt with in this paper.

In the first place, the authors have obtained good agreement between theory and experiment for post divergence flutter. The possibility of such a phenomenon has been predicted theoretically for related problems in this class, such as fixed ended plates and shells in axial flow, but has always been the subject of controversy. The few experiments which have been carried out in the past have generally proven inconclusive as the observed flutter behavior has departed significantly from theoretical predictions (see, for example, reference [1]). In this regard, it would be helpful if the authors could elaborate on their flutter observations. Presumably, the power spectral density of tube response showed a clear peak or narrow band of peaks characteristic of a much more regular motion than that induced by turbulence. Did the frequency behavior follow the trend predicted theoretically such as is shown in Fig. 5? What happened to the maximum tube amplitude in flutter as compared with that in divergence?

Secondly, the amplitude versus velocity plots of Fig. 3 very nicely illustrate the difficulties in defining the stability threshold from experimental data, even when the latter has been obtained meticulously from careful and repeated experiments. This is a common problem in flow induced vibrations and is aggravated by turbulence [2] and strong fluid coupling which produces a multiplicity of structural response frequencies [3]. Interestingly, the static buckling of conservative elastic systems may also depart significantly from the ideal theoretical behavior and an extensive literature on the effects of "imperfections" has developed (see, for example, reference [4]). In the present paper, the regions marked "2" in Fig. 3(*a*) represent the actual uncertainty limits in defining the stability threshold. The "tangent" method used by the authors is probably the best approximation in this instance but this is not always the case [3]. The important point here is that when experiments are being used to validate a theory, a method must be used which is consistent with the assumptions implicit in the theory. For a linear theory, this means a small amplitude departure from the static equilibrium state.

Finally, the authors' observations of the band of frequencies associated with fluid-coupled modes of the tubes are very similar to those seen for tubes in a cross-flow. The assumption that one would expect a number of peaks equal to twice the number of tubes is based on the ideal behavior of those tubes in quiescent fluid. Each tube has two degrees of freedom in each axial mode and the effects of fluid added

[1] Professor, Department of Mechanical Engineering, McMaster University, Hamilton, Ontario, Canada L8S 4L7

mass in a heavy fluid produce a number of distinct relative modes equal to twice the number of interacting tubes. The effects of turbulence and strong fluid coupling in a flowing fluid could cause random disturbances to the ideal fluid added mass. Thus the tube response spectra would generally show more peaks than expected from structural considerations alone. The present experiments show that the separation in coupled mode frequencies increases with increase in flow velocity. It might be expected that the individual relative modes and perturbations about these would become more distinct. Was this observed at higher flow velocities? Also, our experiments for tube bundles in cross-flow show that instability is associated with many different relative modes depending on the velocity excess over the stability threshold [5]. Was similar behavior observed for the flutter of the tubes in axial flow?

Additional References

1 Weaver, D. S., Paidoussis, M. P., "On Collapse and Flutter Phenomena in Thin Tubes Conveying Fluid," *J. Sound and Vibration*, Vol. 50, No. 1, 1977, pp. 117–132.

2 Irwin, H. P. A. H., and Schuyler, G. D., "Experiments on a Full Aeroelastic Model of Lions Gate Bridge in Smooth and Turbulent Flow," National Research Council of Canada NAE Report LTR-LA-206, 1977. For a brief summary, see R. L. Wardlaw, "Approaches to the Suppression of Wind-Induced Vibrations of Structures," Practical Experiences with Flow Induced Vibrations, edited by E. Naudascher, D. Rockwell, Springer-Verlag, Berlin, 1980, pp. 650–670.

3 Yeung, H. C., and Weaver, D. S., "The Effect of Approach Flow Direction on the Flow Induced Vibrations of a Triangular Tube Array," ASME Design Engineering Tech. Conf. paper no. 81-DET-25, Hartford, Conn., 1981. To appear in the ASME *Journal of Mechanical Design*.

4 Roorda, J., "Concepts in Elastic Structural Stability," from *Mechanics Today*, Vol. 1, 1972, pp. 322–372, editor, S. Nemat. Nasser, Pergamon Press, New York.

5 Weaver, D. S., and Koroyannakis, D., "The Cross Flow Response of a Tube Array in Water—A Comparison with the Same Array in Air," to be presented at the ASME PVP Conference, Orlando, Fla., June 28–July 2, 1982.

M. J. Pettigrew[2]

The authors are to be congratulated for a very thorough and enlightening presentation on fluidelastic instability of clusters of cylinders subjected to axial flow. This discusser would like to express a few comments as follows:

(1) The dynamic behavior of a cluster of cylinders is dependent on the dynamic properties of the individual cylinders. The resulting mode shapes, particularly during instability, would be affected by the degree of similarity between cylinders. Were the properties of the individual cylinders, i.e., natural frequencies and internal damping very similar? In practice there often are large differences in dynamic properties of say tubes in a heat exchanger tube bundle or in fuel elements in a nuclear fuel cluster. What would be the effect of such dissimilarities? Should a statistical approach be used to treat the problem of large clusters of somewhat dissimilar cylinders?

(2) The generally observed dynamic behavior of the cylinders is very similar to that of a single cylinder subjected to confined annular flow[3]. This is not surprising. The authors may wish to comment on the similarities and the differences between the two situations.

(3) Generally the agreement between theory and experiment is remarkably good considering that the theory is linear and that when the cylinders move close to each other there are nonlinear relationships. Would the authors be prepared to comment on the benefit versus the added complexity of a nonlinear theory.

(4) This discusser sympathizes with the authors' difficulties in defining the flow velocity for instability. This problem also exists in studies of fluidelastic instability in tube bundles subjected to cross-flow. The important point is to document how the velocity is defined as the authors have done.

(5) In the reported experiment the ratio of inter-cylinder spacing D and cylinder radius R, i.e., D/R is relatively large. In practice, in nuclear fuel bundles and in heat exchanger tube bundles the ratio D/R is smaller. Would the theory be equally applicable for smaller D/R? Probably not because of increased nonlinear effects. Would the authors care to comment on this?

[2]Atomic Energy of Canada, Ltd., Chalk River Nuclear Laboratories, Engineering Research Branch, Chalk River, Ontario K0J 1J0 Canada.

[3]Paidoussis, M. P., and Pettigrew, M. J., "Dynamics of Flexible Cylinders in Axisymmetrically Confined Flow," ASME *Journal of Applied Mechanics*, Vol. 46, 1978, pp. 37–44.

Authors' Closure

We are very grateful to Professsor D. S. Weaver and Dr. M. J. Pettigrew for their thoughtful discussion of our paper and for giving us the opportunity to clarify some points and to add information which may be potentially useful to other readers as well. We shall respond to Dr. Weaver's discussion first.

With regard to post-divergence flutter, we agree that observations rarely accord well with theoretical predictions. Nevertheless, the case of cylindrical structures subjected to external flow appears to be an exception. Thus, in experiments with a *single* flexible cylinder (with pinned ends) in axial flow [1], the measured critical flow velocities for post-buckling flutter, u_{cf}, were within 20 percent of the theoretically predicted values [2]; the limit-cycle frequencies and those predicted by linear theory were not so close, but still they were within a discrepancy margin of 50 percent, and usually much better. In this light, it was not totally unexpected, but gratifying nonetheless, that theoretical and experimental values of u_{cf} in the case of *clusters* of cylinders would be in fair agreement.

One of the difficulties of obtaining u_{cf} experimentally, both for a single cylinder and for clusters, is that the oscillation starts in the form of unsteadiness in the buckled state of the cylinders, with the cylinder flip-flopping (snapping through) from a buckled form on one side of the straight equilibrium configuration to another; as the flow velocity is increased, this irregular square-wave form of the oscillation gradually becomes transformed into a more coherent sinusoidal form with a predominant frequency. (Incidentally, theory agrees with these observations, to the extent that it predicts that at the flutter threshold the frequency of oscillation is usually vanishingly small [2, 3], but that it increases sharply with increasing flow velocity.) The observed oscillations were almost never quite continuous, being disrupted by quasi-quiescent interludes during which the system seemed to be buckled once more in a specific modal pattern, suggesting that several forms of instability were present concurrently (again as predicted by linear theory, despite the highly nonlinear character of the motions involved). Here, in answer to one of the questions raised, the amplitude of the fluttering cylinders was initially as large as that of the buckling instability and of the same order as intercylinder spacings; in some cases the amplitude exceeded that, resulting in impact between cylinders. Most observations here were made optically. Cylinders instrumented with strain gauges (requiring lengthy and painstaking preparation and some expense) have very short lives under such conditions; once the experimental program currently under way has progressed sufficiently, it is planned to "sacrifice" a number of these instrumented cylinders in order to better study system behavior around $u = u_{cf}$.

Concerning the second point raised by the discussion, namely the difficulties of defining the instability threshold for divergence, we fully agree with him. In this connection, it should be incumbent on all authors to show some of their raw data in some such form as Fig. 3 and to state clearly the exact method by which they derive therefrom the critical condition for instability.

Regarding the frequency content of vibration, this proved to be one of the most interesting aspects of the work; it is not elaborated in the paper, because it is peripheral to the instability problem, which is its main concern. The reasons advanced by Dr. Weaver are undoubtedly among those leading to the absence of identifiable discrete frequencies in the vibration spectrum. This, incidentally, persists even at high flow velocities.

The PSDs of Fig. 6 are typical for vibration of one of the cylinders in a direction corresponding to one of the sides of an imaginary square joining the centers of the four cylinders in the cluster in a cross-sectional plane. For this cluster geometry, however, the theoretical characteristic cross-sectional modal patterns—corresponding to those shown in Fig. 4 for the three-cylinder cluster—are predominantly in the directions of the diagonals to that imaginary square, or at 90 deg to these diagonals. Taking PSDs in one of these directions, it was interesting to see that (*i*) the dominant frequencies in the spectra corresponded to the theoretical frequencies associated with cross-sectional modal patterns for which the theoretical cylinder motions were in that direction; (*ii*) the theoretical frequencies for which the modal patterns involved motion normal to the direction being measured corresponded to low points in the measured PSDs. Thus there is closer correspondence between theory and experiment than might appear from the results presented in this paper. Some of these results have recently been presented in a conference paper [4].

Finally, on the question of different modes appearing at different flows, in excess of the lowest instability threshold at u_{cb}, the experiments did not show a clear sequential succession from one modal pattern to another, which would follow the theoretical sequential loss of stability of the system in each one of the group of $2N$ modes (where N is the number of cylinders). This is not surprising, even if one supposes the linear theory to apply; for at $u > u_{cb}$, the system can be unstable in several of these modes concurrently. (In one case where theory predicted that higher modes became unstable just as lower ones were restabilized, the experiments did exhibit a clear succession of instabilities of increasing modal complexity [5]; but this was not the case here.) Nevertheless, with increasing flow the modal pattern did change [3], sometimes to another modally identifiable pattern, but sometimes not; occasionally the buckling pattern would alternate between two modal states, at the same flow velocity. These observations tend to support the theoretical prediction that the system is simultaneously unstable in more than one mode.

We shall next respond to the points raised by Dr. Pettigrew, in the same order as they were posed.

1 We agree with the discusser as to the importance of uniformity of properties in the system of cylinders. In early experiments there were significant differences in the physical properties of the cylinders. As a result, it was sometimes noted that one of the cylinders would behave somewhat differently from the others, e.g., in the imploding pattern of buckling of the cylinders one would deform less than the others; yet, agreement with theory was similar to that achieved in the later set of experiments, where all physical properties and dimensions were carefully controlled to within 5 percent or better. The near-identity of properties was found to be more important insofar as sub-critical vibration behavior is concerned [4]. Therefore, for industrial systems, perhaps the statistical approach would be indicated.

2 The similarities in behavior of this system to that of a single cylinder in confined annular flow [5] were indeed quite marked. One important difference is that the various modes of instability, predicted and observed, involved different *axial* modal shapes in that case, whereas here they involved the first axial mode shapes but different cross-sectional modal patterns. The other difference has already been referred to in connection with the last point raised by the other discusser, namely that in the present experiments, unlike those of reference [5], we could not observe the transition of instability from mode to mode, sequentially in ascending mode-number order, as predicted by theory. It should be noted, however, that to be absolutely certain that these sequential transitions did not occur, further experiments should be conducted, where all four cylinders would be instrumented and their motions simultaneously monitored.

3 It would, of course, be of considerable fundamental interest to conduct an analytical study of the effect of nonlinearities on the dynamics of the system. However, in view of the complexity of the task, such a study would not really be warranted, because of the very success of linear theory—unless there is a sufficiently strong practical interest in the results.

4 We fully agree with the last statement made by the discusser, and reiterate that it is essential for authors to state clearly how they define the point of instability from their experimental data. This also applies to fluidelastic instability of cylinder clusters in cross flow, where this most important definition is often omitted.

5 Of course, for clusters with smaller D/R, such as nuclear reactor fuel bundles, nonlinear effects would be more pronounced, but it is expected that theory would still hold, at least so far as the initial onset of instability is concerned. Some support for this is found in reference [5], where the results for the narrowest annulus (annular gap-to-radius ratio of ~ 0.11) agree with theory at least as well as for wider annuli. However, for still smaller inter-cylinder gaps (say, $D/R < 0.1$), theory would be on more shaky ground, since in that case even small motions of the cylinders about equilibrium would significantly affect the mean flow field, something that present theory does not take into account. This matter should be decided by means of further experimentation.

Additional References

1 Paidoussis, M. P., "Dynamics of Flexible Slender Cylinders in Axial Flow. Part 2: Experiments," *Journal of Fluid Mechanics*, Vol. 26, 1966, pp. 737-751.

2 Paidoussis, M. P., "Dynamics of Cylindrical Structures Subjected to Axial Flow," *Journal of Sound and Vibration*, Vol. 29, 1973, pp. 365-385.

3 Paidoussis, M. P., "The Dynamics of Clusters of Flexible Cylinders in Axial Flow: Theory and Experiments," *Journal of Sound and Vibration*, Vol. 65, 1979, pp. 391-417.

4 Paidoussis, M. P., and Gagnon, J. O., "Experiments on the Dynamics of Cylinder Clusters in Axial Flow," Paper 1.3, *Third Keswick International Conference on Vibration in Nuclear Plant*; Keswick, U.K., 11-14 May 1982.

5 Paidoussis, M. P., and Pettigrew, M. J., "Dynamics of Flexible Cylinders in Axisymmetrically Confined Flow," ASME *Journal of Applied Mechanics*, Vol. 46, 1979, pp. 37-44.

Curved Ducts With Strong Secondary Motion: Velocity Measurements of Developing Laminar and Turbulent Flow

A. M. K. P. Taylor
Research Assistant.

J. H. Whitelaw
Professor of Convective Heat Transfer

M. Yianneskis
Research Assistant.

Department of Mechanical Engineering,
Imperial College, London, England

Two orthogonal components of velocity and associated Reynolds stresses have been measured in a square-sectioned, 90 degree bend of 2.3 radius ratio using laser-Doppler velocimetry for Reynolds numbers of 790 and 40,000. The boundary layers at the bend inlet were 0.25 and 0.15 of the hydraulic diameter and resulted in secondary velocity maxima of 0.6 and 0.4 of the bulk flow velocity respectively. Comparison with fully-developed inlet flow shows that the boundary layer thickness is important to the flow development (mainly in the first half of the bend), particularly so when it is reduced to 0.15 of the hydraulic diameter. Turbulent flow in an identical duct with a radius ratio of 7.0 gives rise to smaller secondary velocities than in the strongly curved bend, although their effect is more important to the streamwise flow development because of the smaller pressure gradients. The detail and accuracy of the measurements make them suitable for evaluation of numerical techniques and turbulence models. Partially-parabolic techniques are applicable to the flows studied and their reduced storage requirements seem essential if satisfactory numerical accuracy is to be achieved.

1 Introduction

1.1 The Flow Considered. Flows in curved ducts occur in diverse applications such as centrifugal pumps, aircraft intakes, river bends, and in the cooling coils of heat exchangers. A characteristic which distinguishes such flows from those in straight ducts is the generation of streamwise vorticity, or "secondary motion," within the duct, resulting in a pressure loss, the spatial redistribution of streamwise velocity and increased heat transfer at the duct wall. The nature of the secondary flow depends, among other parameters, on the radius ratio of the pipe $R_r = R_c/d$ (where R_c is the mean radius of the bend and d is the hydraulic diameter of the duct), the distribution of cross-stream vorticity on entering the curved duct (that is to say, the boundary layer thickness) and the flow Reynolds number.

This paper presents measurements of the velocity characteristics in 90 deg bends of square cross section and comparatively strong curvature for both laminar and turbulent flow with short upstream tangents. The latter condition is particularly relevant to the case of aircraft intake ducts.

1.2 Previous Work. The wall pressure distributions and corresponding pressure losses are comparatively well documented for a wide range of operating conditions see, for example, Ward-Smith [1] and Itō [2]. Observations of the redistribution of streamwise velocities and Bernoulli surfaces have been reported by, for example, Mori , Uchida, and Ukon [3], Rowe [4], Mullin and Greated [5], and particulary extensively by Nippert [6]. In contrast, measurements of the cross stream velocities are much more scarce. Bruun [7] measured these velocities in a rectangular duct with an aspect ratio of two for turbulent flow and Agrawal et al. [8] have published measurements for laminar flow in a curved pipe.

1.3 The Present Contribution. This paper is concerned with hydrodynamically developing flow at the entrance to square cross section, 90 deg bends of 2.3 radius ratio for laminar and turbulent flows. The work is an extension of those previously reported by Humphrey, Taylor, and Whitelaw [9] and Humphrey, Whitelaw, and Yee [10] which were concerned with fully-developed flows at the entry plane of the bend. The results are also compared with turbulent flow in a duct of larger radius ratio.

The purpose of the measurements is twofold. The first is to provide a basis for the understanding of the influence of developing entry flow in the bends under laminar and turbulent regimes. The second is to provide detailed observations, particularly of the secondary motion velocities, in a form suitable for the evalution of numerical solution techniques (such as that presented by [9] and [10]). The laminar and turbulent flows can be used to study, respectively, the numerical accuracy of the technique and to provide an assessment of approximations made to represent turbulence characteristics.

The following section describes the experimental procedure

Contributed by the Fluids Engineering Division for publication in the JOURNAL OF FLUIDS ENGINEERING. Manuscript received by the Fluids Engineering Division, May 27, 1981.

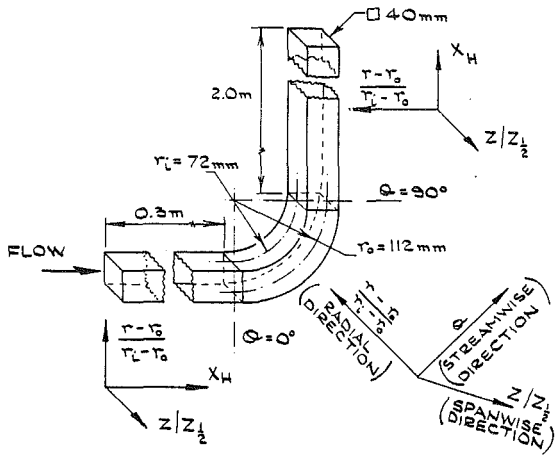

Fig. 1 Dimensions of bend and coordinate definition sketch

and includes estimates of the errors associated with the measurements presented in Section 3. The results are discussed in Section 4 and a summary of the conclusions is provided in Section 5.

2 Experimental Procedure

2.1 Flow Configuration. The test section was manufactured from Plexiglass and consisted of a 90 deg bend of mean radius 92 mm and of radius ratio 2.3, identical to that used in [10], but with upstream and downstream tangent lengths of 0.3 and 2.0 m respectively. The dimensions of the cross-section ($40 \pm 0.1 \times 40 \pm 0.1$ mm) conform closely to those of the tangents. Within the bend, the method of manufacture restricted optical access so that measurements of only the streamwise and radial velocities could be made. The geometry is illustrated in Fig. 1 together with the coordinate system adopted. The flow rate through the bend was controlled and measured by precision-bore flowmeters. The bulk velocities, V_c, were 1.98 cm/s and 1.00 m/s for the laminar and turbulent flows respectively, corresponding to the Reynolds numbers, Re, of 790 and 40,000 and Dean numbers, De, of 368 and 18,700. The temperature of the water was maintained at $20° \pm 2°C$ for all the experiments.

2.2 Velocimeter Configuration, Doppler Signal Processing and Measurement Technique. The optical arrangement of the laser-Doppler velocimeter is similar to that described by Taylor [11] except that frequency shifting of the laser light was not employed. It operated in forward scatter and made use of a 5 mW He-Ne laser, a diffraction grating, a collimating and an imaging lens. The principal characteristics of the optical system are summarized in Table 1.

The Doppler signals were detected by a photomultiplier tube (E.M.I. 9658B) and demodulated by a frequency tracker (Cambridge Consultants CC01). The voltage analogue of the Doppler frequency was time-averaged to give a mean and root-mean-square voltage. For the turbulent flow measurements, the flow was seeded (see Durst et al. [12]) with minute quantities of milk to increase the scattering particle concentration and thereby increase the particle arrival rate.

The local streamwise (U) and radial (V) components of velocity, and for turbulent flow the fluctuating components $\tilde{u}$, $\tilde{v}$, and cross-correlation $\overline{uv}$, were obtained by making measurements of the Doppler frequency in the $X-r^*$ plane in three directions ($0°, \pm 45°$) relative to the local streamwise direction at each measurement point. The method of data reduction involves resolving these measured frequencies into streamwise and radial components as described by Melling and Whitelaw [13]. The third component of velocity, W, and the associated correlations $\tilde{w}$ and $\overline{uw}$ were measured in a similar manner, with the three measurements being made in the $X \sim z^*$ plane downstream of the bend. Wall pressure measurements were made with a water micromanometer by means of pressure tappings. In laminar flow the pressure differences amounted to about 20 μm of water column which was too small for reliable measurement.

2.3 Accuracy and Precision. Table 2 summarizes the estimates of maximum inaccuracy (systematic error) and imprecision (random error) associated with each measurement presented in Section 3. No corrections have been applied to the measurements to take account of finite transit time, mean velocity gradient, and instrument noise broadening.

Only velocity gradients have a significant effect and this is included as a systematic error in the table. This accounts for the 2 and 3 percent errors associated with nondimensional mean velocities; the systematic errors for all but a few measurement points located in the region of high velocity gradients are less than 1 percent.

Nomenclature

C_p = pressure coefficient (Figure 15)

De = Dean number: $\text{De} \equiv \left(\frac{\frac{1}{2} d}{R_c} \right)^{1/2} \text{Re}$

d = hydraulic diameter (40 mm)

k = turbulent kinetic energy: $k \equiv \frac{1}{2} \rho(\tilde{u}^2 + \tilde{v}^2 + \tilde{w}^2)$

p = pressure at wall

p_{ref} = reference value of $p(\theta = 0°, r^* = 0, z^* = 0)$

r = radial coordinate direction (Fig. 1)

r_i = radius of curvature of suction surface

r_0 = radius of curvature of pressure surface

Re = Reynolds number: $\text{Re} \equiv \frac{V_c d}{\nu}$

R_c = mean radius of curvature: $R_c \equiv 0.5(r_i + r_0)$

R_r = radius ratio: $R_r = \frac{R_c}{d}$

r^* = normalized radial coordinate: $r^* \equiv \frac{r - r_0}{r_i - r_0}$

U = mean velocity in θ (streamwise) direction

$\tilde{u}$ = rms fluctuating velocity in θ direction

$\overline{uv}$ = cross-correlation between $\tilde{u}$ and $\tilde{w}$

$\overline{uw}$ = cross-correlation between $\tilde{u}$ and $\tilde{w}$

V = mean velocity in r (radial) direction

V_c = bulk mean velocity

$\tilde{v}$ = rms fluctuating velocity in r direction

W = mean velocity in z (spanwise) direction

$\tilde{w}$ = R.m.s. fluctuating velocity in z direction

X_H = axial distance along straight duct, expressed in hydraulic diameters

z = spanwise coordinate direction (Fig. 1)

$z_{1/2}$ = duct half-width (20 mm)

z^* = normalized spanwise coordinate $z^* \equiv \frac{z}{z_{1/2}}$

θ = axial (streamwise) coordinate direction (Fig. 1)

ν = kinematic viscosity of water

ρ = density of water

ϕ = half-angle of beam intersection

Table 1 Characteristics of the optical arrangement

	Laminar flow	Turbulent flow
Focal length of imaging lens (mm)	300	200
Half-angle of intersection	5.9 deg	9.3 deg
Fringe separation (line-pair spacing)	3 μm	2 μm
Number of fringes in measuring volume	52	86
Intersection volume diameter calculated at $1/e^2$ intensity (mm)	0.158	0.167
Intersection volume length calculated at $1/e^2$ intensity (mm)	1.500	1.357
Pholomultipler pinhole diameter (mm)	0.33	0.50
Transform constant (MHz/ms^{-1})	0.324	0.510

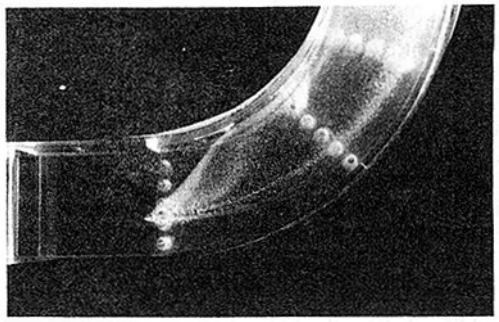

Fig. 2 Visualization of secondary flow near the side wall. Flow direction from left to top right. Wire inserted at $\theta = 0$ deg, $r^* = 0.3$.

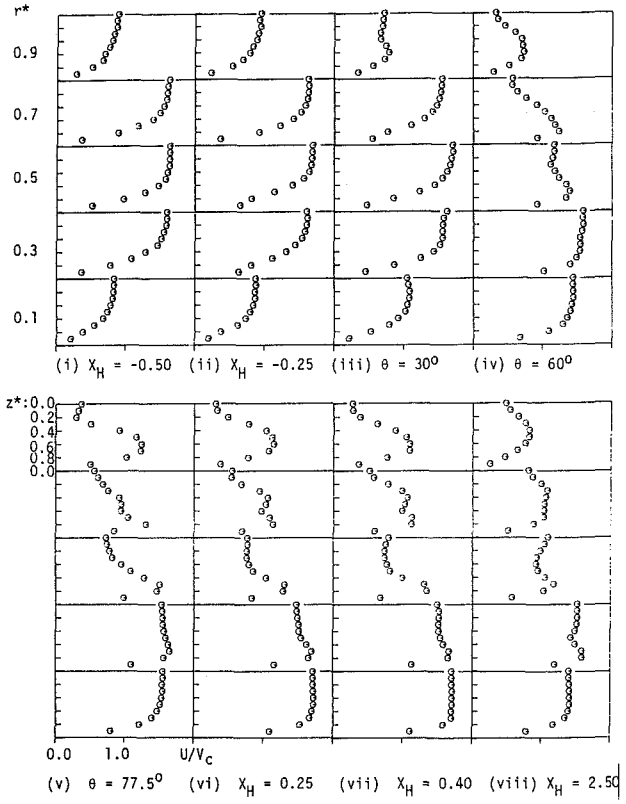

Fig. 3 Laminar flow: profiles of U/V_c at successive streamwise stations

3 Results

This section presents the experimental results under three headings: laminar (3.1) and turbulent (3.2) for a bend of 2.3 radius ratio, and turbulent flow (3.3) for a bend of 7.0 radius ratio. The behaviour of the irrotational core is first described and then related to that of the secondary flow. Section 3.2 also presents measurements of the wall pressure and turbulence quantities.

Table 2 Maximum possible measurement errors

Quantity	Systematic error	Random error
X_H	±0.5 mm	±0.02 mm
r^*, z^*	±0.2 mm	±0.02 mm
θ	±0.3°	±0.17°
ϕ	±0.05°	nil
V_c(laminar)	±0.8%	±0.8%
V_c(Turbulent)	± ½%	± ½%
U/V_c	up to 2½%	±1½%
V/V_c	up to 3%	±1½%
W/V_c	up to 3%	±1½%
$\bar{u}/V_c$	up to 3%	±1 to 3%
$\bar{v}/V_c$	up to 3%	±1½% to 5%
$\bar{w}/V_c$	up to 3%	±1½% to 5%
$\overline{uv}/V_c^2$	±1½%	±2½% to 8½%
uw/V_c^2	±1½%	±2½% to 8½%
k/V_c^2	±7%	±8%

3.1 Laminar Flow Results: Radius Ratio $R_r = 2.3$. The laminar and steady nature of the flow was confirmed by extensive visualization using hydrogen bubbles produced on 0.375 mm diameter Nichrome wires inserted through the pressure tappings. Still and cine photography recordings were made. The photograph presented as Fig. 2 shows the secondary velocity convecting fluid from the pressure (outer) wall along the sidewall to the suction (inner) wall, for Re = 1275. Flow visualization did not reveal a region of longitudinal recirculation on the pressure wall as was observed in reference [9] with a Reynolds number of 790.

Preliminary measurements were obtained to evaluate the symmetry of the flow and to determine the extent to which the bend influenced the flow upstream. It was found that measurements at equivalent locations on either side of the symmetry plane of the duct agreed within the precision of the measurement. There were no discernable trends and the flow may be regarded as symmetric. Profiles of streamwise velocity at $X_H = -0.25$ and -0.50 showed that the influence of the bend was detectable but was very small and is unlikely to be present at $X_H = -0.75$.

The development of the streamwise velocity is depicted in Fig. 3 and the same results are presented as isotachs of streamwise velocity in Fig. 4 for ease of presentation and subsequent discussion. The contours have been drawn using linear interpolation between the measurement points; no extrapolation outside the measured grid has been carried out. Figure 4 (i) shows that the edge of the boundary layers at $X_H = -0.25$ (defined at 0.95 of the maximum velocity) are located at a distance of about 0.25 of the hydraulic diameter (40 mm) from the wall. In the subsequent presentation, it is useful to refer to the behaviour of the "core" fluid (defined as fluid of velocity greater than about 0.9 of the maximum at each streamwise station). The isotachs in Fig. 4 (i) suggest that the bend has little effect on the flow upstream of the inlet and Fig. 4 (ii) - (v) show that the core is found progressively nearer to the outer wall and along the sidewalls with a corresponding

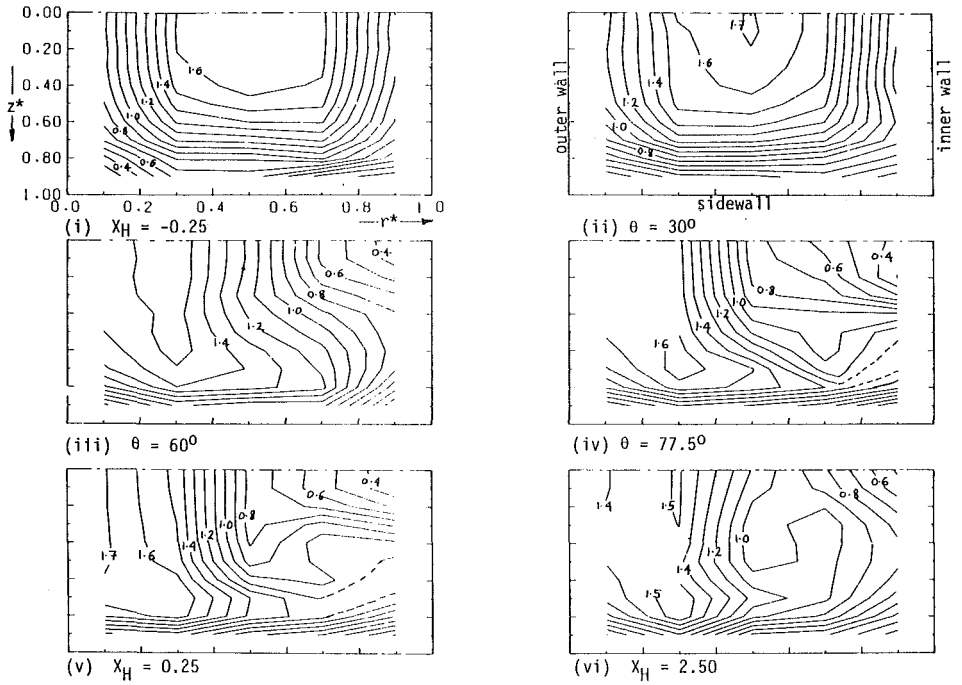

Fig. 4 Laminar flow: isotachs of U/V_c at successive streamwise stations

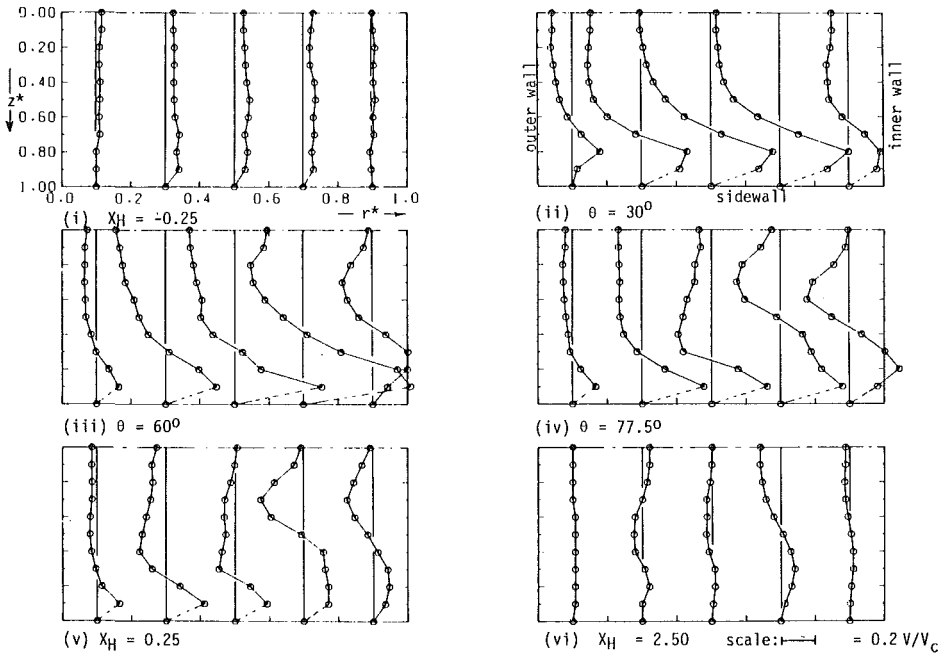

Fig. 5 Laminar flow: profiles of V/V_c at successive streamwise stations

low velocity region adjacent to the suction surface. The development of the streamwise velocity is influenced by the streamwise pressure gradient. Although wall pressures were not measured, their form can be expected to be similar to that calculated by Humphrey et al. [10] which showed that the gradient is strongly adverse over the suction surface for about 45 deg while it is strongly favorable over the pressure surface for the same region.

The generation of streamwise vorticity (that is, secondary flow) is responsible for the convection of core fluid from the pressure surface along the sidewalls, and the accumulation of low momentum boundary layer fluid from the sidewalls at the inner wall. Figure 5 shows profiles of the radial component of

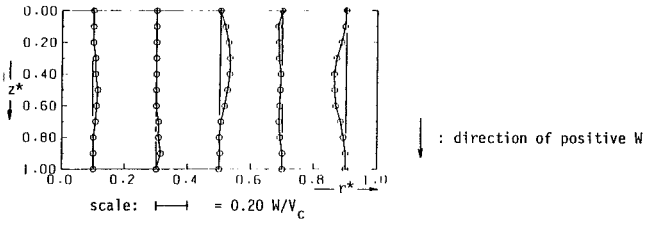

Fig. 5(vii) Laminar flow: profiles of W/V_c at $X_H = 2.50$

secondary velocity. At $X_H = -0.25$ (Fig. 5 (i)), the velocity is small ($0.05 V_c$) but directed towards the suction surface of the straight duct. This flow is evidence of a radial pressure

gradient upstream of the bend. The profiles in the bend confirm that the fluid near the symmetry plane moves away from the suction surface and the fluid near the sidewalls moves towards the suction surface. This results in a pressure-driven secondary flow which is a strong helical motion near the suction surface. The largest velocities measured occur at $\theta = 60$ deg with values of the order of $0.6V_c$, although the velocity near the symmetry plane and suction surface has decayed and is close to zero. This feature is seen to continue at $\theta = 77.5$ deg and $X_H = 0.25$. It is important to remark that the size of the core flow, rather then the degree of distortion of the streamwise isotachs at the inner wall, indicates the importance of the secondary flow: the smaller the core, the larger the magnitude of the secondary velocities.

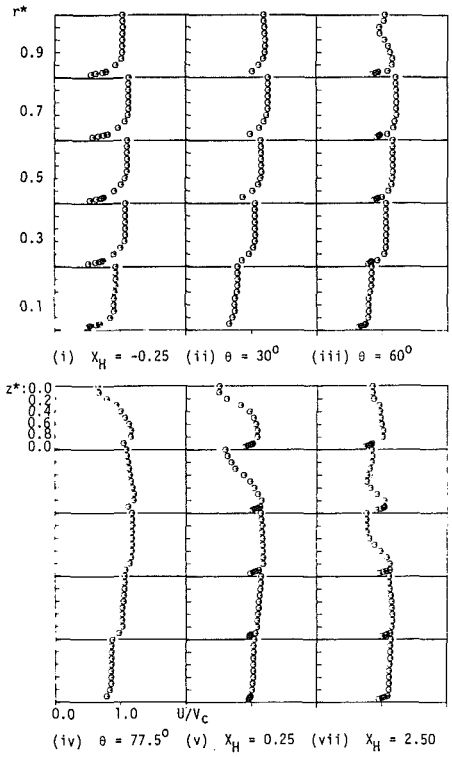

Fig. 6 Turbulent flow: profiles of U/V_c at successive streamwise stations

Downstream of the bend, Fig. 4 (vi) shows that the streamwise velocity has decelerated on the pressure side of the duct. Figure 5 (vi) presents the corresponding profile of the radial velocity which has decreased greatly from the exit plane of the bend and has also reversed direction at $r^* = 0.3$. For this station, the spanwise (W) component of velocity was measured (Fig. 5 (vii)) and confirms that the secondary flow consists of two counter-rotating vortices which is in agreement with the predictions of reference [9], although the calculated values are generally larger over the cross-section. The generation of the second vortex is associated with the rapid deceleration of streamwise velocity around $r^* = 0.1$ causing a positive radial velocity near the symmetry plane.

3.2 Turbulent Flow Results: Radius Ratio $R_r = 2.3$. As for the laminar flow, symmetry tests were carried out with similar results. The influence of the bend on the flow upstream was again examined and found to be more extensive than for the laminar flow, being present at $X_H = -0.50$ and -0.75.

The development of the streamwise component of velocity is shown as profiles in Fig. 6 and as the corresponding isotachs in Fig. 7. The growth of the turbulent boundary layers in the upstream tangent is slower than for the laminar flow so the boundary layers at $X_H = -0.25$ are thinner (about 0.15 of the hydraulic diameter). At $X_H = -0.25$, the core fluid is displaced further toward the inner wall surface than for the laminar result of Section 3.1: measurements at $X_H = -0.75$ (not presented) did not show significant displacement. The core fluid remains at the inner wall, with no evidence of low momentum fluid being accumulated at this surface, until $\theta \simeq 60$ deg, Fig. 7 (iii). Thereafter the rapid creation of a region of low streamwise momentum, at the inner wall, is evident and continues to the exit of the bend with the corresponding migration of core fluid toward the outer wall.

The profiles of radial velocity are presented in Fig. 8 and, as expected at $X_H = -0.25$, the velocity is directed toward the suction surface, for the same reasons as in the laminar flow. The streamwise vorticity generated within the bend develops

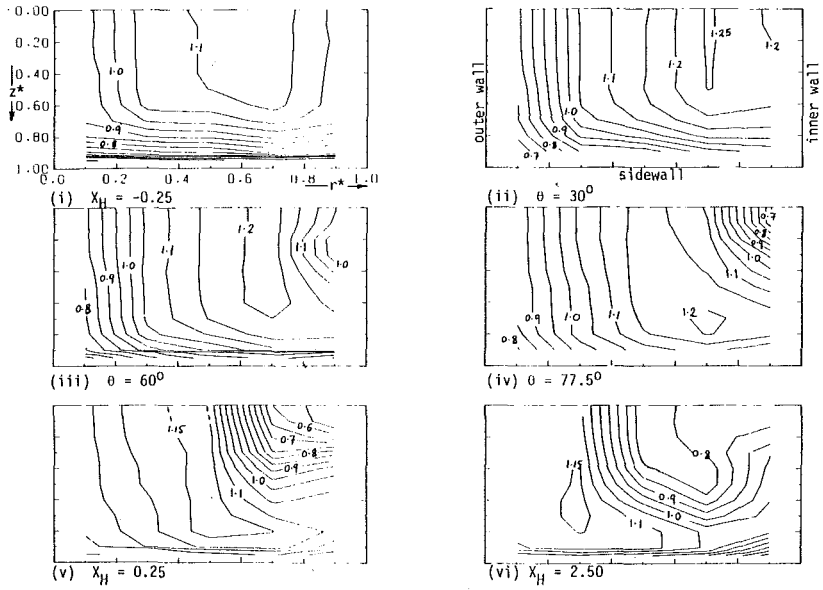

Fig. 7 Turbulent flow: isotachs of U/V_c at successive streamwise stations

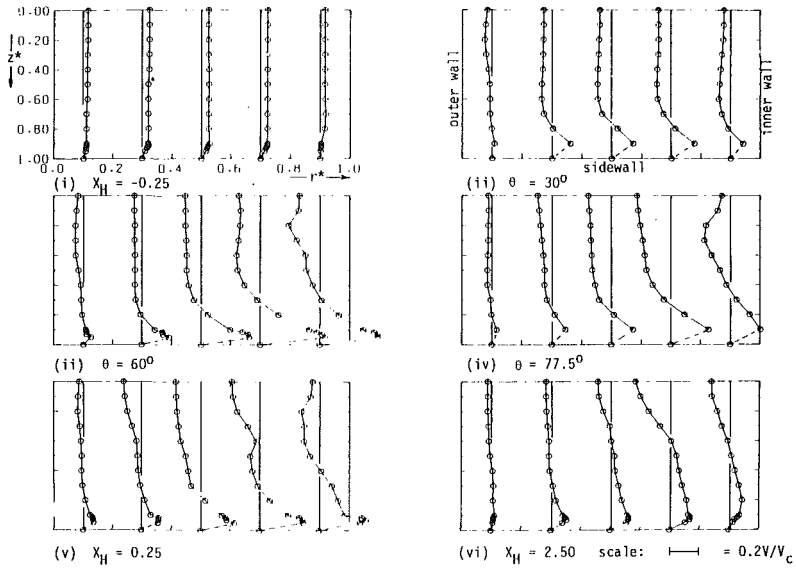

Fig. 8 Turbulent flow: profiles of V/V_c at successive stations

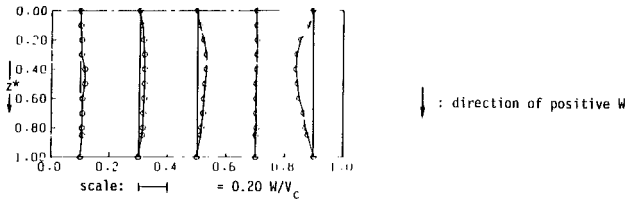

Fig. 8(vii) Turbulent flow: profiles of W/V_c at $X_H = 2.50$

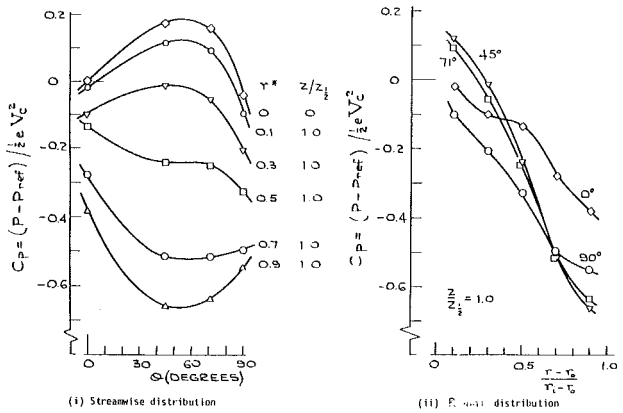

Fig. 9 Turbulent flow: wall static pressure measurements

more slowly that for the laminar flow, while the positive velocities occur in the region very close to the sidewalls. The maximum velocities are again found at $\theta = 60$ deg and are about 0.4 V_c, thus smaller than for the laminar flow. In common with the laminar flow, the profiles of radial velocity show that the flow is directed away from the inner wall within the core and towards it in the sidewall boundary layers. Local distortions occur, however, in the region of low streamwise momentum near the inner wall. A similar result has also been reported by Agrawal et al. [8] in their laminar flow.

The development downstream of the bend is shown in Figs. 7 (vi) and 8 (vi). The position of maximum streamwise velocity lies closer to the pressure wall while fluid near the suction wall has accelerated. The radial velocity has decayed less than was the case for the laminar flow and only one sense of circulation is evident at $X_H = 2.50$. The third component of velocity, W, is presented in Fig. 8 (vii) with the positive velocity direction defined as for laminar flow.

The wall pressures are presented in Fig. 9 (i) as $p(\theta)$ with r^* as parameter and in Fig. 9 (ii) as $p(r^*)$ with θ as parameter. The large radial pressure gradient at the inlet plane confirms the influence of the bend on the upstream duct. Initially an adverse pressure gradient develops on the pressure surface, and a favorable gradient on the suction surface, causing the observed deceleration and acceleration of the fluid near the respective surfaces. These trends are reversed after $\theta \simeq 50$ deg Fig. 9 (ii) shows that, as expected, the largest values of radial pressure gradient are associated with the large radial velocities at $\theta = 60$ deg and $\theta = 77.5$ deg. The pressure loss due to the bend is of the order of 0.1 ρV_c^2, which is comparable to the value reported by Ward Smith [1] for a similar configuration.

Figure 10 presents sample results of the turbulence quantities measured for the $\theta = 60°$ and $X_H = +2.50$ stations. A complete set of results is to be found in [14]. Figure 10 (i), (ii) gives contours of the Reynolds stress uv. Upstream of the bend values are low, corresponding to the small boundary layer thicknesses. At successive streamwise planes, large values of uv are found near the pressure surface and near the sidewalls indicating that momentum transport is large in the region coinciding with large streamwise-velocity gradients. The change in the sign uv is closely associated with changes in the sign $\partial U/\partial r^*$, at least for the region $z^* \lesssim 0.8$. On the suction side of the bend, the shear stress is generally small except for $\theta = 60$ deg.

Figures 10 (iii), (iv) and (v), (vi) show the corresponding development of $\tilde{u}$ and $\tilde{v}$, Initially, high values are to be found only within the boundary layers. The influence of the secondary motion can be detected at $\theta = 60$ deg and, at the exit, the turbulence is anisotropic with high $\tilde{v}$ near the pressure surface and high $\tilde{u}$ near the suction surface. At $X_H = 2.50$ the behavior of uv is complex with a large area on the suction surface being occupied by positive values of $-uv$ and near zero values on the pressure side. Momentum transfer in the spanwise (z^*) direction is accomplished through uw, which is plotted in Fig. 10 (vii). Values are large near $z^* = 0.5$, as could be expected, because of the large streamwise velocity gradients present. The maximum values of uv and uw are similar ($0.003 V_c^2$) although present in dif-

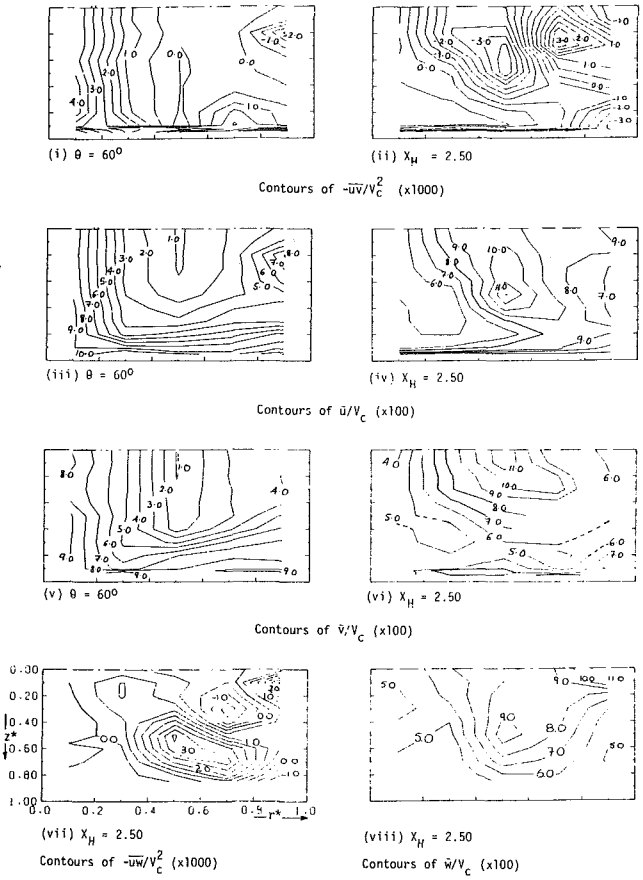

Fig. 10 Turbulent flow: Fluctuating velocities and cross-correlations

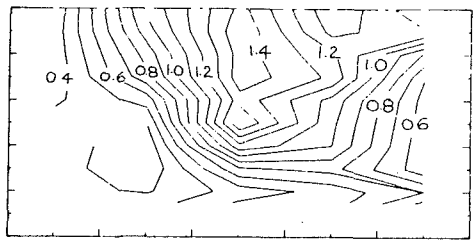

Fig. 11 Turbulent flow: contours of k/V_c^2 (x100) at $X_H = 2.50$

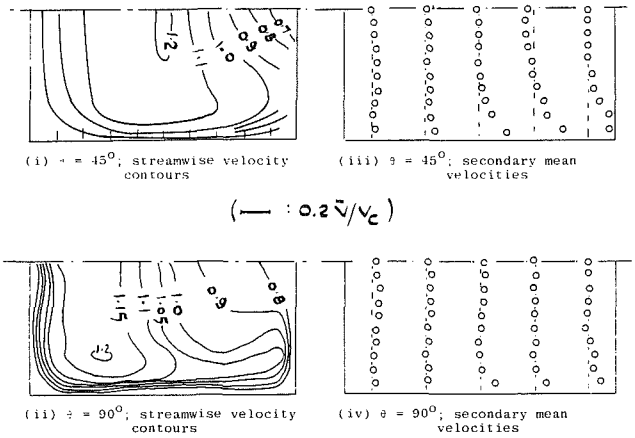

Fig. 12 Bend of 7.0 radius ratio: mean velocities

ferent regions. The contours of $\tilde{u}$ and $\tilde{v}$ also show large changes, with maximum values of the order of 0.11 V_c. Figure 10 (viii) shows contours of the $\tilde{w}$ component of fluctuating velocity. The contours of turbulent kinetic energy were constructed from $\tilde{u}$, $\tilde{v}$, and $\tilde{w}$ measurements and are presented in Fig. 11.

3.3 Turbulent Flow Results: Radius Ratio $R_r = 7.0$. Figure 12 presents results described by Enayet et al. [15] for a 90 deg bend of radius ratio 7.0, and with the same cross-section and length of straight upstream duct as the 2.3 radius ratio bend. Streamwise isotachs and radial velocity profiles at stations 45 and 90 deg around the bend are shown for a Reynolds number of 35,200. Measurements were not made at the entrance plane of the bend, but it is expected that the thickness of the wall boundary layers is almost identical to those of Subsection 3.2.

Comparison of the streamwise isotachs at $\theta = 45$ deg, Fig. 12 (i), with Figs. 7 (ii) and (iii) shows that increasing the radius ratio displaces the core fluid towards the mean radius of the bend ($r^* = 0.5$) although the influence of the secondary flow is less than in the laminar flow. Figure 12 (ii) shows that, by the exit plane of the bend, the core has been displaced to the outer wall which was not the case for $R_r = 2.3$, Fig. 7(v). It is noted that the maximum magnitudes of the radial velocity, given in Fig. 12 (iii) and (iv), are only 0.21 V_c and 0.09 V_c at these two planes and are substantially less for the smaller radius ratio bend.

4 Discussion

This section discusses the influence of the initial boundary layer thickness and radius ratio on the flow development. It closes by considering the calculation of this flow with particular reference to the type of the numerical technique to be used.

Influence of Boundary Layer Thickness at Bend Entry. Given that the upstream tangent to the bend is of fixed length, the primary result of increasing the Reynolds number is to decrease the boundary layer thickness in the entry plane of the bend. The presence of shear, whether laminar of turbulent, is mostly restricted to the near-wall regions and not directly relevant to the core flow development (see below, however, under the heading of calculation). To explain the differences between the laminar and turbulent flows, it is necessary to discuss those forces which dominate the transport of streamwise velocity.

The core flow develops under the separate influences of the streamwise pressure gradients and cross stream convection by the secondary flow. The pressure field within the duct (Fig. 9) qualitatively resembles that which would exist in a potential flow: over the first 45 deg or so of the suction surface the pressure gradient is favorable and thus tends to accelerate the fluid. The secondary flow, which is an inviscid, rotational fluid phenomenom, convects low momentum (boundary layer) fluid along the sidewalls towards the inner wall surface; the accumulation of this fluid tends to displace the core. Despite the difference in the laminar boundary layer thickness between this paper ($\simeq 0.25\ D_d$) and reference [9] ($0.50\ D_d$), the resulting isotachs at $\theta = 60$ deg and at the bend exit are very similar which suggests that the influence of boundary-layer thickness had diminished by $\theta = 60$ deg.

The thickness of these layers at inlet is, however, important in determining the magnitude of the secondary velocity, particularly in the first 30 deg or so of the bend, see Fig. 4 (ii) and 7 (ii). The formal connection is

$$d\left(\frac{\partial W}{\partial r} - \frac{\partial V}{\partial z}\right) = -2\left(\frac{\partial U}{\partial z} - \frac{\partial W}{\partial \theta}\right)d\theta \qquad (1)$$

which is the Squire and Winter result derived from inviscid

flow theory. The equation suggests, and measurements confirm, that the thinner entry boundary layers in the turbulent flow give rise to smaller cross stream velocities. The consequence is that the turbulent flow is dominated, over the first 45 deg, by acceleration of the core by the pressure gradient near the inner wall surface.

The positive cross-stream velocities are restricted to a small region adjacent to the side walls in the turbulent flow case. The same has been observed in the developing laminar flow of reference [8] with very thin inlet boundary layers and confirms that the phenomenon is related to the inlet streamwise velocity distributions rather than the Reynolds number. The measurements of Enayet et al. [15] also show the effect of increasing Reynolds number in a circular pipe bend for Reynolds numbers of 500 and 1093; the boundary layer thicknesses are comparable in the two cases (23 and 21 percent of the hydraulic diameter respectively) and the secondary flow generation is similar. The inviscid core flow moves nearer the outer wall in the higher Reynolds number flow as the centrifugal forces imparted to it are higher due to the higher bulk flow velocity. However, the measurements in the same pipe bend with a Reynolds number of 43,000 show a much thinner boundary layer and the core flow nearer the inside of the bend. The effect of Reynolds number change is thus related to the increase of the centrifugal forces imposed on the inviscid core flow.

Comparison with the turbulent flow results of reference 10 shows differences in the redistribution of the streamwise isotachs over the first 60 deg of the bend, due to the larger secondary flows present as a result of the thick inlet boundary layers. For example, the locus of maximum streamwise velocity in the symmetry plane of the bend ($z^* = 0$) remains very close to the mean radius of curvature ($r^* = 0.5$). Beyond this station, both sets of results show qualitatively similar behaviour with the locii of maximum streamwise velocity occurring near the mean radius of the bend. This coincides with the change in sign of the pressure gradient at the inner wall. The quantitative differences in the behaviour of the streamwise isotachs suggest differences in the streamwise vorticity. Thus, in the exit plane of the present bend, there are higher negative radial velocities ($-0.3\ V_c$ as opposed to $-0.15\ V_c$) and smaller velocities on the symmetry plane ($0.2\ V_c$ as opposed to $0.28\ V_c$). The flow of reference [10] is also affected by secondary flows driven by normal stresses and effectively absent, due to the shorter length of upstream duct, in the measurements of this paper.

For the fluctuating velocities there is qualitative agreement between the developing and fully-developed bend flows; for example, $-\overline{uv}$ is large near the suction surface and, at the exit of the bend, $\tilde{v}$ is larger near the suction surface while $\tilde{u}$ is large near the pressure surface. Quantitative agreement is not found and is not expected. At the inlet $\overline{uv}$ is up to $0.0013\ V_c^2$ in the present flow as compared to $0.004\ V_c^2$ with the thicker boundary layers; at exit, the respective values are $0.003\ V_c^2$ and $0.007\ V_c^2$. The influence of streamline curvature is expected to increase turbulence levels near the pressure surface and to decrease them near the suction surface and the behaviour of $\overline{uv}$ and $\tilde{v}$ support this expectation although the increase in $\tilde{u}$ at the inner wall might appear anomalous.

The effect of streamline curvature on the turbulence structure can best be analysed by examining the structural parameters $R = \overline{uv}/\tilde{u}\tilde{v}$ and $\alpha_1' = -\overline{uv}/1.5\ (\tilde{u}^2 + \tilde{v}^2)$, see for example Hoffmann and Bradshaw [16], which were calculated at each measurement station. Although it is important to note that these are strictly appropriate only for two-dimensional flows, where $\overline{uv}$ is the dominant shearing stress, they should be sufficiently accurate for qualitative interpretation of this flow.

The correlation coefficient, R, increases from an initial maximum value of 0.4 near the outer wall to about 0.8 by $\theta = 60$ deg and thereafter decreases. The trends near the inner wall are more complicated, presumably because of the strong three-dimensionality of the boundary layer. The anisotropy coefficient, α_1', follows very similar trends to the correlation coefficient, reaching a maximum value of about 0.25 by $\theta = 60$ deg. The correlation and anisotropy coefficients are typically 0.4 and 0.15, respectively, for turbulent shear flows: the increase in their values which is observed on the pressure surface, corresponding to destabilizing curvature, is consistent with the expected influence of streamline curvature.

Influence of the Radius Ratio of the Bend. The discussion of the previous paragraphs can be extended to explain the development of the streamwise isotachs for the larger radius ratio.

An order-of-magnitude estimate of the induced pressure gradients and the associated secondary flow velocities in the 2.3 and 7.0 radius ratio bends show that the pressure gradient is larger by a factor of $(7/2.3)^2 \simeq 10$ in the strongly curved duct and the corresponding secondary velocities are larger by a factor of nearly $(7/2.3)^{1/2} \simeq 2$. The streamwise pressure gradient is expected to be nearly zero over most of the mildly curved bend (see Ward Smith [1]) and has an effect only in the vicinities of the bend inlet and exit. As a result, the inner wall acceleration is not observed at $\theta = 45°$ for $R_r = 7.0$, Fig. 12 (i), and the influence of the secondary flow redistribution is more apparent than for $R_r = 2.3$, Figs. 7 (ii) and (iii). Comparison of the 45 and 90 degree station isotachs shows the movement of the core flow towards the outer wall near the bend exit as the secondary flow redistributes the streamwise isotachs.

Ward Smith [1] concluded from his exit plane total pressure measurements that the secondary flows are weaker and distributed over a larger part of the bend cross-section in bends of milder curvature. The second observation is made from fully-developed bend flow results, and it is not in accordance with the present findings, nor with his own thin inlet boundary layer results. In general, a smaller region of weaker secondary flow is present in bends of milder curvature compared to that of strongly curved bends. The shear stresses, although they were measured to be of the same order in the bends of mild and strong curvature, are shown by an order-of-magnitude analysis to be ten times more significant in relation to the pressure gradient in the large radius ratio bend. While the pressure losses become less significant, the frictional losses are expected to be more important in bends of milder curvature (Ward Smith [1], Eskinazi and Yeh [17]), an observation which is in accordance with the aforementioned estimate. It is noted, however, that the rapid decay of the secondary velocities on approaching the exit plane of the bend, which has been observed in all the bends, is also an irrotational, and not a viscid, fluid phenomenon. The decay is associated with the production of streamwise vorticity of the opposite direction to that produced at the bend inlet by the presence of positive $\partial U/\partial z$ at the inner wall of the bend. This can be seen from equation (1) and has been noted by Rowe [4]. This mechanism explains the measurements of positive radial velocity at the inner wall surface by Argrawal et al. [8].

Calculation of the Flow in Curved Ducts. The calculation of flows in curved ducts can be performed, in principle, by numerical integration of the equations of fluid motion (see, for example, Humphrey et al. [9] and [10], Leschziner and Rodi [18], and Moore and Moore [19]. In turbulent flow, the Reynolds-averaged equations are used, together with turbulence models of various degrees of complexity. Although it is possible to understand the flow on the basis of inviscid, rotational theory, the inclusion of viscous effects in the equations of motion is important for a number of reasons. The presence of rotational flow at the inlet plane of the bend, in the absence of which there would be no secondary flow, is

due to viscous effects; the continued generation of vorticity at the outer and side walls within the bend is also important (particularly, say, in river bend flows: see Scorer [20]); and Rowe [4] has suggested that vortex dissipation at the inner wall is also important.

Previously reported calculations of laminar flow [9] have shown that numerical meshes of 20 (streamwise) × 15 (radial) × 10 (spanwise) nodes are insufficient to resolve the flow field in the 90 deg bend accurately. Calculations of the laminar flow of this paper by Buggeln, Briley and McDonald [21], with the numerical scheme of Briley and McDonald [22] and [23] and 26 × 28 × 13 nodes, still show some quantitative, though not qualitative, disagreement. This represents an increase in the spatial resolution of between 1.3 and 1.9 in the various coordinate directions. Since the upwind-differencing representation of convection, which is probably used at least for the streamwise convection fluxes, possesses a truncation error proportional to the grid spacing the reduction in this error is also related to the factors quoted above. The storage requirement is, however, greater by a factor of 3.2. These two examples well illustrate that grid node resolution hinders accurate numerical solution: however a further increase in the number of nodes may result in exceeding the core storage of many machines. The use of "partially parabolic," rather than "fully elliptic" numerical solution schemes (Pratap and Spalding [24]), may offer an attractive way of increasing the resolution of the area of integration, provided that the flow fulfills the physical requirements of the partially parabolic approximation. These are the existence of a predominant flow direction along which diffusion fluxes are small and convective influences are exerted only in that direction. The measurements suggest that these requirements are fulfilled, although Buggeln et al. [21] report a small (calculated) region of flow separation on exit from the bend. Whatever the chosen numerical scheme, the results of this paper describe, in careful detail, the flow conditions at the inlet to the bend and these may form the boundary conditions at this station. As a result it is not necessary for the calculation scheme to expend effort on the flow in the upstream tangent (cf. [9]). The measurements are available on magnetic tape from the NASA Lewis Research Center to facilitate future comparisons with calculation methods.

In the absence of truly grid-independent solutions for laminar flow, it is premature to judge the comparative virtues of various turbulence models for flows in bends. The ratio of boundary layer thickness at inlet to the mean radius of curvature is sufficiently large ($\simeq 10^{-1}$) to cause a large influence of streamline curvature (an "extra rate of strain") on the turbulence. Hence, the use of advanced turbulence models, such as Reynolds stress closures, would be indicated. It should be added, however, that the calculation of Buggeln et al. [21], using a simple Prandtl-Kolmogorov relationship, give results which are in closer agreement with the measurements than is the case for the laminar flow.

5 Concluding Remarks

1. The paper has reported in detail on the velocity and pressure characteristics of the flow in a square duct of strong curvature with a short upstream tangent for laminar and turbulent flows.
2. Secondary flows of the first kind are present and are more pronounced in the laminar flow, reaching a maximum of 0.6 V_c as a compared with 0.4 V_c in the turbulent case. This is attributed mainly to the thicker (0.25 d versus 0.15 d) boundary layers at the bend inlet.
3. In laminar flow, the coreflow migrates from the mean radius of the bend towards the pressure surface. In the turbulent flow case, the thinner boundary layers result in the predominance of the streamwise pressure gradient and the coreflow initially migrates towards the suction surface.
4. Comparisons have been made with laminar and turbulent flows with fully developed profiles at the inlet to the bend. Large differences in the development of the streamwise isotachs are evident only in the case of 0.15 d entry boundary layer thickness. For turbulent flow, the comparison shows the fluctuating velocity and shear stress distributions to be similar although, as expected, the levels are smaller in the case presented here.
5. The results for turbulent flow in a identical duct of mild curvature show that the secondary flows reach a peak value of 0.2 V_c and are confined to a smaller region near the sidewalls. Their relative effect on the streamwise flow development is greater than for the strongly curved bend.
6. The detail and accuracy of the measurements is sufficient for the evaluation of both numerical techniques (laminar flow results) and turbulence models (turbulent flow results). Consideration of the nature of the flows and of previously reported elliptic calculations suggests that partially-parabolic techniques are adequate and appropriate.

Acknowledgments

The authors gratefully acknowledge financial support from the National Aeronautics and Space Administration, Lewis Research Center, and the Science Research Council. We thank Mr. B. Anderson and Dr. L. Povinelli of the Lewis Research Center and Dr. M. M. Gibson and Mr. M. M. Enayet of Imperial College for their contributions.

References

1 Ward Smith, A. J., *Pressure Losses in Ducted Flows*, Butterworths, London, 1971.

2 Itō, H., "Pressure Losses in Smooth Pipe Bends," ASME *Journal of Basic Engineering*, Vol. 82, 1960, p. 131.

3 Mori, Y., Uchida, Y., and Ukon, T., "Forced Convective Heat Transfer in a Curved Channel With a Square Cross-Section," *International Journal Heat Mass Transfer*, Vol. 14, 1971, p. 1787.

4 Rowe, M., "Measurements and Computations of Flow in Pipe Bends," *J. Fluid Mech.*, Vol. 43, 1970, p. 771.

5 Mullin, T., and Greated, C. A., "Oscillatory Flow in Curved Pipes. Part 1. The Developing-Flow Case. Part 2. The Fully Developed Case, *J. Fluid Mech.*, Vol. 98, 1980, p. 383.

6 Nippert, H., "Über den Strömunqsverlust in gekrümmten Kanälen," VDI-Forschungsarbeiten 320, 1929.

7 Bruun, H. H., "An Experimental Investigation of Secondary Flow Losses in Bends With Rectangular Cross-Sections," Univ. of Cambridge, Dept. of Eng. Report CUED/A-Turbo/TR 95, 1979.

8 Agrawal, Y., Talbot, L., and Gong, K., "Laser Anemometer Study of Flow Development in Curved Circular Pipes," *J. Fluid. Mech.*, Vol. 85, 1978, p. 497.

9 Humphrey, J. A. C., Taylor, A. M. K. P., and Whitelaw, J. H., "Laminar Flow in a Square Duct of Strong Curvature," *J. Fluid Mech.* Vol. 83, 1977, p. 509.

10 Humphrey, J. A. C., Whitelaw, J. H., and Yee, G., "Turbulent Flow in a Square Duct With Strong Curvature," *J. Fluid. Mech.*, Vol. 103, 1981, p. 443.

11 Taylor, A. M. K. P., "Confined Isothermal and Combusting Flows Behind Axisymmetric Baffles," Ph.D thesis, University of London, 1981.

12 Durst, F., Melling A., and Whitelaw, J. H., *Principles and Practice of Laser Doppler Anemometry*, 2nd Edition, Academic Press, London, 1981.

13 Melling, A., and Whitelaw, J. H., "Turbulent Flow in a Rectangular Duct," *J. Fluid Mech.*, Vol. 78, 1976, p. 289.

14 Taylor, A. M. K. P., Whitelaw, J. H., and Yianneskis, M., "Measurements of Laminar and Turbulent Flow in a Curved Duct with Thin Inlet Boundary Layers," NASA Contractor Report 3367, 1981.

15 Enayet, M. M., Gibson, M. M., Taylor, A. M. K. P., and Yianneskis, M., "Measurements of Laminar and Turbulent Flow in Curved Ducts," Imperial College, Mech. Eng. Dept. Report, FS/81/7, 1981.

16 Hoffmann, P. H., and Bradshaw, P., "Turbulent Boundary Layers on Surfaces of Mild Longitudinal Curvature," Imperial College, Aeronautics Dept. Report 78-04, 1978.

17 Eskinazi, S., and Yeh, H., "An Investigation of Fully-Developed Turbulent Flows in a Curved Channel," *J. Aero. Sci.*, Vol. 23, 1956, p. 23.

18 Leschziner, M. A., and Rodi, W., "Calculation of Strongly Curved Open

Channel Flow," *Journal of the Hydraulics Division*, ASCE, Vol. 105, 1979, p. 1297.

19 Moore, J., and Moore, J. G., "A Calculation Procedure for Three-Dimensional, Viscous, Compressible Duct Flow. Part 1 - Inviscid Flow Considerations. Part 11 - Stagnation Pressure Losses in a Rectangular Elbow," ASME *J. Fluids Engineering*, Vol. 101, 1979, p. 415.

20 Scorer, R. S., *Environmental Aerodynamics*. Ellis Horwood, Chichester, 1978.

21 Buggeln, R. C., Briley, W. R., and McDonald, H., "Computation of Laminar and Turbulent Flow in Curved Ducts, Channels, and Pipes Using the Navier-Stokes Equations," Science Research Associates Report R80-920006-F, prepared for the Office of Naval Research, 1980.

22 Briley, W. R., and McDonald, H. "Solution of the Multi-Dimensional Compressible Navier-Stokes Equations by a Generalized Implicit Method, *J. of Comp. Physics*, Vol. 24, 1977. p. 372.

23 Briley, W. R., and McDonald, H., "On the Structure and Use of Linearized Block ADI and Related Schemes," *J. of Comp. Physics*, Vol. 34, 1980, p. 54.

24 Pratap, V. S., and Spalding, D. B., "Numerical Computations of the Flow in Curved Ducts," *Aero. Quart.* Vol. 26, 1975, p. 219.

J. O. Cruickshank
Carrier Corporation,
Research Division,
Syracuse, N.Y. 13221

B. R. Munson
Department of Engineering
Science and Mechanics,
Engineering Research Institute,
Iowa State University,
Ames, Iowa 50011

The Viscous-Gravity Jet in Stagnation Flow

Simple solutions are presented for the equation governing one-dimensional flow of very viscous jets that issue from a round orifice and fall against a flat plate. Due to the viscous axial stresses developed, the jet may be either in tension or compression, depending on the values of various dimensionless parameters involved. The comparison of the theoretical and experimental results is good.

Introduction

The flow of a jet of fluid from a round orifice has been the subject of many experimental and theoretical investigations for a number of years. Although the flow geometry is quite simple, a detailed, nearly exact modeling of the jet flow problem is very complex. It is possible, however, to develop rather simple solutions that, although lacking in some detail, do predict many of the essential phenomena of the flow. The simple solution given by Trouton [1] for a very viscous, semi-infinite jet is such an example.

The purpose of this note is to provide simple approximate solutions for the flow of a very viscous jet against a solid surface, as shown in Fig. 1. A comparison with experimental results is also presented.

The One-Dimensional Jet Model

The equations governing the one-dimensional flow of a viscous fluid from a circular orifice into the air or other fluids of negligible viscosity have been derived by several persons. The paper by Matovich and Pearson [4] contains detailed discussions of these equations.

The basic assumption is that the jet is one-dimensional; that is, velocity components normal to the jet axis can be neglected compared to that along the axis, v. It is also assumed that this axial velocity is constant across the jet. Thus, the dimensionless velocity of the fluid within the jet is assumed to be given $v=v(x)$, where x is the dimensionless axial distance along the jet measured from the orifice. The velocity and jet radius at the orifice, v_0, and a_0, are used as the characteristic speed and length parameters.

The resulting governing equation can be written in dimensionless form as

$$Fvv' = 1 + (3/R)[v'' + (v')^2/v] - (F/2W)v'/v^{1/2} \qquad (1)$$

where F, W, and R are the Froude, Weber, and Reynolds number defined by $F = v_0^2/ga_0$, $W = \rho a_0 v_0^2/\sigma$, and $R = \rho a_0 v_0/\mu$. Here ρ, μ, and σ are the fluid density, viscosity, and surface tension, g is the acceleration of gravity and

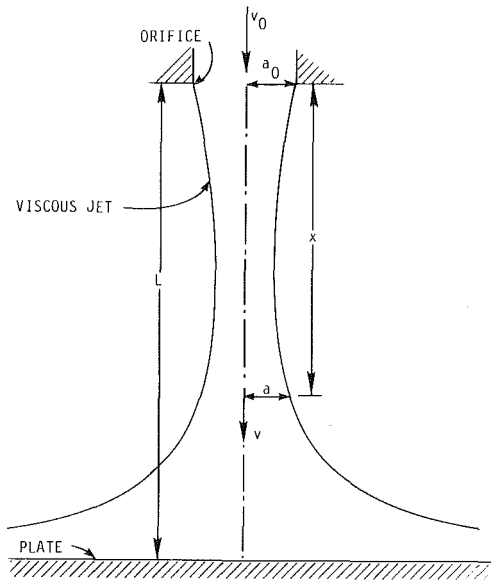

Fig. 1 A circular jet in stagnation flow

$(\ )' = d/dx$. Equation (1) includes the effects of gravity, viscosity, surface tension, and inertia.

Previous solutions to this equation have dealt with the problem of the semi-infinite jet – one that starts at $x=0$ and continues unimpeded to $x \to \infty$ [4, 1]. As yet there are no known analytical solutions for arbitrary values of F, W, and R. If, however, the Froude and Reynolds numbers are small (slowing moving, very viscous jet) and the Weber number is large (small surface tension jet), the left hand side (inertia effects) and the last term on the right hand side (surface tension effects) of equation (1) may be neglected. For such flows only viscous and gravitational forces are important. Analytic solutions for this viscous-gravity jet flowing against a plate as shown in Fig. 1 are presented below. In addition, these solutions are compared to numerical solutions of the complete equation (1).

Rather than solve directly for the velocity distribution along the jet, $v(x)$, we solve the governing equation in terms of the jet radius, $a(x)$. This can be done easily by using continuity considerations which state that $a^2 v = 1$. When written in terms

Contributed by the Fluids Engineering Division for publication in the JOURNAL OF FLUIDS ENGINEERING. Manuscript received by the Fluids Engineering Division, July 23, 1980.

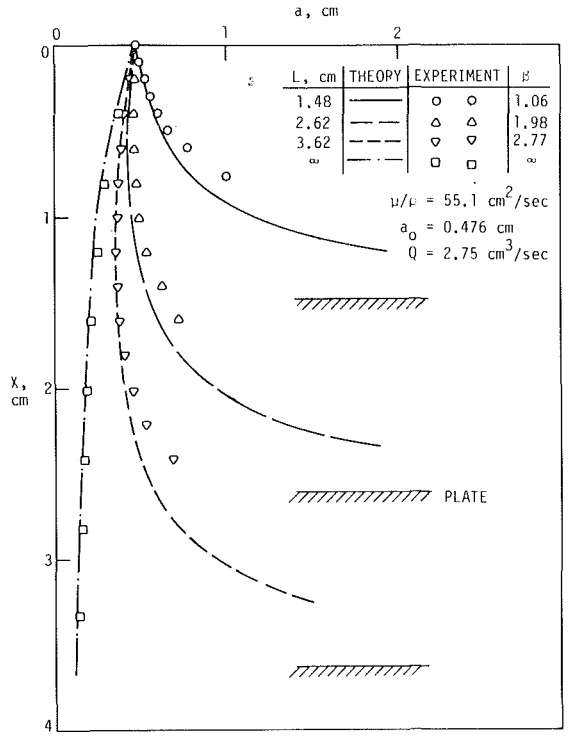

Fig. 2 Jet profiles for constant flow rate but variable orifice-to-plate distance. The theoretical curves are for both the viscous-gravity jet and the numerical solution of equation (1) (20:1 odds uncertainty estimates are a ± 5 percent, x ± 5 percent).

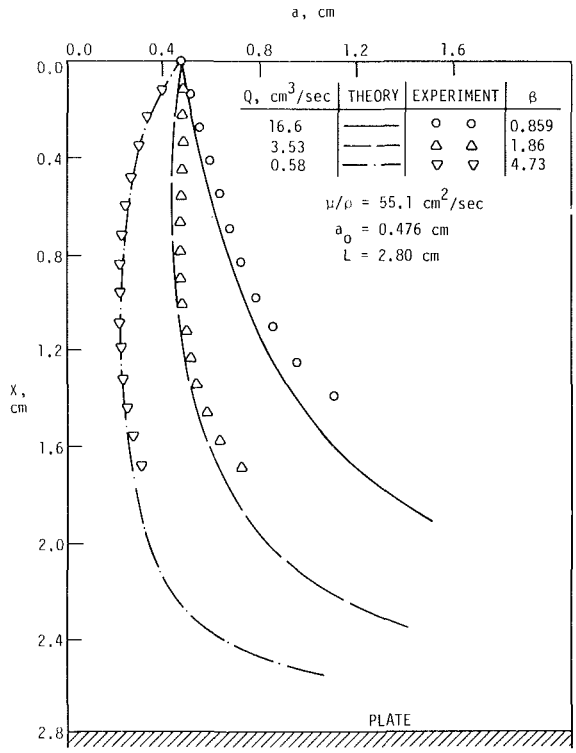

Fig. 3 Jet profiles for constant orifice-to-plate distance but variable flow rate. The theoretical curves are for both the viscous-gravity jet and the numerical solutions of equation (1) (20:1 odds uncertainty estimates are a ± 5 percent, x ± 5 percent).

of the jet radius, the governing equation for the viscous-gravity jet becomes

$$aa'' - (a')^2 = a^4K^2 \tag{2}$$

where $K^2 = 6F/R = 6\mu v_0/\rho g a_0{}^2$ is a dimensionless parameter representing the ratio of viscous to weight forces. The non-dimensional boundary conditions for the stagnation flow jet with the plate a distance L below the orifice are

$$a = 1 \text{ at } x = 0$$

and

$$a \to \infty \text{ at } x = H \tag{3}$$

where $H = L/a_0$ is the nondimensional distance from the orifice to the stagnation surface.

One of the basic assumptions of the one-dimensional approximation is that the radial component of velocity is much smaller than the axial component. Obviously, this assumption is severely violated near the plate ($x = H$) where the actual flow is essentially radial. Although it seems questionable to impose the boundary conditions of equation (3), comparison of the resulting solutions with experimental results is quite good.

The solution to the nonlinear governing equation (2), depends on the value of the parameter $\beta \equiv H/K$ and can be written as shown below:

$$\text{If } \beta = 1, \text{ then a } = 1/(a - x/K) \tag{4}$$

$$\text{If } \beta <, \text{ then } a = \sinh c_1/\sinh\left(c_1 - \frac{x}{K}c_1\right) \tag{5}$$

where c_1 is a constant given by the solution of

$$c_1 - \beta\sinh c_1 = 0, (c_1 \neq 0)$$

$$\text{If } \beta > 1, \text{ then a} = \cos c_2/\cos\left(\frac{x}{K}\cos c_2 + c_2\right) \tag{6}$$

where c_2 is a constant given by the solution of

$$\beta\cos c_2 + c_2 = \pi/2, (c_2 \neq \pi/2)$$

A few important properties of the above simple solutions can be easily shown. The axial normal stress within the jet, τ_{xx}, depends directly on the velocity gradient. In dimensional form $z_{xx} = 3\mu v'$. The jet is in tension or compression depending on whether $a' < 0 (v' > 0)$ or $a' > 0 (v' < 0)$, respectively. It can be shown that the jet starts out in tension provided $\beta > \pi/2$, and that it starts out in compression provided $\beta < \pi/2$. In either case, however, at least the portion of the jet near the plate is in compression since $a' > 0$ for at least the lower portion of the jet.

Results

We compare the simple analytic solutions discussed above with experimental results and with numerical solutions of the complete one-dimensional governing equation, equation (1).

The fluid used was 5,510 centistoke silicone oil which is more than three orders magnitude more viscous than water. The orifice diameter was 0.952 cm with flow rates from 0.58 cm^3/s to 16.6 cm^3/s and orifice-to-plate distances from 1.48 cm to "infinity." The jets were produced by using a variable-speed-drive gear pump to pump the oil through a round orifice. The jet profiles were measured from photographs of the jet.

The results shown in Fig. 2 indicate the jet profile for a given flow rate ($Q = 2.75$ cm^3/s), but for different orifice-to-plate distances, L. The theoretical results are those obtained for the viscous-gravity solution (equations (4) through (6)) and by numerical integration of the full one-dimensional equation including inertia and surface tension (equation (1) with boundary conditions, as in equation (3)). In all cases, the viscous-gravity jet solutions and the numerical solutions agree to within a width of the line on the graph. Therefore only one theoretical curve is indicated for each value of L.

It follows that for the jets shown, inertia and surface tension are indeed negligible. That this is reasonable can be seen by considering the important dimensionless parameters involved. For the conditions of Fig. 2 the following values are obtained: $F = 0.032$, $W = 0.314$, and $R = 0.033$. Thus, the important parameters of equation (1) are $F = 0.032$, $3F/R = 2.9$, and $F/2W = 0.051$, indicating that gravity and viscosity are the dominant forces.

The agreement between the theoretical and experimental results is quite good, especially in light of the rather severe restrictions imposed by the one-dimensional assumption. The assumption that da/dx is small is certainly not valid near the plate, nor over a large portion of some of the jets /especially the small length to diameter ones). In spite of this, the simple one-dimensional solution provides a reasonable approximation of the jet shape.

The results shown in Fig. 3 show the jet profile for a given orifice-to-plate distance ($L = 2.80$ cm), but for different flow rates. The characteristics are similar to those of Fig. 2. As in Fig. 2, the simple viscous-gravity jet solutions are indistinguishable from the numerical solution of the full equation (including inertia and surface tension), so that only one theoretical line is plotted for each Q. The comparison between the theoretical and experimental results is quite good.

Obviously, there are limitations to the applicability of the viscous-gravity solutions. The fact that the inertia and surface tension parameters are small ($F << 1$ and $F/2W << 1$) does not guarantee that the actual flow will agree with the viscous-gravity jet. For example, for the semi-infinite jet ($\beta = \infty$), inertia effects may become important far from the orifice even though they are negligible near the orifice. Also, for small plate-to-orifice ratios the one-dimensional assumption may not be reasonable.

Conclusions

The flow of a very viscous jet against a flat plate has been determined using the rather strict assumptions that the jet can be modeled as one-dimensional flow governed by viscous and gravity forces only. Obviously, the one-dimensional assumption breaks down completely in the region near the plate. In spite of this fact, the simple solutions presented compare favorably with experimental results. More accurate results could be obtained by various means – numerical integration of the full axisymmetric Navier-Stokes equations or a matching of the one-dimensional jet flow presented here with other approximate flows near the plate. However, it is felt that for many applications the simple solutions presented here will be useful as reasonable approximations to a very complex flow.

Acknowledgment

The support of the Engineering Research Institute of Iowa State University through funds provided by the National Science Foundation, Grant No. ENG78-19373, has been appreciated.

References

1 Trouton, F. T., "On the Coefficient of Viscous Traction and Its Relation to that of Viscosity," *Proc. R. Soc. Edinburgh, Sect. A*, Vol. 77, May 1906, pp. 426–440.

2 McCarthy, M. J., and Malloy, N. A., "Review of Stability of Liquid Jets and the Influence of Nozzle Design," *Chem. Engr. J.*, Vol. 7, 1974, pp. 1–20.

3 Cruickshank, J. O., and Munson, B. R., "Viscous Fluid Buckling of Plane and Axisymmetric Jets," *J. Fluid Mech.*, in press.

4 Matovich, M. A., and Pearson, J. R. A., "Spinning of Molten Threadline," *Ind. Eng. Chem. Fundam.*, Vol. 8, No. 3, 1969, pp. 512–519.

R. F. Gans
Associate Professor.
Mem. ASME

S. M. Yalisove[1]
Graduate Student.

Department of Mechanical Engineering,
University of Rochester,
Rochester, N.Y. 14627

Observations and Measurements of Flow in a Partially-Filled Horizontally Rotating Cylinder

The authors report measurements of azimuthal velocity versus radius in a partially-filled horizontally rotating cylinder. These data confirm theoretical calculations for laminar flow. Three nonlaminar flow states are described and a map shows boundaries separating the laminar state, and two of the nonlaminar states, in a two parameter space.

Introduction and Outline of Theory

A liquid partially filling a cylinder rotating rapidly about its principal axis, held horizontal, exhibits several possible flow states. All but the simplest of these appear too complex for theoretical analysis. To date no criteria have been established for the transformation from one state to another, nor has there been a comprehensive description of these flow states in the literature. It is the purpose of this note to present velocity measurements confirming the results of linear theory for the simplest flow state, and to describe the other flow states observed in this system, and map their occurrence in a parameter space.

The former purpose bears on an experimental discrepancy, discussed below, and the latter on the general problem of the stability of rotating bodies partly filled with liquid. Examples include fuel tanks in spinning rockets, and certain fluid-filled projectiles which contain more than one fluid. Theoretical and experimental work addressing these problems directly has been done by Hendricks and Morton [1], who address the question of fluid-rotor interaction assuming relatively simple fluid dynamics, and Scott [2], [3] and Scott and D'Amico [4], who deal more specifically with the projectile problem. The last cited paper presents experimental results dealing with container-fluid interaction in vertically-oriented cylinders.

The simplest flow state will be termed the laminar state. (See Fig. 1.) In this state the liquid is held against the walls by centripetal forces. There is a well defined, smooth cylindrical interface between the liquid and the air which occupies the rest of the cylinder. The interface is displaced downward with respect to the cylinder axis. Theoretical understanding of this flow is a necessary first step in any effort to understand transitions from this flow state to any of the others.

The theory is presented in considerable detail elsewhere [5]–[9]. We outline the details necessary to make this note reasonably self-contained.

The analysis is performed using a combined amplitude and boundary layer expansion. Two small dimensionless parameters are defined: $\epsilon = g/\Omega^2 a$ measures the amplitude of the departure of the flow from solid rotation; $E = \nu/\Omega a^2$ measures the viscous effects. The physical constants g, Ω, a, and ν denote gravitational acceleration, container rotation rate, container radius and liquid kinematic viscosity respectively. We term the part of the perturbation solution

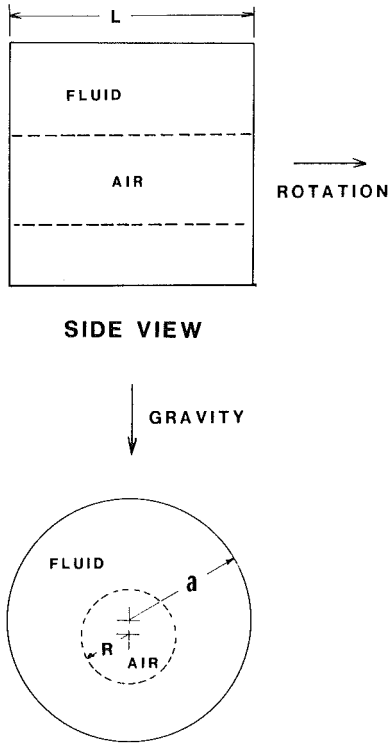

Fig. 1 Side and end views of the experiment

[1] Present Address: Department of Materials Science & Engineering, University of Pennsylvania, Philadelphia, Pa.

Contributed by the Fluids Engineering Division and presented at the Winter Annual Meeting, Washington, D.C., November 16–19, 1981, of THE AMERICAN SOCIETY OF MECHANICAL ENGINEERS. Manuscript received by the Fluids Engineering Division, November 12, 1980.

proportional to ϵ the linear, or first order, part. That proportional to ϵ^2 is called the second order part.

The linear and second order solutions each have "inviscid" and boundary layer components. The method of solution is perhaps easier to follow after some notation has been introduced. Thus we let $\mathbf{u}$ denote the velocity vector in the fluid, made dimensionless by dividing by Ωa. The theory expands $\mathbf{u}$ as

$$\mathbf{u} = \frac{\Omega \times \mathbf{r}}{\Omega a} + \epsilon(\hat{\mathbf{u}}_1 + \tilde{\mathbf{u}}_1) + \epsilon^2(\hat{\mathbf{u}}_2 + \tilde{\mathbf{u}}_2) + \ldots,$$

where the carat denotes an inviscid solution and the tilde a boundary layer correction. To the level to which the analysis has been carried the inviscid solutions satisfy equations in which E is identically zero, eliminating the viscous terms, and the boundary layer corrections satisfy equations in which the coordinate normal to the boundary in question has been rescaled to bring the viscous terms back. (The scaling is different at different orders and on different boundaries.)

The overall solution is constructed by solving successive approximations to the Navier-Stokes equations with appropriate boundary conditions. Each element of the solution generates a term which enters the next approximation as an inhomogeneous terms. The sequence is as follows:

1. The action of gravity on the density contrast at the air-liquid interface forces $\hat{\mathbf{u}}_1$.
2. Since $\hat{\mathbf{u}}_1$ cannot satisfy tangential boundary conditions these conditions force $\tilde{\mathbf{u}}_1$.
3. Self-interaction of $\hat{\mathbf{u}}_1$, through the nonlinear term, $\hat{\mathbf{u}}_1 \cdot \nabla \hat{\mathbf{u}}_1$, forces $\hat{\mathbf{u}}_2$.
4. Finally, both interactions among $\hat{\mathbf{u}}_1$ and $\tilde{\mathbf{u}}_1$, and unsatisfied tangential boundary conditions, force $\tilde{\mathbf{u}}_2$.

The successive approximations are all written in an inertial cylindrical coordinate system, the z axis of which is parallel to the rotation vector and perpendicular to gravity. In such a coordinate system the gravity vector is singly-periodic in the azimuthal coordinate ϕ. Thus the first order (linear) solutions $\hat{\mathbf{u}}_1$ and $\tilde{\mathbf{u}}_1$ are also singly-periodic in ϕ. Their interactions have components which are axisymmetric and components which are doubly-periodic. Only the former are of interest here. They drive what we term the retrograde rotation, described below.

The theory provides predictions of the linear velocity, the displacement from the center of the air core, and the axisymmetric second order flow. The displacement has been verified previously [10]. The results reported below verify the velocity we have called $\hat{\mathbf{u}}_1$.

The second order flow at the interface is not in agreement with theory. To best visualize the experimental discrepancy imagine a small, slightly buoyant particle floating at the interface, almost totally submerged in the liquid. Its average rotation rate, the interface rotation rate, will be different from that of the container. One can calculate the interface rotation rate from the axisymmetric second order solution. The measured rotation rate is different. The discrepancy in the quantity $\Delta\Omega$, which we have called the "retrograde rotation," representing the difference between the particle rotation rate and the container rotation rate, can be as much as a factor of seven. Such a discrepancy is disturbing.

We believe the discrepancy to arise from nonideal behavior at the interface because: (1) the retrograde rotation at a rigid interface, for which the boundary condition is well-defined, agrees with theory [9]; (2) the measured retrograde rotation lies between that predicted from a free surface and a rigid interface [9]–[10]; (3) the magnitude of the nonlinear driving terms involving $\tilde{\mathbf{u}}_1$, the boundary layer component, is extremely sensitive to the boundary condition; and (4) the measurements we report here verify that the theory is in essence correct.

After discussing the experimental procedure we present direct velocity measurements verifying the linear theory: profiles of azimuthal velocity as a function of radius, followed by unpublished data taken several years ago by one of us (RFG) defining the location in parameter space of other flow states, which can be important in problems of the stability of fluid filled rotors.

Experimental Procedure

We measured the azimuthal velocity on vertical ($\phi = \pi/2$) and horizontal ($\phi = 0$) planes, using a locally assembled laser Doppler anemometer, working in the reference beam mode. We used a diffuse plate as a beam splitter, and collected the frequency information using a photo-multiplier tube. The Doppler signal was analyzed and tracked using a a prototype of the frequency tracker described by Wilmshurst and Rizzo [11]. Details of the experimental apparatus are reported elsewhere [12]. (The cylinder is made of plexiglas. Its inside dimensions are $a = 79.5$ mm, $L = 170$ mm. Rotation rates ranged from 7.67 hz to 17.7 hz. The working fluid for all experiments was tap water, for which $\nu \approx 1 \times 10^{-6}\text{m}^2/\text{s}$). We have chosen $\epsilon(= g/\Omega^2 a)$, $c = R/a$ and $\text{E}(= \nu/\Omega a^2)$[2] as dimensionless numbers to describe the parameter space. This choice was inspired by Phillips' early work [5].

The procedure for a single experimental session was as follows: The cylinder was completely filled and brought up to speed. A profile of frequency versus radius was taken at all the speeds to be used during the run. This gave a system calibration between frequency and azimuthal velocity and established the position (measured on the dial of a milling machine crank) corresponding to zero radius, necessary for comparison to theoretical predictions. The center was not directly accessible because of the axles. (Extrapolation of the calibration curves to the position for which the frequency vanished determined the origin more precisely than subtracting the container radius from the position of the outer wall, determined by occlusion of the beam.)

[2] For the work reported here $\text{E} << 1$ is all that is necessary. No explicit dependence on E is expected, or was found.

Nomenclature

a = container radius
A,B = parameters in data curve fit
c = ratio of core radius to container radius, R/a
E = Ekman number, $\nu/\Omega a^2$
f_c = Doppler frequency for calibration runs
f_e = Doppler frequency for experimental runs
δf = $f_c - f_e$
g = acceleration of gravity (vector quantity boldface)
L = length of the container
r = radial coordinate
R = core radius
$\mathbf{u}$ = vector velocity in the liquid
$\hat{\mathbf{u}}_1$ = inviscid first order velocity
$\hat{\mathbf{u}}_2$ = inviscid second order velocity
$\tilde{\mathbf{u}}_1$ = boundary layer first order velocity
$\tilde{\mathbf{u}}_2$ = boundary layer second order velocity
v = azimuthal velocity
y = normalized frequency difference
$\hat{y}$ = "best fit" for y
z = axial coordinate
ϵ = $g/\Omega^2 a$, measure of the first order flow
ν = kinematic viscosity
ϕ = azimuthal coordinate
Ω = container rotation rate (vector quantity boldface)
$\Delta\Omega$ = difference between container and interface rotation rates

The container was stopped and enough liquid removed to set R, hence c. Radial profiles were measured, and the container was refilled and the calibration rechecked. Runs for which the initial and final calibration did not agree were discarded.

Results

Table 1 shows the ranges of ϵ and E for the $\phi = \pi/2$ experiments. Each pair corresponds to a single rotation rate. The parameter c ranged from 0.4 to 0.8 in intervals of 0.1. Experiments were performed at 24 of the 25 possible combinations. The combination $\epsilon = 2.06 \times 10^{-2}$ and $c = 0.6$ was omitted.[3]

We denote the Doppler frequency profiles versus radius for the full cylinder by $f_c(r)$, and the Doppler frequency profiles for the partially-filled cases, $f_e(r)$. Values of f_c and f_e were in the range of 100-1000 khz, and their difference, $\delta f = f_c - f_e$, was in the range of 0-20 khz. The complete set of $\phi = \pi/2$ data contains 312 points.

The normalized frequency difference

$$y(r) = \frac{2[f_c(r) - f_e(r)]}{\epsilon f_c(a) c^2}$$

is predicted by theory [5] to be equal to $1 + (a/r)^2$ at $\phi = \pi/2$. We calculated the mean and standard deviation of y at each r, using the data for all ϵ and c at that r. The result shown in Fig. 2, in which the solid line represents the theoretical result, and the error bars represent $\pm$ one standard deviation.

(We also fit all 312 points to a curve of the form

$$\hat{y} = A\left(\frac{a}{r}\right)^2 + B,$$

obtaining $A = 0.992$ and $B = 0.779$. These are consistent with the scatter of the individual points.)

We made measurements at $\phi = 0$, and at two other axial (z) positions. The $\phi = 0$ measurements gave δf measurements of two khz or less with no systematic radial structure. There was no significant difference at the other two axial positions from the data reported above. Both of these are necessary consequences of the theory and reinforce our conclusion that the discrepancy at second order arises from local causes near the interface, and not from any defect in the linear solution $\hat{\mathbf{u}}_1$.

The uncertainty in any individual frequency measurement was less than 0.5 khz. This uncertainty is an estimate given by the experimenter, who watched varying digital frequency readout, estimating the extent of the excursion as well as the center frequency. An additional uncertainty in the final result is caused by fluctuations in container rotation rate. Separate measurements indicate these to be quasi-periodic with an amplitude of 0.5 percent and a "period" of two to three seconds.

These uncertainties are consistent with the statistical errors indicated in Fig. 2. They are also consistent with repeated extrapolations of calibration curves to the center. Typical discrepancies in the location of the center were less than one percent of the extrapolation distance.

Other Flow States

As there is considerable interest in the literature in flows other than the laminar flow which we have measured, it seems appropriate to describe briefly other flow states we have observed, and to provide a stability map for these. The latter is important as no such unified map exists beyond the simple single boundary given in [5].

Figure 3 is a map depicting regions in ϵ, c space where flows of three different types have been observed. The laminar state

[3] This was an unintentional blunder which remained undiscovered until the apparatus was no longer operable.

Table 1 Ranges of ϵ and E

$\epsilon \times 10^2$	$E \times 10^6$
1.00	1.38
1.52	1.70
2.06	1.97
2.44	2.15
5.32	3.18

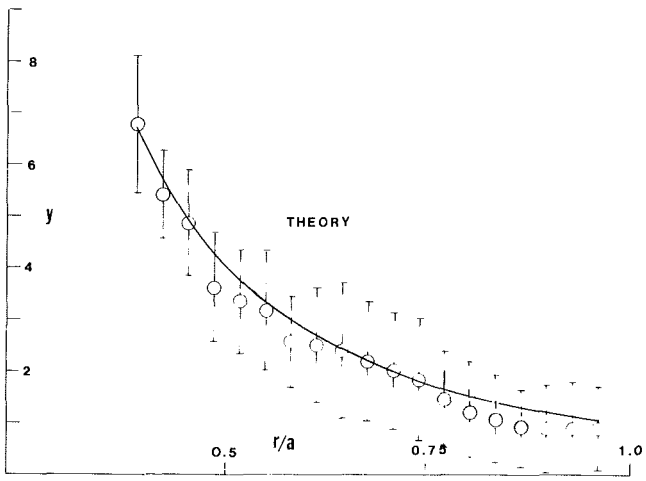

Fig. 2 Normalized frequency difference as a function of position. The error bars represent $\pm$ one standard deviation. The solid line is the theoretical prediction. "The vertical axis of Fig. 2 is mislabelled. The correct value of y is one greater than that shown."

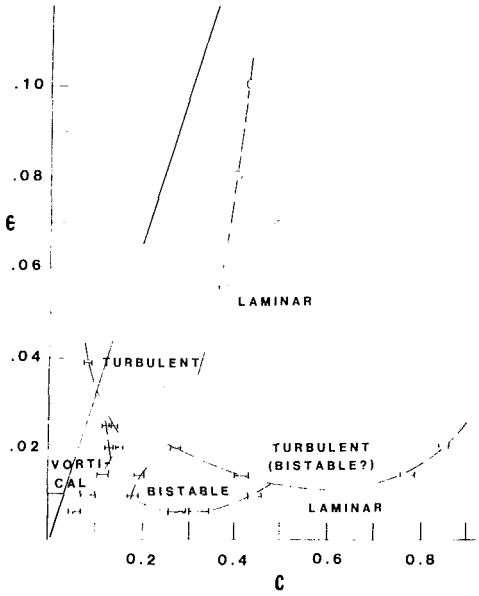

Fig. 3 Stability map. $L/2a = 1.07$. The fluid was tap water. The solid line ($\epsilon = c/3$) is an absolute stability criterion [5], for which gravity exceeds centripetal force. In practice the flow is unstable at smaller ϵ.

is that to which the third section of this paper is given. There are at least three other states attainable in partially-filled rotating cylinders. Two of these are shown on Fig. 3. The third is only attainable in cylinders which are long compared to their diameter.

In the following paragraphs we describe the flow states mentioned, and discuss briefly the precision with which the boundaries between states were determined. We cite previous scattered descriptions of these flows as we discuss each.

The "vortical" state [6], [8], [9] is somewhat disordered. It is time-dependent, characterized by the aperiodic shedding of vortices from the interface. One to four vortices are created in any one episode, most commonly, two or three. The length of

time between episodes depends on how far one is from the boundary in parameter space separating the laminar and vortical states. Episodes recur more rapidly as one moves deeper into the vortical region.

Just inside this boundary it is possible to see the process in some detail under stoboscopic illumination. The behavior is cyclical. At one point in the cycle the flow looks like that in the laminar state, but the retrograde rotation increases with time. (Recall that this means the absolute rotation rate of the interface *decreases*, reducing the centripetal force and making the interface more susceptible to gravitational disturbance.) As the interface decelerates, it begins to distort. Eventually the retrograde rotation becomes so rapid one cannot measure it with the naked eye, the vortices are formed, and are ejected. Immediately upon ejection, the interface distortion vanishes, and its apparent rotation rate jumps to approximately that of the container. (The rotation rates may be equal; existing observations are not sensitive enough to tell.)

The cycle continues. The retrograde rotation increases and the vortices decay. At what may be some critical retrograde rotation rate a new set of vortices is ejected. Near the stability boundary the old vortices decay before the new set appears. Deeper into the vortical region the ejection and decay overlap, the new vortices destroying the old.

The "turbulent" state [5], [8] is characterized by the complete lack of a well-defined interface or vortices. The flow in the body of the fluid is very different from solid rotation. We have made preliminary laser Doppler measurements which show a mean azimuthal velocity varying linearly with radius, but going through zero near where the (laminar) interface would be, rather than near the center of the cylinder.

A third flow state occurs in tubes long compared to their diameter. It is marked by a series of cells of the less dense fluid. Balmer [13] has termed these hygrocysts. Figure 1 of [14] is an excellent photograph of the phenomenon. This state has not been seen in this laboratory because the aspect ratio of the cylinders we used has always been near unity.

Bistable denotes regions in which either laminar or turbulent flow states can occur, depending on the initial conditions. Imagine the flow to be in the laminar state. As the rotation rate is decreased a critical value is reached at which the flow changes to the turbulent state. It requires a large increase in rotation rate to return to the laminar state. There is a bistable band in which the flow depends on initial conditions.

The data on which the map of the flow states is based were taken by adding the desired amount of water to the cylinder, spinning the cylinder up to the desired speed and observing the state of flow. The boundary lines drawn on the figure pass between points at which two different flow states are clearly identifiable. The typical width of a boundary in the c direction is 0.02. In the ϵ direction the width cannot be seen.

Summary and Conclusions

We have measured the azimuthal velocity in a partially-filled horizontally rotating cylinder at $\phi = 0$ and $\phi = \pi/2$. For the latter plane we looked at three axial positions. The results of these measurements confirm the linear inviscid theory. We believe the discrepancy between measured and calculated retrograde rotation to be caused by conditions at the air water interface, and are presently engaged in experiments to examine this region more closely.

We offer the map of parameter space as a preliminary guide to those using fluid-filled rotors. We hope some day to be able to explore the parameter space in more detail, and eventually to understand the transitions theoretically.

Acknowledgments

We wish to thank J. Rizzo for the loan of the frequency tracker. This work was supported in part by the ONR under the CNA contract with the University of Rochester, in part by the National Science Foundation Atmospheric Research Program and in part by Rochester Gas and Electric Corporation. We also wish to thank an anonymous reviewer for his helpful commentary on an earlier version of this note.

References

1 Hendricks, S. L., and Morton, J. B., "Stability of a Rotor Partially-Filled With a Viscous Incompressible Fluid," ASME *Journal of Applied Mechanics*, Vol. 46, Dec. 1979, pp. 913–918.

2 Scott, W. E., "The Large Amplitude Motion of a Liquid-Filled Gyroscope and the Noninteraction of Inertial and Rossby Waves," *Journal Fluid Mechanics*, Vol. 72, Dec. 1975, pp. 649–660.

3 Scott, W. E., "Free Surface Breakdown in a Rapidly Rotating Liquid," *Journal Fluid Mechanics*, Vol. 86, June 1978, pp. 417–463.

4 Scott, W. E., and D'Amico, W. P., "Amplitude-Dependent Behavior of a Liquid Filled Gyroscope," *Journal Fluid Mechanics*, Vol. 60, Oct. 1973, pp. 751–758.

5 Phillips, O. M., "Centrifugal Waves," *Journal Fluid Mechanics*, Vol. 7, Mar. 1960, pp. 340–352.

6 Greenspan, H. P., "On a Rotational Flow Disturbed by Gravity," *Journal Fluid Mechanics*, Vol. 74, Mar. 1976, pp. 335–352.

7 Wood, W. W., "Torque-Free Rotation of a Cylinder," *Physics Fluids*, Vol. 20, Nov. 1977, pp. 1953–1954.

8 Gans, R. F., "On Steady Flow in a Partially Filled Rotating Cylinder," *Journal Fluid Mechanics*, Vol. 82, Sept. 1977, pp. 415–427.

9 Gans, R. F., "On the Flow Around a Buoyant Cylinder Within a Rapidly Rotating Cylindrical Container," *Journal Fluid Mechanics*, Vol. 93, Aug. 1979, pp. 529–548.

10 Whiting, R. D., "An Experimental Study of Steady Flow in a Partially-Filled Rotating Cylinder," Ph.D. dissertation, University of Rochester, Dept. of Mech. and Aerospace Sci., Jan. 1978.

11 Wilmshurst, T., and Rizzo, J. E., "An Autodyne Frequency Tracker for Laser Doppler Anemometry," *Journal Physics Engineering*, Vol. 7, Nov. 1974, pp. 924–930.

12 Yalisove, S. M., "Measurements of Flow in a Partially-Filled Horizontally-Rotating Cylinder," M.S. thesis, University of Rochester, Dept. of Mech. and Aerospace Sci., Jan. 1979.

13 Balmer, R. T., "The Hygrocyst—a Stability Problem in Continuum Mechanics," *Nature*, Vol. 227, Aug. 1970, pp. 600–601.

14 Balmer, R. T., and Wang, T. G., "An Experimental Study of Internal Hygrocysts," ASME JOURNAL OF FLUIDS ENGINEERING, Vol. 98, Dec. 1976, pp. 688–694.

15 Karweit, M. J., and Corrsin, S., "Observations of Cellular Patterns in a Partly-Filled, Horizontal, Rotating Cylinder," *Physics Fluids*, Vol. 18, Jan. 1975, pp. 111–112.

M. M. M. El Telbany[1]
Research Fellow.

A. J. Reynolds
Professor.
Department of Mechanical Engineering,
Brunel University,
Uxbridge,
Middlesex, England

The Structure of Turbulent Plane Couette Flow

Measurements of time-mean velocity, of longitudinal, normal and lateral velocity fluctuation intensities (u', v', w') and of shear stress have been made for four cases of pure shear flow in a flat channel, one of whose walls is stationary while the second moves. Both walls are effectively smooth. General expressions for the mean velocity profile and a prediction of the friction coefficient are developed. Comparisons of the experimental results with existing data are made. The profiles of v', w', turbulence kinetic energy and production of turbulence energy across the channel are the first to be published.

Introduction

Plane Couette flow has been studied by several investigators since the original work of M. Couette [1] in 1890. Experimental investigations of plane turbulent Couette flow are scarce owing to the difficulty involved in generating a flow within which measurements are possible. Reichardt [2, 3], Robertson [4], Chue [5] and Leutheusser and Chu [6] have examined channel flows with zero pressure gradient, but their measurements were limited to mean velocities. The turbulence structure of pure shear flow was studied experimentally by Johnson [7] and Robertson and Johnson [8], but they did not succeed in measuring accurately the distribution of turbulent shear stress, while Johnson [7] measured only centerline values of v' and w'. A compilation of test conditions of known experiments on plane Couette flow is given in Table 1. The results of Reichardt [3], Robertson [4], Johnson [7], Chue [5], and Robertson and Johnson [8] are reasonably detailed and will be drawn upon for comparisons with the present measurements.

Correlating Relations

The mean-velocity distribution for plane Couette flow is symmetric and exhibits two distinct regimes. In the vicinity of the wall the profile is in good accord with the logarithmic law of the wall:

$$\frac{U}{u*} = A\ln y^+ + B \tag{1}$$

In the central region the universal velocity distribution can be approximated by a defect-law of the form

$$\frac{U-U_c}{u*} = \mathrm{R}_f(1-y/h) \tag{2}$$

The friction coefficient for plane Couette flow is usually defined as

$$C_f = \frac{2\tau_w}{\rho U_c^2} \tag{3}$$

Robertson [4] suggested that the skin-friction could be predicted from the following expression:

$$\sqrt{\frac{C_f}{2}} = \frac{G}{\log \mathrm{R}_e} \tag{4}$$

where G is a constant chosen to fit experimental results. The value $G=0.19$ was found by Robertson; values ranging from $G=0.188$ to 0.196 were found in Johnson's [7] study.

Table 1 Characteristics of channel flow apparatus for plane Couette flow

Name	Year	Channel Depth (cm)	Aspect Ratio	Length Half Depth Ratio	Fluid	Reynolds Number Range $R_e = U_c h/\nu$
REICHARDT (2)	1956	16 16	5 5	6 6	Oil Water	600, 1450 6000
REICHARDT (3)	1959	16 12	5 9	6 80	Water Air	4500 - 10000 3000 - 17000
ROBERTSON (4)	1959	4.85	10	41	Air	4600 - 16500
JOHNSON (7)	1965	4.9	10	41	Air	7050 - 16500
ROBERTSON & JOHNSON (8)	1970	3.78 4.9	13 10	53 41	Air	7050 - 16500
CHUE (5)	1969	3.2	-	16	Water	6000, 9150
LEUTHEUSSER & CHUE (6)	1971	15.85 7.9	7 14	74 158	Air	200 - 2000
GADA (9) HAI (10) SZERI et al. (11)	1970 1976 1976	1.27	11	100	Air	338 - 2831
HUEY & WILLIAMSON (12)	1974	6.35	10	19	Air	9650 - 27300
PRESENT	1980	4.4 6.6	28 18	45 30	Air	9500 - 19000

[1]Seconded from Faculty of Engineering, Helwan University, Elmataria, Cairo, Egypt.

Contributed by the Fluids Engineering Division for publication in the JOURNAL OF FLUIDS ENGINEERING. Manuscript received by the Fluids Engineering Division, October 3, 1980.

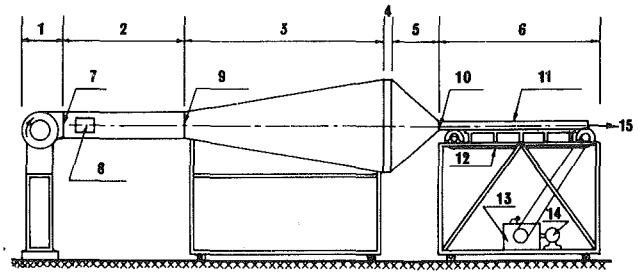

Fig. 1 General layout of the rig. 1-fan, 2-intermediate section, 3-diffuser, 4-filters, 5-nozzle, 6-test channel, 7-mesh, 8-access door, 9-screen, 10-grid, 11-upper plate, 12-moving wall, 13-gear box, 14-motor, 15-air exit

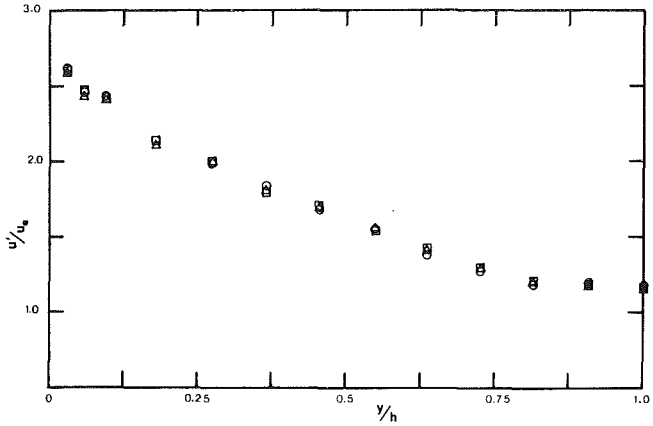

Fig. 2 Longitudinal intensity profiles for Poiseuille flow. Δ, $x/2h = 30$; 0, $x/2h = 25.4$; □, $x/2h = 20.8$

Robertson introduced also a dimensionless slope parameter defining the core velocity:

$$S = \frac{h}{U_c}\left(\frac{dU}{dy}\right)_c \tag{5}$$

and adopted an expression for this parameter as a function of the flow Reynolds number:

$$S = \frac{0.78}{\log \mathrm{R_e}} \tag{6}$$

Experimentally he found the parameter S to be very sensitive to minor changes in the flow and difficult to evaluate accurately. Reynolds [13] introduced a parameter R_τ related to R_f, S, and C_f through

$$\mathrm{R}_\tau = \frac{u_*(2h)}{\nu_c} = 2\mathrm{R}_f = 2S\left(\frac{C_f}{2}\right)^{-0.5} \tag{7}$$

Evidently R_τ is Reynolds number based on eddy viscosity ν_c, channel depth $2h$, and friction velocity u_*. It was found that $\mathrm{R}_\tau = 7.5$ on the basis of Reichardt's [2] and Robertson's [4] measurements.

Experimental Apparatus

The measurements reported here were made in air in a belt-type Couette-flow apparatus, whose general form is indicated in Fig. 1.

The flow through the test channel is supplied by a specially constructed open-circuit wind tunnel, consisting of centrifugal fan, diffuser, filters, and contraction. To expedite the development of the flow, turbulent activity is introduced before the air enters the parallel-sided duct, by a coarse mesh of expanded metal located some 150 mm upstream of the parallel section. The parallel section of the channel is 2440 mm long; the main measurements were made in the central vertical plane of the channel, at a station $x_m = 1980$ mm from the blowing end. The belt forming the moving floor is 1200 mm wide, some 20 mm less than the channel breadth measured between the separating bars which form the vertical sides. Two channel depths have been used; 44 mm and 66 mm, giving aspect ratios (breadth/depth) of about 28 and 18. Even the smaller aspect ratio can be expected to minimize the possibility of secondary recirculating flow across the channel (Schlichting [15]). Moreover, preliminary tests carried out by Mr. M. Kalirai (unpublished report, 1975) indicated no significant variation in velocity profiles in the central half of the channel. The development ratio (development length/depth) is then either 30 or 45. The introduction of a turbulence-generating grid at the entrance to the duct increases the effective length (Hussain and Reynolds [16] and Patel [17]). The longitudinal intensity profiles of Fig. 2 (for

Nomenclature

A = constant in law of wall
B = constant in law of wall
$C_f = \frac{2\tau_w}{\rho U_c^2}$ = friction coefficient
G = constant in equation for friction coefficient
h = channel half depth
k = time-averaged turbulence kinetic energy per unit mass = $\frac{1}{2}(u'^2 + v'^2 + w'^2)$
$\mathrm{R_e} = \frac{U_c h}{\nu}$ = Reynolds number based on centerline velocity, channel-half depth and kinematic viscosity
$\mathrm{Re}_\delta = U_\infty \delta/\nu$ =
R_f = constant in velocity core law
$\mathrm{R}_\tau = 2\mathrm{R}_f = \frac{u_*(2h)}{\nu_c}$ = Reynolds number based on friction velocity, channel depth, and constant eddy viscosity
S = slope parameter
U = time-averaged velocity component in x-direction
U_∞ = free-stream velocity in a boundary layer
U_c = centerline velocity
$U_b = 2U_c$ = belt velocity
$u_* = \left(\frac{\tau_w}{\rho}\right)^{1/2}$ = wall friction velocity
u', v', w' = turbulent velocity fluctuations in longitudinal, normal, and lateral directions, respectively
$-\overline{uv}$ = turbulent shear stress
x = coordinate in the direction of main flow
y = coordinate direction normal to plate surface, origin at upper plate
$y^+ = \frac{yu_*}{\nu}$ = nondimensional length
τ_w = shear stress on the wall
ρ = fluid density
ν = fluid kinematic viscosity
ν_t = eddy viscosity
ν_c = constant eddy viscosity in the core region
δ = boundary-layer thickness

Table 2 Details of tests

Case	2h (mm)	U_b (m/s)	R_e	u_* (m/s)	C_f	R_f	S
1	44	12.84	9500	0.293	0.00417	5.7	0.260
2	44	17.08	12640	0.378	0.00392	5.1	0.226
3	66	12.84	14250	0.282	0.00386	5.1	0.224
4	66	17.08	18960	0.363	0.00361	4.5	0.191

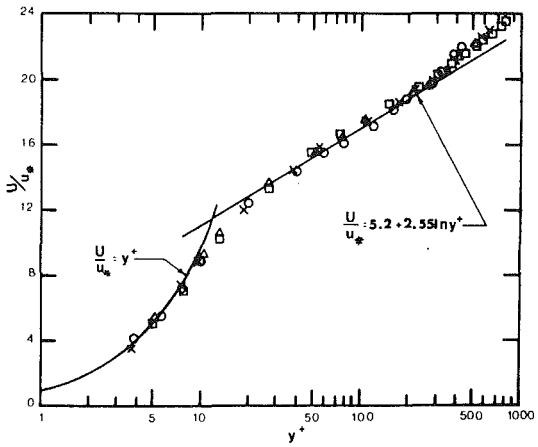

Fig. 3 Mean velocity data in wall coordinates for Couette flows. 0, $R_e = 9500$; Δ, $R_e = 12640$; X, $R_e = 14250$; □, $R_e = 18960$.

measuring stations $x = 1370$ mm, 1675 mm and 1980 mm and for pure pressure flow) demonstrate that the turbulent motion is substantially fully developed at the standard measuring station, $x_m = 1980$ mm.

The mean-velocity profile and the longitudinal velocity fluctuation were measured using a DISA normal hot-wire probe (type 55P11) in conjunction with a DISA 55M system constant-temperature anemometer, a 55M25 linearizer, a 55D35 rms voltmeter (used for the velocity fluctuation) and a Datron 1045 digital voltmeter. Vertical and lateral velocity fluctuations and the turbulent shear stress were measured with a DISA X-wire probe (type 55P61) in conjunction with two such channels, the rms voltmeter and the digital voltmeter. The interpretation of hot-wire signals used in the present study is that described by El Telbany and Reynolds [18].

The probes were calibrated in pure pressure flow through the test channel itself, and the shear stress measurements from the X-wire probe were compared with values obtained from the linear velocity variation near the wall in Couette flow and from pressure-deep measurements in pure Poiseuille flow. The friction velocity u_* deduced from the X-wire probe measurements will be used in the present study.

The position of hot-wire probes within the channel could be controlled within 0.01 mm by a micrometer traversing mechanism. The belt speed was determined by a counter activated by magnetic strips on the belt.

Results and Discussion

Table 2 gives details of the four Couette flows examined.

The velocity profile has an S shape and is "centrosymmetrical," exhibiting complete symmetry about the central plane; hence $U_b = 2U_c$. Some measurements were taken across the entire flow to demonstrate this centrosymmetry, but the discussion will, in the main, be confined to measurements made in the upper half-width, that is, the half adjacent to the fixed surface.

The mean-velocity profiles are plotted in universal coordinates in Fig. 3. It is clear that in the "inner layer" the universal law of the wall accurately represents the mean-velocity distributions. The two constants of equation (1) were found to be $A = 2.55$, and $B = 5.1 \pm 0.1$ over this range of Reynolds numbers, in good agreement with those found by Reichardt [3] and Robertson [4].

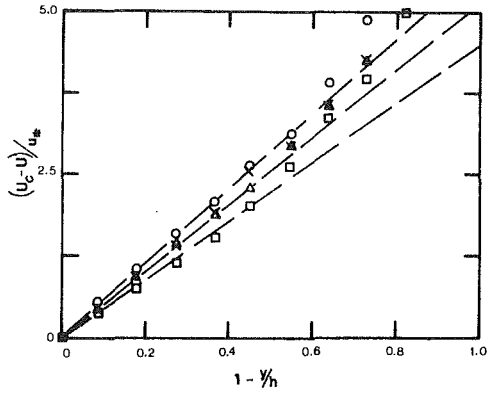

Fig. 4 Core region presentation of mean velocity. For symbols see Fig. 3.

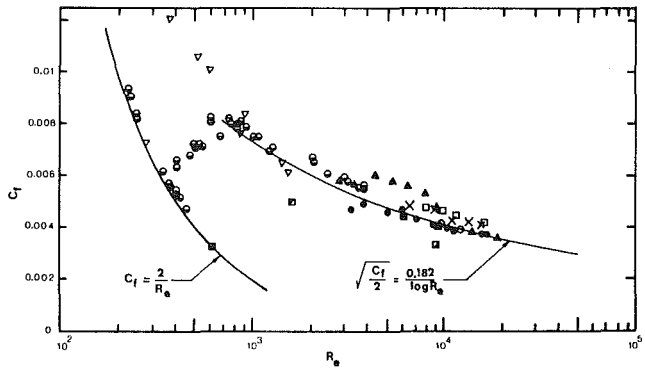

Fig. 5 Skin-friction coefficient as a function of Reynolds number in Couette flow. Couette [1], ⊖-air, ⊜-water; Reichardt [2], ⧈-water, ⧄-oil; Reichardt [3], ●-air; Robertson [4], □-air; Chue [5], ■-water; Leutheusser and Chu [6], ▽-air; Robertson and Johnson [8], ▲ and X-air; present results, 0 and △-air.

The mean-velocity profiles are plotted in Fig. 4 to check the validity of equation (2) in the core region. It is clear that equation (2) represents the mean velocity profiles reasonably well in the region $0.4 < y/h < 1.6$. However, there is a marked Reynolds number dependence, with $R_f = 4.5$ to 5.7. The values suggested for this slope parameter by Reynolds [19] and Townsend [20] are $R_f = 3.75$ and 4.25, respectively. The slopes of the core regions of most of the more varied Couette-type flows studied by El Telbany and Reynolds [21] are $R_f = 5.0$.

In Fig. 5 the friction factor C_f is plotted as a function of Reynolds number, with results found by earlier workers. The present results are intermediate to those of other experiments and serve to define the high-Reynolds-number end of the friction law more precisely.

The turbulent-friction results are well represented by equation (4) if we take the constant $G = 0.182$. There is good agreement between the present results for the friction coefficient and Reichardt's measurements, but the values by Robertson and Johnson are rather higher. It is perhaps significant that Reichardt and the present authors measured the shear stress directly, while Robertson and Johnson deduced the wall shear stress from velocity profiles.

In Table 2 we see that the slope parameter S of equation (5) has an average value around 0.22 and decreases with flow Reynolds number. Equation (6) does not in fact define this

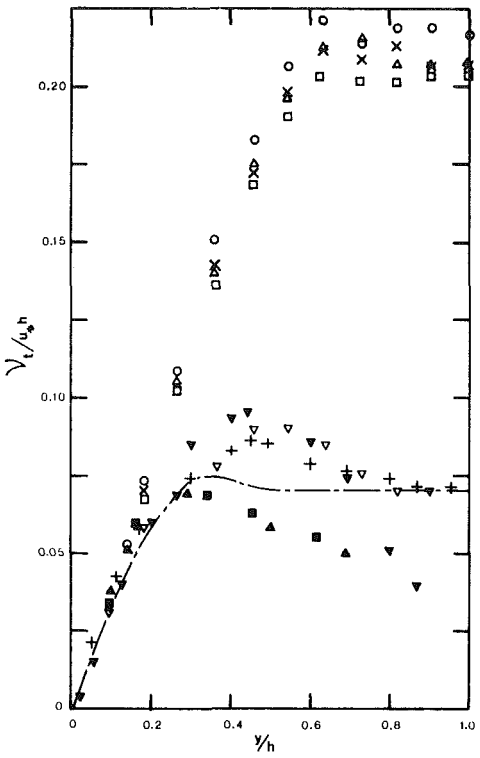

Fig. 6 Eddy-viscosity distribution compared with other data (for channel, h = half depth; for pipe, h = radius; for boundary layer, h = nominal thickness). ▽, El Telbany [14] (plane Poiseuille flow, $R_\theta = 38180$); +, Hussain and Reynolds [16] ($R_\theta = 32300$); – · – Laufer [22] ($R_\theta = 50000$); ■, Townsend [23] ($R_{\theta_\delta} = 35000$); ▲, Klebanoff [24] ($R_{\theta_\delta} = 80000$); ▼, Ueda et al. [25] ($R_{\theta_\delta} = 34400$); for symbols of the present data see Fig. 3

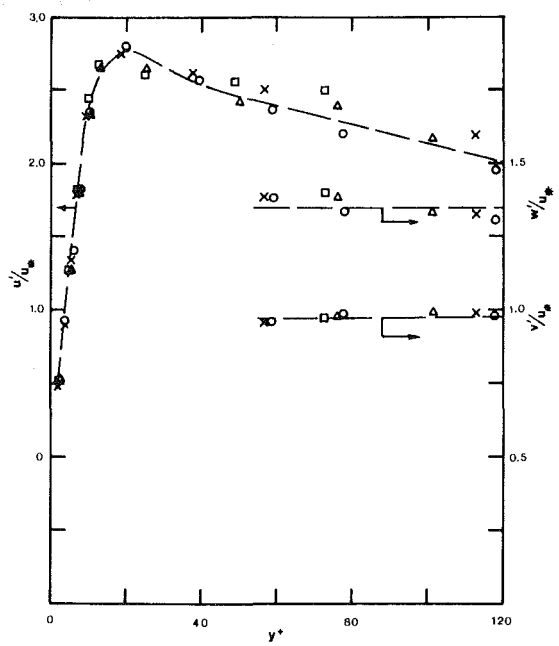

Fig. 7(a) Distribution of turbulence intensities near the wall. For symbols see Fig. 3.

variation very accurately. Incidentally, this parameter has the value unity for a laminar-viscous plane Couette flow.

The nondimensional eddy viscosity is compared in Fig. 6 with data obtained by Laufer [22] in a pipe; Hussain and Reynolds [16] and El Telbany [14] in a channel; and by Townsend [23], Klebanoff [24], and Ueda et al. [25] in flat-plate boundary layers. As would be expected, all of these

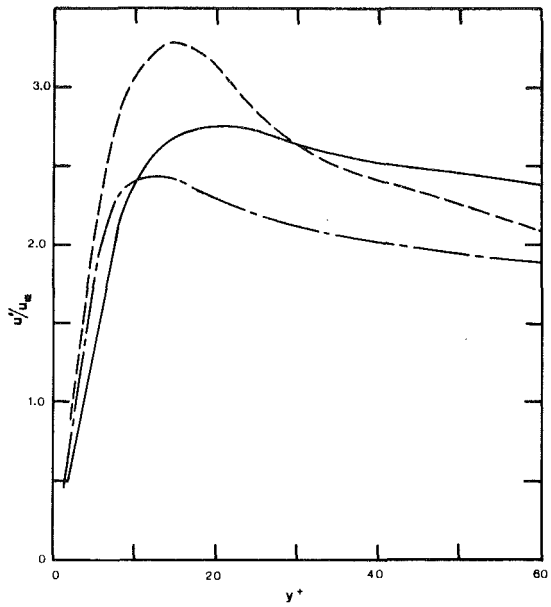

Fig. 7(b) Turbulent intensity data compared with other experiments – Present data, R_θ (9500-18960); – · – Hussain and Reynolds [16], $R_\theta = 13800$; – – – Clark [27], $R_\theta = 15200$.

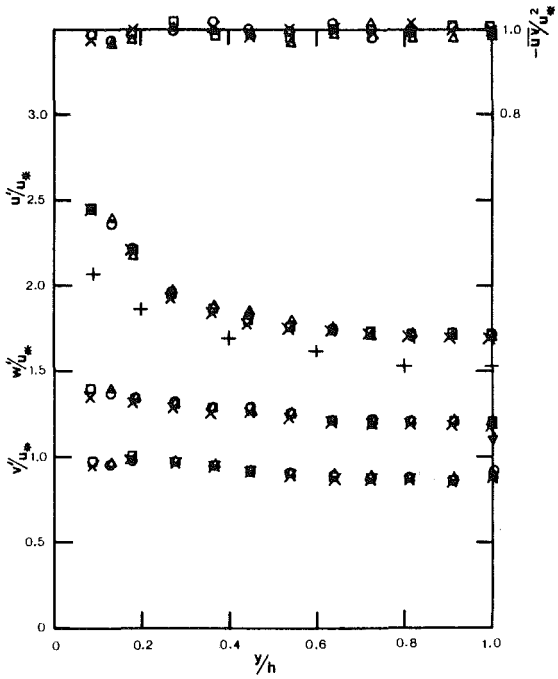

Fig. 7(c) Distributions of turbulent shear-stress and turbulence intensities compared with Johnson's data [7], R_θ (7050-16500): +, u'/u_*; 0, v'/u_*; ▽, w'/u_*. For symbols for the present data see Fig. 3.

values are in good agreement near the wall ($y/h < 0.1$, say). Away from the wall, however, the values of ν_t display quite different trends. For the boundary layers, the eddy viscosity tends to zero at large distances from the wall; for Poiseuille flow (pipe or channel) it tends to a constant value of about $\nu_t = 0.07\, u_* h$; while in the core region of plane-Couette flow it tends to a constant value of about $\nu_t = 0.21\, u_* h$.

Figure 7(*a*) gives measured distributions of turbulence intensities near the wall and Fig. 7(*b*) compares the distribution of u'/u' near the wall with the channel data of [16] and [27]. The maximum of u'/u_* in the present data is about 2.75 and is independent of Reynolds number. Hussain and Reynolds' value for the maximum of u'/u_* is about 2.45

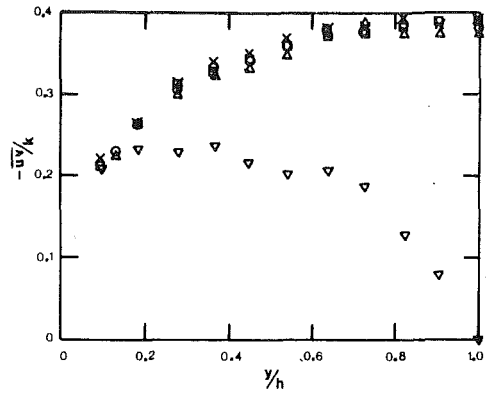

Fig. 8 Distribution of ratio of turbulent shear stress to kinetic energy. ▽, El Telbany [14] (plane Poiseuille flow, $R_e = 38180$); for other symbols data see Fig. 3.

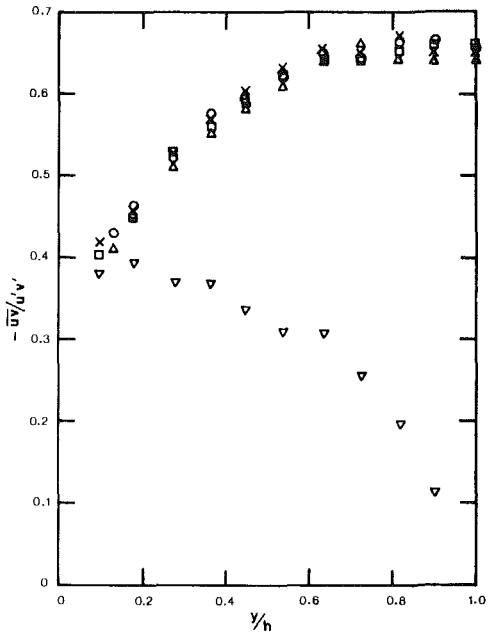

Fig. 9 Variation of shear correlation coefficient. For symbols see Fig. 8.

while Clark's value is about 3.25 [Fig. 7(*b*)]. Figure 7(*c*) shows the measured variations of the turbulent shear stress across the channel. As is required for Couette flow, the turbulent shear stress is sensibly constant across the channel. The u', v', and w' distributions are shown also in Fig. 7(*c*) and compared with data obtained by Johnson [7]. The fact that Johnson's values of the scaled intensities are generally some 10 percent lower than ours is probably a consequence of the rather higher values of shear stress he has found (see Fig. 5), since they influence u_* as well as C_f. The shapes of the intensity profiles for the three components differ significantly, emphasising the strongly anisotropic nature of the turbulence, even in the core region. The region near the wall is very similar to other wall layers. The core region exhibits strong indications of homogeneity in turbulence structure as predicted by von Kármán [26]. There is no significant Reynolds-number dependence of the normalized turbulence intensities over the Reynolds-number range considered.

The ratio of the turbulent shear stress to the turbulence kinetic energy is plotted in Fig. 8 and compared with measurements of El Telbany [14] for pure pressure flow. For plane Poiseuille flow the ratio $\overline{uv}/k$ is constant for $y/h \simeq 0.1$ to 0.6, then decreases rapidly and reaches zero at the center of the channel. In contrast, for plane Couette flow the ratio

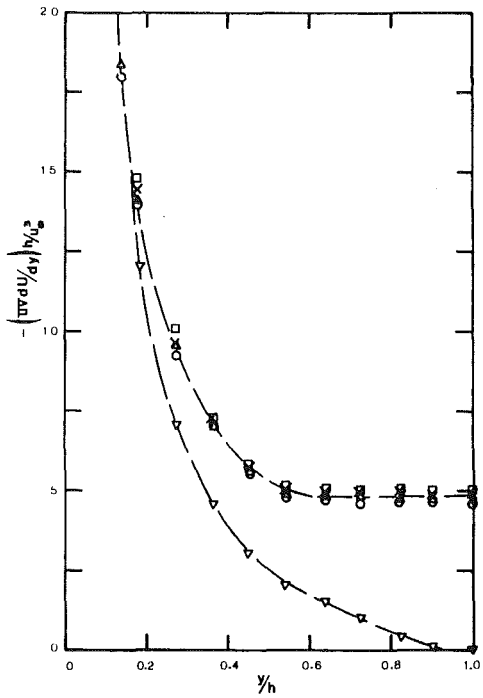

Fig. 10 Production of turbulence energy. For symbols see Fig. 8.

$\overline{uv}/k$ increases for $y/h = 0.1$ to 0.6, then remains constant in the core region. The maximum value of the ratio $\overline{uv}/k$ for plane Couette flow is typically 0.38.

Correlation coefficients, $-\overline{uv}/u'v'$, are plotted in Fig. 9, again in comparison with values for plane Poiseuille flow. In Poiseuille flow it is known that the correlation coefficient is virtually constant and equal to about 0.38 over a considerable region of the flow near the wall. For plane Couette flow the coefficient is close to 0.4 near the wall but rises to about 0.65 for $y/h > 0.6$.

Figure 10 displays the variation of the production of turbulence energy ($\overline{uv}\, dU/dy$) across the channel in comparison with plane Poiseuille flow. The channel half-depth and the friction velocity have been chosen as non-dimensionalising length and velocity scales. As usual there is a good agreement near the wall between Poiseuille and Couette flows; but further from the wall the generation of turbulence energy in Poiseuille flow decreases and reaches zero at the centre of the channel, while the generation of turbulence energy in plane Couette flow retains a fairly high level throughout the core region.

Conclusions

The reported studies of plane Couette flow over a Reynolds-number range of 8500 to 19000 have established the following conclusions:

(*a*) The form of the law of the wall is confirmed to be essentially that found by earlier workers.

(*b*) The slope of the central linear velocity variation is found to be some 25 percent higher than has earlier been suggested and to be significantly dependent upon Reynolds number.

(*c*) Friction at high Reynolds numbers has been found to be in close agreement with Reichardt's earlier measurements, and to be some 15 percent below the measurements of Robertson and Johnson.

(*d*) In the central 40 percent of the channel the mean shear and turbulence intensities are nearly uniform, as are quantities dependent upon them, such as turbulence kinetic energy and the rate of its production.

References

1 Couette, M., "Etudes sur le Frottement de Liquides," *Ann. Chem. and Phy. Series 6*, Vol. 21, 1890, pp. 433-510.

2 Reichardt, H., "Über die Geschwindigkeitsverteilung in einer Geradlinigen Turbulenten Couetteströmung," *Z. Angew. Math. Mech.*, Vol. 36, 1956, pp. 26-29.

3 Reichardt, H., "Gesetzmässigkeiten der Geradlinigen Turbulenten Couetteströmung," Max Planck Institut für Strömungsforschung, Mitteilung Nr. 22, 1959.

4 Robertson, J. M., "On Turbulent Plane Couette Flow," *Proceedings of the 6th Midwestern Conference on Fluid Mech.*, Univ. of Texas, Austin, 1959, pp. 169-182.

5 Chue, S. H., "An Experimental Investigation on Turbulent Plane-Couette Flow in Dilute Polymer Solutions," M.Sc. thesis, School of Mech. Eng. Purdue University, Lafayette, Ind., 1969.

6 Leutheusser, H. J., and Chu, V. H., "Experiments on Plane Couette Flow," *J. of Hydraulic Division, Proc. ASCE*, Vol. 97, 1971, pp. 1269-1284.

7 Johnson, H. F., "An Experimental Study of Plane Couette Flow," M.Sc. thesis, Theoretical and Applied Mech. in the Graduate College of the University of Illinois, 1965.

8 Robertson, J. M., and Johnson, H. F., "Turbulence Structure in Plane Couette Flow," *J. of Eng. Mech. Div. Proc. ASCE.*, Vol. 96, 1970, pp. 1171-1182.

9 Gada, M. J., "Development of an Apparatus for Pure Shear Flow Investigations," M.Sc. thesis, the University of Pittsburgh, 1970.

10 Hai, S. M., "Pressure Development in the Entrance Region and Fully Developed Region of Generalized Channel Turbulent Flows," ASME *Journal of Applied Mechanics*, Vol. 43, 1976, pp. 13-19.

11 Szeri, A. A. A., Yates, C. C., and Hai, S. M., "Flow Development in Parallel Plate Channel," ASME *Journal of Lubrication Technology*, Vol. 98, 1976, pp. 145-156.

12 Huey, L. J., and Williams, J. W., "Plane-Turbulent Couette Flow with Zero-Net Flow," ASME *Journal of Applied Mechanics*, Vol. 41, 1974, pp. 885-890.

13 Reynolds, A. J., "Analysis of Turbulent Bearing Films," *J. Mech. Eng. Science*, Vol. 5, 1963, pp. 258-272.

14 El Telbany, M. M. M., "Generalized Turbulent Channel Flow," Ph.D. thesis, Mech. Eng. Dept., Brunel University, Uxbridge, Middlesex, England, 1980.

15 Schlichting, H., *Boundary Layer Theory*, 7th Edn. McGraw-Hill, New York, 1979.

16 Hussain, A. K. M. F., and Reynolds, W. C., "Measurements in Fully Developed Turbulent Channel Flow," ASME JOURNAL OF FLUIDS ENGINEERING, Vol. 97, 1975, pp. 568-578.

17 Patel, R. P., "A Note on Fully Developed Turbulent Flow Down a Circular Pipe," *Aeronautical J.*, Vol. 78, 1974, pp. 93-97.

18 El Telbany, M. M. M., and Reynolds, A. J., "Turbulence in Plane Channel Flows," *J. Fluid Mech.*, Vol. III, 1981, pp. 283-318.

19 Reynolds, A. J., *Turbulent Flows in Engineering*, J. Wiley, London, 1974.

20 Townsend, A. A., *The Structure of Turbulent Shear Flow*, Cambridge University Press, London, 1976.

21 El Telbany, M. M. M., and Reynolds, A. J., "Velocity Distribution in Plane Turbulent Channel Flows," *J. Fluid Mech.*, Vol. 100, 1980, pp. 1-29.

22 Laufer, J., "The Structure of Turbulence in Fully Developed Pipe Flow," NACA Report 1174, 1954.

23 Townsend, A. A., "The Structure of the Turbulent Boundary Layer," *Proceedings of the Cambridge Philosophical Soc.*, Vol. 47, 1951, p. 375.

24 Klebanoff, P. S., "Characteristics of Turbulence in a Boundary Layer with Zero Pressure Gradient," NACA Tech. Note 1247, 1955.

25 Ueda, H., Moller, R., Komori, S., and Mizushina, T., "Eddy Diffusivity Near the Free Surface of Open Channel Flow," *Int. J. Heat Mass Transfer*, Vol. 20, 1977, pp. 1127-1136.

26 Von, Karman, T., "The Fundamentals of the Statistical Theory of Turbulence," *J. of the Aeronautical Sciences*, Vol. 4, 1937, pp. 131-138.

27 Clark, J. A., "A Study of Incompressible Turbulent Boundary Layers in Channel Flow," ASME *Journal of Basic Engineering*, Vol. 90, 1968, p. 455.

Schedule of Uncertainties

Table 1 The values describing the authors' apparatus, given in the final row of this table, are correct to 1 percent.

Fig. 3 U/u_* accurate within 2 percent
y^+ accurate within 0.2

Fig. 4 $(U_c - U)/u_*$ accurate within 0.06
y/h accurate within 0.02

Fig. 5 C_f accurate within 2 percent
R_e accurate within 300

Fig. 6 $\nu_t/u_* h$) accurate within 3 percent
y/h accurate within 0.02

P. S. Granville
Specialist,
Ship Performance Department,
David W. Taylor Naval Ship R&D Center,
Bethesda, Md. 20084

Drag-Characterization Method for Arbitrarily Rough Surfaces by Means of Rotating Disks

An indirect similarity-law characterization method is presented for any arbitrary irregular roughness covering a circular disk. Formulas are presented for converting the measured torques and rotary speeds of this rough rotating disk into appropriate local values at the disk edge required for the characterization.

Introduction

The drag properties of any rough surface in a turbulent shear flow may be completely characterized by a similarity-law parameter as a function of a roughness Reynolds number. Such characterizations are essential inputs to the development of turbulent boundary layers over rough surfaces [1] and the associated drags for varieties of flow situations and Reynolds numbers. The rough surface may have an irregular geometry such as encountered in engineering practice.

Direct determinations of such drag characterizations of arbitrarily rough surfaces require the measurement of the wall shear stress at a station and the velocity profile in the immediate vicinity of the rough wall to satisfy an inner similarity-law analysis.

Often it may be simpler or more convenient to undertake an indirect characterization which involves more readily attainable measurements.

Historically the first indirect method may be ascribed to Nikuradse [2] who conducted an experimental study of the drag of densely packed sand grains glued to the inside of a pipe in fully-developed turbulent flow. Here the average velocity across the pipe is substituted for measurements of the velocity profile. The average velocity is readily obtainable from the gross rate of flow through the pipe while the velocity profile requires extensive measurement. The roughness characterization is calculated from a formula based on the average velocity derived from the similarity laws. Excellent agreement was found by Nikuradse between the direct and indirect determinations.

In a study of the turbulent boundary layer over a rough flat plate, Hama [3] devised an indirect method which involves the displacement thickness of the boundary layer. An interesting feature of the roughness characterization here is the consideration of deviations of the rough results from the smooth results, a procedure which tends to reduce experimental error. Such a procedure may be called characterization by appropriate difference in contrast to that by Nikuradse which may be called characterization by formula.

Contributed by the Fluids Engineering Division of THE AMERICAN SOCIETY OF MECHANICAL ENGINEERS at the Joint ASME/ASCE Bioengineering, Fluids Engineering and Applied Mechanics Conference, June 22-24, 1981, Boulder, Colorado. Manuscript received by the Fluids Engineering Division, March 2, 1981. Paper No. 81-FE-33.

Later Robertson et al. [4] showed that the procedure of appropriate differences is also readily applicable to pipe flow.

Another indirect method [5] was devised for rough flat plates, towed or otherwise, which involves only the measurement of total drag and speed. The wall shear stress at the trailing edge of the plate is related to the total drag by a similarity-law boundary-layer analysis.

There are advantages and disadvantages to the indirect methods just mentioned. It is easier to apply roughness to the outside surface of a flat plate than to apply it to the inside of a pipe which may have to be split lengthwise for easy access [6, 7]. Required full-scale speeds are difficult to attain on a flat plate when towed. If the flat plate is immersed in the flow of a facility such as a water tunnel in order to obtain high speeds, the experiments can be quite costly. In contrast an indirect method based on a rotating disk has the advantage of an outside surface for ease of application of roughness and of easily attainable high speeds. Furthermore the technology for rotating a disk is also well developed.

The indirect method to be described here involves measuring only the torque and rotary speed of a rotating disk uniformly covered with the roughness under investigation. It will be shown that the logarithmic law of friction obtained from the similarity laws is the basis of the method. The torque is related to the wall shear stress at the edge of the disk by analytical relations derived from a three-dimensional boundary-layer analysis [8].

To start with, pertinent aspects of the similarity laws are reviewed as they relate to arbitrary roughnesses. The modification to be followed for the case of a rotating disk in a confined-flow situation is also included in the presentation.

Finally the method is illustrated by an appropriate example.

Velocity Similarity Laws

For reference purposes a brief account is presented of the velocity similarity laws which form the basis of drag characterizations of arbitrarily rough surfaces in a turbulent shear flow.

Inner Law or Law of the Wall. In the close proximity of an arbitrarily rough surface defined by a sufficient number of

length factors k, k_1, k_2, . . . the inner similarity law or law of the wall for turbulent shear flows may be stated in the Reynolds-number mode as

$$\frac{u}{u_\tau} = f\,[y^*, k^*, T] \tag{1}$$

or in the relative-roughness mode as

$$\frac{u}{u_\tau} = f\left[\frac{y}{k}, k^* T\right] \tag{2}$$

Here $y^* = u_\tau y/\nu$, $k^* = u_\tau k/\nu$ (roughness Reynolds number), $u_\tau = \sqrt{\tau_w/\rho}$ (shear velocity) and $T = k/k_1$, k_1/k_2, . . . (roughness texture). Also u is the streamwise mean-velocity component. τ_w is the wall shear stress, ρ is the fluid density, ν is the fluid kinematic viscosity and y is the normal distance away from the rough wall (the zero position of y may vary with roughness geometry).[1]

Outer Law or Velocity-Defect Law. For the outer part of the turbulent shear layer, the similarity law is stated as a velocity defect which is a function of relative position

$$\frac{U-u}{u_\tau} = f\left[\frac{y}{\delta}\right] = F\left[\frac{y}{\delta}\right] \tag{3}$$

Here U is the streamwise velocity at the outer edge of a shear layer of thickness δ. The outer law is functionally independent of roughness. There is, however, an indirect dependence on roughness through shear velocity u_τ.

Logarithmic Velocity Laws and Roughness Characterizations. If the inner and outer laws are considered applicable in a common overlapping region, the analytical consequences are logarithmic relationships. For the inner law in the Reynolds-number mode

$$\frac{u}{u_\tau} = A \ln y^* + B_1\,[k^*, T] \tag{4}$$

or in the relative-roughness mode

$$\frac{u}{u_\tau} = A \ln \frac{y}{k} + B_r\,[k^*, T] \tag{5}$$

[1] The empirical location of the zero position of y is required in the direct characterization wherein the velocity profile is probed close to the wall. Happily, this is not required for the indirect characterization by means of rotating disks described here.

B_1 and B_r are related by

$$B_r = B_1 + A \ln k^* \tag{6}$$

For the usual roughness regimes (1) hydraulically smooth: B_1 = constant = $B_{1,s}$; $B_r = B_{1,s}$ + A ln k^*, (2) intermediate: B_1 and B_r both vary with k^* and T, (3) fully rough: $B_r = \hat{B}_r$ is constant with respect to k^* and is only a function of T; $B_1 = \hat{B}_r(t) - A \ln k^*$.

Either $B_1(k^*, T)$ or $B_r(k^*, T)$ may be termed similarity-law roughness drag characterization. Another form of B_1 arises when the value for a smooth surface $B_{1,s}$ is subtracted to give

$$\Delta B[k^*, T] = B_1[k^*, T] - B_{1,s} \tag{7}$$

ΔB as defined is always negative in value. Nikuradse used the B_r characterization while Hama preferred the ΔB (actually $-\Delta B$) characterization.

The outer law in turn develops a logarithmic relation over the overlapping region:

$$\frac{U-u}{u_\tau} = -A \ln \frac{y}{\delta} + B_2 \tag{8}$$

B_2 is a velocity-defect factor which does not vary with roughness but does vary with streamwise pressure gradient. $B_2/2A$ is also called the Coles Wake Factor.

A direct similarity-law drag characterization of a roughness with texture T requires the determination of B_1, B_r, or ΔB as a function of roughness Reynolds number k^* from measurements of wall shear stress τ_w and velocity u in the region where the logarithmic inner law holds, equation (4) or (5). For a thin shear layer this may not be too feasible. Hence an indirect method like that based on overall measurements on a rotating disk may be more practicable.

Equivalent Sand-Grain Roughness. Although an arbitrary nominal value for k, k_{nom}, may be assigned to a given roughness, it will not affect the values for the B_1 (and ΔB) characterizations per se. From equation (6) it is seen that the values of B_r are strongly affected and hence B_r should be designated accordingly as $B_{r,\text{nom}}$. For the fully-rough regime and hence may be further designated $\hat{B}_r$.

As shown by Schlichting [9] a value for k may be determined which gives the same drag in the fully rough regime as the sand-grain roughness of Nikuradse, which will be denoted the equivalent sand-grain roughness or k equiv. Since B_1 is unaffected by k, equation (6) gives $\hat{B}_{r,\text{nom}} - A \ln u_\tau k_{\text{nom}}/\nu = \hat{B}_{r,sg} - A \ln u_\tau k_{\text{equiv}}/\nu$. With u_τ/ν the same,

Nomenclature

A = boundary-layer factor
B_1 = inner-law factor, equation (4)
$B_{1,S}$ = value of B_1 for fully-developed roughness
C_m = moment or torque coefficient for rotating disk, equation (13)
F = outer-law velocity profile, equation (3)
g = cross-flow velocity profile, reference [8]
k = roughness height
$k_1, k_2, \ldots$ = other roughness lengths
k^* = roughness Reynolds number
M = moment or torque of one side of rotating disk
r = disk radius
R = rotating-disk Reynolds number, equation (14)
T = roughness texture
u = mean velocity component in shear layer parallel to the wall
U = velocity outside boundary layer (for rotating disk, $U = r\omega$)
u_τ = shear velocity, $u_\tau = \sqrt{\tau_w/\rho}$
y^* = normal distance from wall (disk surface)
y = nondimensional y, $y^* = u_\tau y/\nu$
δ = boundary-layer thickness
ΔB = similarity-law roughness characterization
$(\Delta B)'$ = derivative of ΔB with respect to $ln\ k^*$
ν = kinematic viscosity of fluid
ρ = density of fluid
σ = local skin-friction coefficient, equation (10)
τ_w = wall shear stress
ϕ = angular-velocity factor for enclosed rotating disk
ω = angular velocity of rotating disk

Subscripts

e = edge of disk
en = enclosed rotating disk
equiv = equivalent
nom = nominal
r = condition of roughness
s = condition of smoothness
sg = sand grain
∞ = unenclosed

$$k_{\text{equiv}} = k_{\text{nom}} \exp\left[\frac{\hat{B}_{r,sg} - \hat{B}_{r,\text{nom}}}{A}\right] \tag{9}$$

$\hat{B}_{r,sg}$ is the value of $\hat{B}_r$ obtained by Nikuradse for sand-grain roughness in the fully-rough regime.

Logarithmic Laws of Friction. The addition of the overlapping inner logarithmic relation, equation (4) or (5), to the outer logarithmic relation, equation (8), results in the logarithmic laws of friction which in the Reynolds-number mode is

$$\sigma = \frac{U}{u_\tau} = A \ln \frac{u_\tau \delta}{\nu} + B_1[k^*, T] + B_2 \tag{10}$$

and in the relative-roughness mode is

$$\sigma = \frac{U}{u_\tau} = A \ln \frac{\delta}{k} + B_r[k^*, T] + B_2 \tag{11}$$

σ is a convenient local coefficient of skin friction. Also from definitions

$$\sigma = (\tau_w / \rho v^2)^{-1/2}$$

The logarithmic laws of friction may be shown to be the basis of indirect roughness drag characterizations.

Rotating Disk

Turbulent Boundary Layer. A circular disk rotating in a fluid at rest develops a resisting torque or moment which is wholly viscous in origin. A boundary layer develops on the disk surface in a three-dimensional manner such that there is a cross-flow velocity component in the radial direction. The streamwise component is the circumferential velocity which is much larger than the radial velocity by an order of magnitude. The relative circumferential velocity is considered to obey the velocity similarity laws while the relative radial velocity is considered to obey Prandtl's relation for cross-flow velocities. As shown in reference [8], the application of these velocity relations to the equations of motion of a turbulent boundary layer on a rotating disk result in a variety of analytical solutions for both the boundary layer and the overall torque. These solutions gave predictions which agreed very well with available measurements.

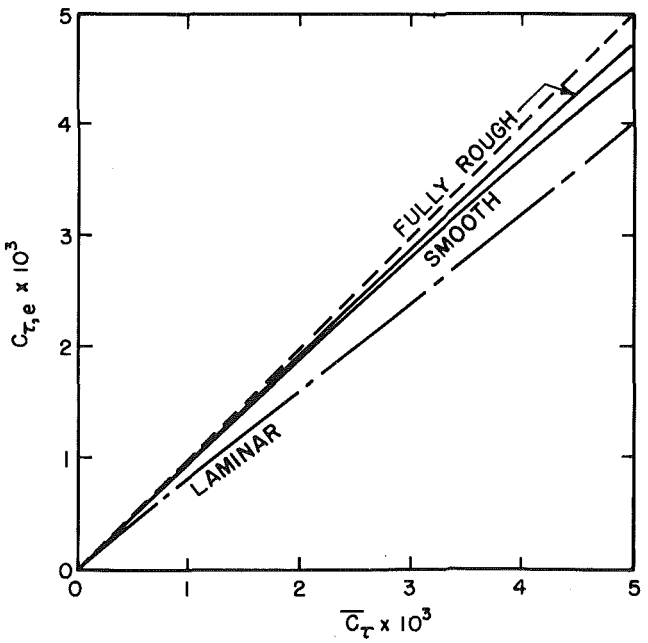

Fig. 1 Comparison of wall shear-stress coefficient at disk edge $C_{\tau,e}$, with average wall shear-stress coefficient, C_τ

Disk Dimensionless Ratios. The moment or torque coefficient C_m of a disk rotating with angular velocity ω covered with roughness k and T is a function of Reynolds number R and relative roughness k/r_e or

$$C_m = f\left[R, \frac{k}{r_e}, T\right] \tag{12}$$

where

$$C_m = \frac{2M}{\frac{1}{2}\rho r_e^5 \omega^2} \tag{13}$$

$$R = \frac{r_e^2 \omega}{\nu} \tag{14}$$

M is the resisting moment on one side of the disk and r_e is the radius of the disk.

At any radius r of the disk the wall shear-stress coefficient in the circumferential direction C_τ is given as

$$C_\tau = \frac{2}{\sigma^2} = \frac{\tau_w}{\frac{1}{2}\rho (r\omega)^2} \tag{15}$$

Local Skin Friction. At the disk edge r_e the local skin-friction coefficient $C_{\tau,e}$ may be related to the moment coefficient C_m by means of equation (62) resulting from the boundary-layer analysis of reference [8]:

$$C_{\tau,e} = \frac{5}{4\pi} C_m \left[1 - \frac{2}{5}(2A + B_1^\dagger)\sqrt{\frac{5}{8\pi}}\sqrt{C_m} + \ldots\right] \tag{16}$$

where at the disk edge

$$B_1^\dagger = (\Delta B)^\dagger = \frac{dB_1}{d(\ln k^*)} = \frac{d(\Delta B)}{d(\ln k^*)} \tag{17}$$

It is interesting to consider the case of a constant local skin-friction coefficient $\bar{C}_\tau$ over the whole disk. For an annulus of width dr at radius r, the differential moment dM is then

$$dM = \tau_w (2\pi r dr) = \bar{C}_\tau \rho \pi \omega^2 r^2 dr \tag{18}$$

Integrating from $r = 0$ to $r = r_e$ produces

$$\bar{C}_\tau = \frac{5}{4\pi} C_m \tag{19}$$

Then from equation (16)

$$C_{\tau,e} = \bar{C}_\tau \left[1 - \frac{2}{5}(2A + B_1^\dagger)\sqrt{\frac{\bar{C}_\tau}{2}} + \ldots\right] \tag{20}$$

Plotted values in Fig. 1 are given for the cases of smooth surfaces ($B_1^\dagger = 0$) and the fully rough regime ($B_1^\dagger = -A$). Also shown is the line for laminar flow ($C_{\tau,e} = 0.8\, C_\tau$).

This shows that the wall shear stress coefficient at the disk edge, $C_{\tau,e}$, is close in value to the average coefficient $\bar{C}_\tau$ for both smooth and rough rotating disks and even closer than for the laminar case.

Indirect Roughness Drag Characterization. The indirect characterization from rotating disks is derived from the logarithmic law of friction as follows:

The logarithmic law of friction, equation (10) at the disk edge represented by subscript e may be stated as

$$\sigma_e = A \ln R + A \ln\left(\frac{\delta}{\sigma r}\right)_e + B_{1,s} + (\Delta B)_e + B_2 \tag{21}$$

Combining equations (13), (15), (39), (56), (57), and (63) of the three-dimensional boundary-layer analysis of reference [8] results in

$$\ln\left(\frac{\delta}{\sigma r}\right)_e = \ln\sqrt{C_m} - \ln\left[\sqrt{10\pi}\, \tilde{F}_g \sqrt{\frac{\tilde{F}^2}{\tilde{g}^2}}\right] \tag{22}$$

where $\tilde{F}_g$, $\tilde{F}^2$, and $\tilde{g}^2$ are constants obtained by integrations across the boundary layer:

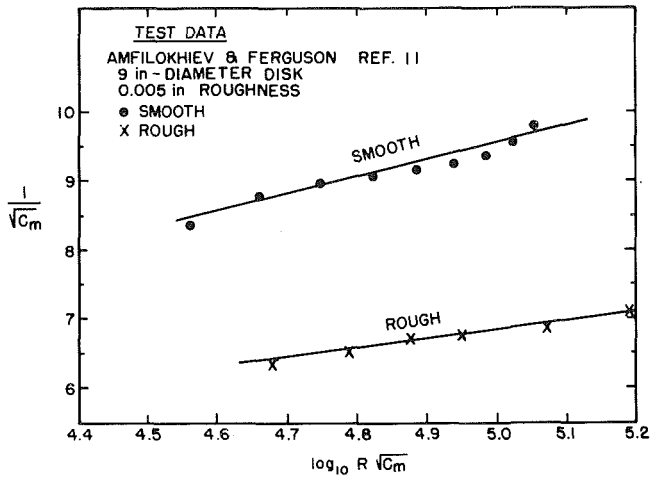

Fig. 2 Test data for a rough rotating disk

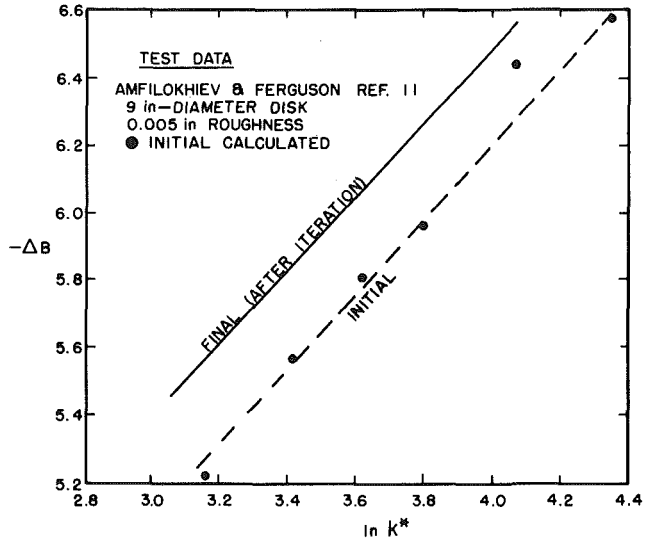

Fig. 3 Similarity-law drag characterization for a rough rotating disk

$$\tilde{F}_g=\int_0^1 Fgd\left(\frac{y}{\delta}\right),\tilde{F}^2=\int_0^1 F^2d\left(\frac{y}{\delta}\right),\tilde{g}^2=\int_0^1 g^2d\left(\frac{y}{\delta}\right)$$

$F\ (y/\delta)$ is the outer law, Equation (3) which is assumed to hold to the wall $y=0$ and $g\,(y/\delta)$ is the Prandtl cross-velocity function.

Futhermore from equations (15) and (63) of reference [8] the relation between the circumferential wall shear-stress coefficient at the disk edge, σ_e, and overall moment coefficient C_m is

$$\sigma_e=\sqrt{\frac{8\pi}{5}}\frac{1}{\sqrt{C_m}}+\frac{1}{5}(2A+B_1')+\ldots \tag{23}$$

Finally equation (21) becomes

$$(\Delta B)_e=\sqrt{\frac{8\pi}{5}}\frac{1}{\sqrt{C_m}}-A\ln R\sqrt{C_m}-B_{1,s}-B_2$$
$$+\frac{2}{5}A+\frac{1}{5}(\Delta B)_e'+A\ln\left[\sqrt{10\pi}\tilde{F}g\sqrt{\frac{\tilde{F}^2}{\tilde{g}^2}}\right]+\ldots \tag{24}$$

$(\Delta B)_e$ may be evaluated from the above formula after the indicated constants have been evaluated. This is in accord with the formula procedure of Nikuradse.

A more convenient and probably more accurate procedure is to use appropriate differences in the manner of Hama. Accordingly for a smooth surface with $(\Delta B)_e=(\Delta B)_e'=0$, equation (24) becomes

$$0=\sqrt{\frac{8\pi}{5}}\frac{1}{\sqrt{C_m}}-A\ln R\sqrt{C_m}-B_{1,s}-B_2$$
$$+\frac{2}{5}A+A\ln\left[\sqrt{10\pi}\tilde{F}g\sqrt{\frac{\tilde{F}^2}{\tilde{g}^2}}\right]+\ldots \tag{25}$$

Subtracting this equation for smooth surfaces from equation (24) for rough surfaces gives for the *same values of* $R\sqrt{C_m}$

$$(\Delta B)_e=\sqrt{\frac{8\pi}{5}}\left[\left(\frac{1}{\sqrt{C_m}}\right)_r-\left(\frac{1}{\sqrt{C_m}}\right)_s\right]+\frac{1}{5}(\Delta B)_e' \tag{26}$$

where subscripts r and s refer to rough and smooth conditions, respectively. The procedure then is to plot $1/\sqrt{C_m}$ against $\log R\sqrt{C_m}$ for both the rough and smooth rotating disks. The characterization $(\Delta B)_e$ is then obtained from the differences in the ordinates at the same values of $R\sqrt{C_m}$.

The corresponding values of roughness Reynolds number k^*_e are obtained from

$$k_e^*=\left(\frac{k}{r_e}\right)\left(\frac{R}{\sigma_e}\right) \tag{27}$$

and equation (64) of reference [8] to give

$$k_e^*=\frac{k}{r_e}\sqrt{\frac{5}{8\pi}}R\sqrt{C_m}\left\{1-\left[2A+(\Delta B)_e'\right]\sqrt{\frac{C_m}{40\pi}}\right\} \tag{28}$$

The values of $(\Delta B)_e'$ may be obtained by reiteration of $(\Delta B)_e$ as a function of $\ln k^*_e$.

Enclosed Rotating Disk. For a disk rotating in a container [10] a swirl may develop which reduces the effective angular velocity to $\phi\omega$ where ϕ is a swirl factor, $0<\phi<1$. Accordingly the moment coefficient C_m and Reynolds number in equations (13) and (14) may be redefined as follows

$$C_m=\frac{4M}{\rho r_e{}^5(\phi\omega)^2} \tag{29}$$

and

$$R=\frac{\phi\omega r_e{}^2}{\nu} \tag{30}$$

For a particular disk and container the swirl factor may be experimentally determined by comparison of data of $1/\sqrt{C_m}$ plotted against $\log(R\sqrt{C_m})$ for enclosed and unenclosed conditions. Since ϕ does not affect the product $R\sqrt{C_m}$ then

$$\phi=\left(\frac{1}{\sqrt{C_m}}\right)_\infty\Big/\left(\frac{1}{\sqrt{C_m}}\right)_{en} \tag{31}$$

where subscripts *en* and ∞ refer to enclosed and unenclosed conditions, respectively. The swirl factor ϕ may be found to be a function of $R\sqrt{C_m}$ which will not affect the procedure for determining roughness characterizations. In a sense determining swirl factor ϕ may be considered to be a calibration of the rotating-disk flow facility.

Numerical Example

To illustrate the procedure described here a typical case is examined. The case to be considered is that of a 9-in. (229 mm) diameter rotating disk with a random roughness machined on both sides with a height of about 0.005 in. (0.127 mm) [11].

The (C_m,R) data are plotted in the form of $1/\sqrt{C_m}$ against $\log R\sqrt{C_m}$ in Fig. 2 for both rough and smooth disks. At the same values of $R\sqrt{C_m}$ the roughness characterization ΔB is obtained from equation (26) with $(\Delta B)'$ considered zero at first. The corresponding k^* is obtained from equation (28) and the results are plotted in Fig. 3. The slope of the correlating line gives the values of $(\Delta B)'$ which is then used to

recalculate the values of ΔB as given by equation (26). The final reiterated results are also plotted in Fig. 3.

Conclusion

The proposed method of using rotating disks to characterize arbitrary roughness may develop into a standard test procedure owing to its relative simplicity. Widespread acceptance probably can only come with experimental verification by direct measurement for a variety of roughness. Any actual rotating-disk apparatus involving confined flows should be calibrated in unconfined flows.

The proper geometric averaging of irregular rough surfaces of various textures for correlation with drag characterizations is still an uncertain procedure. If a representative sample is used, a nominal value may be assigned to k for predictive purposes.

References

1 Dvorak, F. A., "Calculation of Turbulent Boundary Layers on Rough Surfaces in a Pressure Gradient," *AIAA Journal*, Vol. 7, No. 9, Sept. 1969, pp. 1752–1759.

2 Nikuradse, J., "Laws of Flow in Rough Pipes," TM 1292, Nov. 1950, NACA (translation from VDI-Forschungsheft 361, July/Aug. 1933).

3 Hama, F. R., "Boundary-Layer Characteristics for Smooth and Rough Surfaces," *Transactions*, Vol. 62, 1954, Society of Naval Architects & Marine Engineers, pp. 333–358.

4 Robertson, J. M., Martin, J. D., and Burkhart, T. H., "Turbulent Flow in Rough Pipes," *Industrial & Engineering Chemistry Fundamentals*, Vol. 7, No. 2, May 1968, pp. 253–265.

5 Granville, P. S., "The Frictional Resistance and Turbulent Boundary Layer of Rough Surfaces," *Journal of Ship Research*, Vol. 2, No. 3, Dec. 1958, pp. 52–74.

6 Sacks, G. M., "Skin Friction Experiments on Rough Walls," *Journal of Hydraulics Division*, HY 3, Part 1, *Proceedings*, Vol. 84, June 1958, American Society of Civil Engineers, pp. 1664-1 to 1664-19.

7 Musker, A. J., and Sarabchi, K., "Wall-Friction and Profilometry Aspects of Coating an Irregularly Rough Surface," *International Shipbuilding Progress*, Vol. 27, No. 306, Feb. 1980, pp. 30–35.

8 Granville, P. S., "The Resisting Torque and Turbulent Boundary Layer of Rotating Disks with Smooth and with Rough Surfaces in Ordinary Fluids and in Drag-Reducing Polymer Solutions," *Journal of Ship Research*, Vol. 17, No. 4, Dec. 1973, pp. 181–195.

9 Schlichting, H., *Boundary-Layer Theory*, 7th Edition, 1979, McGraw-Hill.

10 Daily, J. W. and Nece, R. E., "Chamber Dimension Effects on Induced Flow and Frictional Resistance of Enclosed Rotating Disks," ASME *Journal of Basic Engineering*, Vol. 82, Mar. 1960, *Transactions ASME*, pp. 217–232.

11 Amfilokhiev, W. B., and Ferguson, A. M., "The Variation of Friction Drag with Surface Roughness in Dilute Polymer Solutions," Experiment Tank Report 8, August 1968, Department of Naval Architecture, University of Glasgow.

On the Prediction of Swirling Flowfields Found in Axisymmetric Combustor Geometries

D. L. Rhode
Graduate Student.
Assistant Professor,
College Station, Texas

D. G. Lilley
Professor.

D. K. McLaughlin
Professor.
Group Manager,
Torrance, Calif.

School of Mechanical
and Aerospace Engineering,
Oklahoma State University,
Stillwater, Okla. 74078

Combustor modeling has reached the stage where the most useful research activities are likely to be on specific sub-problems of the general three-dimensional turbulent reacting flow problem. The present study is concerned with a timely fluid dynamic research task of interest to the combustor modeling community. Numerical computations have been undertaken for a basic two-dimensional axisymmetric flowfield which is similar to that found in a conventional gas turbine combustor. A swirling nonreacting flow enters a larger chamber via a sudden or gradual expansion. The calculation method includes a stairstep boundary representation of the expansion flow, a conventional k-ϵ turbulence model and realistic accommodation of swirl effects. The results include recirculation zone characterization and predicted mean streamline patterns. In addition, an experimental evaluation using flow visualization of neutrally-buoyant helium-filled soap bubbles is yielding very promising results. Successful outcomes of the work can be incorporated into the more combustion- and hardware-oriented activities of gas turbine engine manufacturers, including incorporating the modeling aspects into already existing comprehensive numerical solution procedures.

Introduction

The combustor of the gas turbine engine contains high intensity combustion and, as far as possible, must burn fuel completely, cause little pressure drop, produce gases of nearly uniform temperature, occupy small volume, and maintain stable combustion over a wide range of operating conditions [1]. In design situations, the engineer has to seek an optimum path between irreconcilable alternatives of, for example, efficiency and pollution. The general aim of most research investigations is to provide information which is useful to designers by "characterizing" or "modeling" certain features of the phenomenon in question [2]. Up to now designers rely heavily on experimental evidence to produce empirical formulae. However, traditional design methods are now being supplemented by analytical methods (numerical solution of the appropriate governing partial differential equations). Computer modeling of combustion processes is now an established fact, but improvements and new developments (both experimental and theoretical) can and should be made, theoretical modeling being aided by carefully chosen experiments [3].

The present paper addresses research that is restricted to steady turbulent flow in axisymmetric geometries, under low speed and nonreacting conditions – a study area highlighted at a recent workshop [1] as a fundamental research requirement in combustion modeling. The particular problem is concerned with turbulent flow of a given turbulence distribution in a round pipe entering an expansion into another round pipe, as illustrated in Fig. 1. The in-coming flow may possess a swirl component of velocity via passage through swirl vanes at angle ϕ [equal approximately to $\tan^{-1}(w_0/u_0)$], and the side-wall may slope at an angle α, to the main flow direction. The resulting flowfield domain may possess a central toroidal recirculation zone CTRZ in the middle of the region on the axis, in addition to the possibility of a corner recirculation zone CRZ near the upper corner provoked by the rather sudden enlargement of the cross-sectional area. Of vital concern is the characterization of flows of this type in terms of the *effects* of side-wall angle α, degree of swirl ϕ, turbulence intensity k_0 of the inlet stream and expansion ratio D/d *on* the resulting flowfield in terms of its time-mean and

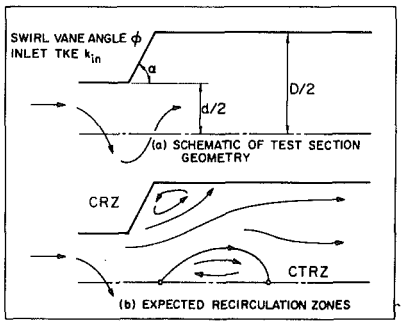

Fig. 1 The flowfield being investigated

Contributed by the Fluids Engineering Division and presented at the Symposium on the Fluid Mechanics of Combustion Systems, Boulder, Colo., Manuscript received by the Fluids Engineering Division, September 2, 1981.

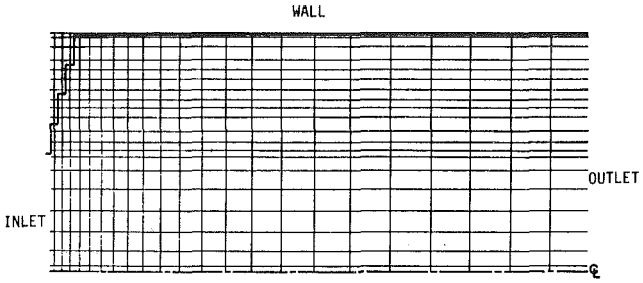

Fig. 2 An example of a coarse grid system being employed to fit the flow domain

turbulence quantities. Such problems have received little attention, yet there is a definite need for work in this area [4-6].

Experimental work in the configuration just described is being complemented by an associated prediction study of the flowfield. Consideration is given to recent work in the finite difference solution, via a primitive variable code, of axisymmetric swirl flow in the combustor geometry of Fig. 1, where the inlet expansion sidewall may slope obliquely to the central axis. Thus a systematic parametric investigation may be contemplated on the effect of sidewall angle α and degree of swirl ϕ on the resulting flowfield produced. Basic governing equations are presented, together with a brief description of the simulation and solution technique. The equations are elliptic in character and are solved via an advanced version of the Imperial College TEACH-T computer program [7], recently developed at Oklahoma State University [8].

Comparison with available experimental turbulent flow measurements assists in confirming the final predictive capability. One such experiment, underway at Oklahoma State University, is concerned with measuring the effects of swirl and side-wall angle on streamlines, mean flow and turbulence parameters in nonreacting flow. The facility and experimental details are included. For the present paper a preliminary evaluation of the accuracy of the computed flowfields is accomplished by comparison with flow visualization using neutrally-buoyant helium-filled soap bubbles as tracer particles. Photographs of the bubbles can be interpreted to yield time-mean flowfield maps which define approximately the boundaries of recirculation regions and regions of highly turbulent flow. Major features of strongly swirling flow characterization are then presented so as to exemplify the current predictive capability in terms of velocity profiles, streamline patterns and recirculation zone characterization. The final closure summarizes the achievements.

Theoretical Model

The turbulent Reynolds equations for conservation of mass, momentum (with x, r, θ velocity components u, v, w), turbulence kinetic energy k, and turbulence dissipation rate ϵ govern this two-dimensional axisymmetric steady flow. They may be expressed in the general form

$$\frac{1}{r}\left[\frac{\partial}{\partial x}(\rho u r\,\phi)+\frac{\partial}{\partial r}(\rho v r\,\phi)-\frac{\partial}{\partial x}\left(r\Gamma_\phi\frac{\partial\phi}{\partial x}\right)-\frac{\partial}{\partial r}\left(r\Gamma_\phi\frac{\partial\phi}{\partial r}\right)\right]=S_\phi$$

where ϕ represents any of the dependent variables, and the equations differ primarily in their final source terms S_ϕ [7-9]. Implicit here is the use of the standard two-equation $k-\epsilon$ turbulence model, whereby the exchange coefficients Γ_ϕ may be specified in each equation [10]. All constants appearing in the simulation are given the usual values. The corresponding finite difference equations are solved via an advanced version of the TEACH computer code [7], using a semi-implicit line-by-line method using the tridiagonal matrix algorithm for values at points of a variable size rectangular grid, with variable under-relaxation. A complete description of the finally-developed computer program is now available, with full details in the form of a user's manual about the solution technique, boundary conditions and their implementation, and the iteration scheme and parameters used [8]. A computer program listing and sample output are included for prospective users. Recent advances include revised cell volumes for the axial and radial velocities, swirl effects on wall functions, and incorporation of sloping boundaries. Figure 2 shows an example of grid specification for the present geometry.

Experimental Approach

Several previous experimenters have investigated nonreacting flows in expansion geometries [11-20]. References [11] and [12] also include flowfield predictions, made with versions of the TEACH-T computer program [7]. These experiments include time-mean velocity measurements [with hot-wire and pitot probes and laser Doppler anemometry], turbulence measurements [with hot-wires and laser anemometers] and flow visualization. The majority of the measurements were made in nonswirling flows [14-20], however some noteworthy experiments were made in swirling confined jets [11, 13]. Direct comparison between the results of the cited experiments and the present experimental results is generally not possible because of differences in geometry. However, in the nonswirling jet comparisons were possible with experiments of Chaturvedi [20], who measured mean and turbulent flow quantities downstream of a sudden expansion of diameter ratio 2.0 and various expansion sidewall angles α. Measurements of mean velocity in regions of high turbulence intensity and where the direction of the velocity vector is unknown were made with a pitot tube. Mean velocity was also measured with a constant temperature hot-wire anemometer using a single wire. In addition, a cross-wire was used to measure all the Reynolds stresses.

Nomenclature

D = chamber diameter
d = nozzle diameter
G = axial flux of momentum
k = kinetic energy of turbulence
S = swirl number = $2(G_\theta/G_x d)$, source term (with subscript)
$v=(u,v,w)$ = time-mean velocity (in x,r,θ direction)
x,r,θ = axial, radial, azimuthal cylindrical polar coordinates
α = side-wall angle
Γ = turbulence exchange coefficient
ϵ = turbulence energy dissipation rate
ρ = time-mean density
ϕ = swirl vane angle [$\tan^{-1}(w_0/u_0)$], general dependent variable

Subscripts

0 = value at inlet to flowfield

The present experiments have been conducted in the Oklahoma State University confined jet facility, and from part of an on-going study aimed at the characterization of time-mean and turbulence quantities in swirling confined flows. It has an axial flow fan whose speed can be changed by altering the varidrive mechanism. Numerous fine screens and straws produce flow in the settling chamber of relatively low turbulence intensity. The contraction section leading to the test section has been designed by the method of Morel [21] to produce a minimum adverse pressure gradient on the boundary layer and thus avoid unsteady problems associated with local separation regions. The sudden expansion consists of a 15 cm diameter circular jet nozzle, exiting abruptly into a 30 cm diameter test section as shown in Fig. 1. The substantial size of this test model provides excellent probe resolution for hot-wire measurements which are currently underway and will be reported in a later paper. The test section is constructed of plexiglas to facilitate flow visualization. The side-wall angle α and swirl vane angle ϕ are variable. The side-wall angle is set by inserting one of three blocks with a sidewall angle α of 90, 70, or 45 deg. The swirl vane assembly consists of ten vanes which are individually adjustable to any vane angle ϕ. The pitch/chord ratio at the half radius location is approximately one, and this assures quite high efficiency in generating a swirling motion to the in-coming flow [6]. Typical operating Reynolds numbers [based on inlet average velocity and inlet diameter] are in the range 70,000 to 130,000 depending upon fan speed and aerodynamic blockage of the swirl vanes. It has been observed that this is in the Reynolds number insensitive range for this facility [9], in terms of nondimensional flow characteristics further downstream.

The basic technique for the experiment discussed in this paper involves the visualization of individual neutrally-buoyant helium-filled soap bubbles. The bubbles which are approximately 0.5 to 1 mm diameter are produced by a Sage Action, Inc. generator-injector, which can be located at various positions in the flowfield. Because of the substantial size of the injector itself (1.5 cm in diameter and 6 cm long) it is not inserted directly into regions of flow interest. Instead it is either mounted upstream in the stilling chamber, or flush mounted to the wall of the large diameter pipe of the test section, to inject bubbles directly into the corner recirculation zone. The bubbles are illuminated by a beam of light from a high-power 35 mm slide projector which is located far downstream of the test facility. Photographs of illuminated bubbles are taken with various shutter speeds and camera positions. At relatively long exposure times (such as 1/8 s) a series of streaks are visible in the field of view corresponding to pathlines of individual bubbles. A 35 mm single lens reflex camera with a 45 mm lens was used. Tri-X Pan black and white film with a normal ASA of 400 was used and developed with a special process which pushed the ASA to 5000. In relatively lower turbulence intensity portions of the flowfield, mean-flow directions can be obtained by ensemble averaging local tangents to pathlines traced out by soap bubbles. This helps to define the gross features of the flowfield in terms of the outline of recirculation regions.

Results and Discussion

Computer Code Operation. The predictions presented here are computer simulations of the isothermal airflow in axisymmetric combustor geometries. As noted earlier diameter expansion ratio D/d is 2.0, inlet Reynolds number $\mathrm{Re}_d = 1.26 \times 10^5$, wall expansion angle $\alpha = 90$, 70, and 45 deg and swirl vane angle ϕ varies from 0 to 70 deg. All results are obtained via a nonuniform grid system which enhances solution accuracy. In the r-direction 21 grid lines are employed, and they are clustered near the shear layer region and along the wall and centerline. Cells in the x-direction are gradually expanding, and from 23 to 35 grid lines are employed as required to produce the desired side-wall angle α. Some grid independence tests have been undertaken with refined mesh systems up to 35 × 55; the present values were found to be adequate in terms of accuracy, and no discernable changes to the mean flow patterns to be presented were found.

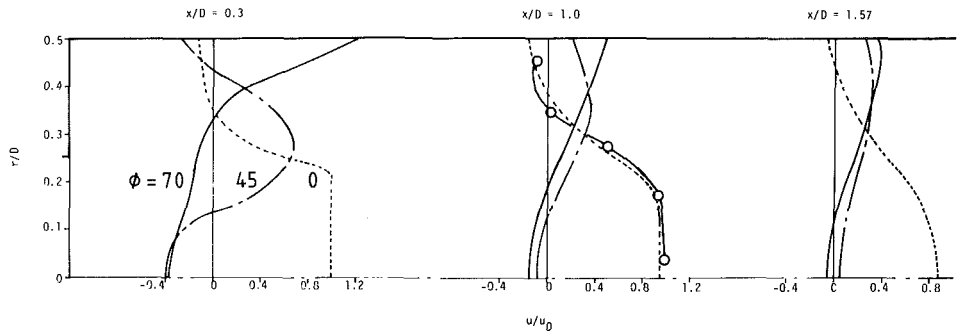

Fig. 3 (a) α = 90 deg

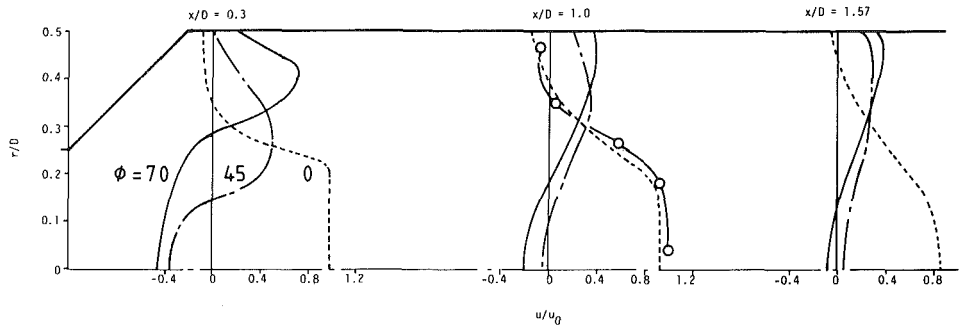

Fig. 3 (b) α = 45 deg

Fig. 3 Predicted axial velocity profiles showing the effect of swirl vane angle ϕ for wall expansion [o – o – o Experiment [20] with $\phi = 0$]

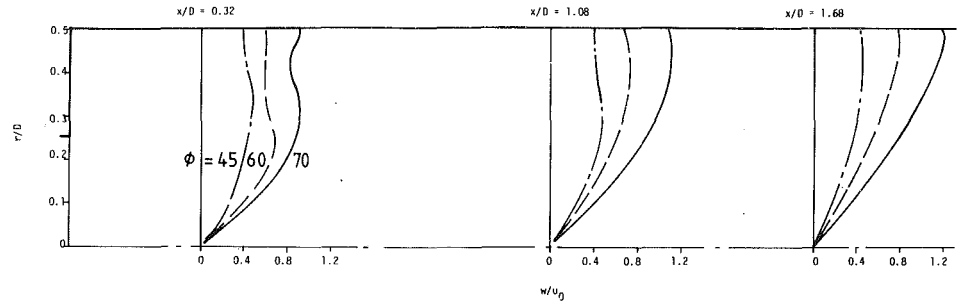

Fig. 4 (*a*) α = 90 deg

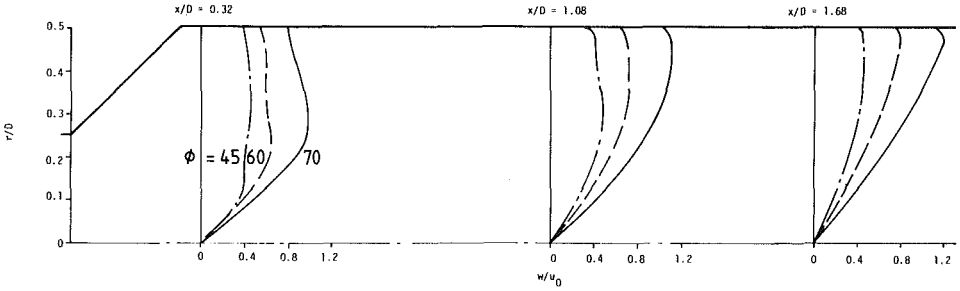

Fig. 4 (*b*) α = 45 deg

Fig. 4 Predicted swirl velocity profiles showing the effect of swirl vane angle ϕ for wall expansion angles α:

Computer runs through a range of seven inlet swirl vane angles ϕ equal to 0, 45, 55, 60, 65, 68, and 70 deg are undertaken for each side-wall angle α. Approximately 200 to 300 iterations [each with 5 field updates for pressure, 4 for axial velocity, and 3 for other primary variables] is needed to converge at each swirl strength, with the solutions for each value of ϕ being used as the initial starting values for the next higher value of ϕ considered. The inlet profiles of axial velocity u and swirl velocity w are idealized as flat (that is, constant-valued). This is consistent with the assumption of a one hundred percent efficient swirler, which is a little incorrect at the higher swirl angles. The in-coming nonswirling plug flow [$u=u_0$ and $v=w=o$] is turned through an angle ϕ to generate the flat out-going flow [$u=u_0$, $w=u_0 \tan\phi$ and $v=o$] with the additional assumption that radial velocity remains zero.

Axial and swirl velocity profiles are presented for the two α values and three ϕ values, clearly showing details of these parameter influences. Then, streamline plots for each value of ϕ, calculated and drawn by computer for each α, allow comparison of the shape and size of recirculation zones. Discussion is primarily aimed at guiding designers in judiciously choosing where experimental emphasis should be placed and/or in interpolating results from a limited amount of experimental data. For comparison with other results, it should be noted [6] that swirl number S and ϕ are related approximately by $S=2/3 \tan\phi$, so that vane angles 45, 60, and 70 deg, for example, correspond to S values of 0.67, 1.15, and 1.83, respectively.

Velocity Profiles. Predicted mean axial velocity profiles for the $\alpha=90$ and 45 deg geometries are shown in Figs. 3(*a*) and 3(*b*), respectively. The nonswirling case ($\phi=0$) exhibits good qualitative agreement with measurements of Chaturvedi [20] in a geometrically similar facility. The influence of ϕ is most dramatic near the combustor inlet, where the $\phi=0$ profile in Fig. 3(*a*) shows a large corner recirculation region, provoked by the sudden increase in flow area. A very large value of $\partial u/\partial r$ occurs near the inlet, which is indicative of high turbulence energy generation in a strong shear layer. Further, the nonswirling centerline velocity exhibits little change in the streamwise direction. With $\phi=45$ deg the mean

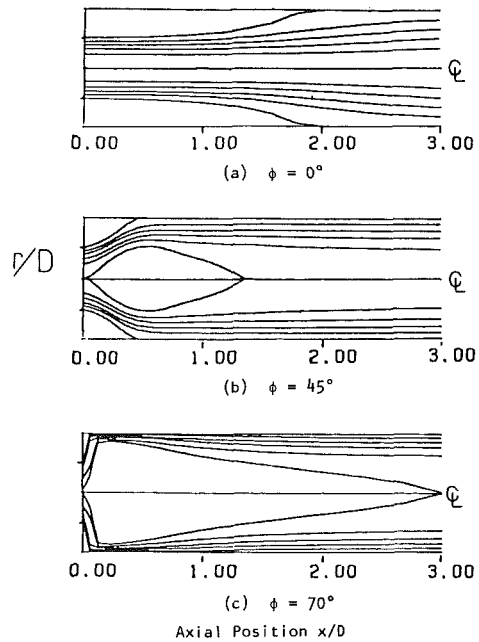

Fig. 5 Predicted streamline plots with wall expansion angle α = 90 deg and various swirl vane angles ϕ: (*a*) 0 deg, (*b*) 45 deg, and (*c*) 70 deg

axial velocity profile is dramatically changed. Near the inlet a central toroidal recirculation zone appears and the corner recirculation zone is considerably smaller. Also, a maximum velocity value occurs in an annular fashion near $r/D=0.25$, although a more flattened shape quickly develops before $x/D=1.0$. It should also be noted that the boundary layer on the outer sidewall is too thin to be seen on the figures. The strong swirl case of $\phi=70$ deg shows a much wider central recirculation region at $x/D=0.3$, which is caused by strong centrifugal effects. This promotes a very high forward velocity near the wall rather than a corner recirculation region. This tendency has been qualitatively observed by combustor designers at high degrees of swirl, but little quantitative data are yet available to precisely substantiate

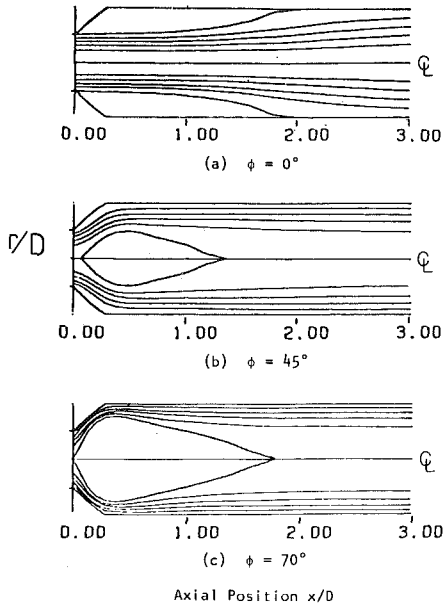

Fig. 6 Predicted streamline plots with wall expansion angle α = 45 deg and various swirl vane angles ϕ: (*a*) 0 deg, (*b*) 45 deg, and (c) 70 deg

this phenomenon. The radial extent of the central recirculation zone and the velocity near the wall quickly diminish downstream as swirl strength is dissipated.

The effect of side-wall angle α is only noticeable on the more strongly swirling flow cases and then only near to the inlet. Figure 3(*b*) with $\alpha = 45$ deg shows little effect of α on the nonswirling flow, but dramatic effects on the $\phi = 45$ and 70 deg flows. In the former case, no corner recirculation zone is present. In the latter case, the reduction of side-wall angle has greatly reduced the velocity near the confining walls and made the central recirculation zone narrower with higher reverse velocities. It should be noted, however, that only a slight effect of α (for the range considered here) remains beyond x/D values of about 1.0.

Figures 4(*a*) and 4(*b*) show swirl velocity profiles for the corresponding geometries with vane angles of 45, 60, and 70 deg. All of these profiles show solid-body-rotation behavior near the centerline, even near the inlet where a flat profile is a specified inlet condition. The radial location of the station maximum for w tends to increase with x/D in Fig. 4(*a*). Also irregularities of the profiles at $x/D = 0.32$ disappear with increasing x. Hence, swirl as well as axial velocity profiles appear to approach those corresponding to swirling flow in a pipe [22] as x increases.

Comparing Fig. 4(*b*) with 4(*a*), it is the weaker swirl cases which show the most appreciable effect of α at $x/D = 0.32$, and again this diminishes with increasing x. Profiles near the inlet are a little flatter in the outer part of the flow, with narrower solid-body-rotation regions near the axis. The profiles at $x/D = 1.68$ exhibit similarity for each geometry and if normalized with respect to their inlet swirl velocity maximum values, the curves will collapse on to a single characteristic curve.

Streamline Plots. Figure 5 shows results calculated and plotted by computer to show the combustor designer the sequence of predicted streamline patterns he should expect upon increasing the vane angle for the $\alpha = 90$ deg combustor. In particular, the size and shape of recirculation bubbles are emphasized. The nonswirling case shown in Fig. 5(*a*) exhibits a large corner recirculation region as indicated also in Fig. 3(*a*). As swirl is introduced, a central recirculation region appears in conjunction with a decrease in size of the corner

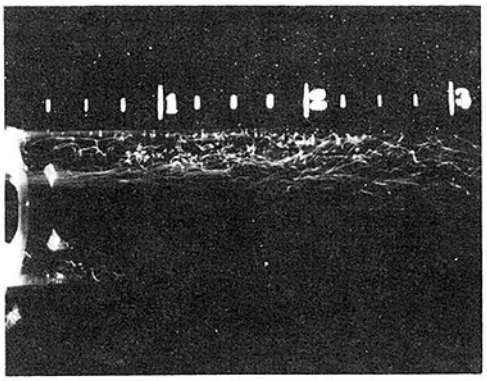

Fig. 7 (*a*) ϕ = 0 deg

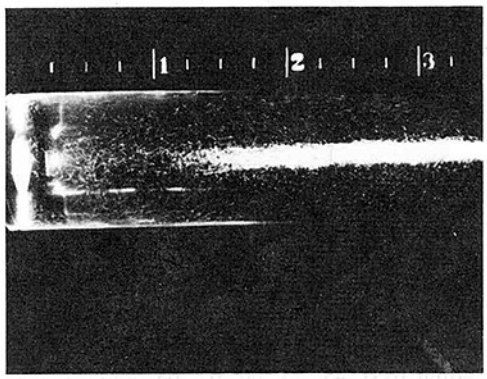

Fig. 7 (*b*) ϕ = 45 deg

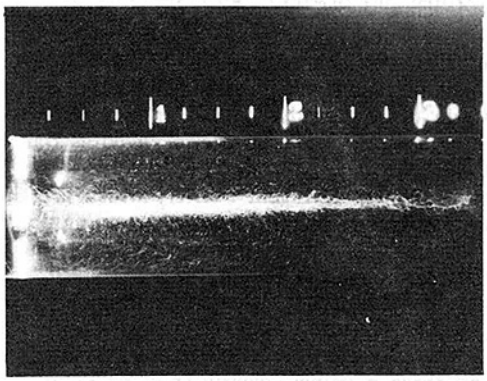

Fig. 7 (c) ϕ = 70 deg

Fig. 7 Flow visualization of pathlines produced by helium-filled soap bubbles with wall expansion angle α = 90 deg for various vane swirl angles ϕ:

recirculation region, as seen in the 45 deg swirl angle case. Further increases in swirl vane angle result in continued enlargement of the center zone. Similarly, the corner recirculation zone is gradually reduced in axial extent until it disappears by $\phi = 70$ deg [see Part (c) of the figure].

The same series of streamline patterns is displayed in Fig. 6 for the 45 deg expansion geometry. The same trend is found as the vane angle is increased, except that in this case the center recirculation zone is generally slightly smaller in both directions. The corner zone is similar in size for nonswirling conditions, but vanishes as swirl strength is increased. Compare, for example, the corresponding Part (b) of Figs. 5 and 6. The combustor designer may obtain further insight by observing a similar series of streamline plots predicted by Novick et al. [23] for an isothermal dump combustor flowfield with the following differences: a 90 deg expansion, an inlet hub, and a constricted exit.

Flow Visualization. An indication of the validity of the computations can be obtained by comparing predicted mean

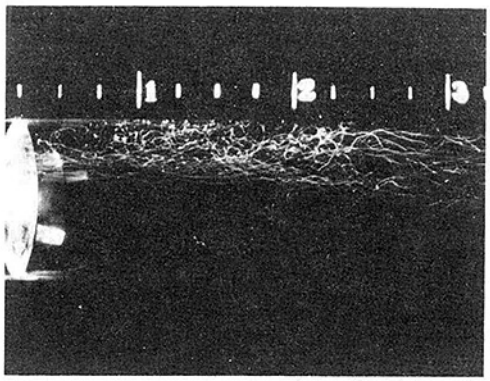

Fig. 8(a) ϕ = 0 deg

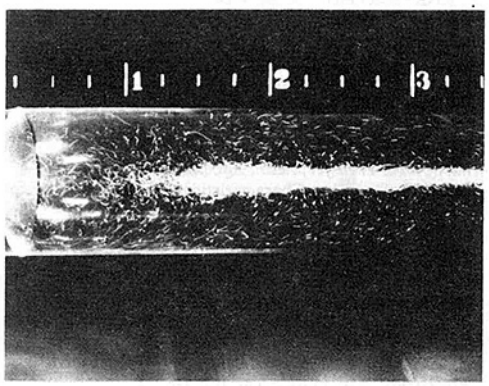

Fig. 8(b) ϕ = 45 deg

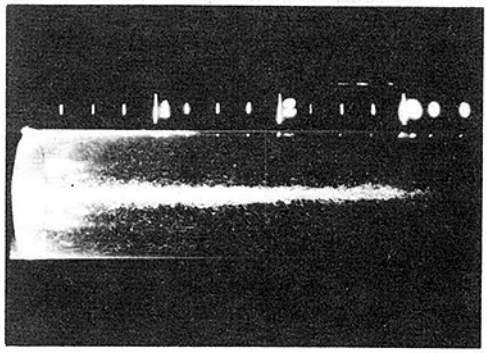

Fig. 8(c) ϕ = 70 deg

Fig. 8 Flow visualization of pathlines produced by helium-filled soap bubbles with wall expansion angle α = 45 deg for various vane swirl angles ϕ: (a) 0 deg, (b) 45 deg, and (c) 70 deg

streamline patterns with the pathlines traced out by the soap bubbles in the flow visualization experiments. Generally, a relatively long exposure time of 1/8 s is used so as to identify pathlines, and infer streamlines therefrom. A sample flow visualization photograph is presented in Fig. 7(*a*) corresponding to the zero swirl, 90 deg expansion angle flowfield. The photograph, with the flow from left to right, clearly shows a great number of individual pathlines. Photographs of this type can be used to distinguish regions of highly turbulent flow from smoother regions (for example near the centerline of the flowfield) which have smoother, straighter pathlines. In addition, the outline of the corner recirculation region can be estimated from Fig. 7(*a*) (and numerous additional photographs taken at the identical run condition). For this geometry the mean stagnation point defining the end of the recirculation zone appears to be at about 2 chamber diameters (8 step heights) downstream of the sudden enlargement. Examination of Fig. 5(*a*) shows that this is in quite good agreement with the numerical prediction.

A photograph with $\phi = 45$ deg is shown in Fig. 7(*b*), where a precessing vortex core, PVC, is clearly seen extending from $x/D = 1.25$ to the exit, although its upstream starting location fluctuates from about $x/D = 1.0$ to 1.5. The PVC is a well-known phenomenon in strongly swirling confined flows, consisting of a central core in the flowfield which exhibits a three-dimensional time-dependent instability. Oscillation is at low frequency [4–6]. A corner recirculation zone is faintly visible in Fig. 7(*b*), and it seems to extend to about $x/D = 0.4$. At stronger swirl $\phi = 70$ deg, the PVC is even thicker and extends further upstream, merging discretely with the central recirculation zone, see Part (c) of Fig. 7. There is now little evidence of a corner recirculation region. All these effects are in general agreement with the predictions of Figs. 3 and 5.

Figure 8 displays a sequence of photographs corresponding to those of Fig. 7, only now the side-wall angle $\alpha = 45$ deg. Comparing Parts (a) of the two figures reveals no significant changes, as found in earlier experiments [20], and in the present predictions, there being little predicted effect of the side-wall angle in the range $\alpha = 90$ to 45 deg on the non-swirling flowfield. The intermediate vane angle case of $\phi = 45$ deg is visualized in Fig. 8(*b*), and careful study of this and other photographs is quite revealing. A large concentration of bubbles is seen centered at about $x/D = 1.5$, probably corresponding to the location of the time-mean rear stagnation point of the central recirculation zone. The PVC extends from here to the exit. Comparison with Part (b) of Fig. 7 reveals that at $\phi = 45$ deg the relatively short corner recirculation zone seen with the $\alpha = 90$ deg geometry does not appear with the $\alpha = 45$ deg geometry. This is in conformity with the predictions given in Part (b) of Figs. 5 and 6. The $\phi = 70$ deg flow shown in Fig. 8(*c*) illustrates no corner recirculation zone as well, with the vortex core being wider and extending even further upstream, again merging almost imperceptibly with the central recirculation zone, as in Fig. 7(*c*).

The flow visualization photographs in general provide an encouraging base of data for comparison with the computations. Further experimental work is in progress at Oklahoma State University including five-hole pitot probe measurements [24] and single- and multi-wire hot-wire measurements. In all flowfields represented here, the calculation does a reasonable job of predicting the general flow patterns but it is expected that inaccuracies in detail will occur, as has been encountered by others in predicting recirculation zones with the standard k-ϵ turbulence model, especially under swirl flow conditions [11, 12]. There are a number of possible reasons for this, but the most likely one is that a turbulence model whose basis and parameters are adequate for simple flow situations is not adequate to handle the more complicated swirling recirculation flow situation.

Closure

Fundamental theoretical studies are being undertaken on swirling axisymmetric recirculating flows, under low speed and nonreacting conditions. Many factors affect the existence, size and shape of the corner recirculation zone and central toroidal recirculation zone. A major outcome of the current work is the ability to characterize and predict more realistically than previously the existence, size and shape of the corner and central recirculation zones as a function of the angle of the sloping wall, the degree of swirl imparted to the incoming flow, and other swirler and geometric parameters. Computations are made with a suitable computer code which includes several refinements to improve accuracy and economy. A few parameter variations were investigated computationally in order to make combustor design in-

formation available in a directly usable form. Comparison with flow visualization studies reveals that gross features of the flowfield are predicted quite well. A problem in swirling flows is the accuracy with which the details may be predicted. This may be partially attributed to the quality of the turbulence model. Further research should emphasize turbulence model development for swirling recirculating flows.

Acknowledgment

The authors wish to express their gratitude to NASA Lewis Research Center and Air Force Wright Aeronautical Laboratories for financial support under NASA Grant No. NAG 3-74.

References

1 Gerstein, M. (ed.), "Fundamentals of Gas Turbine Combustion," NASA-CP-2087, 1979. Workshop held at NASA Lewis Research Center, Cleveland, Ohio, Feb. 6-7, 1979.

2 Lefebvre, A. H., (ed.), *Gas Turbine Combustion Design Problems*, Hemisphere-McGraw-Hill, New York, 1980.

3 Lilley, D. G., "Flowfield Modeling in Practical Combustors: A Review," *Journal of Energy*, Vol. 3, July-Aug. 1979, pp. 193-210.

4 Syred, N., and Beér, J. M., "Combustion in Swirling Flows: A Review," *Combustion and Flame*, Vol. 23, 1974, pp. 143-201.

5 Lilley, D. G., "Swirl Flows in Combustion: A Review," *AIAA Journal*, Vol. 15, No. 8, Aug. 1977, pp. 1063-1078.

6 Gupta, A. K., Lilley, D. G., and Syred, N., *Swirl Flows*, Abacus Press, Tunbridge Wells, England, 1982 (in press).

7 Gosman, A. D., and Pun, W. M., "Calculation of Recirculation Flows," Rept. No. HTS/74/2, 1974, Dept. of Mechanical Engineering, Imperial College, London, England.

8 Lilley, D. G., and Rhode, D. L., "A Computer Code for Swirling Turbulent Axisymmetric Recirculating Flows in Practical Isothermal Combustor Geometries," NASA CR-3442, Feb. 1982.

9 Rhode, D. L., "Predictions and Measurements of Isothermal Flowfields in Axisymmetric Combustor Geometries," Ph.D. thesis, School of Mech. and Aero. Engrg., Okla. State Univ., Stillwater, Okla., 1981.

10 Launder, B. E., and Spalding, D. B., "The Numerical Computation of Turbulent Flows," *Comp. Methods in Appl. Mech. and Engrg.*, Vol. 3, Mar. 1974, pp. 269-289.

11 Habib, M. A., and Whitelaw, J. H., "Velocity Characteristics of Confined Coaxial Jets With and Without Swirl," ASME Paper No. 79-WA/FE-21, New York, Dec. 2-7, 1979.

12 Srinivasan, R., and Mongia, H. C., "Numerical Computations of Swirling Recirculating Flows," Final Report, NASA-CR-165196, Sept. 1980.

13 Vu, B. T., and Gouldin, F. C., "Flow Measurement in a Model Swirl Combustor," AIAA Paper No. 80-0076, Jan. 14-16, 1980, Pasadena, Calif.

14 Ha Minh, H., and Chassaing, P., "Perturbations of Turbulent Pipe Flow," *Proc. Symposium on Turbulent Shear Flows*, Pennsylvania State University, Apr. 1977, pp. 13.9-13.17.

15 Moon, L. F., and Rudinger, G., "Velocity Distribution in an Abruptly Expanding Circular Duct," ASME JOURNAL OF FLUIDS ENGINEERING, Mar. 1977, pp. 226-230.

16 Phaneuf, J. T., and Netzer, D. W., "Flow Characteristics in Solid Fuel Ramjets," Report No. NPS-57Nt-74081, July 1974, Prepared for the Naval Weapons Center by the Naval Postgraduate School.

17 Back, L. H., and Roschke, E. J., "Shear Layer Flow Regimes and Wave Instabilities and Reattachment Lengths Downstream of an Abrupt Circular Channel Expansion," ASME *Journal of Applied Mechanics*, Sept. 1972, pp. 677-781.

18 Roschke, E. J., and Back, L. H., "The Influence of Upstream Conditions on Flow Reattachment Lengths Downstream of an Abrupt Circular Channel Expansion," *Journal of Biomech.*, Vol. 9, 1976, pp. 481-483.

19 Krall, K. M., and Sparrow, E. M., "Turbulent Heat Transfer in the Separated, Reattached, and Redevelopment Regions of a Circular Tube," ASME *Journal of Heat Transfer*, Feb. 1966, pp. 131-136.

20 Chaturvedi, M. C., "Flow Characteristics of Axisymmetric Expansions," *Proceedings Journal Hydraulics Division, ASCE*, Vol. 89, No. HY3, 1963, pp. 61-92.

21 Morel, T., "Comprehensive Design of Axisymmetric Wind Tunnel Contractions," ASME Paper 75-FE-17, Minneapolis, Minn., May 5-7, 1975.

22 Weske, D. R., and Sturov, G. Ye, "Experimental Study of Turbulent Swirled Flows in a Cylindrical Tube," *Fluid Mechanics - Soviet Research*, Vol. 3, No. 1, Jan. -Feb. 1974, pp. 77-82.

23 Novick, A. S., Miles, G. A., and Lilley, D. G., "Numerical Solution of Combustor Flowfields: A Primitive Variable Design Capability," *Journal of Energy*, Vol. 3, No. 2, Mar.-Apr. 1979, pp. 95-105.

24 Rhode, D. L., Lilley, D. G., and McLaughlin, D. K., "Mean Flowfields in Axisymmetric Combustor Geometries with Swirl," Paper AIAA 82-0177, Orlando, Fla., Jan. 11-14, 1982.

A. K. Gupta

J. M. Beér

J. F. Louis

Massachusetts Institute of Technology, Cambridge, Mass.

A. A. Busnaina

D. G. Lilley

Oklahoma State University, Stillwater, Okla.

Flow Aerodynamics Modeling of an MHD Swirl Combustor: Calculations and Experimental Verification

This paper describes a computer code for calculating the flow dynamics of constant density flow in the second stage trumpet shaped nozzle section of a two stage MHD swirl combustor for application to a disk generator. The primitive pressure-velocity variable, finite difference computer code has been developed to allow the computation of inert nonreacting turbulent swirling flows in an axisymmetric MHD model swirl combustor. The method and program involve a staggered grid system for axial and radial velocities, and a line relaxation technique for efficient solution of the equations. Turbulence simulation is by way of a two-equation κ-ϵ model. The code produces as output the flowfield map of the nondimensional stream function, axial, and swirl velocity. Good argeement was obtained between the theoretical predictions and the qualitative experimental results. The best seed injector location for uniform seed distribution at combustor exit is with injector located centrally on the combustor axis at entrance to the second stage combustor.

1 Introduction

Most coal fired combustors employ a cyclonic design. In this system a mixture of coal and a small amount of combustion air is introduced into a cylindrical combustion chamber, either axially or tangentially through several ports, while the rest of the combustion air is preheated to a high temperature (1200 - 1500K) and then introduced at high velocities through an array of tangential inlets. Alternatively, preheated air can be replaced by oxygen. The slag is removed in liquid form at one end of the cyclone combustor. Two stage combustor geometry is more favorable than the single stage slagging combustors due to the simplicity of slag removal and to prevent substantial vaporization of the alkali metals present in coal. In a two stage MHD combustor arrangement, the seed is introduced into the second stage and therefore relatively little or no seed is lost during the liquid slag removal process from the first stage.

The two stage model combustor utilized here is a multi-annular swirl burner which is placed at the exit of the first stage tangential-axial type swirl combustor, Fig. 1. The multi-annular design permits the variation of radial distribution of swirl velocity in the combustor which in turn can be used to vary the turbulent shear between the individual swirling concentric annuli [1-3]. This design permits ultra high swirl in the second stage with swirl vanes, if any, to be placed outside the very high temperature regions of the combustor in the oxygen or clean preheated air. The gas burns completely in the second stage combustor and turns 90 deg into the disk generator along a trumpet shaped exit nozzle.

In a previous paper by Gupta, et al. [4] results were presented for one swirl number ($S=1.85$) of the flowfield calculations and their experimental verification. In this paper further theoretical calculations and experimental verifications

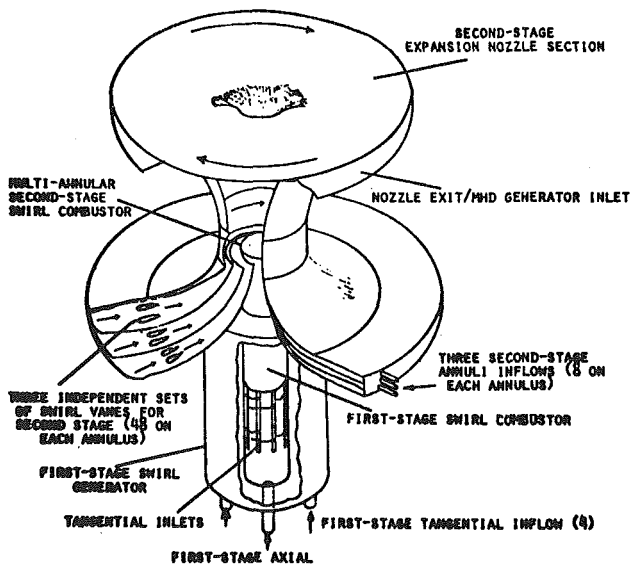

Fig. 1 Schematic diagram of the higher swirl, two stage, MHD water model test facility

Contributed by the Fluids Engineering Division for publication in the JOURNAL OF FLUIDS ENGINEERING. Manuscript received by the Fluids Engineering Division, September 2, 1981.

are made at different swirl numbers, flow rates, and flow distribution of the fluid dynamics in the second stage nozzle section of the model swirl combustor. Special emphasis is given on the avoidance of the boundary layer separation as the flow turns into the MHD disk generator with change in input swirl number and distribution, flow rates, and distribution into the combustor. For a separated flow a hot spot is formed at the point of separation, with consequent damage to the wall material from the hot combustion gases which enter the diffuser at a temperature of the order of 2500 - 3000K. The performance of MHD generators can be seriously influenced by inhomogenous distribution of such properties created by incomplete mixing of seed material with the plasma, heat loss from the combustor gas regions, wakes of cooled surfaces immersed in fluid or due to the presence of cooler boundary layer over the walls of the MHD generators. Another objective is to find the suitable seed injection point into the combustor exit at the disk generator. These are carried out both qualitatively and quantitatively using dye and salt tracer techniques respectively.

In the nozzle section flow separation is prevented by the use of an aerodynamically designed shape nozzle and also by the use of strongly swirling jet in place of the plug flow. The large-scale effects on the flowfield are characterized by the swirl number, S, defined as [5].

$$S = \frac{G_\phi}{G_x R}$$

where G_ϕ and G_x are the axial flux of angular momentum and linear momentum respectively. These can be written as:

$$G_\phi = \int_0^R (wr)\,\rho u 2\pi r dr = \text{constant}$$

$$G_x = \int_0^R u\rho u 2\pi r dr + \int_0^R p 2\pi r dr = \text{constant}$$

where u, w, and p are the axial velocity, tangential velocity, and static gauge pressure, respectively.

The effect of combustion upon swirl flow is to reduce the swirl number according to [6]:

$$S_{\text{combustion}} \approx S_{\text{isothermal}} \times \frac{T_{\text{inlet}} K}{T_{\text{outlet}} K}$$

$$\approx S_{\text{isothermal}} \times \frac{\rho_{\text{outlet}}}{\rho_{\text{inlet}}}$$

where T and ρ are the average temperature and density, respectively, over the cross-section.

Strongly swirling jets (with $S > 0.6$) possess sufficient radial and axial pressure gradient to cause a central torroidal recirculation zone, which is not observed at low degrees of swirl [5, 6]. This paper is concerned with the simulation and solution of these strongly, nonreacting swirl flows encountered in the MHD combustors utilizing swirl. The solution procedure can also be adapted to other types of swirl combustors with some minor modification in the code. The data enables a determination to be made of the effect of variation in input swirl number, flow rates and distribution upon the flow pattern, mixing and residence time distribution in the second stage nozzle section of the MHD swirl combustor. The predictions from the code are compared with the qualitative experimental data of water model study for code evaluation.

2 The Mathematical Problem

The prediction procedure starts from equations representing conservation of mass, momentum, turbulent kinetic energy and its dissipation rate. They are represented in the general form for axisymmetric flow via [6–12]

$$\frac{1}{r}\left[\frac{\partial}{\partial x}(\rho u r\phi) + \frac{\partial}{\partial r}(\rho v r\phi) - \frac{\partial}{\partial x}\left(r\Gamma_\phi \frac{\partial \phi}{\partial x}\right) - \frac{\partial}{\partial r}\left(r\Gamma_\phi \frac{\partial \phi}{\partial x}\right)\right] = S_\phi$$

where ϕ represents any of the dependent variables u, v, w, k, and ϵ. These equations are the Reynolds equations for axisymmetric flow written in divergence form. The standard two-equation k-ϵ turbulence model [11] is employed, whereby the exchange coefficients Γ_ϕ may be specified in each equation by way of

$$\mu = c_\mu \rho k^2/\epsilon,$$
$$\Gamma_\phi = \mu/\sigma_\phi.$$

This implies the use of simple isotropic Stokesian stress sensor although there is some evidence of the need for nonisotropy in certain swirling flow situations [6]. The present model has been used in a wide variety of turbulent flow situations and good predictive capability has been achieved [8]. The equations differ primarily in their final source terms S_ϕ as given in reference [12]. The corresponding finite difference equations are solved via an advanced version of the TEACH computer code [10], using a semi-implicit line-by-line method for values at points of a variable size rectangular grid, with variable under-relaxation.

Figure 2 shows an example of grid specification for the particular 2-D axisymmetric MHD geometry under consideration. The flowfield is covered with a nonuniform rectangular grid system; typically the boundary of the solution domain falls halfway between its immediate nearby parallel gridlines; and clearly specification of the x and r coordinates of the gridlines, together with information concerned with the position of the upper and curved boundary, is sufficient to determine the flowfield of interest. The curved boundary is simulated by means of a stairstep approach with sloping boundary segments where appropriate. The optional centerbody is not used in the present study and is discussed in another paper by Gupta et al. [13].

The present prediction procedure uses the primitive pressure-velocity variables [10] in contrast to earlier studies which use the stream function and vorticity approach [9]. The philosophy and general advantages of the present approach are discussed elsewhere [10]. A complete description of the finally developed computer program [with a full description of the equations, source terms, constants occurring and techniques for handling turbulent swirling flow near curved boundaries] is available [12]. Estimates for mean velocities at the inlet are employed as boundary conditions, while the inlet values for k and ϵ are presumed in the standard manner [11]. Further, previous swirling flow measurements are incorporated as wall functions to avoid the expense of computing within the boundary layer. Zero velocities on all walls are assumed, with symmetry conditions for most variables along the centerline, except swirl velocity which is given a definite zero value.

3 Experimental Water Model Facility

The experimental water model test facility, shown in Fig. 1, consists of an octagonal water tank having first-stage model swirl combustor placed outside the tank and second-stage multi-annular model swirl combustor inside. The first stage is a tangential-axial entry type of swirl generator with the swirl number imparted to the flow of approximately 1.85. The second stage is of the disk type having three annuli with independent inflows through each. Aerodynamically designed swirl vanes located in each annulus at the upstream end can be

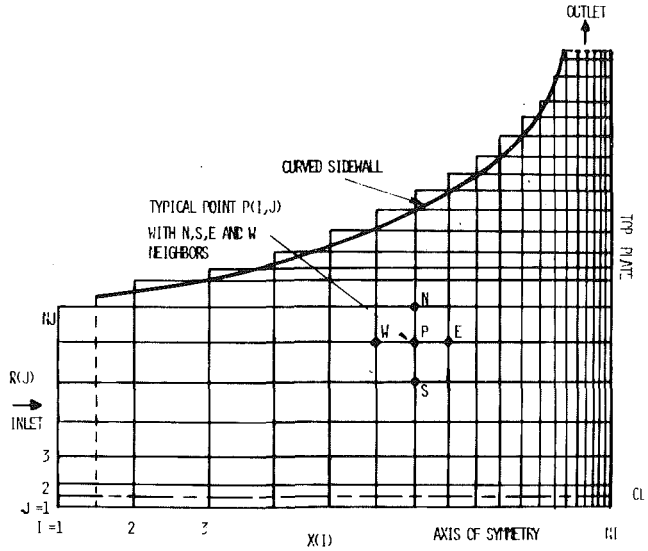

Fig. 2 Grid structure employed in the code (20 × 21)

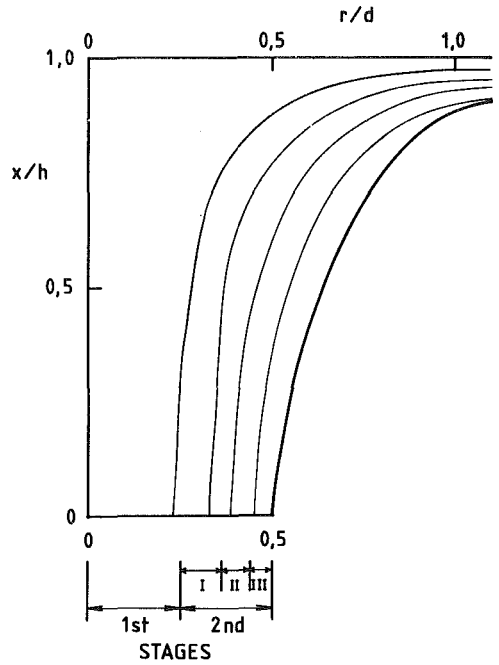

Fig. 3 Calculated streamlines with $S = 0$ ($\phi = 0$ deg) and u = 15 m/s

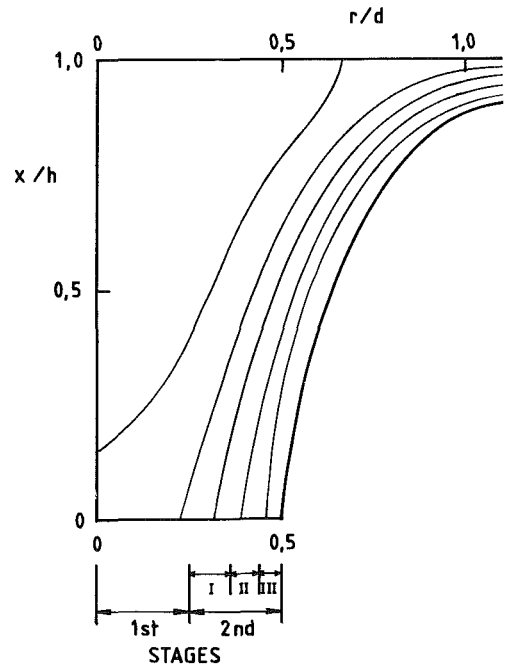

Fig. 4 Calculated streamlines with $S = 0.66$ ($\phi = 45$ deg) and u = 15 m/s

independently adjusted to achieve the desired swirl number in an annulus. The first stage is located centrally inside the disk of the second stage and then this assembly is bolted under the bottom plate of the tank, with only a small portion protruding through, Fig. 1. The second stage trumpet shaped nozzle section is then clamped onto this projecting portion of the combustor assembly. Thus the second stage nozzle section is located inside the tank. A top flat disk is attached to the second stage model combustor by means of four spacers-holding bars. Water is circulated through the model by a water pump.

4 Flowfield Calculations and Experimental Verification

General trendwise predictions are made in order to demonstrate the capability of the code in simulating strongly swirling recirculating flows, in the trumpet shaped nozzle section of the second stage model swirl combustor. The main emphasis is on the application of the code to MHD swirl combustors to assist in combustor design and development. The predictive capability of the code is now demonstrated for the corresponding flowfield. Appropriate boundary conditions simulating the various flow strengths (swirl number, flow rates, and flow distribution) in the first stage and three annuli of the second stage are taken exactly to conform with the experiments. Discussion is primarily aimed at guiding designers in judicially deciding where experimental emphasis should be placed and/or in interpolating results from a limited amout of experimental data. Computations are portrayed which deal with the verification of the analysis by comparison with the qualitative experimental data (using flow visualization technique) for a problem of coaxial multi-annular swirl flow into a confined trumpet shaped enlargement.

Computations were performed for isothermal case with varying swirl vane angle and input flow velocity distribution. For comparison purposes, it is worth noting that vane angle ϕ and swirl number S are related approximately by $S = 2/3 \tan \phi$ so that the angle of 0, 45, 60, 70, and 76 deg correspond to swirl numbers of 0, 0.66, 1.15, 1.83, 2.67, respectively. Results presented here are with flat head input velocity of 15 m/s at entrance to the model combustor; calculations performed at $S = 1.83$ with nonuniform input velocity distribution (e.g., with flow velocity reduced to 1 m/s in outermost annulus of second stage) showed little change in flow pattern as compared to the case with flat head input velocity.

Figure 2 shows the schematic diagram of the grid system (20 × 21) used having an expansion ratio of 0.85 in x-direction. For zero degree of swirl approximately 200 iterations were used to obtain convergence. As the degree of swirl or vane angle was successively increased the value at the previous swirl number was taken as the starting point and approximately 200 further iterations were performed to obtain convergence. General predictions are now given for the effect of swirl number upon flowfield in the model combustor. Figure 3 shows the calculated streamlines produced with input flow velocity of 15 m/s and zero swirl. The results are plotted

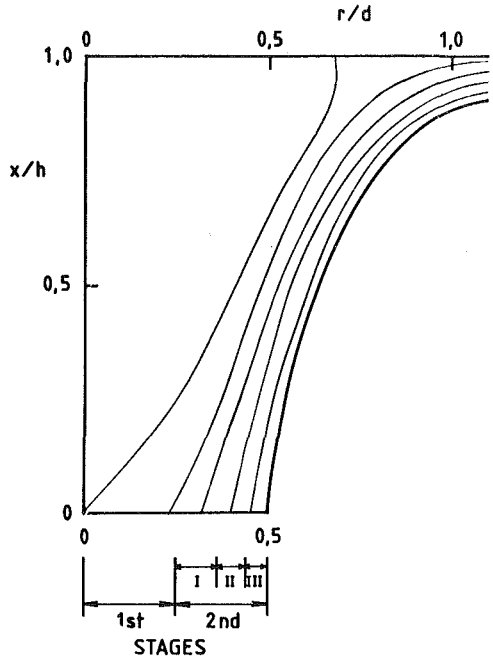

Fig. 5 Calculated streamlines with $S = 1.15$ ($\phi = 60$ deg) and u = 15 m/s

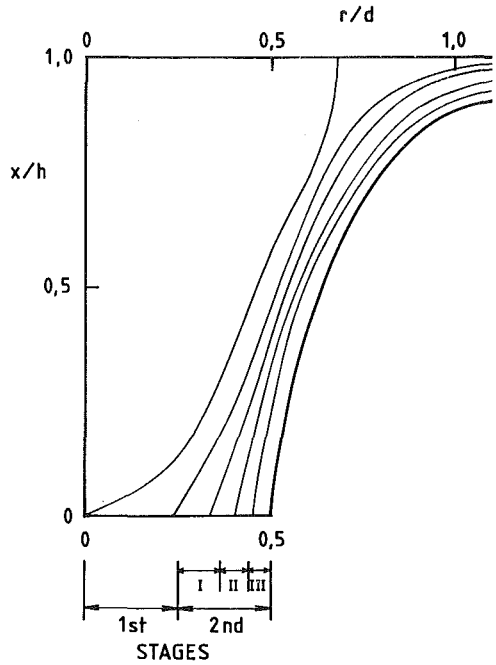

Fig. 6 Calculated streamlines with $S = 1.83$ ($\phi = 70$ deg) and u = 15 m/s

in the form of the nondimensional stream function (Ψ/Ψ_0), where

$$\Psi = \int_0^R \rho u r dr, \Psi_0 = \int_0^{d/2} \rho u r dr$$

and d is the inlet diameter of the second stage nozzle section.

As expected the maximum velocity is through the center of the model with rapid decay in axial velocity e.g., at half the distance downstream in the nozzle section the axial velocity is reduced to about 5 to 6 m/s. As the degree of swirl was increased to 0.66 a central recirculation zone was established within the flow having an upstream stagnation point located at approximately half the distance downstream in the second stage nozzle section, Fig. 4. The length of the recirculation zone extended right down to the downstream flat plate and the streamlines hit the downstream plate at $r/d \simeq 0.7$. The existence of a central recirculation zone with moderate degree of swirl to the flow is in agreement with the available experimental evidence [6]. Some evidence of the flow separation from the side wall of the model combustor could be seen. A further increase in swirl number to 1.15 resulted in fatter size of the recirculation zone, Fig. 5. The upstream stagnation point shifted right at inlet to the second stage. The shift in streamlines to the side wall is as expected and is associated with higher velocities due to increased centrifugal forces. Again the streamlines hit the downstream plate at approximately $r/d = 0.7$. The increase in the degree of swirl assisted the flow to remain better attached to the side wall all along the second stage nozzle section. As the swirl number was further increased to 1.83 and 2.67 the general flowfield trend was the same as that calculated for $S = 1.15$ except for the increase in the size of the central recirculation zone having larger recirculation velocities and mass flow rates, Figs. 6 and 7. Increase in the degree of swirl to the flow crushed the streamlines even more to the side wall to yield higher velocities and the location of the stagnation points remained approximately the same. For a swirl number of 2.67 maximum axial velocity was obtained near to the side wall approximately half way downstream of the nozzle. The results calculated with the code at swirl numbers beyond 1.15 with various flow rates and flow distribution revealed no evidence

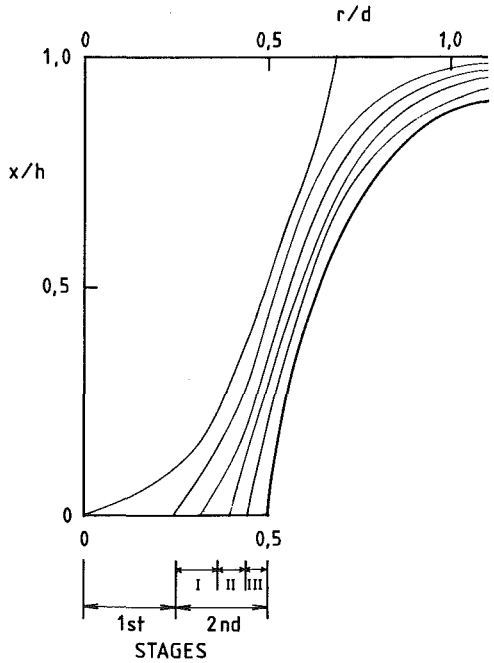

Fig. 7 Calculated streamlines with $S = 2.67$ ($\phi = 76$ deg) and u = 15 m/s

of the flow separation from the side wall of the model combustor.

A comparison of the calculations at various swirl numbers revealed that bigger size of the central recirculation zone and large velocity gradient are obtained at high swirl numbers, and that for the same swirl number velocity gradients are larger with flow through all inlets than those obtained with partial blocking of the inlets.

Experimental results were obtained with many different input swirl numbers, flow rates and distribution into the first and second stage model swirl combustor. The experimental observations of the flow pattern are compared with the calculated results from the code. Provision was made to take photographs of the flow in the axial plane or in the radial

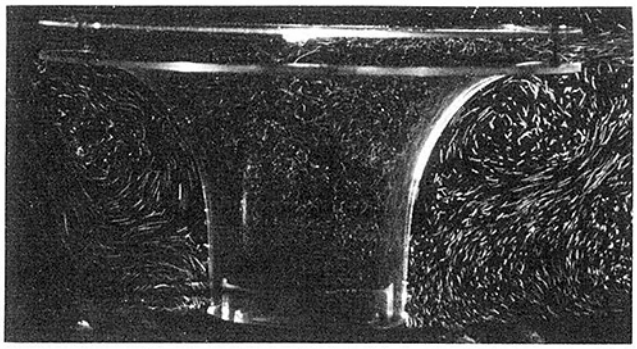

Fig. 8 Flow pattern obtained with flow through all inlets in the first and second stage at swirl number of 1.83

plane using a mirror placed at 45 deg angle to the flow. In this paper only the photographs obtained in the axial plane are reported.

Flowfield photographs in the second stage nozzle section of the MHD model swirl combustor were taken by slit light beam technique in the longitudinal plane. In the slit beam technique, polystyrene beads of approximately 1 mm diameter are added to the flow and any cross-section of the flow is visualized by illuminating it with a thin high intensity slit light beam against a dark background.

Figure 8 shows the longitudinal section of the flowfield in the second stage nozzle section of the model combustor with flows through both the first stage (axial and tangential) and the three annuli of the second stage at a swirl number of 1.83. Water flow rates through all the inlets were 96 gpm except for the axial inlet in the first stage – which was 10 gpm. No separation of the flow from the walls of the model could be observed except for the last 2 in. The size of the recirculation zone formed was found to be approximately 60 percent of the inlet diameter, having an upstream stagnation point located at the nozzle inlet throat section. A vortex located near the downstream plate just before the exit was also observed which shed alternatively from the two sides. It is well known that flows with strong swirl exhibits a three-dimensional time dependent instability called the precessing vortex core (PVC). The rotational frequency of the PVC increases with Reynolds number [6, 14]. The gradient of this increase increases with swirl number [6]. Our flow visualization studies results carried out with the water model at various swirl numbers is in agreement with that reported in references [6 and 8]. The PVC are useful for mixing of the reactants in the swirl flows but can cause low frequency high amplitude oscillations [6, 14].

Without any axial flow to the first stage combustor, low frequency oscillations in the flow of approximately 1.5 Hz were observed. These oscillations were of very distinct nature and the flow moved gradually downstream in phase with the oscillatory frequency. The effect of axial flow through the first stage was to decrease both the size of the internal recirculation zone and the magnitude of reverse flow velocity. Vortex shedding occurred from the boundary layer and the flow separation from the nozzle wall was found to be approximately one inch before the downstream exit. The PVC was again found to be present. For the scaling of swirl combustors, operating under high swirl number conditions (>0.6), the PVC frequency can be estimated as follows:

$$\text{Reynolds No. (Re)} = \frac{ud}{\nu}; \quad \text{Strouhal No. (St)} = \frac{fd}{u}$$

therefore

$$\frac{fd}{\text{St}} = \frac{\text{Re}\nu}{d}$$

or

$$f = \frac{\text{ReSt}\nu}{d^2}$$

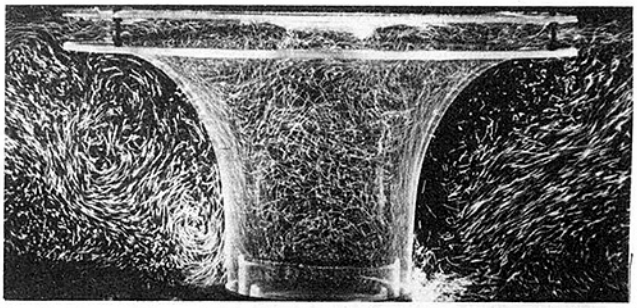

Fig. 9 Flow pattern obtained with flow through all inlets in the first and second stage at swirl number of 1.5

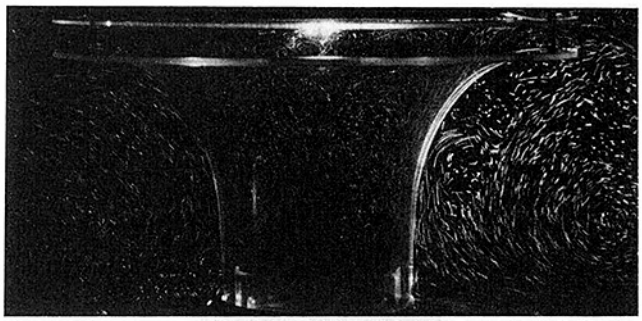

Fig. 10 Flow pattern obtained with flow through tangential inlet in the first stage and central and inner annuli in the second stage at a swirl number of 1.83

Figure 9 shows the flow pattern produced with flows through all inlets in the first and second stages but with the swirl number decreased to 1.5 in the second stage. Two small size recirculation zones were observed, one lying on the central axis just downstream of the inlet section of the second stage nozzle and the other one lying adjacent to the top downstream plate. The flow oscillated at low frequency and the PVC observed in the previous cases was also found to be present. As expected the flow separation from the nozzle walls increased with decrease in swirl number, in agreement with the theoretical predictions.

Figure 10 shows the flow pattern obtained with flows through tangential inlet in the first stage and inner and central annuli of the second stage at a swirl number of 1.83. For this case two recirculation zones could be clearly observed. Flow separation from the nozzle wall was found to occur at approximately 2 inches before the exit.

A comparison of the qualitative water model experimental results with the model predictions reveal that the flow remains essentially attached to the nozzle wall all along its surface only at high degrees of swirl. In the experimental model combustor the dramatic increase in the curvature of the nozzle wall near the exit tend to cause the flow to break away from the wall. However this was not found in the computer predictions. This disagreement between calculations and experimental results for the last two inches of the nozzle section could partially be due to the use of turbulence model which is established for relatively simple flows and is applied here for a very complex flow situation.

The present experimental water model study, however, reveals that in order to obtain no flow separation from the nozzle walls and controlled size of the recirculation zone within the nozzle an aerodynamically designed trumpet-shaped nozzle, in place of the top flat plate, placed inside the second stage nozzle of the model combustor should be used. Results obtained with such a second stage nozzle geometry are given elsewhere [13].

4.1 The Injection Study. The dye injection experiments

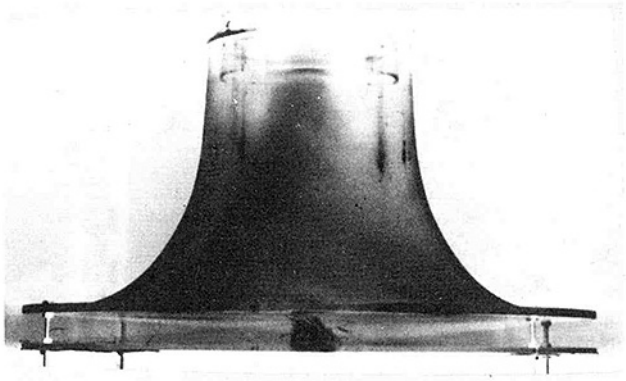

Fig. 11(*a*) Dissipation of colored dye injected centrally at entrance to the second stage with flow through tangential and axial inlets in the first stage and all inlets in the second stage at $S = 1.83$

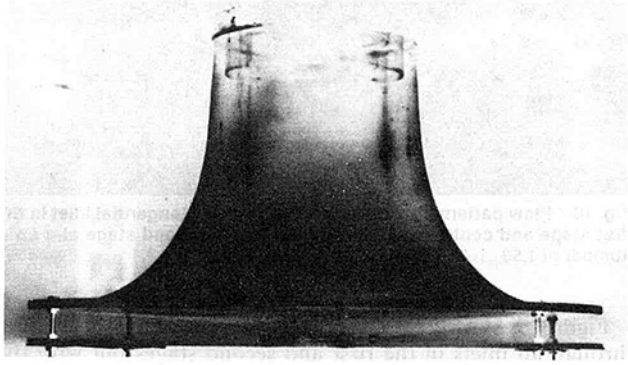

Fig. 11(*b*) Dissipation of colored dye injected centrally at entrance to the second stage with flow through tangential inlet in the first stage and all inlets in the second stage at $S = 1.83$

were conducted to obtain qualitative results of the mixing occurring within the second stage nozzle section. In these experiments concentrated red dye solution was injected at the entrance to the second stage combustor. A pump was used for dye injection and the injection rate was controlled to match the injection velocity with the actual flow velocity. Various radial locations were tried and it was observed that the best mixing occurred with central injection of the dye. Once the best injection location was determined the flow parameters were varied to determine their effect on mixing. During the test the first stage of the combustor had a swirl number of approximately 1.83 while that in the second stage was either 1.83 or 1.50. The best mixing was observed for the case of water flow through all the inlets of the first and second stage, Fig. 11(*a*). The results showed rapid mixing of the dye with water within a distance of approximately 1/2 the length of the nozzle and the dye concentration was very uniform at the nozzle exit. Another flow geometry which gave good mixing was with flow entering through the tangential inlets of the first stage and the two annuli (inner and center) of the second stage. The worst mixing occurred for the case of water flow through the tangential inlets of the first stage and the three annuli of the second stage swirl combustor, Fig. 11(*b*). For this case no mixing of the dye was found and the dye remained in the form of a jet until the downstream end of the nozzle section. The only mixing that occurred was when the dye jet impinged on the downstream plate. Mixing of the dye with the surrounding fluid increased with increases in swirl number.

4.2 Salt Tracer Study. These experiments were conducted to obtain some quantitative information upon mixing occurring within the nozzle section. In these experiments a salt

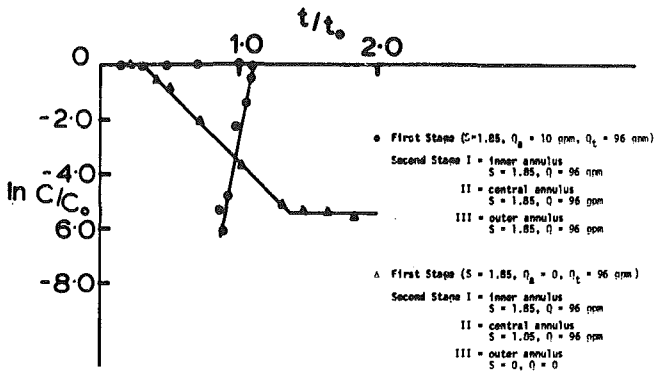

Fig. 12 Salt traces concentration decay as a function of time

solution of known concentration was injected into the fluid and its concentration measured at various locations downstream in the measurement volume. A conductivity probe was employed for obtaining the tracer salt concentration. The conductivity probe essentially measures the conductivity of the solution and yields a measure of the salt concentration. The probe was inserted from the top of the model and could traverse both vertically and horizontally. Ideally the water should not be recirculated during the experiment to prevent the buildup of the salt concentration. However, in the present system, a compensating circuit (zero offset) was employed to correct for the variation in the background salt concentration.

The conductivity probe consisted of two platinum wire electrodes (approximately 0.75 inches long). The oxide coating was applied by a platinizing kit using platinum chloride solution. Before platinizing the electrodes were thoroughly cleaned by a cleaning solution. The platinizing is done to prevent the atmospheric oxidation of the electrode, as the conductivity measurement depends greatly upon the physical condition of the electrode. A small change in the amount of oxidation of the electrodes will appreciably affect the measured conductivity. It is recommended to recalibrate the probe periodically and to store it in distilled water to prevent any degradation of the oxide coating. The electrodes should be periodically replatinized.

During the experiment the salt solution was injected continuously till such time that a steady state concentration was registered by the probe. This value was used as the measured concentration at the point under consideration. The time required for the salt tracer to reach the probe was also measured from the oscilloscope.

Figure 12 shows the graph of $\ln C/C_0$ versus t/t_0 where C is the measured salt concentration, C_0 is the injected salt concentration, t is the time that a particle should take to cover the distance from the point of injection to the point of measurement, based on the mean flow velocity (assuming a plug flow). Uncertainty estimates on ordinate and abscissa in Fig. 12 were estimated to be about 5 percent. The figure shows that in a multi-annular swirl combustor one can change the reactor configuration (i.e., plug flow or perfectly stirred) by changes in input swirl numbers, flow rates and flow distribution. The residence time distribution found here may be obtained by combinations of plug flow and perfectly stirred reactors in either order [15]. However, the ideal residence time distribution is obtained by the combination of two types of reactors in such a way that the perfectly stirred part is followed by the plug flow in series. This combination of two combustor types enables the highest volumetric rates of combustion to be obtained for a given combustion efficiency.

5 Conclusions

Development of a primitive pressure-velocity variable,

finite difference technique has been discussed, together with its application to strongly swirling and chemically inert recirculating flow in MHD model swirl combustor. The analysis and computer program involve a staggered grid system for axial and radial velocities, a line relaxation technique for the efficient solution of the equations, and a two-equation $\kappa - \epsilon$ turbulence model. The code calculates the flow dynamics of constant density flow in the second stage trumpet shaped nozzle section of a two stage MHD swirl combustor and shows the effects of swirl number, flow rates and flow distribution into the model combustor in the form of nondimensional stream function and other details throughout the flowfield. Predictions of this type, which are trendwise indicative, allow some design concepts to be investigated more economically and faster than by the exclusive use of experimental means. Further development and application of full flowfield calculations will provide a valuable supplementary technique for designers of practical combustion equipment.

A water model flow visualization technique was used to study the flowfield within and any flow separation from the walls of the trumpet shaped divergent nozzle. Flow separation was usually found to occur within the last two inches of the nozzle section before the exit for all the flow rates and flow distribution and swirl number distribution tested. General agreement between the theoretical predictions and the experimental data is encouraging. The calculated results revealed no flow separation at high swirl numbers, flow rates and flow distribution into the model combustor and that the size of the internal recirculation zone increases with increase in swirl number. In order to obtain no flow separation and controlled internal recirculation within the second stage at all swirl numbers, the use of an aerodynamically designed trumpet shaped nozzle in place of the top flat plate, placed within the second stage combustor is recommended. Best location for the seed injection into the MHD combustor, in order to obtain uniform mixing at the exit before entry into the channel, was found to be that located centrally at the inlet to the second stage and with flow through all inlets of both the first and second stages. Salt tracer concentration measurements revealed that in a multi-annular swirl combustor one can change the reactor configuration (i.e., plug flow and perfectly stirred) by changes in input swirl numbers and flow rates and flow distribution.

Acknowledgments

The work was supported by a DOE contract No. DE-ACO1-79ET15518. Preliminary computer studies were supported by NASA Lewis Research Center in the form of NASA Grant No. NAG 3-74, 1980, technical monitor Dr. C.J. Marek.

References

1 Beér, J. M., British Patent No. 1099959, 1968.

2 Gupta, A. K., Beér, J. M., and Swithenbank, J., "Concentric Multi-Annular Swirl Burner: Stability Limits and Emission Characteristics," *Proceedings of the 16th International Symposium on Combustion*, The Combustion Institute, 1977, p. 79.

3 Gupta, A. K., Beér, J. M., and Swithenbank, J., "On the Operational Characteristics of a Multi-Annular Swirl Burner," *Combustion Science and Technology*, Vol. 17, Nos. 5 and 6, 1977, p. 199.

4 Gupta, A. K., Khan, H., Beér, J. M., and Lilley, D. G., "Flowfield Calculations in an MHD Combustor," AIAA Paper 81-0044, St. Louis Mo., Jan. 12-15, 1981.

5 Beer, J. M., and Chigier, N. A., "Swirling Jet Flames from an Annular Burner," 5 me Journee d'Etudes sur les Flammes, Paris, 1963. Also Doc. No. K20/a91, International Flame Research Foundation, Ijmuiden, Holland, 1963.

6 Gupta, A. K., Lilley, D. G., and Syred, N., *Swirl Flows*, Abacus Press, Tunbridge Wells, England, 1982 (in press).

7 Lilley, D. G., "Primitive Pressure-Velocity Code for the Computation of Strongly Swirling Flows," *AIAA Journal*, Vol. 14, June 1976, p. 749.

8 Gupta, A. K., and Lilley, D. G., *Flowfield Modeling and Diagnostics*, Abacus Press, Tunbridge Wells, Kent, England, 1982 (in press).

9 Gosman, A. D., Pun, W. M., Runchal, A. K., Spalding, D. B., and Wolfshtein, M. W., *Heat and Mass Transfer in Recirculating Flows*, Academic Press, London, England, 1974.

10 Gosman, A. D., and Pun, W. M., "Calculation of Recirculating Flows," Report No. HTS/74/2, Dept. of Mechanical Engineering, Imperial College, London, England, 1974.

11 Launder, B. E., and Spalding, D. B., *Mathematical Models of Turbulence*, Academic Press, London, 1972.

12 Lilley, D. G., and Rhode, D. L., "STARPIC: A Computer Code for Swirling Turbulent Axisymmetric Recirculating Flows in Practical Isothermal, Combustor Geometrics," NASA-CR-3442, 1981.

13 Gupta, A. K., Beér, J. M., Louis, J. F., Lilley, D. G., and Busnaima, A. A., "Predictions of MHD Swirl Combustor Flows Using a Primitive Variable Solution Procedure," 19th Symposium on Engineering Aspects of Magnetohydrodynamics, Univ. of Tennessee Space Institute, June 15-17, 1981.

14 Gupta, A. K., "Combustion Instabilities in Swirling Flows," *Gas Wärme International*, Vol. 28, No. 1, Jan., 1979, p. 55.

15 Beér, J. M., and Lee, K. B., "The Effect of Residence Time Distribution on the Performance and Efficiency of Combustors," Tenth Symposium (International) on Combustion, The Combustion Institute, 1965, p. 1187.

finite difference technique has been discussed, together with its application to strongly swirling and chemically inert recirculating flow in MHD model swirl combustor. The analysis and computer program involve a staggered grid system for axial and radial velocities, a line relaxation technique for the efficient solution of the equations, and a two-equation $\kappa-\epsilon$ turbulence model. The code calculates the flow dynamics of constant density flow in the second stage trumpet shaped nozzle section of a two stage MHD swirl combustor and shows the effects of swirl number, flow rates and flow distribution into the model combustor in the form of nondimensional stream function and other details throughout the flowfield. Predictions of this type, which are trendwise indicative, allow some design concepts to be investigated more economically and faster than by the exclusive use of experimental means. Further development and application of full flowfield calculations will provide a valuable supplementary technique for designers of practical combustion equipment.

A water model flow visualization technique was used to study the flowfield within and any flow separation from the walls of the trumpet shaped divergent nozzle. Flow separation was usually found to occur within the last two inches of the nozzle section before the exit for all the flow rates and flow distribution and swirl number distribution tested. General agreement between the theoretical predictions and the experimental data is encouraging. The calculated results revealed no flow separation at high swirl numbers, flow rates and flow distribution into the model combustor and that the size of the internal recirculation zone increases with increase in swirl number. In order to obtain no flow separation and controlled internal recirculation within the second stage at all swirl numbers, the use of an aerodynamically designed trumpet shaped nozzle in place of the top flat plate, placed within the second stage combustor is recommended. Best location for the seed injection into the MHD combustor, in order to obtain uniform mixing at the exit before entry into the channel, was found to be that located centrally at the inlet to the second stage and with flow through all inlets of both the first and second stages. Salt tracer concentration measurements revealed that in a multi-annular swirl combustor one can change the reactor configuration (i.e., plug flow and perfectly stirred) by changes in input swirl numbers and flow rates and flow distribution.

Acknowledgments

The work was supported by a DOE contract No. DE-ACO1-79ET15518. Preliminary computer studies were supported by NASA Lewis Research Center in the form of NASA Grant No. NAG 3-74, 1980, technical monitor Dr. C.J. Marek.

References

1 Beér, J. M., British Patent No. 1099959, 1968.

2 Gupta, A. K., Beér, J. M., and Swithenbank, J., "Concentric Multi-Annular Swirl Burner: Stability Limits and Emission Characteristics," *Proceedings of the 16th International Symposium on Combustion*, The Combustion Institute, 1977, p. 79.

3 Gupta, A. K., Beér, J. M., and Swithenbank, J., "On the Operational Characteristics of a Multi-Annular Swirl Burner," *Combustion Science and Technology*, Vol. 17, Nos. 5 and 6, 1977, p. 199.

4 Gupta, A. K., Khan, H., Beér, J. M., and Lilley, D. G., "Flowfield Calculations in an MHD Combustor," AIAA Paper 81-0044, St. Louis Mo., Jan. 12-15, 1981.

5 Beer, J. M., and Chigier, N. A., "Swirling Jet Flames from an Annular Burner," 5 me Journee d'Etudes sur les Flammes, Paris, 1963. Also Doc. No. K20/a91, International Flame Research Foundation, Ijmuiden, Holland, 1963.

6 Gupta, A. K., Lilley, D. G., and Syred, N., *Swirl Flows*, Abacus Press, Tunbridge Wells, England, 1982 (in press).

7 Lilley, D. G., "Primitive Pressure-Velocity Code for the Computation of Strongly Swirling Flows," *AIAA Journal*, Vol. 14, June 1976, p. 749.

8 Gupta, A. K., and Lilley, D. G., *Flowfield Modeling and Diagnostics*, Abacus Press, Tunbridge Wells, Kent, England, 1982 (in press).

9 Gosman, A. D., Pun, W. M., Runchal, A. K., Spalding, D. B., and Wolfshtein, M. W., *Heat and Mass Transfer in Recirculating Flows*, Academic Press, London, England, 1974.

10 Gosman, A. D., and Pun, W. M., "Calculation of Recirculating Flows," Report No. HTS/74/2, Dept. of Mechanical Engineering, Imperial College, London, England, 1974.

11 Launder, B. E., and Spalding, D. B., *Mathematical Models of Turbulence*, Academic Press, London, 1972.

12 Lilley, D. G., and Rhode, D. L., "STARPIC: A Computer Code for Swirling Turbulent Axisymmetric Recirculating Flows in Practical Isothermal, Combustor Geometrics," NASA-CR-3442, 1981.

13 Gupta, A. K., Beér, J. M., Louis, J. F., Lilley, D. G., and Busnaima, A. A., "Predictions of MHD Swirl Combustor Flows Using a Primitive Variable Solution Procedure," 19th Symposium on Engineering Aspects of Magnetohydrodynamics, Univ. of Tennessee Space Institute, June 15-17, 1981.

14 Gupta, A. K., "Combustion Instabilities in Swirling Flows," *Gas Wärme International*, Vol. 28, No. 1, Jan., 1979, p. 55.

15 Beér, J. M., and Lee, K. B., "The Effect of Residence Time Distribution on the Performance and Efficiency of Combustors," Tenth Symposium (International) on Combustion, The Combustion Institute, 1965, p. 1187.

DISCUSSION

F. Boysan[1] and J. Swithenbank[1]

This paper contributes to the growing applications of fundamentally based mathematical models to complex engineering flows, not only to facilitate the arduous initial stages of design but also to analyze the performance of existing equipment without resorting to full scale experiments. The reliability of these models, however, is largely governed by the performance of the particular turbulence hypothesis employed and our discussion is directed at the choice of a suitable turbulence closure for strongly swirling flows.

Although the widely used κ-ϵ model of turbulence has been proven to be adequate in a variety of flows, it has been our experience that it performs poorly in confined vortex flows. This is illustrated dramatically in Figs. 1 and 2 which display

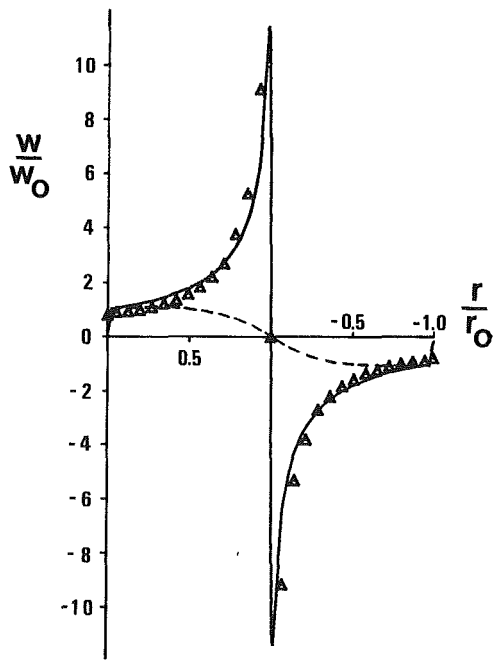

Fig. 1 Predicted and experimental tangential velocity profiles in the vortex tube—ASM, --- κ-ϵ model Δ experimental [1]

[1]Department of Chemical Engineering and Fuel Technology, Sheffield University, Sheffield S1 3JD, U.K.

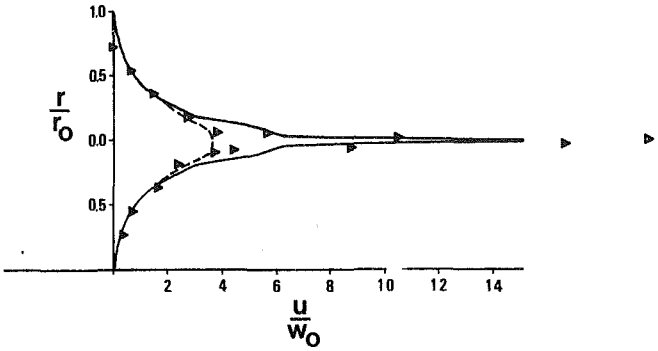

Fig. 2 Predicted and experimental axial velocity profiles in the vortex tube. For legend see Fig. 1.

the predicted and measured [1] tangential axial velocity profiles in a vortex tube. It is clear in this case that while κ-ϵ model is inadequate to reproduce even the qualitative features of the flow, an algebraic stress closure similar to that of Gibson and Launder [2] can lead to quite satisfactory quantitative agreement.

It is difficult to come to any firm conclusions with respect to the applicability of these considerations in the paper since the water model experiments which are reported only yield qualitative results. Nevertheless, we would recommend extreme caution in the use of the κ-ϵ model in highly swirling flows [3].

Additional References

1 Escudier, M. P., Bronstein, J., and Zehnder, N., *JFM*, Vol. 98, 1980, pp. 49–63.

2 Gibson, M. M., and Launder, B. E., ASME *Journal of Heat Transfer*, Vol. 98, 1976, p. 80.

3 Boysan, F., Ayers, W. H., and Swithenbank, J., "A Fundamental Modelling Approach to Cyclone Design," to be published in the *Transactions of I.Chem.E.*, Vol. 16, No. 4, July, 1982, pp. 222–230.

Authors' Closure

Our paper uses the popular k-ϵ turbulence model and shows qualitative predictions and trends which are discussed in the light of the experimental aspects of the study. We are well aware of recent developments on differential and algebraic stress turbulence models in swirling flows, and eagerly await general recommendations from researchers in this field. Algebraic stress models are proving to be very successful and the work of Boysan and Swithenbank on strongly swirling flow in vortex tubes is commendable. However, these models, and others for three-dimensional transient precessing vortex cores and coherent structure development, are not yet ready for use in application-oriented studies. In addition, such approaches will appreciably increase the computer code complexity and time requirements.

A Study of Shock Waves in Three-Dimensional Transonic Flow

W. N. Dawes[1]
Research Student.

L. C. Squire
Reader.

Cambridge University Engineering Department,
Trumpington Street,
Cambridge CB2 1PZ, U.K.

Although a number of inviscid numerical methods have been developed for the calculation of three-dimensional transonic flow in turbomachinery blade passages it is often difficult to compare the results of these calculations directly with experiment. For instance in real machines the overall flow is very complex and it is usually impossible to model the full geometry of the machine, thus it is difficult to trace the sources of the discrepancies which inevitably arise between the measured and calculated results. Even in simpler test cases the experimental results are often strongly affected by viscous effects and flow separations. This paper presents the results of an experimental investigation which generates three-dimensional transonic flow with shock waves using relatively simple geometries and where the influence of viscous effects has been reduced as far as possible. Comparisons with the output of various calculation methods show that even with these simple geometries it is essential to use fully three-dimensional methods to predict the flow development.

1 Introduction

A number of numerical methods are now available for the calculation of the flow field in transonic blade-to-blade passages (for example [1] and [2]). However, most of these methods tend to smear the pressure rise through shocks, particularly away from the blade surface. As a result it is often difficult to compare the accuracy of the various methods, especially in cases where the position and strength of the shock is important. Furthermore the complexity of the three-dimensional flow in real turbomachines (see, for example [3] and [4]) makes it difficult to isolate the causes of the discrepancies which inevitably arise between measured results and calculations.

In order to overcome some of these problems it was decided to study the position and strength of three-dimensional shocks in relatively simple experimental situations and to use the measured results as test cases for the predictions of numerical methods. In this way it was hoped that the causes of any shortcomings in the numerical methods would be more readily understood.

In developing the test cases the aim was to produce a fully three-dimensional transonic flow field with a single embedded shock, and to do so with an experimental arrangement of simple geometry which nevertheless modelled some features of the turbomachine environment. Since most of the numerical methods currently available are limited to inviscid flow fields it is important to control the influence of viscous effects in the experiments. In particular, it is important that the blade boundary layers are fully turbulent so as to minimize the effect of shock-boundary layer interactions on the character of the flow field [5] and that gross blade boundary layer separation is not allowed to occur. Even so, it is well known ([6] for example) that the overall pressure rise through a shock impinging a curved surface with a turbulent boundary layer is less than the corresponding Rankine-Hugeniot value.

The basic experimental arrangement chosen was an uncambered, untwisted blade mounted at zero incidence in the center-plane of a rectangular working-section (with the blade completely spanning the section). The working-section is formed from nonporous sidewalls and operated with a high subsonic inflow. This arrangement models a linear cascade of blades and choking of the blade-passage, an essential feature of blade-to-blade flow, can occur.

Two contrasting blades were used in the experiments, a so-called "thin-thick-thin" blade and a swept blade. The thin-thick-thin blade had a spanwise variation in thickness-chord ratio intended to produce a flow field which was transonic in both the streamwise and spanwise directions.

The present paper describes the experimental arrangements and discusses some of the results. In addition a brief comparison is made with the corresponding flow fields calculated by various methods. Calculations were made by the first author using a fully three-dimensional version of Denton's [2] time-marching method and a two-dimensional version of the same program used in strip-theory mode[2].

Denton's method expresses the inviscid equations of compressible motion in time-dependent finite-volume form and advances some initially guessed flow distribution to an asymptotic steady state. Stability and accuracy are ensured by using one-sided spatial differencing with lagged correction factors to produce a steady state solution with second-order

[1] Now at Central Electricity Generating Board, Marchwood Engineering Laboratory, Marchwood, Southampton, SO4 4ZB.

Contributed by the Fluids Engineering Division for publication in the JOURNAL OF FLUIDS ENGINEERING. Manuscript received by the Fluids Engineering Division, November 17, 1980.

[2] The first author is indebted to Dr. J. D. Denton for providing copies of his programs and for a number of discussions concerning the operation and application of his method.

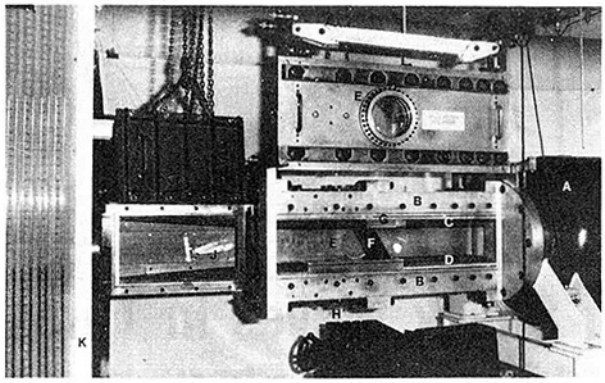

KEY:
A-settling chamber
B-metal beams
C-"upper liner"
D-"lower liner"
E-sidewalls containing 8" schlieren windows
F-model aerofoil (the swept aerofoil) in position in the working-section
G-probe traverse box
H-static pressure lead outs from the model aerofoil
J-the "second throat aerofoil"
K-manometer banks

Fig. 1 General configuration of the wind tunnel and working-section

spatial accuracy. Shocks are captured as the computation proceeds.

2 Experimental Arrangements

2.1 The Wind Tunnel Working-Section. The experiments were carried out in the Cambridge University Engineering Department high speed tunnel which operates as a blowdown tunnel exhausting to atmosphere from air stored at up to 60 atmospheres.

The tunnel settling chamber pressure can be maintained at a constant value (p_{01}) throughout a run by means of a hand operated valve. From the settling chamber, which contains the usual screens and a metal honeycomb, a contraction converts the tunnel smoothly to a uniform rectangular section (0.112 m wide, 0.270 m high by about 1.2 m long) contained within heavy metal beams forming an area within which any desired working section could be constructed. Sidewalls, containing either 8 in. schlieren windows or static pressure tappings, and suitable liners, forming top and bottom walls, are bolted and sealed to the beams. A rectangular working section (0.112 m wide, 0.164 m high, and about 0.9 m long) was formed with two solid wooden liners as illustrated in Fig. 1. The top and bottom walls were diverged in the streamwise direction to compensate for the growth of boundary layers on the test section walls. The degree of divergence was determined experimentally so as to optimize the uniformity of Mach number in the empty working section. Within the region of interest, the streamwise variation of Mach number was about ± 0.002. No measurements of inflow turbulence level were made.

2.2 The Model Blades. The thin-thick-thin blade, unswept and with a constant chord of 0.100 m, was designed with a spanwise variation in section thickness such that under certain conditions there could be a region of completely subsonic flow over part of the span with a region of supercritical flow elsewhere. The model used had a maximum thickness-chord ratio of 12 percent at mid-span (where a NACA-0012-34 profile was used) with a symmetrical linear reduction of thickness to 6 percent thick section (i.e., NACA-0006-34) at both tips. The blade was mounted at zero incidence in the center plane of the working-section parallel to the top and bottom walls and spanning the 0.112 m width. To prevent damage to the schlieren windows and because the nature of transonic flow precludes sting mounting the blade was mounted at each tip on narrow supports from the bottom wall of the working section. These supports also served to take the pressure measurement lines to the outside of the tunnel. The incidence effect associated with the use of the supports was found to be small.

Table 1 Measured streamwise section of the swept blade

x/mm	y/mm
0	0
5	1.22
10	1.79
20	2.47
30	2.78
40	2.875
50	2.79
60	2.52
70	2.09
80	1.53
90	0.90
95	0.46
100	0.06

NOTE: the blade thickness was measured with an uncertainty of ± 0.05 mm.

The swept blade, of contstant thickness and a chord of 0.100 m, was swept at 30 deg across the working-section. The section used was 5.75 percent thick (based on streamwise chord) and the profile is given in Table 1. This blade was mounted at zero incidence in the center-plane of the working-section parallel to the sidewalls spanning the 0.164 m height. No support within the working-section was used for this model, the mounting being direct to the liners.

2.3 Control of the Working-Section Flow Field. The flow conditions in the working-section are controlled by means of a variable area throat downstream of the working section. This took the form of a variable incidence aerofoil (see Fig. 1). The tunnel is operated at a high enough settling chamber pressure to choke the downstream throat, thus isolating the working-section from any disturbances downstream of the throat and allowing accurately reproducible test conditions [7]. A settling chamber pressure of 48 kN/m^2 gauge was used for all the experiments. This pressure level allows a run time of about 45 seconds and fixes the unit Reynolds number at about 2×10^7/m.

The working-section may choke with the models in place so it is appropriate to use the back-pressure (i.e., the asymptotic value of static pressure downstream of the blade) as the independent variable. This back-pressure ratio (p_B/p_{01}) is a unique function of the area of the choked downstream throat and was calibrated for each model/working-section combination. Over the range of interest (p_B/p_{01}) was repeatable to within ± 0.001.

2.4 Measurements. Blade surface static pressure distributions were obtained from pressure tubes set into slots milled in the blade surface. Static pressure tappings could be drilled at any desired location, existing tappings being blocked with wax. In this way pressures could be measured at typically a hundred locations on each blade. The pressures were read on large banks of mercury filled manometers (visible in Fig. 1). The manometers readings could be frozen and read immediately after a run, the run time itself being more than

Nomenclature

p_B = downstream back pressure p_{01} = upstream stagnation pressure p = local static pressure

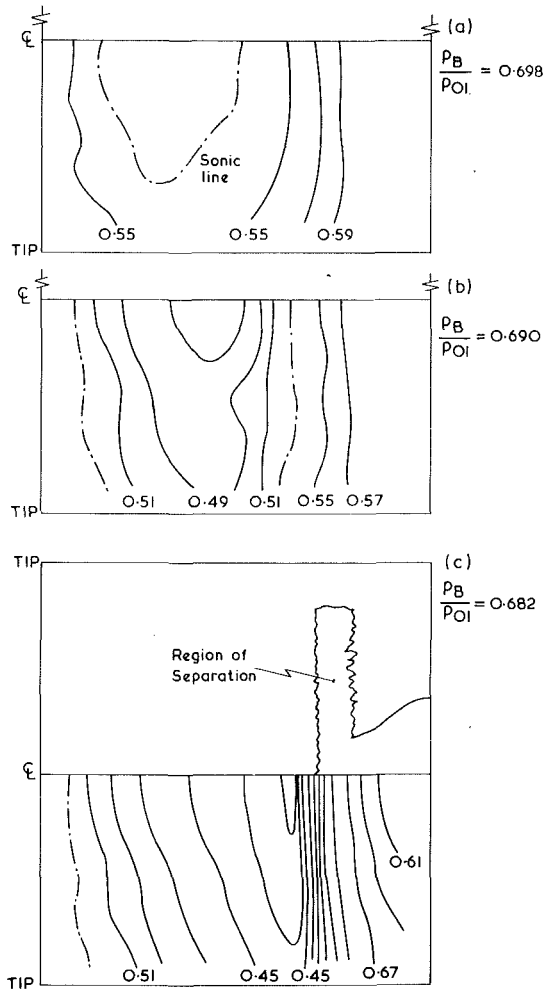

Figs. 2(*a-c*) Measured isobars on the thin-thick-thin blade (0.02 intervals in p/p_0). (Uncertainties in (p/p_0) and spatial location of isobars are ± 0.7 percent and ± 0.5 percent chord, respectively.)

sufficient for the readings to stabilize. The pressures were nondimensionalized with respect to the settling chamber pressure.

Following [13] the experimental uncertainty of the nondimensionalized static pressure was estimated as the product σt_{95} (where σ is the standard deviation of a set of repeated measurements and t_{95} is the 95th percentile of the student-t distribution) and was found to be ± 0.0035, i.e., about ± 0.7 percent over the middle pressure range. This includes the effect of any fixed errors.

The oil-flow technique [8, 9] was used to visualize blade surface streamline patterns and to locate boundary layer transition and separation.

2.5 Preliminary Experiments. Since it is the intention that the measured results be used as test-cases for the shocks predicted by inviscid calculation methods it is important that the blade boundary layers are turbulent and remain attached. Holder [10] suggested that these conditions may be met if the Reynolds number, based on chord, exceeds 1.5×10^6 and the peak Mach number on the blade surface remains less than about 1.2.

For both blades the Reynolds number, based on streamwise chord, is around 2×10^6 and oil-flow studies confirmed that natural transition occurred satisfactorily close to the leading edge. However, initial tests showed that the shock position on the blades was unsteady. This unsteadiness could only be reduced to an acceptable level by fixing transition on the blades near the leading edge. The most suitable method of

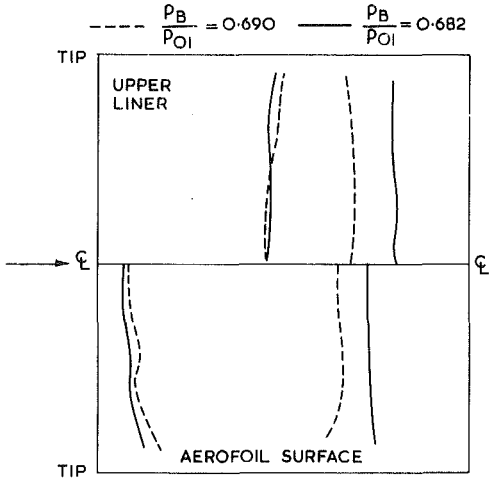

Fig. 3 Sonic-line positions on the blade surface and the upper line at two values of the back pressure

achieving this was found to be a band of sparsely distributed 0.06 mm diameter carborundum grit on the first 10 percent of the chord. Spark-schlieren photographs showed that the maximum variation in the shock position during a run (and from run to run) was less than 1 percent chord. The frequency of the motion was about 2 Hz. This is much less than any shedding frequency from the blades [11] and it is assumed that the residual unsteadiness arose from the high turbulence levels often associated with working-sections of this type [7].

3 Experimental Results

3.1 The Thin-Thick-Thin Blade. Measured pressure distributions on the surface of the thin-thick-thin blade are presented in the form of isobars of p/p_{01}, for three back pressures[3] in Figs. 2(a)-(c).

At the lowest speed ($p_B/p_{01} = 0.698$) the flow is entirely subsonic over the thin section near the walls and becomes supersonic on the thicker section at mid span. The isobars are highly curved both upstream and immediately downstream of the supersonic region, and the sonic line is highly curved. However, toward the trailing edge the isobars become straighter and almost parallel to the edge. As the back-pressure ratio drops to 0.690 the isobars in the vicinity of the sonic lines and the sonic lines themselves tend to become normal to the inlet flow. Nevertheless, the isobars within the supersonic region (which now completely spans the blade surface) remain highly curved.

At the highest speed ($p_B/p_{01} = 0.682$) a fully developed shock is present and completely spans the blade surface terminating the embedded supersonic region. The shock is almost straight and occurs at a constant chordwise position all across the span with its strength decreasing towards the tips. The supersonic region upstream of the shock is still three-dimensional in character, with the isobars curving downstream from the thicker to the thinner sections of the blade. In spite of the spanwise pressure gradients in this region the oil-flow streamlines showed little evidence of spanwise flow. Downstream of the shock the flow is subsonic all across the span and immediately downstream of the shock there is virtually no spanwise pressure gradient, although closer to the trailing edge the isobars start to become curved again.

Although it was the intention to avoid boundary layer separations, oil flow studies showed that, in fact, the blade boundary layers did separate to a certain extent. The regions where separation occurred are indicated in Fig. 2(c) for the

[3] Results for other speeds, with more details of the pressure distributions, for both the thin-thick-thin blade and the swept blade are given in reference [12].

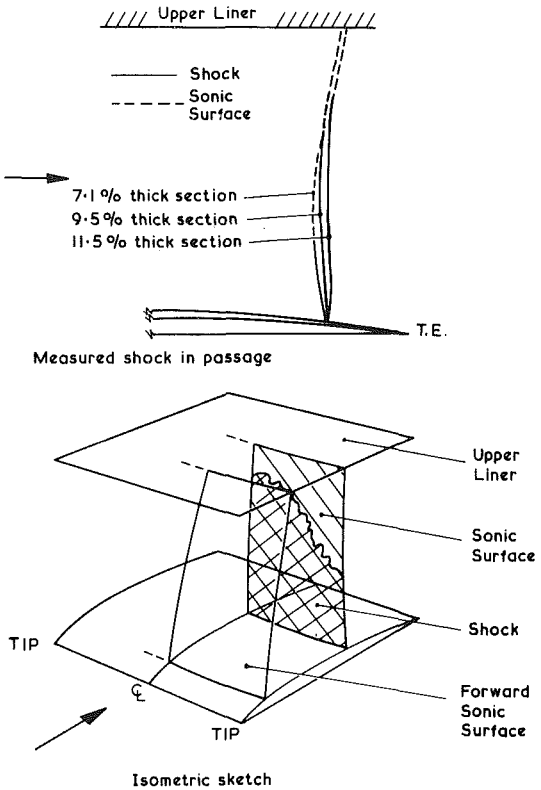

Fig. 4 Details of the shock and sonic surfaces in the blade passage at $p_B/p_{01} = 0.682$

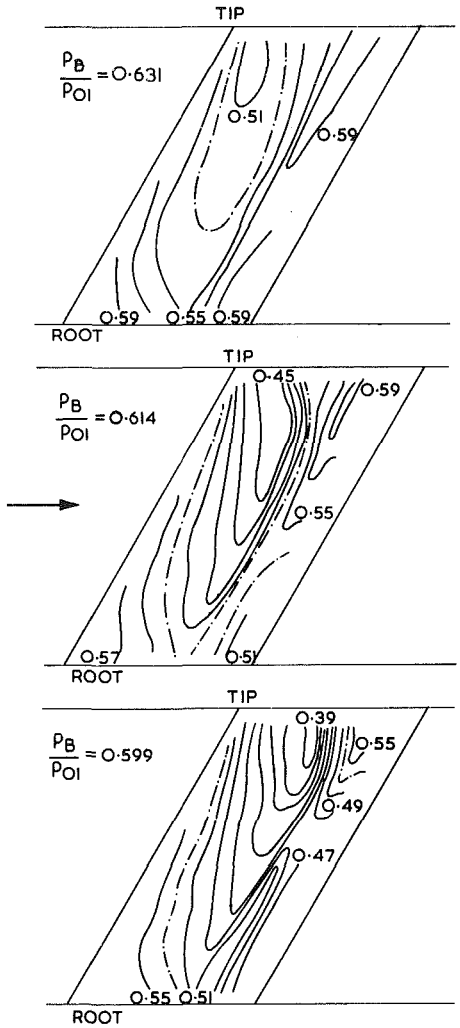

Fig. 5 Measured isobars on the swept blade (0.02 intervals in p/p_0). (Uncertainties in (p/p_0) and spatial location of isobars are ± 0.7 percent and ± 0.5 percent chord, respectively.)

highest speed case. Essentially there were three regions of separation: a local separation bubble forming under the shock once the upstream Mach number exceeded about 1.17; a gross separation induced by the shock once the upstream Mach number exceeded 1.21; and a region of separation near the trailing edge where the section thickness exceeded 9 percent (this trailing-edge separation was present in all the tests). In Fig. 2(*c*) the shock-induced separation joins the trailing-edge separation to form a single large region of separation.

Measurements of static pressure were also made on the top wall of the working section; this wall represents the center plane of the modelled blade passage. It was found that the blade passage choked when the back pressure ratio fell to 0.693 so that the flows shown in Figs. 2(*b*) and 2(*c*) correspond to choked flow conditions. The choking of the blade passage could influence the shape of the shock but, unfortunately, this influence could not be investigated since a measurable shock was not present in the unchoked flows.

The three-dimensional choking behavior is shown in Fig. 3 by means of the sonic line positions on the top wall and on the blade surface for two values of p_B/p_{01}, 0.690 and 0.682. As will be seen the upstream sonic lines are virtually independent of p_B/p_{01} whereas the downstream sonic lines remain a function of the back-pressure ratio. It is thought that the prediction of this choking behavior should be a good test of numerical modelling of the flowfield since the modelling must be capable of representing the flow both on and at some distance from the blade surface.

A static probe was also used to measure the shock position in the actual blade passage and typical results are shown in Fig. 4, for $p_B/p_{01} = 0.682$. Although it was possible to measure the position of the shock to within 1 mm (1 percent of chord) the measurement of the actual shock strength was less accurate. However, it was possible to follow the weakening of the shock away from the blade surface and the gradual transition to a sonic surface near the wall as illustrated in Fig. 4. As will be seen the shock surface is of similar shape all across the blade passage.

All these results show that the shock wave is nearly planar within the blade passage. It is not clear, however, whether this planar nature of the shock is associated with choking of the passage or with some form of spanwise relief in the subsonic region downstream of the shock. Whatever the cause, the effect is a genuine three-dimensional feature of the flow. Were this not so, that is were spanwise pressure gradients to have little influence on the overall flowfield, then the shock would be expected to be highly curved with the strongest portion furthest downstream on the thick section of the blade. This interpretation is confirmed by the calculations presented below in section 4, where it is found that a planar shock is predicted by fully three-dimensional methods, whereas a highly curved shock is predicted by two-dimensional methods used in strip theory mode.

3.2 The Swept Blade. Isobars of p/p_{01} for the swept blade are presented in Fig. 5 for back-pressure ratios of 0.631, 0.614, and 0.599.

In the lowest speed case the flow is supercritical but appears to be free of shocks. The supersonic region extends from the tip towards the root, but does not reach it. Within the supersonic region the maximum suction occurs near the tip. At first sight this is a surprising result, since from swept wing results it might have been expected that the supersonic region

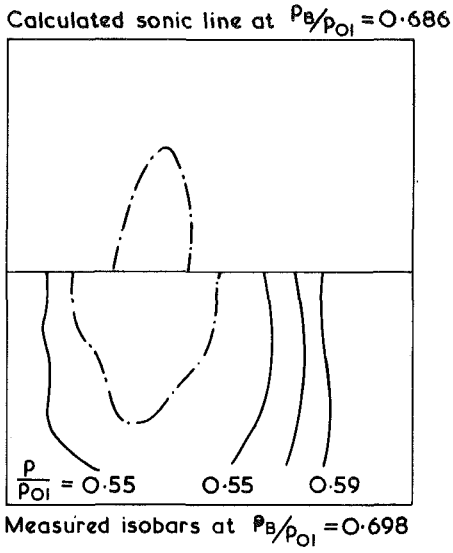

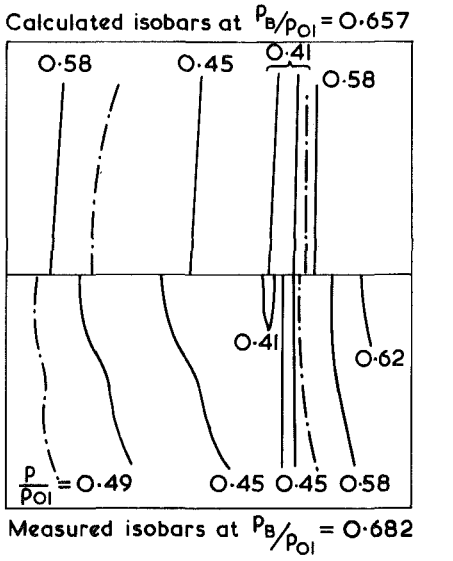

Fig. 6 Comparison of measured results on the thin-thick-thin blade with calculations by Denton's three-dimensional method

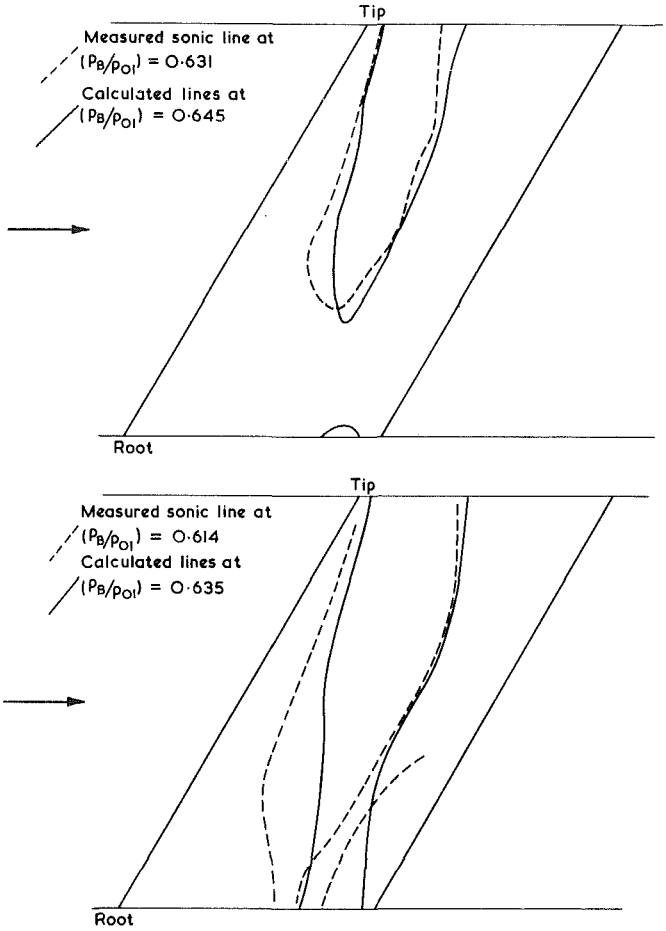

Fig. 7 Comparison of measured sonic-line positions on swept blade with calculations by Denton's three-dimensional method

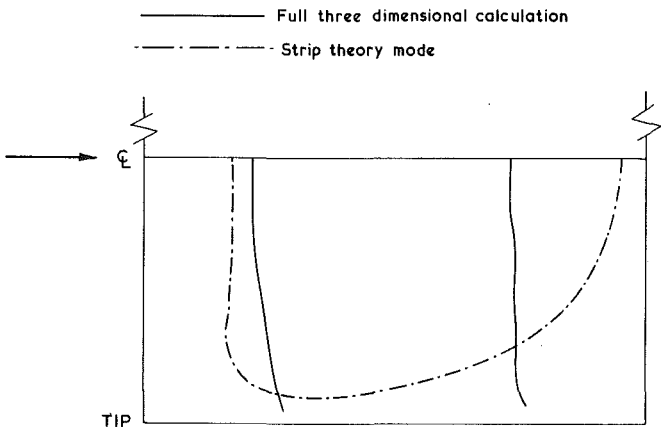

Fig. 8 Comparison of calculated sonic-line positions at p_B/p_{01} = 0.657 using Denton's three-dimensional method and two-dimensional method in strip theory mode

would develop from the root. The physical reason seems to lie in the interaction between the blade and the side walls, so that the tendency for the blade sweep to induce spanwise flow means that the flow must expand faster near the tip than near the root to maintain continuity. Downstream of the supersonic region the flow is initially compressed, but further aft it starts to expand again towards the trailing edge all across the span. Again, this may be attributed to the interaction with the side walls.

At $p_B/p_{01} = 0.614$ a well developed shock is present. This shock is normal to the side wall at the tip, as it is physically constrained to be. Away from the tip the shock curves upstream becoming parallel to the trailing edge at mid-chord as would be expected from simple sweep theory. The shock is clearly strongest at the tip and weakens across the span completely disappearing near the root.

Upstream of the shock there is a large spanwise pressure gradient, with the maximum suction increasing toward the tip. However, immediately downstream of the shock there is little spanwise pressure gradient, especially just downstream of a straight portion of the shock. This suggests that, as in the case of the thin-thick-thin blade, the spanwise relief of pressure gradient in the subsonic region downstream of the shock exercises a tendency to straighten the shape of the shock. Further downstream of the shock region, the flow starts to expand again, actually attaining supersonic speeds over part of the span near the root, so that the exit flow is transonic.

This general pattern of flow development continues at the lowest back pressure where the shock extends almost to the root.

Oil-flow studies showed that although separation of the

blade boundary layer occurred in a small bubble at the foot of the shock, no gross separation was present. This absence of gross separation can be attributed to the favorable pressure gradients in the trailing edge region.

4 Comparison Between Some Calculations and the Measurements

This section presents the results of a comparison between the measured flows and the numerical predictions from a limited number of calculation methods developed for inviscid flow.

Initial calculations showed that direct comparisons of the measured and calculated flow fields at the same back pressure ratio were unsatisfactory. The reasons for the discrepancies are believed to be associated with the growth of the boundary layers on the tunnel side wall and with the presence of the wake. Instead, in the comparisons presented below the back pressure ratio in the calculations has been chosen to give the best overall agreement with the measured flow field in respect of both shock position and peak suction. The changes in back pressure ratio needed are relatively small and it should be pointed out that Denton's fully three-dimensional method [2] predicts flows developing in just the same way as in the experiments.

Figure 6 shows the measured isobars on the surface of the thin-thick-thin blade at each of two back pressures compared with corresponding sonic lines from Denton's three-dimensional program at two slightly lower back pressures. The higher speed case is particularly interesting, showing the predicted shock to be planar, just as measured; there is, however, some discrepancy near the leading edge. A similar comparison for the swept blade is shown in Fig. 7, where, for clarity, only sonic-line positions are shown. The failure of the numerical method to reproduce the measured flow near the root is believed to be due to the coarse grid which had to be used because of computer storage restrictions.

Figure 8 shows a comparison between sonic lines calculated by Denton's three-dimensional program and those calculated by a two-dimensional version of the program used in strip theory mode. These calculations were made at the same back pressure ratio and correspond to the measured results shown in Fig. 6. As will be seen the strip theory approach fails completely to reproduce the main features of the flow giving a highly three-dimensional shock far too close to the trailing edge.

All of the calculations were made on an IBM 370-165. The fully three-dimensional calculations used about 2800 nodes in the flowfield, this being the maximum for which storage was available. These nodes were distributed more-or-less uniformly throughout the flowfield with a certain amount of refinement near the blade leading and trailing edges. Computations were continued for about 1000 iterations, requiring about 12-15 minutes of c.p.u.

5 Conclusions

The test results reported in this paper show that it is possible to generate highly three-dimensional transonic flows with embedded shock waves using relatively simple test geometries. Furthermore, it has been demonstrated that it is possible to avoid gross viscous effects by suitable choice of test conditions. Thus the results would appear to form ideal test cases for the inviscid calculation methods currently available for treating flows in blade-blade passages.

From the limited comparisons made with the predictions of some of these methods it is clear that in order to calculate the main features of the highly three-dimensional flows it is essential to use fully three-dimensional methods. Simple strip theory approaches are shown to be completely inadequate and this has important implications for the use and applicability of simple two-dimensional cascade testing of blade sections.

References

1 Oliver, D. A., and Sparis, P., "A Computational Study of Three Dimensional Transonic Shear Flow in Turbomachine Cascades, A.I.A.A. Paper 71-88, 1971.

2 Denton, J. D., "Transonic Flows in Axial Turbomachinery. Extension of the Finite Area Time-Marching Method to 3D," Von Karman Inst. for Fluid Mechanics. Lecture Series 84, 1976.

3 Epstein, A. H., "Quantitative Density Visualisation in a Transonic Compressor Rotor," G.T.L. Report No. 124, Gas Turbine Laboratory, M.I.T., 1975.

4 Wisler, D. C., and Mossey, P. W., "Gas Velocity Measurements Within a Compressor Rotor Passage Using a Laser Doppler Velocimeter," ASME Paper 72-WA/GT-2, 1972.

5 Ackeret, J., Feldmann, F., and Rott, N., "Investigations of Compression Shocks and Boundary Layers in Gases Moving at High Speed," NACA TM No. 1113, 1946.

6 Murman, E. M., "Computational Methods for Inviscid Transonic Flow With Embedded Shock Waves," AGARD Lecture Series 48, 1972.

7 Pope, A., and Goin, K. L., *High-Speed Wind Tunnel Testing*, Wiley, 1976.

8 Stanbrook, A., "The Surface Oil-Flow Technique for Use in High Speed Wind Tunnels," AGARDograph No. 70, pp. 39-49, 1962.

9 Squire, L. C., "The Motion of a Thin Oil Sheet Under the Steady Boundary Layer on a Body," *Jour. Fluid Mech.*, Vol. 11, 1961, pp. 161-179.

10 Holder, D. W., "The Transonic Flow Past Two-Dimensional Aerofoils," *Jour. Roy. Aero. Soc.*, Vol. 68, 1964, pp. 501-516.

11 Finke, K., "Shock Oscillations in Transonic Flows and Their Prevention," Symposium Transsonicum II, Springer-Verlag, 1975, pp. 57-65.

12 Dawes, W. N., "A Study of Shock Waves in Three-Dimensional Transonic Flow," Ph.D. dissertation. Cambridge University, 1979.

13 Pope, T. C., Reed, T. D., and Cooksey, J. M., "Calibration of Transonic and Supersonic Wind Tunnels," NASA Contractor Report 2920, 1976.

blade boundary layer occurred in a small bubble at the foot of the shock, no gross separation was present. This absence of gross separation can be attributed to the favorable pressure gradients in the trailing edge region.

4 Comparison Between Some Calculations and the Measurements

This section presents the results of a comparison between the measured flows and the numerical predictions from a limited number of calculation methods developed for inviscid flow.

Initial calculations showed that direct comparisons of the measured and calculated flow fields at the same back pressure ratio were unsatisfactory. The reasons for the discrepancies are believed to be associated with the growth of the boundary layers on the tunnel side wall and with the presence of the wake. Instead, in the comparisons presented below the back pressure ratio in the calculations has been chosen to give the best overall agreement with the measured flow field in respect of both shock position and peak suction. The changes in back pressure ratio needed are relatively small and it should be pointed out that Denton's fully three-dimensional method [2] predicts flows developing in just the same way as in the experiments.

Figure 6 shows the measured isobars on the surface of the thin-thick-thin blade at each of two back pressures compared with corresponding sonic lines from Denton's three-dimensional program at two slightly lower back pressures. The higher speed case is particularly interesting, showing the predicted shock to be planar, just as measured; there is, however, some discrepancy near the leading edge. A similar comparison for the swept blade is shown in Fig. 7, where, for clarity, only sonic-line positions are shown. The failure of the numerical method to reproduce the measured flow near the root is believed to be due to the coarse grid which had to be used because of computer storage restrictions.

Figure 8 shows a comparison between sonic lines calculated by Denton's three-dimensional program and those calculated by a two-dimensional version of the program used in strip theory mode. These calculations were made at the same back pressure ratio and correspond to the measured results shown in Fig. 6. As will be seen the strip theory approach fails completely to reproduce the main features of the flow giving a highly three-dimensional shock far too close to the trailing edge.

All of the calculations were made on an IBM 370-165. The fully three-dimensional calculations used about 2800 nodes in the flowfield, this being the maximum for which storage was available. These nodes were distributed more-or-less uniformly throughout the flowfield with a certain amount of refinement near the blade leading and trailing edges. Computations were continued for about 1000 iterations, requiring about 12-15 minutes of c.p.u.

5 Conclusions

The test results reported in this paper show that it is possible to generate highly three-dimensional transonic flows with embedded shock waves using relatively simple test geometries. Furthermore, it has been demonstrated that it is possible to avoid gross viscous effects by suitable choice of test conditions. Thus the results would appear to form ideal test cases for the inviscid calculation methods currently available for treating flows in blade-blade passages.

From the limited comparisons made with the predictions of some of these methods it is clear that in order to calculate the main features of the highly three-dimensional flows it is essential to use fully three-dimensional methods. Simple strip theory approaches are shown to be completely inadequate and this has important implications for the use and applicability of simple two-dimensional cascade testing of blade sections.

References

1 Oliver, D. A., and Sparis, P., "A Computational Study of Three Dimensional Transonic Shear Flow in Turbomachine Cascades, A.I.A.A. Paper 71-88, 1971.

2 Denton, J. D., "Transonic Flows in Axial Turbomachinery. Extension of the Finite Area Time-Marching Method to 3D," Von Karman Inst. for Fluid Mechanics, Lecture Series 84, 1976.

3 Epstein, A. H., "Quantitative Density Visualisation in a Transonic Compressor Rotor," G.T.L. Report No. 124, Gas Turbine Laboratory, M.I.T., 1975.

4 Wisler, D. C., and Mossey, P. W., "Gas Velocity Measurements Within a Compressor Rotor Passage Using a Laser Doppler Velocimeter," ASME Paper 72-WA/GT-2, 1972.

5 Ackeret, J., Feldmann, F., and Rott, N., "Investigations of Compression Shocks and Boundary Layers in Gases Moving at High Speed," NACA TM No. 1113, 1946.

6 Murman, E. M., "Computational Methods for Inviscid Transonic Flow With Embedded Shock Waves," AGARD Lecture Series 48, 1972.

7 Pope, A., and Goin, K. L., *High-Speed Wind Tunnel Testing*, Wiley, 1976.

8 Stanbrook, A., "The Surface Oil-Flow Technique for Use in High Speed Wind Tunnels," AGARDograph No. 70, pp. 39-49, 1962.

9 Squire, L. C., "The Motion of a Thin Oil Sheet Under the Steady Boundary Layer on a Body," *Jour. Fluid Mech.*, Vol. 11, 1961, pp. 161-179.

10 Holder, D. W., "The Transonic Flow Past Two-Dimensional Aerofoils," *Jour. Roy. Aero. Soc.*, Vol. 68, 1964, pp. 501-516.

11 Finke, K., "Shock Oscillations in Transonic Flows and Their Prevention," Symposium Transsonicum II, Springer-Verlag, 1975, pp. 57-65.

12 Dawes, W. N., "A Study of Shock Waves in Three-Dimensional Transonic Flow," Ph.D. dissertation, Cambridge University, 1979.

13 Pope, T. C., Reed, T. D., and Cooksey, J. M., "Calibration of Transonic and Supersonic Wind Tunnels," NASA Contractor Report 2920, 1976.

DISCUSSION

G. S. Settles[4]

Shock wave/turbulent boundary layer interactions are inherently complex phenomena. Transonic flow adds another order of complexity, and in the full three dimensions these interactions must surely be the most difficult of all. (The fact that chemical reactions are not involved is small comfort.) Thus the authors are congratulated for making a start in a useful area where very little is known.

The primary value of this work lies in its exploratory nature: some phenomenology of 3D transonic flows is revealed, suggesting directions for future work. In such a case one expects that more questions will be raised than answers provided.

I agree with the authors' conclusion that it is possible – indeed desirable – to study such flows using simple test geometries. What we know today about shock/boundary layer interactions comes mainly from basic, parametric experimental studies. However, I am less sure that gross viscous effects have been avoided in this study, especially since the important sidewall effects were not investigated *per se*.

As the authors demonstrate, their experiment is a useful initial benchmark with which to test the results of 3D transonic computations. In order to achieve the stature of a true "ideal" test case, detailed flowfield measurements and a more rigorous definition of the experimental boundary conditions would be required. (See, for example, the standards applied in establishing the Data Library of the recent AFOSR-HTTM-Stanford Conference on Complex Turbulent Flows.) I hope the present work will serve as a starting point for future studies along such lines.

[4] Mechanical and Aerospace Engineering Department, Princeton University, Princeton, N.J. 08544.

C. C. Horstman[5]

The authors are to be commended for undertaking a very difficult task. It is essential that experimental data of this type be generated to provide suitable test cases for three-dimensional transonic computational methods. Although the geometries used are simple, resulting flow fields have most of the features found in complex three-dimensional flow fields. It was the intent of this experimental investigation to reduce the viscous effects as much as possible which I feel was accomplished. However, it may not be possible to reduce them to the extent where they need not be included in a computation used for comparisons with the data. This can only be determined by testing both inviscid and viscous computations for these geometries.

Since the authors intended these data to be used to test computation methods, there are a few points left out of this paper which should be addressed. For transonic flows of this type the boundary conditions employed in the computations can sometimes dominate the computed flow fields. The use of solid walls in this experiment provide well documented top and side boundary conditions for the computer. However, little is mentioned about the upstream and downstream boundaries. Many of the test cases are choked which makes the downstream boundary condition extremely important. The axial locations of both boundaries must be stated along with the measured pressures at these boundaries. In a computation one would like to prescribe the Mach number and total pressure at the upstream boundary and fix the static pressure at the downstream boundary. A minor point which is not clear to me is how accurately one determines boundary layer transition from surface oil-flow studies. Also, the data from the oil-flow studies should be made available as a check for those using viscous computations.

The calculations presented are extremely disappointing since substantial changes in free stream m ach number (0.02 to 0.04) were required to obtain qualitative agreement with the data. There could be several reasons for this. Were tunnel side walls included in the calculations and if so, was an allowance made for side wall boundary layer growth? What type of boundary conditions were applied up and down stream of the test section? These points should be addressed. Finally, it could be viscous effects on the test models which cause these differences. I believe that if one is "allowed" to vary the wind tunnel test Mach number in a computation to obtain agreement with the data, the computational method is not completely validated as a predictive tool.

[5] Experimental Fluid Dynamics Branch, NASA Ames Research Center, Moffett Field, Calif. 94035.

Authors' Closure

The authors thank Dr. Settles and Dr. Horstman for their helpful and constructive comments. The authors agree that despite the effort taken to reduce the influence of viscous effects it is necessary to compute the flow with a method which includes some allowance for viscous effects, although it is hoped that these can be taken into account without using a fully interactive program. A certain amoung to work has been carried out by other workers (e.g. [14]) since the completion of the present work to try and quantify the extent of the influence of viscosity (including wall effects).

The success of any given computation method is very dependent on the boundary conditions employed. The method (2) used by the present authors treats the upstream boundary by fixing the total pressure, total temperature and flow angle and extrapolates the static pressure from interior points. Since there are no loss mechanisms upstream of the blade (i.e. no changes in total pressure) and since the manner of specifying the upstream boundary allows for non-uniform velocity, pressure and density fields then the boundary need not be more than about a chord length upstream of the blade. At the downstream boundary the static pressure (the "back-pressure") is fixed and other variables extrapolated. The back-pressures quoted for the experiments are the asymptotic values measured downstream of the blade. In the calculations the downstream boundary was sited far enough downstream for further downstream movement of it not to affect significantly the calculated pressure distribution on the blade itself. Although of course sidewalls were included in the calculations, no allowance could be made for sidewall boundary layer growth. One of the present authors (WND) is currently coding and testing a computational method for viscous compressible flow [15] and it is his intention to apply this method to the experimental configuration when the method is sufficiently developed.

Additional References

14 Baker, C. J., and Squire, L. C., "Turbulent Boundary Layer Development on a Two Dimensional Aerofoil with Supercritical Flow at Low Reynolds Number," *Aero. Quarterly*, Vol. XXXIII, May 1982.

15 Dawes, W. N., "An Efficient Implicit Algorithm for the Equation of 2D Viscous Compressible Flow: Application to Shock Boundary Layer Interaction," CEGB Note TPRD/M/1231/N82, Mar. 1982.

Journal of Fluids Engineering

Technical Briefs

Spreading Rate and Reattachment of Coaxial Jets of High Mean-Velocity Ratio

N. W. M. Ko[1] and H. Au[2]

Nomenclature

b_i = characteristic shear layer with inside inner mixing region or inside the locus $\partial\bar{U}/\partial y = 0$ and is defined as $|y_{0.9} - y_{0.1}|$

b_0 = characteristic shear layer width in the outer mixing region or outside the locus $\partial\bar{U}/\partial y = 0$ and is defined as $|y'_{0.9} - y'_{0.1}|$

D_i, D_0 = inner and outer nozzle diameter, respectively

r = ratio (= 0.1, 0.9)

$\bar{U}$ = axial mean velocity

$\bar{U}_i, \bar{U}_0$ = mean velocity at inner and outer nozzle exit, respectively

$\bar{U}_m, \bar{U}_{\min}$ = maximum and minimum mean velocity at a given axial plane

x, y = axial and radial coordinates

x_r = axial distance of the reattachment point from the jet exit plane

y_r = radial location within the inner mixing region where the local mean velocity equals $r(\bar{U}_m - \bar{U}_{\min})$

y_r' = (i) in the initial merging zone: the radial distance in the outer mixing region where the local mean velocity is $r.\bar{U}_0$
(ii) in the intermediate merging zone: the radial distance outside the locus $\partial\bar{U}/\partial y = 0$ (other than the centreline) where the local mean velocity is $r.\bar{U}_m$
(iii) in the fully merged zone: the radial distance where the local mean velocity is $r.\bar{U}_m$

λ = mean velocity ratio, outer to inner $(\bar{U}_0/\bar{U}_i = \lambda^{-1})$

Introduction

Previous investigations of coaxial jets issuing into stagnant air surroundings [1-2] concerned mainly jets of mean-velocity ratio $(\bar{U}_0/\bar{U}_i)$ less than unity. The few jets of mean-velocity ratio higher than unity [1] concerned the flow characteristics in the fully merged zone. In this respect, the flow characteristics inside the initial merging and the intermediate merging zone have not been investigated in details. Thus, the present note describes an experimental study on the flow characteristics, such as the spreading rate and reattachment of coaxial jets of five mean-velocity ratios.

Experimental Techniques

The experimental setup consisted of an inner nozzle of diameter D_i of 20 mm and an outer nozzle of diameter D_0 of 40 mm [3]. The lip thickness of the inner nozzle was 1 mm. The outer jet mean exit velocity $\bar{U}_0$ was kept constant at 50 m/s while the inner jet exit velocity $\bar{U}_i$ varied. The reciprocal of the mean-velocity ratio λ^{-1} $(\bar{U}_i/\bar{U}_0)$ was 0.15, 0.2, 0.4, 0.6, and 0.8.

The mean velocity measurements were obtained with a constant temperature type hot-wire anemometer with linearized output. The wire has a diameter of 5×10^{-6} m and a length of 2 mm.

Results and Discussion

Detailed measurements of the local mean velocity across the coaxial jets at the five different mean-velocity ratios have been obtained. From the results the characteristic widths of the outer and inner mixing regions and in different zones were derived. The distributions of the characteristic width $b_0/(D_0/2)$ are shown in Fig. 1. The characteristic width b_0 is defined as the absolute value of the difference of $y'_{0.9}$ and $y'_{0.1}$ at any axial plane. $y'_{0.9}$ and $y'_{0.1}$ are the radial position outside the locus $\partial\bar{U}/\partial y = 0$ (this corresponds to the part of the mean velocity profile where $\partial\bar{U}/\partial y$ is negative in the positive y direction) where the local mean velocity is equal to 0.9 and 0.1 of the maximum mean velocity, respectively. Figure 1 indicates that over the axial distance considered, the characteristic width distribution seems to be divided into three zones. The first zone terminates at $x/D_0 \approx 1.5$ and corresponds to the initial merging zone suggested by Ko and Kwan [2]. The second zone terminates at $x/D_0 \approx 5$ and corresponds to the intermediate merging zone. For $x/D_0 > 5$ the fully merged zone starts to exist [3]. Within each zone the widths of the coaxial jets of different λ^{-1} are the same, suggesting the independence of the mixing region width with the mean-velocity ratio. The slope $d(2b_0)/dx$, which is a measure of the spreading rate of the outer mixing region, is

[1] Reader and Graduate Student, respectively, Department of Mechanical Engineering, University of Hong Kong, Hong Kong.

Contributed by the Fluids Engineering Division of THE AMERICAN SOCIETY OF MECHANICAL ENGINEERS. Manuscript received by the Fluids Engineering Division, July 6, 1981.

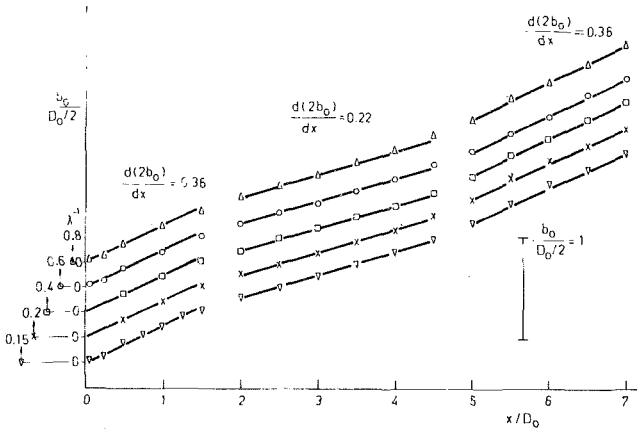

Fig. 1 Characteristic widths b_0

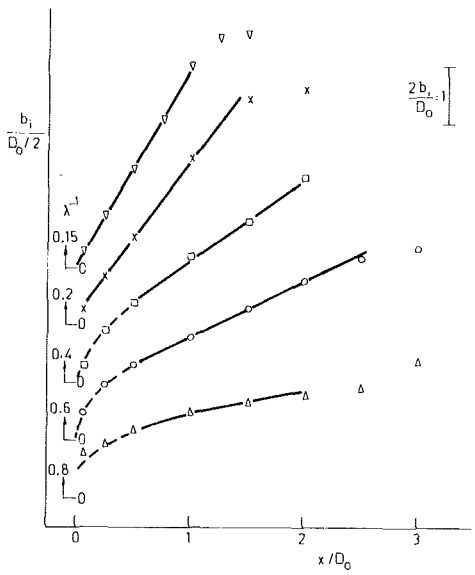

Fig. 2 Characteristic width of inner mixing region

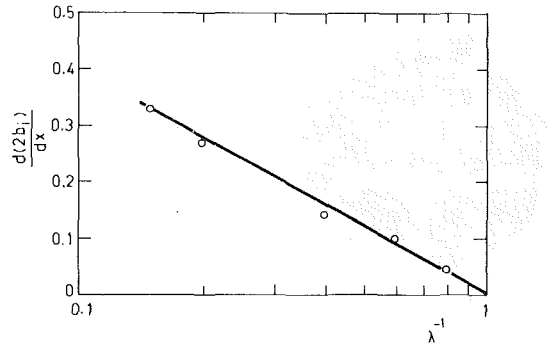

Fig. 3 Variation of $\frac{d(2b_i)}{dx}$ with mean-velocity ratio

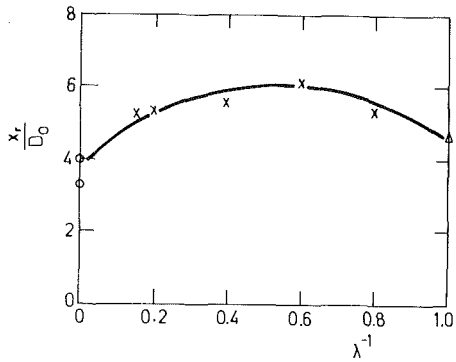

Fig. 4 Variation of reattachment distance with mean-velocity ratio

also independent of the mean-velocity ratio. For the initial merging and fully merged zone a value of 0.36 is found. For the intermediate zone a value of 0.22 is obtained, suggesting lower spread. The accuracy in these slopes was estimated to be ± 0.02.

The distributions of the characteristic width $b_i/(D_0/2)$ of the inner mixing region are shown in Fig. 2. The width b_i is the absolute value of the difference of $y_{0.9}$ and $y_{0.1}$ at any axial plane. $y_{0.9}$ and $y_{0.1}$, however, are the radial position inside the inner mixing region [3] where $(\bar{U}-\bar{U}_{\min})$ is equal to 0.9 and 0.1 of $(\bar{U}_m-\bar{U}_{\min})$ respectively. $\bar{U}_m$ and $\bar{U}_{\min}$ are the maximum and minimum streamwise velocities at the same axial plane. The width of the inner mixing region is different for different λ^{-1}. Apart from a small region close to the jet exit plane, where the width of the inner mixing layer is strongly affected by the presence of the inner nozzle lip, increase in b_i with axial distance is fairly linear. The slope $d(2b_i)/dx$ was estimated from the linear portion using least square fitting. All accuracy of ± 0.02 was estimated. As expected, a decrease of $d(2b_i)/dx$ with increase in λ^{-1} is observed. The curve approaches a value of zero at λ^{-1} equals to unity. This is also expected as the mean shear in the inner mixing region is zero when the inner jet exit velocity is the same as that of the outer jet.

Because of the lower inner jet exit velocity, the high velocity flow of the outer annular potential core merges at the central axis. The axial distance x_r/D_0 of the reattachment of the outer high velocity flow is shown in Fig. 4. The results of the limiting cases of annular jets ($\lambda^{-1}=0$) of Ko and Chan [4] and of single jet ($\lambda^{-1}=1$) are also shown. The reattachment distance seems to vary between four to six outer diameters.

Conclusions

The spreading rate in the mixing regions of the coaxial jets of high mean-velocity ratio depends on the zone where it is located. The rates in outer mixing region of the initial merging zone and in the fully merged zone is the same and slightly higher than that in the intermediate merging zone. These rates seem to be independent of the mean-velocity ratio. The spreading rate of the inner mixing region, however, depends greatly on the mean-velocity ratio. It approaches that of the single jet. Reattachment of the outer high velocity flow at the central axis also depends on the mean-velocity ratio, though to a lesser extent.

References

1 Chigier, N. A., and Beer, J. M., "The Flow Region Near the Nozzle in Double Concentric Jets," ASME *Journal of Basic Engineering*, Vol. 86, 1964, pp. 797–804.

2 Ko, N. W. M., and Kwan, A. S. H., "The Initial Region of Subsonic Coaxial Jets," *Journal of Fluid Mechanics*, Vol. 73, 1976, pp. 305–335.

3 Ko, N. W. M., and Au, H., "Initial Region of Subsonic Coaxial Jets of High Mean-Velocity Ratio," ASME JOURNAL OF FLUIDS ENGINEERING, (to be published).

4 Ko, N. W. M., and Chan, W. T., "The Inner Regions of Annular Jets," *Journal of Fluid Mechanics*, Vol. 93, 1979, pp. 549–584.

Journal of Fluids Engineering

Discussion

Laminar Boundary Layer Near the Rotating End Wall of a Confined Vortex[1]

T. J. Kotas[2]

The experimental results presented by the authors in this paper make a welcome contribution toward a better understanding of confined vortex flows.

An experimental investigation of this type may be looked upon as a fragment of the total range of experimental conditions.

The two particular distinctive features characterising this investigation are:

1. low swirl ratios
2. rotating end-walls

The swirl ratios used are very low and could be said to correspond to the extreme end of the range of practical interest. Because of this, the present flow is characterised by the absence of a number of phenomena which feature prominently in flows with high swirl ratios [1, 2]. The principal ones of these are:

(i) Main flow radial and tangential velocities are independent of the axial coordinate i.e., $v=v(r)$ and $u=u(r)$. This clearly is not the case in the present investigation particularly (see Figs. 3 and 4) as far as the radial component of velocity is concerned.

(ii) The mass flow rate of the fluid "leaking" through the end-wall boundary layers is large, exceeding in some cases the total flow throughput, which leads to the flow recirculation phenomena. In the present investigation the "leakage" through the end-wall boundary layers is small as a fraction of the total mass throughput although it will be noticed that the radial velocity overshoot increases with the swirl ratio (see Figs. 8 and 12). There is no doubt that the rotation of the end-walls contributes significantly to the slow development in the inward radial direction of the overshoot phenomena since this feature is dependent on the imbalance between the radial pressure gradient generated by the main flow and the centrifugal acceleration resulting from the retardation of the flow in the end wall boundary layers. It would be interesting, from the theoretical point of view, to investigate the secondary flows produced by rotation of the end walls at an angular velocity higher than that of the cylindrical wall so that the tangential velocity of the main flow would match that of the wall at some intermediate radial position. This would lead to a situation when the accelerating effect of the end walls at larger radial positions could result in an opposite overshoot in the radial velocity profiles to that at smaller radial positions.

The final point I should like to refer to is the assumption made by the Authors with regard to the laminar nature of the boundary layer flow on the end walls. There does not seem to be any experimental confirmation of this assumption mentioned in the paper. If this assumption is not correct, it might account for the rather large discrepancies between the experimental and calculated radial velocity profiles.

Additional References

1 Kotas, T. J., "Streamline Pattern in a Confined Vortex," *Journal of Mechanical Engineering Science*, Vol. 19, No. 1, 1977, p. 38

2 Kotas, T. J., "An Experimental Study of a Confined Vortex Flow," *Archiwum Budowy Maszyn*, Vol. 24, No. 3, 1977, p. 375.

Authors' Closure

The authors are grateful to Dr. Kotas for his remarks concerning our work. He is correct in pointing out that there is a wide range of possible flow configurations which are often identified as confined vortex flows; and the nature of these depends on factors such as the magnitude of the swirl ratio, the geometry of the chamber and the rotational velocity of the end walls. The set of experimental conditions studied in the present investigation was chosen because of the application to centrifugal fluidization. In that case the chamber geometries utilized, the presence of the rotating end wall, and the magnitude of swirl ratios studied are all of practical consequence [references 1, 2, 3].

In the course of this investigation, the authors were keenly aware of the potential effects of the rotation of the end walls on the development of the flow. We agree with Dr. Kotas that the difference between a stationary and rotating end wall might be extremely significant. His suggestion that theoretical studies be carried out with end walls that rotate with angular velocities greater than that of the cylindrical wall is intriguing. It would indeed be very interesting to see what it does to the velocity overshoot.

Finally, the assumption of laminar boundary layer flow on the end walls was based on two factors. Early in the study a hot wire probe was inserted in the end wall boundary layer and monitored for turbulent fluctuations. The results of those measurements showed that the flow was laminar. Furthermore, the Reynolds numbers encountered in these experiments were below those normally used to indicate transitions in flows of this type. It was on this basis that the laminar boundary layer analysis was performed.

[1] By W. J. Shakespeare and E. K. Levy, published in the June, 1982, issue of the JOURNAL OF FLUIDS ENGINEERING, Vol. 104, No. 2, pp. 171-177.

[2] Department of Mechanical Engineering, Queen Mary College, University of London, London, England.

Additional References

1 Levy, E., et al., "Centrifugal Fluidized Bed Combustion," *Proceedings Fifth International Conference on Fluidized Bed Combustion*, Washington, D.C., December 1977.

2 Metcalfe, C., and Howard, J., "Combustion Experiments within a Rotating Fluidized Bed," Proceedings 1977 International Fluidized Bed Combustion Conference, Washington, D.C., December 1977.

3 Levy, E., Shakespeare, W. J., Tabatabie-Raissi, A., and Chen, J. C., "Particle Elutriation from Centrifugal Fluidized Beds," in *Recent Advances in Fluidization and Fluid Particle Systems*, ed. by D. V. Punwani, AIChE Symposium Series No. 205, Vol. 77, 1981.

Preston Tube Calibrations and Direct Force Floating Element Measurements in a Two-Dimensional Turbulent Boundary Layer[1]

K. C. Brown[2]

It is unfortunate that, after so many attempts, a definitive calibration of Preston tubes has yet to be achieved. Perhaps this reflects upon the difficulty of the task, but this paper helps clarify the issue.

I am not happy to support using the measurements reported by Brown & Joubert to help substantiate the proposition that existing Preston tube calibrations underestimate the wall shear stress. Even with the doubts about calibration of Preston tubes I am inclined to prefer them to my own direct measurements. It is difficult to envisage direct measurements underestimating wall shear stress, but easy to suggest reasons for overestimates. Direct measurements are indeed a delicate task.

I must take issue with the implication of the introduction—that we may obtain a different calibration equation for different flow geometries—pipe, boundary layer, etc. Firstly it makes the whole Preston tube concept useless. If one must calibrate individually, then one might as well use different devices especially adapted to the situation. Secondly it makes nonsense of the principle upon which the calibration is based. In the limiting case of very small tubes the calibration relies only on the no-slip condition at the wall. Therefore, if small enough tubes are used a universal calibration must apply and our efforts should be directed toward determining it, and the limits of tube size for its application to all situations. The conclusion follows that initial calibration should be achieved using pipe flows (since they lead to the simplest independent estimates of wall shear stress) and direct measurements are only necessary for the investigation of the effects of pressure gradients, local variations, etc.

Authors' Closure

The authors appreciate the comments of Professor Brown. His remark on the delicacy (and difficulties) of direct measurements (of local wall shear stress) can be appreciated only by those, who like himself, have tried seriously to make such measurements, particularly in low speed flows.

The question of different calibration equations for Preston tubes in different flow circumstances—boundary layers and pipe flows—is, as Professor Brown notes, the same as the question of different near wall similarity laws for these two classes of flows. While this latter question has been debated in the past, the authors' perception is that the current concensus favors a single law for both classes of flows. This view is intuitively satisfying and it is difficult to generate sound physical arguments to support a contrary view. Just as there is at least a modest degree of uncertainty in the two-dimensional near wall similarity law as evidenced by the differences in even more recent law of the wall constants,[3] so too one can except a corresponding uncertainty in the uniqueness of Preston tube calibration formulas. This paper attempts to give some quantitative measure to this uncertainty, and particularly by looking at different flow circumstances, since relatively few data are available for the boundary layer case.

[1] By J. E. McAllister, F. J. Pierce, and M. H. Tennant, published in the June 1982 issue of the ASME JOURNAL OF FLUIDS ENGINEERING, Vol. 104, No. 2, pp. 156-161.

[2] Department of Mechanical and Industrial Engineering, University of Melbourne, Melbourne, Australia.

Flow Behind Two Coaxial Circular Cylinders[1]

P. K. Stansby[2]

The authors have presented some most interesting results about the influence of a prominent discontinuity on vortex shedding from cylinders. An important and surprising conclusion is that there appears to be little effect of the discontinuity at distances greater than two diameters from it.

A minor point of concern exists about the choice of a diameter ratio of 2:1 for the coaxial cylinders. For a single cylinder there are peaks in the pressure spectrum at the Strouhal frequency and at twice this frequency. In the coaxial case, the Strouhal frequency for the small cylinder is nearly twice the Strouhal frequency for the large cylinder and there must be some doubt about the origin of a peak at this frequency on a pressure spectrum. Choosing a diameter ratio away from 2:1 would avoid this problem.

The flow at the discontinuity must be rather complicated. However the trailing vortices generated at the leading edge of the big cylinder are likely to be prominent. These streamwise vortices rotate to produce a downwash behind the big cylinder. (The same mechanism can cause smoke from a chimney in a high wind to be entrained in its wake.) Fluid from outside the wake will thus be entrained at the base of the big cylinder, effecting base bleed which can suppress vortex shedding as mentioned in the paper. The influence of the trailing vortices on one another will cause them to be deflected downwards. These vortices are likely to be a prominent feature of the "discontinuity wake" discussed in the paper. It is interesting to note that their rotation is such that they could join up with the vorticity separating from the big cylinder, thus providing an "end" for the vortices of the big cylinder. The vortices of the small cylinder presumably end in a more conventional manner as the flat end of the big cylinder acts to some degree as an end plate as mentioned in the paper.

A final interesting point concerns the maximum values of C_p' away from the discontinuity; they are higher for the big cylinder than for the small cylinder (see Fig. 6). At first sight this might be thought to be a permanent influence of the discontinuity. However the influence of the "other" ends could well be significant. The aspect ratio for the big cylinder is 5.6 while that for the small cylinder is 11.2. The greater relative proximity of the tunnel wall could make the big

[3] Pierce, F. J., McAllister, J. E., and Tennant, M. H., "Near-Wall Similarity in Three-Dimensional Turbulent Boundary Layers Part I: Model Review," ASME Paper FE-33, 1982.

[1] By N. W. M. Ko, published in the June 1982 issue of THE JOURNAL OF FLUIDS ENGINEERING, Vol. 104, No. 2, pp. 223-227.

[2] Simon Engineering Laboratory, University of Manchester, Manchester M13 9PL England.

Additional References

1 Levy, E., et al., "Centrifugal Fluidized Bed Combustion," *Proceedings Fifth International Conference on Fluidized Bed Combustion*, Washington, D.C., December 1977.

2 Metcalfe, C., and Howard, J., "Combustion Experiments within a Rotating Fluidized Bed," Proceedings 1977 International Fluidized Bed Combustion Conference, Washington, D.C., December 1977.

3 Levy, E., Shakespeare, W. J., Tabatabie-Raissi, A., and Chen, J. C., "Particle Elutriation from Centrifugal Fluidized Beds," in *Recent Advances in Fluidization and Fluid Particle Systems*, ed. by D. V. Punwani, AIChE Symposium Series No. 205, Vol. 77, 1981.

Preston Tube Calibrations and Direct Force Floating Element Measurements in a Two-Dimensional Turbulent Boundary Layer[1]

K. C. Brown[2]

It is unfortunate that, after so many attempts, a definitive calibration of Preston tubes has yet to be achieved. Perhaps this reflects upon the difficulty of the task, but this paper helps clarify the issue.

I am not happy to support using the measurements reported by Brown & Joubert to help substantiate the proposition that existing Preston tube calibrations underestimate the wall shear stress. Even with the doubts about calibration of Preston tubes I am inclined to prefer them to my own direct measurements. It is difficult to envisage direct measurements underestimating wall shear stress, but easy to suggest reasons for overestimates. Direct measurements are indeed a delicate task.

I must take issue with the implication of the introduction—that we may obtain a different calibration equation for different flow geometries—pipe, boundary layer, etc. Firstly it makes the whole Preston tube concept useless. If one must calibrate individually, then one might as well use different devices especially adapted to the situation. Secondly it makes nonsense of the principle upon which the calibration is based. In the limiting case of very small tubes the calibration relies only on the no-slip condition at the wall. Therefore, if small enough tubes are used a universal calibration must apply and our efforts should be directed toward determining it, and the limits of tube size for its application to all situations. The conclusion follows that initial calibration should be achieved using pipe flows (since they lead to the simplest independent estimates of wall shear stress) and direct measurements are only necessary for the investigation of the effects of pressure gradients, local variations, etc.

Authors' Closure

The authors appreciate the comments of Professor Brown. His remark on the delicacy (and difficulties) of direct measurements (of local wall shear stress) can be appreciated only by those, who like himself, have tried seriously to make such measurements, particularly in low speed flows.

The question of different calibration equations for Preston tubes in different flow circumstances—boundary layers and pipe flows—is, as Professor Brown notes, the same as the question of different near wall similarity laws for these two classes of flows. While this latter question has been debated in the past, the authors' perception is that the current concensus favors a single law for both classes of flows. This view is intuitively satisfying and it is difficult to generate sound physical arguments to support a contrary view. Just as there is at least a modest degree of uncertainty in the two-dimensional near wall similarity law as evidenced by the differences in even more recent law of the wall constants,[3] so too one can except a corresponding uncertainty in the uniqueness of Preston tube calibration formulas. This paper attempts to give some quantitative measure to this uncertainty, and particularly by looking at different flow circumstances, since relatively few data are available for the boundary layer case.

[1] By J. E. McAllister, F. J. Pierce, and M. H. Tennant, published in the June 1982 issue of the ASME JOURNAL OF FLUIDS ENGINEERING, Vol. 104, No. 2, pp. 156-161.

[2] Department of Mechanical and Industrial Engineering, University of Melbourne, Melbourne, Australia.

Flow Behind Two Coaxial Circular Cylinders[1]

P. K. Stansby[2]

The authors have presented some most interesting results about the influence of a prominent discontinuity on vortex shedding from cylinders. An important and surprising conclusion is that there appears to be little effect of the discontinuity at distances greater than two diameters from it.

A minor point of concern exists about the choice of a diameter ratio of 2:1 for the coaxial cylinders. For a single cylinder there are peaks in the pressure spectrum at the Strouhal frequency and at twice this frequency. In the coaxial case, the Strouhal frequency for the small cylinder is nearly twice the Strouhal frequency for the large cylinder and there must be some doubt about the origin of a peak at this frequency on a pressure spectrum. Choosing a diameter ratio away from 2:1 would avoid this problem.

The flow at the discontinuity must be rather complicated. However the trailing vortices generated at the leading edge of the big cylinder are likely to be prominent. These streamwise vortices rotate to produce a downwash behind the big cylinder. (The same mechanism can cause smoke from a chimney in a high wind to be entrained in its wake.) Fluid from outside the wake will thus be entrained at the base of the big cylinder, effecting base bleed which can suppress vortex shedding as mentioned in the paper. The influence of the trailing vortices on one another will cause them to be deflected downwards. These vortices are likely to be a prominent feature of the "discontinuity wake" discussed in the paper. It is interesting to note that their rotation is such that they could join up with the vorticity separating from the big cylinder, thus providing an "end" for the vortices of the big cylinder. The vortices of the small cylinder presumably end in a more conventional manner as the flat end of the big cylinder acts to some degree as an end plate as mentioned in the paper.

A final interesting point concerns the maximum values of C_p' away from the discontinuity; they are higher for the big cylinder than for the small cylinder (see Fig. 6). At first sight this might be thought to be a permanent influence of the discontinuity. However the influence of the "other" ends could well be significant. The aspect ratio for the big cylinder is 5.6 while that for the small cylinder is 11.2. The greater relative proximity of the tunnel wall could make the big

[3] Pierce, F. J., McAllister, J. E., and Tennant, M. H., "Near-Wall Similarity in Three-Dimensional Turbulent Boundary Layers Part I: Model Review," ASME Paper FE-33, 1982.

[1] By N. W. M. Ko, published in the June 1982 issue of THE JOURNAL OF FLUIDS ENGINEERING, Vol. 104, No. 2, pp. 223-227.

[2] Simon Engineering Laboratory, University of Manchester, Manchester M13 9PL England.

cylinder wake more two-dimensional than the small cylinder wake causing higher fluctuating pressures (2). Making the aspect ratios equal through the use of end plates would be enlightening.

Authors' Closure

The authors welcome the comments of Dr. Stansby on their paper. Dr. Stansby has pointed out that the choice of the diameter ratio of 2:1 for the coaxial cylinders might introduce some uncertainty in the identification of the peaks on a pressure spectrum. In fact, this effect has been observed during the early stage of the investigation and the well established single cylinder results were used to confirm the peak. As can be seen from Fig. 2, the Strouhal frequency for the small cylinder is clearly different from that of the twice the Strouhal frequency for the large cylinder. Furthermore, the present results form only part of a detailed investigation in which other diameter ratios were adopted.

The authors agree with Dr. Stansby that the flow at the discontinuity is very complicated. The exact mechanism of the trailing vortices of the big cylinder and of the "discontinuity wake" and their interaction are still not yet known. These trailing vortices and the entrained fluid outside the wake, besides those of the vortices of the small cylinder, may affect base bleed which may suppress vortex shedding of the big cylinder. Further investigation is being directed to the understanding of this basic mechanism.

For the difference in the maximum value of C_p' away from the discontinuity the authors did not know the exact cause. The suggestion for the use of end plates of Dr. Stansby in maintaining equal aspect ratio is worth pursuing.

Effects of Free-Stream Turbulence on Diffuser Performance[1]

S. V. Horn[2]

The author is congratulated on providing experimental data on the pressure recovery enhancement of two-dimensional subsonic diffusers by means of the stationary turbulence generators as rods.

The highlight of the paper is an introduction of effects of turbulence structure parameters as the free-stream integral scale of turbulence in addition to the turbulence intensity.

The overall analysis lacks the information about the energy loss of the rod turbulence generator which would enable us to compare optimum systems with and without turbulence generators. Can the author provide this additional information?

The pressure recovery of investigated diffusers was established from the wall taps. More consistent experimental data are usually provided by the mass-averaged pressure recovery. Can the author estimate or measure a difference between the mass-averaged and the wall pressure recovery at diffuser exit?

In turbomachinery applications, the high turbulence downstream of blading can allow us to design annular diffusers with larger deceleration than for cases with a low turbulence level [25].

The swinging turbulence flag generators were used to model the turbulent flow field downstream of blading. The turbulence structure downstream of these generators was closer to the turbomachine turbulence structure than one generated by stationary generators. The best results were achieved by a combination of both which modeled both stationary and rotating turbomachine rows.

Pressure loss of the turbulence flag generators was unusually high which excluded them from potential use in diffuser applications. Successful applications, however, were made by placing the ring-star generators within axisymmetric diffusers [26].

Additional References

25 Horn, S. V., "Optimization of Axi-radial Diffuser Wall Contours Based on the Skin Friction Coefficient Distribution," Aero-Thermodynamics of Steam Turbines, WAM ASME, 1981.

26 Kmoníček, V., and Hibš, M., "Results of Experimental and Theoretical Investigation of Annular Diffusers (in Czech), Volume "Major Developments in the Gas Turbine Design," Czechoslovak Academy of Sciences, 1962.

Authors' Closure

I thank Dr. Horn for his questions and comments.

To obtain the total pressure loss across the rods and the inlet to the channel (ΔP), the difference in pressure between static pressure taps located in the topplate and baseplate upstream of the rods and a total pressure probe located in the free-stream at the diffuser inlet (section 1) was measured and is presented below as a dimensionless loss coefficient for each rod set

Rod Set	$\Delta P/\rho\bar{U}^2/2(\%)$	Rod Set	$\Delta P/\rho\bar{U}^2/2(\%)$
none	0.1	H	0.6
A	1.7	I	0.3
B	0.8	J	0.5
C	2.5	JH	1.5
D	0.8	K	1.1
E	2.4	KH	2.3
F	0.9	L	1.1
G	0.5	M	1.7
GH	1.5	N	0.7

I have not measured mass averaged static pressures at the diffuser exit and do not know of a reliable way to obtain this information. The work of Ashjaee [24] has shown that for $10° < 2\Theta < 20°$, approximately three percent larger exit wall C_p's exist on the unstalled wall due to streamline curvature near the intersection of the diffuser wall and the parallel-walled tailpipe, while for $2\Theta < 8°$, no measurable differences in wall C_p's exist. For two-dimensional straight-walled subsonic diffusers with free discharge, I would expect less streamline curvature at the exit plane and I estimate that the C_p's presented in my report based on the discharge static pressures as measured with wall taps are within one percent of the C_p's based on the mass averaged exit static pressures.

Additional References

24 Ashjaee, J., and Johnston, J. P., "Straight-Walled, Two-Dimensional Diffusers—Transitory Stall and Peak Pressure Recovery," ASME JOURNAL OF FLUIDS ENGINEERING, Vol. 102, Sept. 1980, pp. 275–282.

Scaling Parameters for a Time-Averaged Separation Bubble[1]

I. P. Castro.[2] The most interesting suggestion made by the

[1] By J. A., Hoffmann, published in the September, 1981 issue of the JOURNAL OF FLUIDS ENGINEERING, Vol. 103, No. 3, pp. 385–390.

[2] Borg-Warner Corporation, Des Plaines, Ill. 60018.

[1] By A. J. Smits, published in the June, 1982, issue of the JOURNAL OF FLUIDS ENGINEERING, Vol. 104, No. 2, pp. 178–184.

[2] Department of Engineering, University of Surrey, Guildford, Surrey GU2 5XH, England.